NOVA SCHOOL OF SCIENCE & TECHNOLOGY

DEPARTAMENT OF MATERIALS SCIENCE

YARN SHAPED FUNCTIONAL NANOCOMPOSITES FOR TRIBOELECTRIC ENERGY HARVESTING SYSTEMS

RAQUEL ALEXANDRA ANTUNES BARRAS

Master in Micro and Nanotechnology Engineering

DOCTORATE IN NANOTECHNOLOGIES AND NANOSCIENCES

NOVA University Lisbon

October. 2023

DEPARTAMENT OF
MATERIALS SCIENCE

YARN SHAPED FUNCTIONAL NANOCOMPOSITES FOR TRIBOELECTRIC ENERGY HARVESTING SYSTEMS

RAQUEL ALEXANDRA ANTUNES BARRAS

Master in Micro and Nanotechnology Engineering

Adviser: Luís Miguel Nunes Pereira
Invited Associate *Professor, NOVA School of Science and Technology*

Co-adviser: Pedro Miguel Cândido Barquinha
Associate Professor, *NOVA School of Science and Technology*

Examination Committee:

Chair: Rodrigo Ferrão de Paiva Martins,
Full Professor, *NOVA School of Science and Technology*

Rapporteurs: Libu Manjakkal,
Assistant Professor, School of Computing Engineering and the Built Environment of Edinburgh Napier University, Scotland

Paula Maria Lousada Silveirinha Vilarinho,
Associate Professor, Department of Materials and Ceramics Engineering of the University of Aveiro

Adviser: Luís Miguel Nunes Pereira,
Invited Associate Professor, *NOVA School of Science and Technology*

Members: João Oliveira Ventura,
Principal Investigator, Faculty of Sciences, University of Porto

Diana Filipa Pereira Gaspar,
Senior Investigator, AlmaScience

DOCTORATE IN NANOTECHNOLOGIES AND NANOSCIENCES

NOVA University Lisbon
October 2023

Yarn Shaped Functional Nanocomposites For Triboelectric Energy Harvesting Systems

ACKNOWLEDGMENTS

I cannot deny that this PhD has been a long, arduous, and often solitary journey. However, it would not have been possible without the unwavering support of the people who walked alongside me, either directly or indirectly. Looking back, I consider myself extremely lucky to have had the opportunity to share this part of my life with such amazing people. This chapter is dedicated to all those who, in their own unique ways, made this journey more manageable. I would like to acknowledge and express my gratitude to each of you in the following lines.

First, I would like to thank Prof. Rodrigo Martins and Prof. Elvira Fortunato has the leaders of my host institution Cenimat (Materials Research Center) and CEMOP (Center of Excellence in Microelectronics and Optoelectronics Processes) for hosting me and providing me with the tools necessary to perform my work plan.

This work would not have been possible without the financial support of Portuguese Foundation for Science and Technology under the scholarships SFRH/BD/139224/2018 and COVID/BD/153294/2023, the IDS-FunMat-INNO project FPA2016/EIT/EIT RawMaterials Grant Agreement 17184 and 2022.04012.PTDC SMART-E project. This work was supported by the Grant Agreements number, 640598 (ERC-2014-STG NEW-FUN), 952169 (SYNERGY, H2020-WIDESPREAD-2020-5, CSA), 101008701 (EMERGE, H2020-INFRAIA-2020-1) and by the project CELLECTIVE with the reference PTDC/CTM-CTM/4653/2021.

To my advisor Prof. Luís Pereira, thank you for providing me with the opportunity to develop scientific research in this field, for the financial support, for sharing your knowledge and mostly for providing me with numerous opportunities to travel. Thank you Prof. Pedro Barquinha for co-supervising my work and for your enthusiastic support in the bureaucratic affairs.

During this journey, I had the opportunity to travel, attending international schools that so greatly contributed to my personal growth. I hereby would like to thank Thierry Toupance for managing the IDS FunMAT INNO II School, as well as all the colleagues with whom I shared this experience. On behalf of this project, I also had the opportunity to spend some time getting to know the Textile Research Institute of Thuringia-Vogtland. I would like to extend my gratitude to Dominique Gampe, Kay Ulrich, Julia Cramer, Jirko, Steffi from Zeulenroda, and all those individuals whom I may not be able to mention individually. Their warm welcome and support made me feel at home during the nearly three months I spent at TITV in Greiz. Thank you also to Essi Glomb and Karina Wirth from Textile Prototyping Lab (TPL) in Berlin, for the collaboration in the weaving activities.

Additionally, on behalf of the Synergy project, I had the opportunity to spend nearly one month at a foreign institution doing scientific research and expanding my knowledge. From here I would like to thank Diana Gaspar for the support during the application and Dr. André Clausner, Sylvia Conzendorf, Julia, Bowen and Stefan, thank you for your support and friendship during my stay at Fraunhofer IKTS in Dresden which I utterly enjoyed.

Thank you to all the team/colleagues from the MEON group: Alexandra Gonçalves, Ana Pimentel, Ana Rovisco, Ana Santa, Andreia dos Santos, Ângelo dos Santos, António Vicente, Asal Kiasadeh, Beatriz Coelho, Bruno Mendes, Carolina Marques, Carlos Silva, Cátia Figueiredo, Cristina Gaspar, Daniela Gomes, Diana Gaspar, Emanuel Carlos, Guilherme Ferreira, Guilherme Ribeiro, Inês Cunha, Ivan Santos, Jenny Boane, Joana Pinto, Jonas Deuermeier, João Coelho, Jorge Martins, José Tiago Carvalho, Madalena Roque, Maria Morais, Mariana Cortinhal, Mariana Matias, Marta Corvo, Marta Luís, Miguel Franco, Miguel Alexandre, Paul Grey, Pedro Moreira, Raquel Martins, Ricardo Ferreira, Rita Branquinho, Rui Igreja, Sara Silvestre, Sofia Ferreira, Tiago Mateus, Tomás Pinheiro, Ugur Menda and Zulema Serrano.

Especially, thanks Ana Pimentel for the DSC measurements, Maria Morais for the XRD, Ana Rovisco e Daniela Nunes for the wonderful SEM images, Tiago Mateus for advice and help build the automatic systems (really, the best part of this work) and 3D printing knowledge, Pedro Moreira for some of the 3D printing pieces at the end and Bruno Mendes for supporting me with your knowledge on all things CNCs !

Special thanks to the colleagues from the Fun Paper lab, particularly in these last months: José, Beatriz, Madalena, Bruno, Mariana, Tomás, Sofia and Mariana for making the work environment more enjoyable. Thank you, Diana, for your support generally in everything from the lab to bureaucratic matters.

Andreia dos Santos, thank you for all the knowledge you shared with me in my first years of PhD and thank you for your friendship. We'd had some great times together traveling, although they were mostly spent before the PhD the joy lasted until today!

To the students whose work I've supervised, particularly Carolina Viegas, Carlos Duarte, and twice Edgar Coimbra, thank you for trusting in me. I'm glad that I had the opportunity to learn from you as well.

D. Angelina, Sr. Sérgio, Raquel, Bruno e Francisco, thank you for kindly taking me into your family and supporting me, it means a lot to me.

My PhD companion and dearest friend Zé Tiago Carvalho, I think I wouldn't have survived this journey without your company. Your support and friendship have been truly important through these years, and you made this journey much more pleasant to navigate. Thank you for sharing the motivation, good spirits, encouraging words, the long hours of travel, gossiping, parties, and most of all for being the greatest friend one can deserve. You are the best!

My dearest and oldest friend Iris Gonçalves, even miles away you were always there for me. Thank you for your true friendship, for always giving me your kind and sincere support over these years. I'm forever grateful to the universe for we have found and kept a friendship like this. You rock, I love you!

To my family, my parents for making of me mostly what I am, thank you for supporting me in the way you could. My grandparents, my auntie Zélia, my cousins Cláudia and Daniel, thank you for being part of my world. My beautiful big brother Ricardo, my beautiful little sister Rita, my beautiful little brother Rafael, thank you for your friendship, I love you.

My dear Tiago Mateus, you were the person who accompanied me every day of the journey. You've always been by my side, sticking up with me with my good and bad moods. It's been a joyful journey to walk with you and grow alongside you over these years in which we've changed and learned so much together. Thank you for this.

"We may not be responsible for the world that created our minds, but we can take responsibility for the mind with which we create our world." (Gabor Maté).

ABSTRACT

Triboelectric Nanogenerators (TENGs) are mechanical to electric energy converters and ideal candidates for exploiting the wasted energy from natural cyclic movements of the human body. In this context, the work of this PhD is focused on the development of Single Electrode Yarn Shaped Triboelectric Generators (Seys-TENGs) through an innovative method of Polydimethylsiloxane (PDMS) curing around conductive carbon fiber yarns (CF yarns), named in-situ curing of PDMS. This process promotes the cure of PDMS inside-out through heat generated by an electric current passing through the conductive yarn. A study regarding the precise control over PDMS thickness by varying the curing parameters is presented, and the correlation between the device dimensions and the power generation is established. Different strategies were adopted to enhance the overall surface charge density, namely, the introduction of porosities into the PDMS matrix, the functionalization of the CFs yarn surface using vertically aligned ZnO nanorods grown by hydrothermal synthesis, loading of PDMS with several amounts of conductive chopped carbon fibers (cCFs) and finally, the introduction of a Cellulose Nanocrystal (CNC) interlayer on the Seys-TENG structure. The best results were obtained using the strategy of mixing cCFs in the PDMS matrix, exploring the enhancement effect provided by polarization at interfaces of conductive particles and the polymer. The optimized loading of 2 % wt. cCFs into the PDMS and in-situ curing using 0.2 A for 4 min resulted in Seys-TENGs with a diameter of 2.16 mm. A maximum power density of 1063.23 μW/m was obtained (using a loading resistor of 20 MΩ) which corresponds to an increase of 53 % compared with the Smooth Seys-TENG.

Keywords: Triboelectricity, Energy Harvesting, Wearables, Triboelectric Nanogenerators, TENGs, Fiber TENGs, Single electrodes fiber TENGs, PDMS, Carbon Fibers.

RESUMO

Os Nanogeradores Triboelétricos (TENGs) são conversores de energia mecânica para elétrica e os candidatos ideais para aproveitar a energia "desperdiçada" dos movimentos cíclicos naturais ao corpo humano. Nesse contexto, o trabalho deste PhD consistiu no desenvolvimento de *TENGs* em formato de fio e compostos por um único elétrodo (*Seys-TENGs*) através de um método inovador de cura de Polidimetilsiloxano (PDMS) ao redor de fios condutores de fibra de carbono (fios de CF), denominado de cura *in-situ* de PDMS. Esse processo promove a cura do PDMS de dentro para fora através de calor gerado por uma corrente elétrica que passa pelo fio condutor. Foi feito um estudo sobre o controle preciso da espessura do PDMS variando os parâmetros de cura, e foi feita a correlação entre as dimensões do dispositivo e a geração de energia. Foram adotadas diferentes estratégias para aumentar a densidade de carga superficial dos *Seys-TENGs*: a introdução de porosidades na matriz de PDMS, a funcionalização da superfície dos fios de CF usando *nanorods* de ZnO alinhados verticalmente e crescidos por síntese hidrotermal, adicionado fibras de carbono cortadas (cCFs) em várias proporções ao PDMS e, finalmente, a intercalação de Nanocristais de Celulose (CNC) na estrutura do *Seys-TENG*. Os melhores resultados foram obtidos através da introdução de cCFs na matriz de PDMS, explorando assim o efeito da polarização nas interfaces entre as partículas condutoras e o polímero. A proporção otimizada de 2% em peso de cCFs no PDMS, seguida da cura *in-situ* usando uma corrente de 0.2 A durante 4 minutos, resultou em *Seys-TENGs* com um diâmetro de 2.16 mm. Foi obtida uma potência linear máxima de 1063,23 μW/m (usando uma resistência de carga 20 MΩ), o que correspondeu a um aumento de 53 % em comparação com o *Seys-TENG* de referência.

Palavras chave: Triboeletricidade, Aproveitamento de energia,a *Wearable*, Nanogerador triboelétrico, *TENGs*, *TENGs* em forma de fibra, TENGs em forma de fibra de elétrodo único, PDMS, fibras do carbono

CONTENTS

LIST OF FIGURES

LIST OF TABLES

ACRONYMS

1D	One dimensional
3D	Three Dimensional
AC	Alternate Current
BB	Bamboo Board
CEMOP	Center of Excellence in Microelectronics and Optoelectronics Processes
Cenimat	Materials Research Center
CF	Carbon Fiber
CNC	Nanocrystalline cellulose
CNT	Carbon Nanotubes
CS	Contact Separation
CxS	Coaxial Structure
$\mathbf{d_{33}}$	Piezoelectric coefficient of 33-mode configuration
DC	Direct Current
DSC	Differential Scanning Calorimetry
EIS	Electrical Impedance Spectroscopy
FTIR	Fourier Transform Infrared Spectroscopy

GFAM	Gravitational Force Actuator Machine
GO	Graphene Oxide
H-CNC	Hydrogenated Nanocrystalline Cellulose
KNN	Potassium Sodium Niobate
MEMS	Micro-Electromechanical Systems
MWCNT	Multi Ealled Carbon Nanotubes
NR	Nanorods
NW	Nanowires
P(VDF-TrFE)	Poly(Vinylidenefluoride-Trifluoroethylene)
PAN	Polyacrylonitrile
PDMS	Polydimethyl Siloxane
PFAM	Pneumatic Force Actuator Machine
PV	Photovoltaic
PVDF	Polyvinylidene Fluoride
PZT	Lead Zirconate Titanate
RF	Radio Frequency
rGO	Reduced Graphene Oxide
SE	Single Electrode
SEM	Scanning Electron Microscopy
Seys-TENG	Single Electrode Yarn Shaped Triboelectric Energy Nanogenerator
TE	Thermoelectric Energy
TENG	Triboelectric Energy Nanogenerator
TGA	Simultaneous Thermal Analyzer

UNINOVA Institute for New Technologies' Development

XRD X-ray diffraction

ZTO Zinc-Tin Oxide

SYMBOLS

2θ	Angular position
A	Area
C	Capacitance
c	Specific heat
f	frequency
F	Farads
I	Current
m	mass
P	Electrical Power
Q	Energy in the form of heat
R	Resistance
R_{Load}	Load Resistance
s	second
t	time
T	Rate of heat transfer
tex	Yarn linear density

V	Voltage
Z	Impedance
Z_{imag}	Imaginary part of Impedance
Z_{real}	Real part of Impedance
ε	Permittivity
ε_0	Absolute Permittivity (8.85×10^{-12} F/m)
θ	Angle
κ	Relative permittivity/ Dielectric constant
π	pi (Archimedes' constant)
σ	Electrical conductivity
ϕ	Phase Shift
Ω	Ohms

1

MOTIVATION

1.1 Context and Motivation

Wearable technology has evolved for ultra-functionality: from portable electronic devices like smartphones and tablets, headsets, earplugs and smartwatches to devices for sensing of vital body parameters, the list goes on. The trend for wearables is growing mainly in the healthcare and consumer electronics sectors, and forecasts point for this market to reach almost USD 400 billion by 2030.[1] However, one evolutionary bottleneck for further massification of this technology is the lack of a reliable energy supply. The advances in this field struggle to accompany the evolution of sensors and electronic devices. The main technology used to power portable electronic devices are based on rechargeable Li batteries, which have limitations in terms of flexibility and portability, power capacity, problems related to raw materials sourcing, waste management and recycling. The usage of electric power on wearable-related electronics makes in-situ wearable energy harvesting, namely the transformation of wasted mechanical energy from body movements to usable electric energy seem like an obvious option. Elimination of the need to replace batteries and better efficiency derived from absence of long-distance electronic transmission are some of the main advantages of adopting this technology.[2]

Triboelectric energy nanogenerator (TENG) devices were recently invented in 2012 by Zhong Lin Wang group[3] and its functioning principles are based on the spontaneous phenomenon of triboelectrification between isolating materials upon contact and cyclic movement

that promotes electrical induction on the electrodes. The naturally low frequency of human movements and the necessary use of flexible systems turn TENGs on the ideal energy-harvesting operation systems for wearables.[4] This new generator technology was received with enthusiasm by the scientific community and a lot of scientific work have been published so far primarily concerning the increase in the energy efficiency of these devices.

Wearable TENGs can be constructed by utilizing textiles as substrates or, alternatively, by using fibers or yarns. The latter approach opens the possibility of a more organic integration by providing enhanced flexibility, malleability, and breathability. However, developing fiber or yarn-shaped devices and scaling up their production poses significant challenges. This is primarily because the technologies for depositing functional layers must be adjusted to align with the 1D geometry of yarns and fibers.

Polydimethylsiloxane (PDMS) is one of the most used materials for the fabrication of TENGs. Its popularity is owed to its ability to generate triboelectric charges, allied to its fast and straightforward preparation methods, superior flexibility and transparency, and easy bulk or surface modification [5][6][7]. It is also non-toxic and relatively cheap [8]. Most PDMS-based TENGs rely on a planar structure that is not meant to fully integrate textile weaving structures[7]. Only a few examples can be found in the literature reporting the use of fiber/yarn PDMS-based TENGs. Tian et al.[9] used a sacrificial heat shrinkable tube as a mold for PDMS core-shell coaxial structure. Kim et al.[10] used a PDMS and Ecoflex mixture to coat a tube-shaped hollow structure. The Wang group[11][12] produced several silicone elastomer-based fiber TENGs in a knitted structure with a peak power intensity of 85 mW/m^2. Their fabrication consisted of curing the silicone elastomer for about 4 h inside a mold where a stainless-steel conductive yarn is placed, in a time-consuming process and using a somehow complex apparatus. While these techniques are capable of consistently producing PDMS coatings, several technical aspects make this method somewhat complex:

- A mold with the exact size of the final PDMS layers is required, so several different molds are necessary to achieve specific thicknesses.
- Centering and hanging the fibers vertically inside the mold is not a straightforward task.

- As both ends of the fiber should be accessible (not incorporated inside the polymer), the base of the mold needs to have a perforation, which enables the possibility of leakage occurring.
- The curing process at room temperature is time consuming.

All these details increase the complexity of applying this type of coating to 1D electrodes.

In addition, PDMS is a silicone elastomer with inherent thermosetting properties, which implies that temperature and time promote its irreversible curing / hardening. Herein, a new alternative in-situ curing method is proposed to take advantage of the inherent property of thermosetting silicone elastomer of irreversible curing/hardening of the polymer with time/temperature. It can be used to deposit a thin or thick layer of thermosetting polymer around any conductive fiber or yarn. By injecting a current through the yarn, energy will be lost in heat, known as the Joule effect. When placed inside the thermosetting polymer, the heat promotes local curing around the fiber and hardens it inside out. CF yarns with high conductivity and mechanical properties were selected to develop Single Electrode Yarn Shaped TENGs (Seys-TENGs) using the new in-situ curing technique of PDMS.

There are several strategies to enhance surface charge density on TENGs. It is known that the introduction of air gaps or the use of porous materials can enhance triboelectric energy conversion as a result of simultaneously enhancing the surficial area of contact, inducing extra friction inside the structure by increasing the elasticity of the material and promoting the accumulation of charges at the polymer/air interface that increases the overall permittivity of the polymer.

Loading of the polymer matrix with high permittivity nanoparticles can also result in an overall increase of surface charge density by contributing with extra polarization from dielectric particles. ZnO is a n-type semiconductor material whose implementation in electronic devices is of particular interest for its semiconductor properties (direct bandgap, high exciton binding energy at room temperature)[13] combined with its nontoxicity and antimicrobial features, biocompatibility, chemical stability and widely abundant in nature.[14][15] Additionally, ZnO is a polar molecule with a permanent dipole that promotes electronic polarization at

low frequencies. Its ability to enhance the overall permittivity of polymers when combined as an additive filler in nanoparticle form was already proven. [15] ZnO NRs are easily synthetized at low-temperature solvothermal synthesis. [13][14]

Filling polymers with conductive particles is another strategy utilized to enhance the surface charge density. This can be achieved through the accumulation of charges at the interfaces of conductive particles and the polymer matrix, leading to an enhancement of the permittivity of polymers. [16] In this regard, chopped CFs (cCFs), often blended with polymer resin to improve its mechanical properties, were chosen, and utilized in this work. To the best of the authors' knowledge, cCF has never been used before as a strategy to enhance the output of TENGs.

Intercalating an ionic layer into the polymer structure enhances surface charge density through additional charge trapping, ionic polarization, and the presence of permanent dipoles.[17] Cellulose, the most abundant biopolymer on Earth, can be derived from various sources, including plants, bacteria, and fungi. [18] Acid dissolution of the amorphous phase results in cellulose nanocrystals (CNCs), which can be used to produce highly oriented self-assembled films. The mesoporous structure of CNC films, the presence of sulphonated groups on CNC surfaces, and hydrogen bonds make these films promising candidates for implementation as charge trapping layers.

Herein, this work reports the development of single electrode yarn shaped (Seys- TENGs) constituted of CF yarn and fabricated through an innovative technique of in-situ Joule heat curing of PDMS around the conductive yarns. Further enhancement of mechanical to electrical energy conversion is investigated by introducing porosities on the PDMS structure, functionalization with aligned ZnO NRs, filling of cCFs on the PDMS structure and introduction of a CNC layer in the Seys-TENG structure.

1.2 Objectives

The goal of this thesis is to develop wearable triboelectric nanogenerator devices capable of converting mechanical energy into electrical power. These devices are designed to be integrated into textiles, enabling them to power wearable devices or extend their battery life. The focus of this work is on a specific type of single-electrode, yarn-shaped triboelectric nanogenerator, referred to as Seys-TENG.

The key objectives of this research can be summarized as follows:

1. Development of Seys-TENGs for wearable applications using the in-situ curing technique:
   - Study and optimization of the in-situ curing technique parameters, including the applied current and curing time.
   - Investigation and optimization of device geometry, specifically the thickness of the PDMS layer.
2. Investigation and implementation of various strategies to enhance the conversion rate of Seys-TENGs, including:
   - Incorporation of porosities within the PDMS structure.
   - Integration of vertically aligned ZnO NRs on the CF surface.
   - Loading cCFs into the PDMS matrix, with an emphasis on optimizing the loading percentage.
   - Incorporation of a nanocrystalline cellulose (CNC) layer positioned between the CF yarns and the PDMS. This involves optimizing the deposition process, the geometry of deposited film layers, and film thickness through control of deposition current and time.

In addition, the need for a standardized system for testing Seys-TENGs and facilitating a comprehensive comparison and analysis of their mechanical-to-electrical energy conversion capabilities led to the creation of an automatic force applicator machine. This machine ensures consistent and reliable testing of these devices.

1.3 Methodologies and thesis outline

This PhD is divided into seven main chapters. **Chapter 1** contains the context, objectives, motivation and the PhD thesis outline, as well as a summary of the scientific disseminations presentations that took place during the period of this thesis.

In **Chapter 2**, a general introduction to the topic of energy harvesting will be given, with particular focus on the types of energy produced by the human body and technologies compatible with wearable application. The fundamentals of triboelectricity and the working principle of TENGs, the different structures of TENG transduction modes and strategies for enhancing energy conversion efficiency will be discussed. Lastly, the state of art regarding fiber and yarn TENG devices will be presented.

In **Chapter 3**, the in-situ curing method, the Seys-TENG devices fabrication methodology, the morphological and structural characterization techniques and the electric characterization procedure will be described. The fabrication methods for developing two different automatic mechanical force application systems are described, as well as the development of a rotary system for the uniform electrophoretic deposition on fiber/yarn shaped electrodes.

Chapter 4 presents the results regarding the development of Seys-TENG, the optimization of the in-situ curing deposition technique, the optimization of the dimensions of PDMS layer of Seys-TENGs and the comparison of energy conversion between a smooth and porous PDMS structure.

Chapter 5 shows the results regarding the implementation of two enhancement strategies of Seys-TENGS. Initially, a study on the optimization of the hydrothermal synthesis to grow vertically aligned ZnO NRs was done. An optimization of the PDMS thickness in combination with ZnO functionalized and both Smooth and Porous Seys-TENGs was performed. The possible contribution of the piezoelectric effect on the performance enhancement was discussed. Additionally, the incorporation of cCFs into the PDMS structure was studied. The optimization of the loading content for an enhanced performance was performed and the influence of different concentrations of cCFs into the PDMS matrix dielectric properties was studied.

In **Chapter 6** a study regarding the electrophoretic deposition of CNC based films over CF yarns, a comparison of the uniformity obtained using this method or conventional EPD and optimization of parameters is presented. The introduction of EPD CNC based layer on the Seys-TENG was studied. The influence of the addition of different NaCl concentrations, as well as the ionic exchange of Na^+ on sulfur terminated CNCs structure to H^+ was studied and a discussion over the mechanisms in which it influences the overall power conversion was made.

Finally, in **Chapter 7** a summary of the results and main achievement of the previous chapter was made, the main conclusions and some suggestions regarding the future perspective of this PhD are presented.

1.4 Scientific dissemination and supplementary education

Several collaborations and dissemination activities were developed during this PhD project, and the most important are highlighted on the chronogram of Figure 1.1.

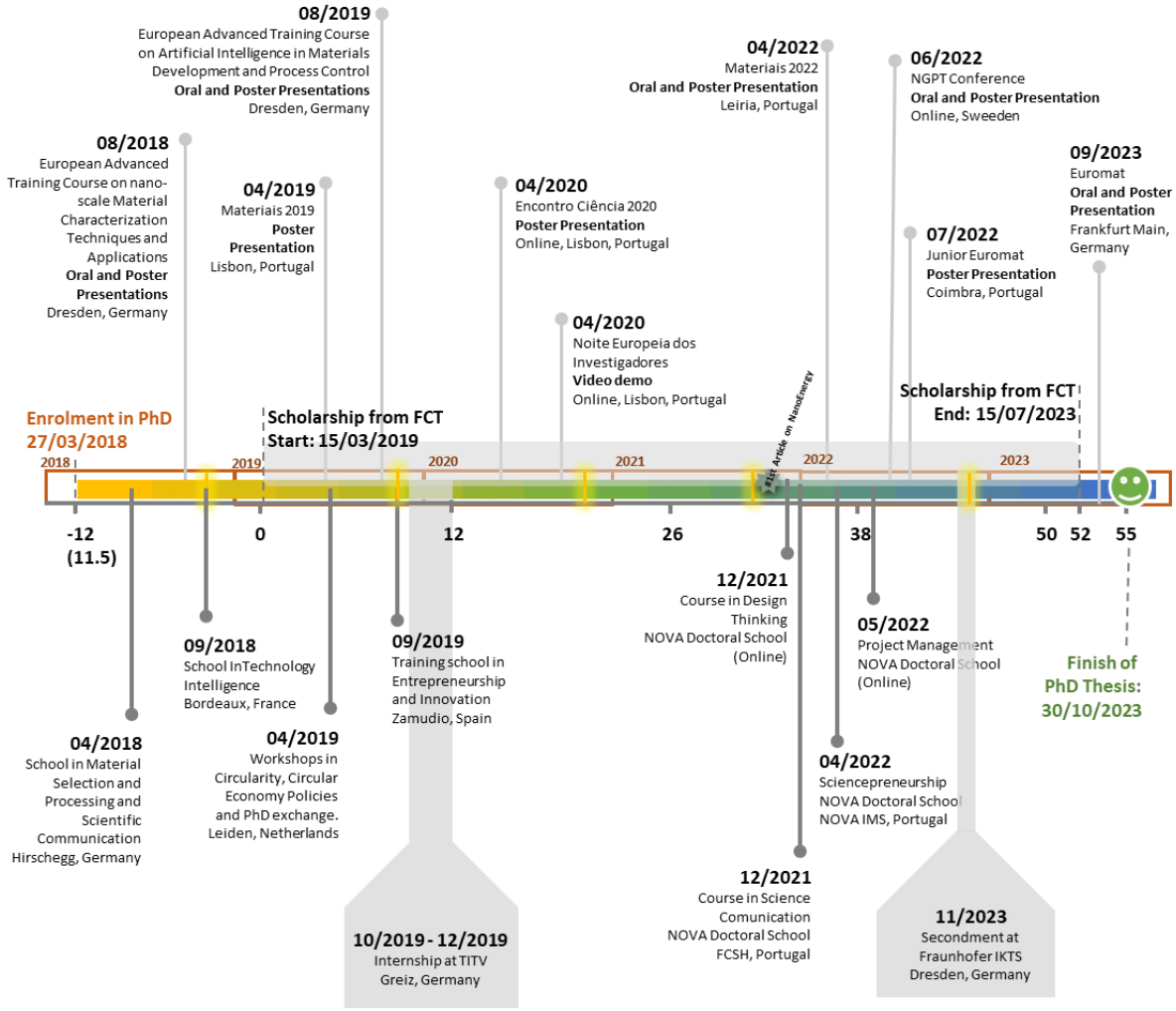

Figure 1.1 -Chronogram of the PhD project output major achievements– scientific writing and dissemination and attending to courses and international schools.

A list of scientific contributions, collaborations and learning opportunities attended during the PhD project are described in the sub-subsections below.

1.4.1 List of scientific publications

1. R. Barras*, A. dos Santos, T. Calmeiro, E. Fortunato, R. Martins, H. Águas, P. Barquinha, R. Igreja, L. Pereira, Porous PDMS conformable coating for high power output carbon fibers/ ZnO nanorod-based triboelectric energy harvesters, Nano Energy, 2021. (IF = 19.069, 2021)

1.4.2 List of oral presentations

1. R. Barras*, E. Fortunato, R. Martins, P. Barquinha, L. Pereira, Functional Oxide Based Nanocomposites For Energy Harvesting Systems, 7th International PhD Seminar, Fraunhofer IKTS, Dresden, Germany (30 of August 2018).
2. R. Barras*, A. dos Santos, E. Fortunato, R. Martins, R. Igreja, P. Barquinha, L. Pereira, Piezo-enhanced triboelectric generator on carbon fiber yarn, 8th International PhD Seminar, Fraunhofer IKTS, Dresden, Germany (28 - 29 of August 2019).
3. R. Barras*, A. dos Santos, T. Calmeiro, E. Fortunato, R. Martins, R. Igreja, P. Barquinha, L. Pereira, Porous PDMS conformable coating for high power output carbon fibers based triboelectric energy harvesters, Materials 2022, Marinha Grande, Portugal (10-13 of April 2022).
4. R. Barras*, A. dos Santos, T. Calmeiro, E. Fortunato, R. Martins, R. Igreja, P. Barquinha, L. Pereira, Porous PDMS conformable coating for high power output carbon fibers based single electrode triboelectric energy harvesters, 6th International Conference on Nanogenerators and Piezotronics - NGPT 2022, Mid Sweden University Sundsvall, online (19-23 of June 2022).
5. R. Barras*, P. Grey, D. Gaspar, R. Martins, P. Barquinha, L. Pereira, Single Electrode Yarn based Triboelectric Nanogenerators Intercalated with CNC Electrophoretic Deposited Films – FEMS EUROMAT 2023, Frankfurt, Germany (6 of September 2023)

1.4.3 List of poster presentations

1. R. Barras*, E. Fortunato, R. Martins, P. Barquinha, L. Pereira, Functional Oxide Based Nanocomposites For Energy Harvesting Systems, 6th Dresden Nanoanalysis Symposium, Fraunhofer IKTS, Dresden, Germany (31 of august 2018).
2. R. Barras*, A. dos Santos, E. Fortunato, R. Martins, R. Igreja, P. Barquinha, L. Pereira, Piezo-enhanced triboelectric generator on carbon fiber yarn, Materiais 2019, Lisbon, Portugal (14-17 of April 2019).
3. R. Barras*, A. dos Santos, E. Fortunato, R. Martins, R. Igreja, P. Barquinha, L. Pereira, Piezo-enhanced triboelectric generator on carbon fiber yarn, 7th Dresden Nanoanalysis Symposium, Fraunhofer IKTS, Desden, Germany (30 of August 2019).
4. R. Barras*, A. dos Santos, T. Calmeiro, E. Fortunato, R. Martins, R. Igreja, P. Barquinha, L. Pereira, Porous PDMS conformable coating for high power output carbon fibers based triboelectric energy harvesters, Materials 2022, Marinha Grande, Portugal (10-13 of April 2022).
5. R. Barras*, A. dos Santos, T. Calmeiro, E. Fortunato, R. Martins, R. Igreja, P. Barquinha, L. Pereira, Porous PDMS conformable coating for high power output carbon fibers based single electrode triboelectric energy harvesters, 6th International Conference on Nanogenerators and Piezotronics - NGPT 2022, Mid Sweden University Sundsvall, online (19-23 of June 2022).
6. R. Barras*, A. dos Santos, T. Calmeiro, E. Fortunato, R. Martins, R. Igreja, P. Barquinha, L. Pereira, Porous PDMS conformable coating for high power output carbon fibers/ ZnO nanorod-based triboelectric energy harvesters, Junior Euromat 2022, Coimbra (19-22 of July 2022).
7. R. Barras*, A. dos Santos, T. Calmeiro, E. Fortunato, R. Martins, H. Águas, P. Barquinha, R. Igreja, L. Pereira, Porous PDMS conformable coating for high power output carbon fibers yarns based triboelectric energy harvesters, Summer School on Materials for Energy Transition, Lisbon (7-9 of September 2022).
8. R. Barras*, A. dos Santos, E. Fortunato, R. Martins, H. Águas, P. Barquinha, R. Igreja, L. Pereira, Porous PDMS conformable coating for high power output carbon fibers-based single electrode triboelectric energy harvesters, 11th European School for Young Materials Scientists, Caparica (27 and 28 of September 2022).
9. R. Barras*, P. Grey, D. Gaspar, R. Martins, P. Barquinha, L. Pereira, Single Electrode Yarn based Triboelectric Nanogenerators Intercalated with CNC Electrophoretic Deposited Films – FEMS EUROMAT 2023, Frankfurt, Germany (6 of September 2023)

1.4.4 List of courses, schools, congresses, and seminars

1. First International Doctoral School on behalf of the European program IDS-FunMat-Inno Spring School on Material Selection and Processing & Scientific Communication, Hirschegg, Germany (8-14 of April 2018).
2. European Advanced Training Course on Nano-scale Materials Characterization Techniques and Applications - Dresden Fraunhofer Cluster of Nanoanalysis, c/o Fraunhofer Institute of Ceramic Technologies and Systems, organized by Gesellschaft für Materialkunde - DGM, Dresden, Germany (27-29 of August 2018).
3. Second International Doctoral School on behalf of the European program IDS-FunMat-Inno on Technology Intelligence, Bordeux, France (24-28 of September 2018).
4. Third International Doctoral School on behalf of the European program IDS-FunMat-Inno Spring School on Circular Economy, Leiden, Netherlands (8-11 of April 2019).
5. TCM NET Graduation School on Materials for Flexible Electronics, Smart Surfaces and Sensing, at the Rectorate of Universidade Nova de Lisboa, Lisbon Portugal, (14 of April 2019).
6. Fourth International Doctoral School on behalf of the European program IDS-FunMat-Inno on Entrepreneurship and Innovation, Zamudio, Spain (30 of September - 4 of October, 2019).
7. European Advanced Training Course on Artificial Intelligence In Materials Development and Process Control - Dresden Fraunhofer Cluster of Nanoanalysis, c/o Fraunhofer Institute of Ceramic Technologies and Systems, organized by Gesellschaft für Materialkunde - DGM, Dresden, Germany (26 - 28 of August 2019).
8. 7th Dresden Nanoanalysis Symposium on Nano-scale characterization for cutting-edge materials research and sustainable materials development, organized by the Dresden Fraunhofer Cluster Nanoanalysis - DFCNA, supported by the European Materials Research Society - EMRS and the European Materials Characterisation Council - EMCC (30 of August 2019).
9. 27th Edition of the Design Thinking Course organized by NOVA Doctoral School from NOVA University of Lisbon, Online Edition (2 - 9 of December 2021 - 28 hours).
10. 20th Edition of the Science Communication Course organized by NOVA Doctoral School from NOVA University of Lisbon, held in Faculdade de Ciências Sociais e Humanas, Lisbon (16 and 17 of December 2021 - 28 hours).
11. 3rd Edition of Sciencepreneur - Entrepreneurship and Science Course, organized by NOVA Doctoral School from NOVA University of Lisbon, held in NOVA IMS- NOVA Information Management School, Lisbon (11 of January - 15 of April 2022 - 56 hours).

12. 28th Online Edition of Project Management Course, organized by NOVA Doctoral School from NOVA University of Lisbon, Online (2 - 30 of May 2022 - 28 hours).

1.4.5 Participation in other scientific events

1. R. Barras, G. Ferreira, A. Rovisco, A. dos Santos, S. Goswami, Mechanical Energy Harvesting Systems for Standalone and Autonomous Power of Low Consumption Electrical Devices, Video Presentation at Encontro Ciência 2020, Hybrid event at Centro de Congressos de Lisboa (2 and 4 of November 2020).
1. Noite Europeia dos Investigadores, Museu Nacional de História Natural e da Ciência, Lisbon (24 of September 2021).
2. Noite Europeia dos Investigadores, Museu Nacional de História Natural e da Ciência, Lisbon (30 of September 2022).
3. Support on the preparation of scientific activities related to the preparation of sensors and Arduino interfaces regarding the scientific program Ciência Viva – 2023.

1.4.6 List of contribution for the scientific monitoring of students

1. Monitoring of a small group of undergraduate students regarding the scientific program Ciência Viva – 2019 with focus on the preparation of printed temperature and humidity sensors.
2. Monitoring of two bachelor students (Carlos Duarte and Catarina Viegas) regarding the scientific course of Introductory Program on Scientific Investigation (PIIC) with the final project: Fiber Nanogenerators. - 2020.
3. Monitoring of one bachelor student (Edgar Camacho) regarding the scientific course of Introductory Program on Scientific Investigation (PIIC) with the final project: Triboelectric Nanogenerator on a Carbon Fiber – 2021.
4. Monitoring of a small group of undergraduate students regarding the scientific program Ciência Viva – 2021 with focus on the preparation of printed temperature and humidity sensors.
5. Monitoring of one bachelor student (Edgar Camacho) regarding his final bachelor's project: Electrophoretic Deposition of CNCs on TENGs based on Carbon Fiber Yarns and PDMS – 2022.

2

INTRODUCTION

2.1 Wearable Energy Harvesting

Ready-to-use and portable electronic devices are progressively becoming essential tools in daily life routine, especially with the impulse of recent advances in artificial intelligence (AI) and the internet of things (IoT). From tablets and mobile phones to small wireless portable devices, smart wearables and standalone monitoring sensors or sensors in remote locations, nowadays, all these devices rely merely on power storage units to operate.[19][20][21] However, the massive increase in the incorporation of sensors that is predicted to occur in the next few years will be difficult to implement by simply connecting each device with an individual and external power energy unit.[22] Wearable devices in healthcare include electrocardiograms, heart and respiratory rate, body temperature, blood pressure, sugar and oxygen continuous monitoring devices. For instance, continuous glucose monitoring (CGM) devices that allows users to be aware of its glucose levels without the need of finger pricking are an example of one of the most successful and helpful biomedical wearable devices, impacting the lives of many million people worldwide suffering from diabetes or pre-diabetic symptoms.[23][24] They exist in the form of sticky patches or implantable devices, collecting the data and sending it to the smartphone or automatic insulin pumps. The global market size of CGM was $20.7 billion in 2020 and is expected to reach $32.7 billion in 2027, with a compound annual growth rate of 9.5%. [25]

Batteries are responsible for the powering of portable off-the-grid electronic systems. But even if there has been significant progress in the field of batteries, many inherent technical disadvantages urge researchers to quickly find alternative or complementary technologies to power portable devices. The high weight and the rigid nature of solid-state batteries makes its integration in portable devices challenging, and the lack of flexibility and stretchability makes it difficult to successfully integrate in wearable applications while preserving comfort for the user. Its limited power capacity shortens the usable life period of electronic devices and requires a periodic replacement or recharging which limits its application.

Additionally, the massive battery demand from the electric car industry[26] accelerated by the European Commission's "Green Deal" urge to reduce greenhouse gas emissions by at least 55% by the end of 2030[27] skyrocketed all the already existing battery problems. Specifically, the increase in the mining of scarce and critical raw materials like lithium, nickel, and cobalt contributes hugely to social and environmental problems and the lack of a functional recycling system. [26], [28]–[31]

In this context, the harvesting of renewable energy sources has been receiving great interest by the scientific community as a potential alternative to periodic replacement of batteries in and reduce the need for high-density power sources by continuously charging from ambient energy sources. The recent miniaturization and optimization of portable electronic devices have significantly reduced their electrical power consumption, typically falling within the range of 10 μW to 100 mW (Figure 2.2 b)), which makes this achievement plausible in the foreseeable future.[32] Various energy sources are available to the wearable realm and can be categorized into human sweat or non-sweat based systems[33]. This technologies include solar, thermal, chemical, and mechanical energy[34] and thus, numerous technologies compatible with wearable integration have been explored for the development of self-powered systems (Figure 2.2 a)).

Thermoelectric energy (TE) generators take advantage of the difference between the constant temperature of the human body and ambient temperature. Typical TE generators are composed of a p-n junction in parallel connected by one perpendicular metal electrode and the effective establishment of a temperature gradient between the up and bottom of the thermocouple promotes the migration of major carriers to the cold side. This phenomenon, known

by Seebeck effect, is responsible for generating a DC voltage. [35] However, the lack of a constant ambient temperature and even fluctuations of skin temperature affect operational stability and the lack of a sufficient thermal difference combined with technical limitations and the use of materials with low figures of merit prevents the establishment of a significant voltage and are responsible for a low conversion efficiency.[36][37][38] Electrokinetic effect, pyroelectricity, ionic thermoelectricity (Soret effect) are other phenomenon's that have been explored in the conversion of heat to electric power but they similarly lack power conversion efficiency.

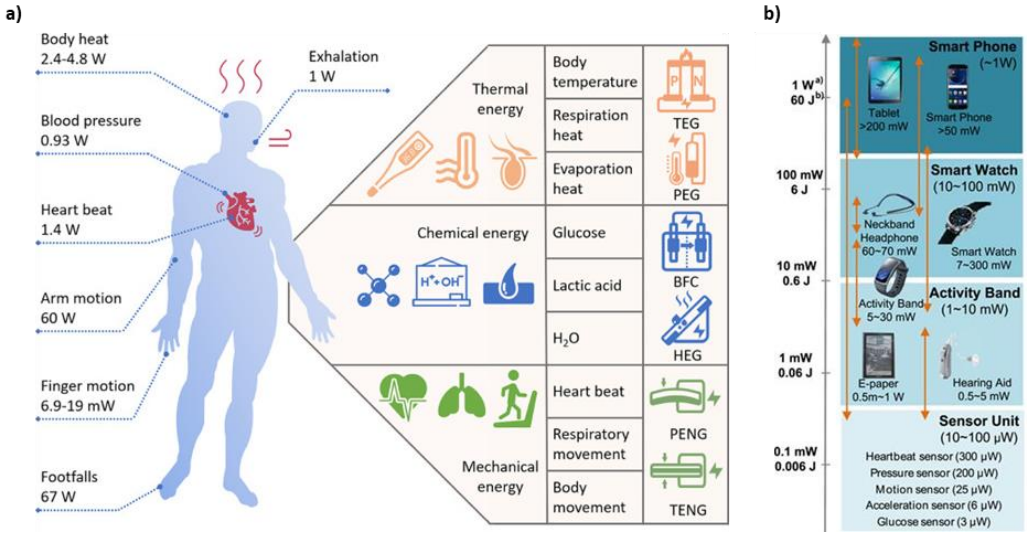

Figure 2.2 – a) Source and distribution of human body energy and applicable energy harvesting technologies (Reproduced from [39]]). b) Power consumption of different types of wearable electronic devices (Adopted from [32]).

Solar energy harvesters convert sunlight into electricity by the photovoltaic (PV) effect and are an effective form of energy conversion with high power generation. [40] Flexible PV cells fabricated from amorphous silicon can be integrated in wearable devices. [41]–[44] Kim et al. developed wearable PVs to be used on different areas of the body and the application of flexible photovoltaic panels mounted on a sleeve tested outdoor in static conditions delivered a maximum of 64 mW.[45] However, the lack of a solar source during the night period, adverse weather conditions and physical indoor permanence pose serious constraints to its applications as a wearable energy source.[42] Batteries and efficient power management circuits can prolong its usability during longer periods of time [41], and the harvesting of artificial light can also extend its usability to indoor activities but still, the normal person will be in complete darkness during around 8 hours for sleep and some additional hours in low intensity

illumination conditions. Additionally, the output is directly proportional to the area of the panel which alongside the limited flexibility of the panels ends resulting in a bulky structure. Another challenge of implementing this technology to wearable applications is the random orientation of the PV cells, will in practice reduce its power generations efficiency.

Chemical sources include enzymatic or microbial biofuel cells that convert chemical energy contained in the biochemical environment of human biofluids (skin-worn, ocular or implantable devices) using enzymes or microbes as catalysts. [46][47] The fundamental challenges regarding this technology are intrinsic enzymatic instability and low output voltage and power, low stability and the emission of CO_2 during operation. [48]

Mechanical energy harvesting technologies can utilize mechanical energy from body motions through electromagnetic, piezoelectric and triboelectric phenomenona. The ubiquitous availability of wasted mechanical energy generated effortlessly from natural movements and motion of the carrier of such devices paves the way for a potentially fantastic opportunity for implementing these types of devices. Walking or running has the greater energy generation ability: it was estimated that a 68 kg person walking at 2 paces per second produces the equivalent of 67 W of power. [49]

Electromagnetic energy generators present high energy conversion capability. The variation of the external magnetic flux near a conductor result in the development of an electromotive force. But the technical aspects of its construction including the presence of moving parts, the linear or rotary geometry, and the requirement of permanent magnets in its construction, results in bulky, rigid and heavy devices that are not ideally compatible with wearable applications.[50] For this reason, piezo and triboelectric generators are more suitable for mechanical energy harvesting in wearable applications.

The transduction mechanism of piezoelectric generators consists of the development of polarization upon mechanical deformation, known as the piezoelectric effect. Conventional piezoelectric materials are ceramic rigid and brittle materials, like Lead Zirconate Titanate (PZT)[51][52][53].Shen et al.[54] produced a micromachined PZT cantilever able to produce a maximum of 416 $\mu W/cm^3$ at its resonant frequency of 183.8 Hz. However, micro-electromechanical systems (MEMS) are rigid, expensive, difficult to manufacture[55][56], and lead is a toxic material that should be avoid on wearable systems. In 2006, the first Piezoelectric

Nanogenerator (PENG) was introduced using ZnO NRs.[57] Since then, the use of micro or nano structured lead-free piezoelectric materials has been explored. Nanostructured ZnO[58][59][60], Zinc-Tin oxide (ZTO)[61][62], Barium Titanate ($BaTiO_3$)[63][64][65] and Potassium Sodium Niobate (KNN)[66][67][68] or polymers like β-phase poly(vinylidenefluoride) (PVDF)[69] and copolymer poly(vinylidenefluoride-trifluoroethylene) (P(VDF-TrFE)[70] made possible the fabrication of small, lightweight, flexible PENGs compatible with wearable applications. These devices can be used to harvest energy from internal processes like heart rate and breathing, or external motion like joint movements, walking, running, etc.[71] However, the output performance of PENGs is significantly lower than that of traditional piezoelectric materials. Additionally, these devices work best under high frequencies that are hardly ever achieved during normal human motion or biological functioning and the implementation of spring actuated mechanisms or another movement converters increases the complexity of the system.

Recently a new mechanical-to-electrical transduction mechanism based on the combination of the triboelectric phenomenon and electrostatic induction has drawn the scientific community's attention for its inherent capacity to function with nearly all types of existing materials and remarkably common polymers. The triboelectric nanogenerators (TENGs) have exceptional qualities over the later energy harvesting technologies arising from their high-power density, high conversion efficiency, light weight, small size, low cost, flexibility and simple structure and fabrication processes.[72][73] These features make is particularly interesting for implementation as an energy sources of wearable devices. Table 2.1 compares the properties of the wearable energy harvesting technologies. Further elaboration on the operating principles and characteristics of TENGs, along with the challenges related to this technology, will be provided in the upcoming subsections.

Hybrid energy generators combine multiple harvesting technologies to obtain higher power conversions that can operate in an enhanced variety of scenarios. Some examples include the combination of piezoelectric and triboelectric effects to enhance the efficiency of the mechanical energy conversion, [74] piezoelectric with electromagnetic [75][76] or the combination of thermoelectric with solar energy [77].

Other examples include the combination of thermomagnetic driven triboelectric devices[78] that could be used extend their operation even without the presence of direct mechanical energy form the human body.

Table 2.1 – Comparison of different wearable energy harvesting technologies. [45][48][79][80]

Technology	Energy Source	Transduction mechanism	Power Output	Advantages	Disadvantages	Ref.
Photovoltaic Energy Generators	Sun light	PV effect	65 mW - Outdoors(DC)	Renewable, inexhaustible energy source, high conversion efficiency.	Bulky, affected by weather, regions and locations (inside or outside buildings), high cost	[45]
Biofuel Cells	Biochemical enzymatic or microbial activity	Internal physiological activity	~ nW	Biodegradable	Low output power, low stability and low shelf life, CO_2 emissions	[48]
Thermoelectric Energy Generators	Temperature gradient	Seebeck, Pyroelectricity, Soret	10 nW – 20 μW (DC)	High durability, precision, small volume, Safety and reliability.	Difficult to miniaturize/ integrate with MEMs, low conversion efficiency	[79]
Electromagnetic Energy Generators	Mechanical	Electromagnetic effect	0.1 μW - 28 W (AC)	High efficiency, high output current, low cost, Easy to scale up;	Rigid, bulky, heavy, and difficult to miniaturize	[79]
Piezoelectric Energy Nanogenerators	Mechanical	Piezoelectric effect	1.2 μW - 45.6 W (AC)	Compact, simple architectures, possible to miniaturized.	Low efficiency, narrow frequency band	[79]
Triboelectric Energy Nanogenerators	Mechanical	Triboelectric effect and electrostatic induction	0.6 μW/cm² - 9.83 mW/cm² (AC)	Simple, low weight, low cost, scalable, robust and reliable, high voltage, high efficiency at low frequencies	High impedance, low current, wear upon friction of materials	[79] [80]

Wearable energy harvesting systems need energy storage units to operate. This can be achieved using rechargeable batteries, capacitors, or supercapacitors. These devices are essential for the successful operation of such systems, as they provide a stable output to the electric systems and also hold electric energy for periods where the energy harvesting cannot function.

2.2 The history of triboelectricity

Effects of triboelectricity are well known to humanity since at least ancient Greeks, 2500 years ago when Thales of Miletus documented experiments rubbing wool and amber together and leading to electrostatic charging[81] but probably way before that, when homo erectus were able to start fires from friction, 1 million years ago[82][83]. Common everyday objects and activities denounce their presence; combing gets hair charged, undressing a sweater or getting out of a car, one may hear a clapping sound and even feel an electrical discharge through touching a conductive material, like the natural phenomenon known as lightening. Charging by triboelectricity is used intentionally on xerographic and laser printing, electrospraying and more recently on TENGs to convert mechanical into electrical energy. It is believed that our planet formed through the sequential aggregation of charged particles[84][85] and that even primary forms of life derived from spark-activated reactions formed the first aminoacids. [86][87] Involuntarily triboelectric charging causes the destruction of microelectronic components or can provoke and ignite dust explosions in barns full of floating particles. Although it is present everywhere in front of our eyes, how these particles and materials charge is still a tremendous unresolved mystery[88][89].

2.2.1 Triboelectric Series

Due to some lacking in fundamental understanding of the mechanisms of triboelectrification, one of the more accurate tools that function as a guide for predicting this phenomenon is the ranking of varied materials in the triboelectric series. It was shortly after the discovery of the two types of electrical charge, baptized by Franklin as positive and negative, and the discovery that material can charge both positively and negatively, that the first triboelectric series was published back in 1757 [89][90][91]. The ranking of materials is done by the empirical observation of how materials charge after contacting each other, and the triboelectric series resembles a scale where materials located on one of the extremes have a stronger tendency to charge negatively or positively with all the remaining materials above or below and vice versa.

However, the problem is that versions published by several authors present differences and contradictions. The constant obtainment of different results, derived from different handling, different ambient conditions of temperature and humidity, different types of contact, mechanical deformation or the use of materials in different sizes and forms, and development of opposite charging between identical materials, clearly indicates that there must be other physical properties apart from chemical composition leading this phenomenon. While this poses an additional challenge for sequencing materials and understanding triboelectric phenomena, it also demonstrate the possibility of tailoring its properties based on specific requirements for various applications which represents an opportunity.

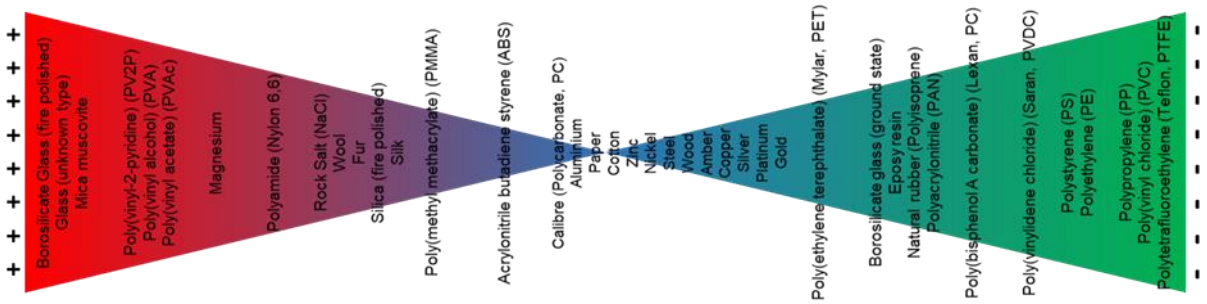

Figure1.3 - Triboelectric series (adapted from [92]). The categorization of compounds solely based on chemical composition is not accurate since there seem to be other numerous physical properties contributing to the triboelectrification phenomenon.

2.2.2 Mechanisms of Triboelectrification

Triboelectrification is the phenomenon occurring after the physical contact of two materials, leading to their surfaces' charging. Although it is generally accepted that this occurs through an exchange of species from one material surface through the other, the type of species is still the focus of an intense and open debate in the scientific community, even if it began millennia ago. [92] The species exchange depends on the nature of the material surfaces in terms of physical state and chemical properties. Electron, ion and material transfer can occur simultaneously. In the lack of a universal theory, it is generally accepted that a dominant mechanism governs the transfer depending on specific cases[93]. The solid-solid interaction is

by far the most studied and the focus of this document, and even in this case, there is controversy.[92]

Electron Transfer

Triboelectrification by electron transfer between metals and semiconductors is a generally accepted theory by the scientific community [92][94] since the work function and fermi level can predict most triboelectric properties.[94] The electrons from the material with the lower work function will be transferred tunnelling [93] to the other until the fermi levels are aligned and reach an equilibrium. But despite the wider band gap on insulating materials, they charge more than semiconductors or metals. [92][94] Main theories suggest either the occurrence of electrons being transferred through intermediate states[92][94] or a lowering of interfacial potential when materials approach at a short distance of a few angstroms facilitating the electron transfer between them[92][95][96]. Additionally, charges at the surface of insulating materials remain longer and do not flow back like in the case of metals, where they may escape due to their conductive nature. [94]

Ionic Transfer

Triboelectrification through ionic transfer is described by the transfer of mobile ions, in the specific case of ionic polymers, and extended to all remaining polymers by a "water-bridge" model that suggests that naturally adsorbed water from the ambient atmosphere is responsible for the exchange of mobile OH^- and H^+ ions that redistribute non symmetrically across different materials upon contact. [92][97] The high triboelectrification of hydrophilic silica beads when in contact with a charged electrode versus the same contact with a hydrophobic material suggests a humidity-dependent contact electrification that sustains this theory. [92][98] Even if some exceptions to this rule still exist [92][97][89] and the universality of this model is incompatible with the existence of nonzero triboelectrification in cases of zero-humidity experiments[92][99][100], a large reduction of its magnitude was found in such

conditions, suggesting that adsorbed water may play a significant role on the triboelectrification of certain materials[92].

Material Transfer

Although the effect of material transfer in the process of triboelectrification was initially disregarded, recent discoveries proving nanomaterial transfers between some insulators after contact have been granting relevance to this phenomenon. [92][101] Specifically, the discovery of a mosaic charge pattern distribution on a conductor after contact with a soft polymer (PDMS) can be explained by the material transfer model since, in the case of a sole electron transfer, a uniform distribution of charge and an equipotential surface would be expected. [92][102] Additionally, it was also found that the mechanical properties of the PDMS are directly related to the amount of triboelectric charge and XPS analysis on PVC after the triboelectrification contact with PDMS revealed the presence of Si 2p characteristics of this material. [92][101] It was also confirmed that material transfer in polymers is often accompanied by cleavage of polymeric chains rendering positive and negatively charged polymer ends in the case of heterolytic cleavage (mechanoions) or non-charged radical polymer ends in the case of homolytic cleavage (mechanoradicals).[92][103][104][105] Several studies targeting the stabilization of this species resulted in the suppression and decay of triboelectric charges[92][106], which indicates that both material transfer generated by friction and electron transfer between mechanoions and mechanoradical species can play significant roles in the triboelectrification between insulating species[92].

2.3 Triboelectric Energy Nanogenerators

Triboelectricity, commonly known as static electricity, is usually seen as an adverse effect and avoided at all costs. In 2012 the way science looks at this phenomenon changed

when Zohn Lin Wang created the first triboelectric nanogenerator. After a decade, this subject continues to captivate the scientific community's interest. Until now, thousands of scientific articles have been written on this subject (Figure 2.4), focusing on the integration and power enhancement of these devices. An introduction to the topic is given in this section.

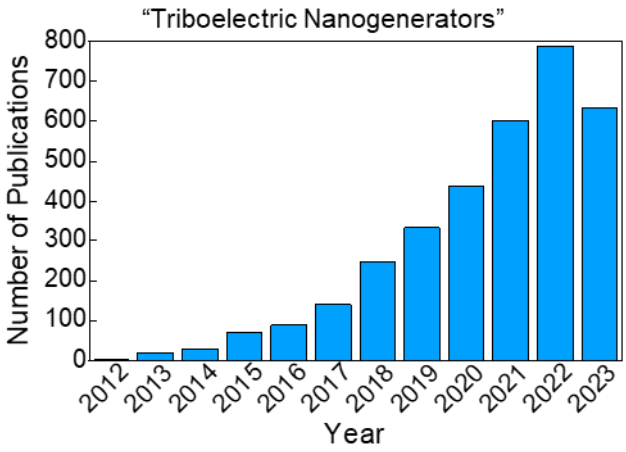

Figure 2.4 – Number of publications per year with the words "Triboelectric Nanogenerators" (Source: www.webofscience.com, visited on 10/2023).

2.3.1 Transduction Modes

TENGs operation consists of four main transduction modes. In Figure 2.5, a schematic representation of the operation modes is shown. The vertical contact-separation mode (Figure 2.5 a)) consists of two electrodes facing each other, each with a dielectric layer that, when brought to contact transfers charge through some triboelectrification mechanisms described in the subsection above. Since the dielectrics can maintain charged, when separated, one becomes positively charged (anode) and the other negatively charged (cathode). The potential difference (or voltage) formed between them creates a flux of charges through the electrodes through electric induction and when brought to contact again, the charges flow back due to cancelling of the potential difference. When done repeatedly, this constant back-and-forth flow of charges results in AC electric power. [92][107][108][109]

Lateral Sliding mode (Figure 2.5 b)) has a similar structure of two electrodes and two dielectric layers. However, they do not separate vertically and are normally associated with translation or rotational motion systems. The charge generation mechanism occurs by

mechanical rubbing/friction via lateral sliding of the dielectric materials against each other. Additionally, the electrode design promotes a change in the effective contact area between the moving electrodes, which translates into a variable potential difference and originates a flux of charges in the electrodes by electric induction and, thus, AC electric power. [92][107][108][109]

Freestanding mode (Figure 2.5 c)) consists of one dielectric layer moving freely over two static dielectrics or electrodes using a no-contact mechanism of triboelectrification occurring from the natural friction of the dielectric layer with air. One clear advantage of this type of device is eliminating material wear caused by friction and prolonging the device's durability. The charge induction on electrodes is promoted by the asymmetric electric field developed upon the presence of a different area of charged dielectric over each electrode, once again creating an AC electric power. [92][107][108][109]

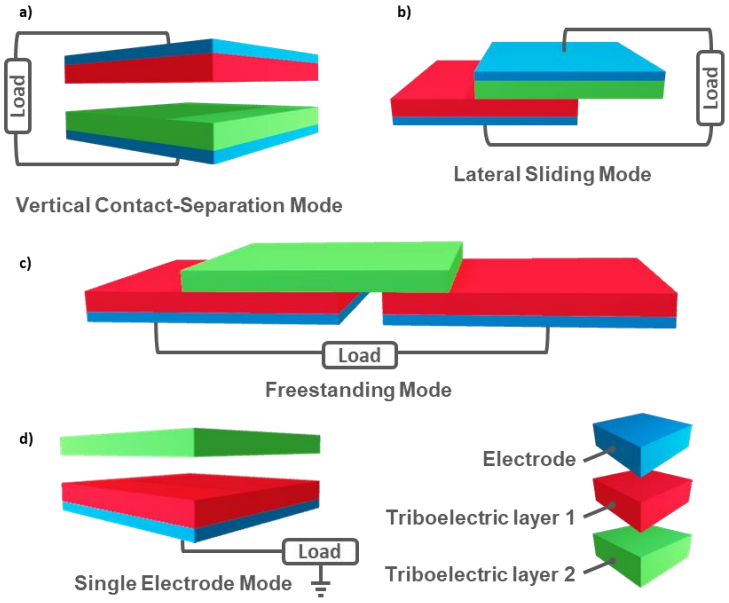

Figure 2.5 – Schematic representation of triboelectric conversion modes: a) Vertical contact separation mode, b) Lateral sliding mode, c) Freestanding mode and d) Single electrode mode.

Each previously described TENG mode can be modified to function in a single electrode configuration. The most common modification is the elimination of one of the electrodes in the vertical contact-separation mode, resulting in a vertical contact-separation single electrode mode configuration and addressed, shorted as Single Electrode mode (Figure 2.5 d)). This type of configuration is advantageous in terms of freedom of construction, simplicity and

flexibility. Since one electrode is virtually grounded, it can be adopted as one element in the environment and exterior of the device itself (e.g. the floor can be used as a virtually grounded dielectric for a single electrode generator incorporated on a shoe). [92][107][108][109]

2.3.2 Theoretical Model of Operation

The operation principle of TENGs is the generation of charge by triboelectric effect and the current induction at electrodes caused by the charge displacement. A definitive model to describe its full operation has still not been found. A theorical model is necessary to fully comprehend, predict and optimize the performance of TENGs. Without it, the process is time consuming, inefficient, and based in trial and error.[110] The most used theoretical mechanism for the four configurations of TENGs has been derived from Maxwell displacement current equations.[111][112] Considering the case of vertical contact mode configuration of a dielectric-dielectric contact (Figure 2.6 a)) and metal-dielectric contact (Figure 2.6 b)), Metal 1 and Metal 2 are the electrodes, d_1 and d_2 are the thickness of Dielectric (layers) 1 and 2. $x(t)$ is the time dependent separation distance, altered while applying a mechanical force.

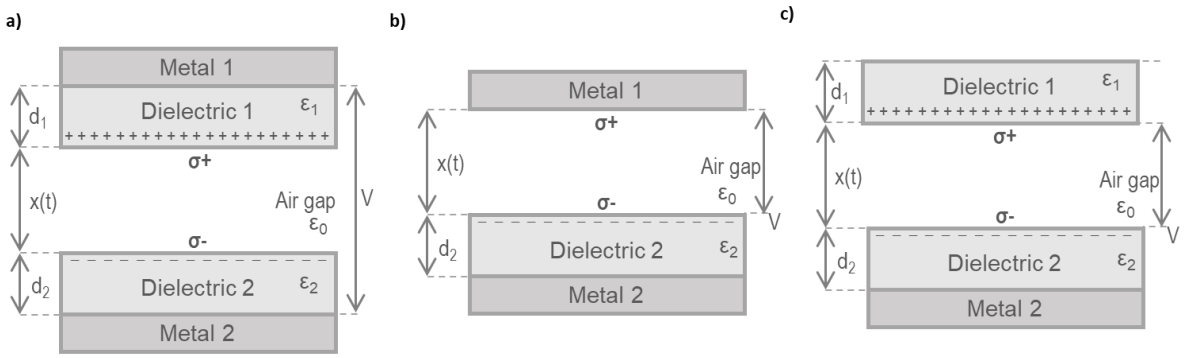

Figure 2.6 – Schematic of a TENG operating in a vertical contact mode configuration in the specific case of a a) dielectric-dielectric, b) metal- dielectric contacts and c) a single electrode dielectric-dielectric contact.

The electric field (E) in the different areas of the device in Figure 2.6 a) can be derived from Gauss Theorem and are given by Equation 2.1-Equation 2.3.

$$E_1 = \frac{Q}{S\varepsilon_0\varepsilon_{r1}} \qquad \text{Equation 2.1}$$

$$E_2 = \frac{Q}{S\varepsilon_0\varepsilon_{r2}} \qquad \text{Equation 2.2}$$

$$E_{Air} = \frac{\frac{Q}{S} + \sigma(t)}{\varepsilon_0} \qquad \text{Equation 2.3}$$

Where Q is the charge flowing through the external circuit, S is the area, $\sigma(t)$ is the charge density, ε_0 is the permittivity of vacuum, ε_{r1} and ε_{r2} are the relative permittivity of dielectric

layers 1 and 2, respectively. The voltage obtained after the separation of the layers can be expressed as:

$$V = E_1 d_1 + E_2 d_2 + E_{Air} x \qquad \text{Equation 2.4}$$

By substituting Equation 2.1-Equation 2.3 in Equation 2.4 the relation between V, Q and x can be obtained:

$$V = \frac{Q}{S\varepsilon_0}\left(\frac{d_1}{\varepsilon_{r1}} + \frac{d_2}{\varepsilon_{r2}} + x(t)\right) + \frac{\sigma x(t)}{\varepsilon_0} \qquad \text{Equation 2.5}$$

Since both dielectric-dielectric and metal-dielectric modes are governed by the same principles, they can be represented by the same equations if redefining the term $\frac{d_1}{\varepsilon_{r1}} + \frac{d_2}{\varepsilon_{r2}}$ by the constant d_0. Rewriting Equation 2.5 the following expression is obtained:

$$V = \frac{Q}{S\varepsilon_0}(d_0 + x(t)) + \frac{\sigma x(t)}{\varepsilon_0} \qquad \text{Equation 2.6}$$

While operating at open circuit, this implies that no current flows in the external circuit ($Q = 0$) and therefor the V_{OC} can be expressed by Equation 2.7:

$$V_{OC} = \frac{\sigma x(t)}{\varepsilon_0} \qquad \text{Equation 2.7}$$

The opposite case, while operating in short circuit condition, the short-circuit current (I_{SC}) can be derived from:

$$Q_{SC} = \frac{S\sigma x(t)}{d_0 + x(t)} \qquad \text{Equation 2.8}$$

$$I_{SC} = \frac{dQ_{SC}}{dt} = \frac{S\sigma d_0}{(d_0 + x(t))^2}\frac{dx}{dt} = \frac{S\sigma d_0 v(t)}{(d_0 + x(t))^2} \qquad \text{Equation 2.9}$$

When the TENG is operating through the connection of a load resistor (R) to the external circuit, the output characteristics are derived from the Ohm's Law:

$$V = IR = R\frac{dQ}{dt} \qquad \text{Equation 2.10}$$

$$R\frac{dQ}{dt} = \frac{Q}{S\varepsilon_0}\big(d_0 + x(t)\big) + \frac{\sigma x(t)}{\varepsilon_0} \qquad \text{Equation 2.11}$$

The numerical solutions for Equation 2.6 and Equation 2.11 can be solved by specifying a boundary condition ($Q(t = 0) = 0$). However, they were not included in this document and can be found elsewhere (here: [112]). The single electrode configuration is identical to the metal-dielectric contact except that the metal is substituted by a dielectric layer and demonstrated to have similar open circuit voltage and short-circuit charge profiles.[111]

Nevertheless, this model was originally developed for parallel plate capacitors, assuming the plates were infinitely large, and it did not consider variations in the field strength over different distances. Utilizing this classical model proved inadequate for describing complex surface topographies. [113]

Recently a new unified theorical model was proposed by Dharmasena et al.[114] It is based on the concept of the distance-dependent electric field and instead of considering triboelectric layer as an infinite plane it accounts for spatial changes of electric field. By integrating the charged microelements along the charged surface, it can be applied to a wide range of geometries and surface topographies. It can be expanded to non surfaces like planar convex or concave planes and it is given by Equation 2.12.

$$E_z = \int dE_z = \frac{\sigma}{\pi\varepsilon}\arctan\left(\frac{L/W}{2(z/W)\sqrt{4\left(\frac{z}{W}\right)^2+\left(\frac{L}{W}\right)^2+1}}\right) = \frac{\sigma}{\pi\varepsilon}f(z) \qquad \text{Equation 2.12}$$

Where E_z and z are the electric field and the distance over the z axis, L and W are the length and width of the plane. The equation can be written in terms of concave and complex planes and can be found here: [114][115].

2.4 Energy Efficiency

Energy efficiency refers to the percentage of conversion from mechanical to usable electrical energy. It is given by the input and output energy ratio. In general, the process of conversion of usable energy can be subdivided into:

- energy harvesting and refers to how well the triboelectric system can promote the creation of surface charges and how this surface charge can promote the induction of electric current in the electrodes.
- the energy transfer efficiency that refers to transforming the random intensity and frequency AC signal output of the triboelectric systems into a stable DC signal by external circuitry.

This process is schematized in Figure 2.7.

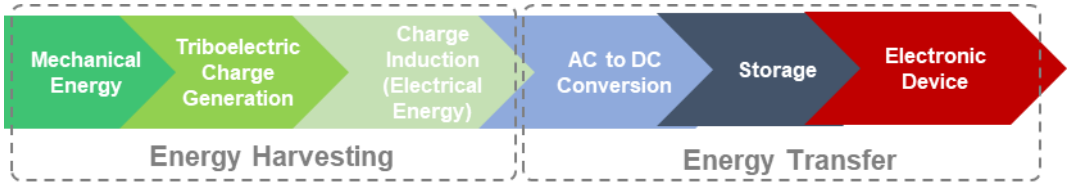

Figure 2.7 – Schematic representation of the various stages of triboelectric energy harvesting and transfer before it can be utilized in the final electronic device.

The first and more obvious way of improving the energy harvesting efficiency when designing a TENG is by selecting the suitable materials, which would be a pair of materials the further apart possible in the triboelectric layer. This would grant that the materials have the higher possible capability to become negatively and positively charged upon contact, as it was empirically determined in the elaboration of the series. However, given the specific application of the TENG and aspects regarding mechanical properties, materials biocompatibility or availability/criticality (critical raw materials), price, technology processing and other factors, it is not always possible to choose a pair of materials that are distanced in the series. For instance, in the case of wearable TENGs, its specific application requires the use of flexible and light materials for comfort and portability, making most polymers good candidates for the purpose, which at the same time limits its performance to a certain extent. A good combination of mechanical properties, energy harvesting capability, cost and environmental impact can be achieved by engineering materials. Some of the methods used to enhance the energy harvesting of materials are described in this sub-subsection.

The electrical output signal of a TENGs is an AC signal, often with variations in both frequency and amplitude derived from the random nature of mechanical energy in the environment, which makes the conversion to a constant DC signal and storage a fundamental requirement before ready to be used in an electrical device. Many energy losses can be suffered in this process, and the techniques used to enhance energy transfer are also discussed in the subsequent sub-subsection.

2.4.1 Enhancement of Energy Harvesting Efficiency

Most techniques used to increase the energy harvesting efficiency of TENGs are either by improving the induced charge in the electrodes by enhancing the surface charge density (σ) or by the magnification of the displacement (D_e) from the mechanical input. The enhancement of D_e is made through non-contact mode operation and force transformation. Other methods include the implementation of a switch, passive or active charge pumping and active charge excitation. Techniques that focus on enhancing σ, like physical and chemical modifications of the triboelectric layer and intercalation of a charge trap layer, are described below.

2.4.1.1 Physical modification

Physical modification through texturization aims to increase the effective contact area and consequently increase the σ. It is a good strategy for soft triboelectric layers that can be deformed upon the pressure used to drive the TENG, such as PDMS. In the case of stiffer layers, texturization can have a negative impact by promoting a decrease in the contact area since surface conformation will not be possible. Non-additive surface modifications can be achieved using templating, electrospinning, 3D printing, or etching. These techniques were successfully used to enhance the output power of TENGs.[92][116] Polymers with thermosetting properties, like silicone elastomers and specifically PDMS, are especially suited for texturization through templating. Nano/micropatterning using ZnO rods[117], Si wafers[118] or laser engraved molds[119]; inverse opal structures using sacrificial staked polystyrene spheres[120]; sponge-like structures by casting PDMS on sugar crystals[121]; mixing of PDMS with low boiling point solvents followed by microwave irradiation to obtain porous PDMS structures[8]; are some examples of patterning techniques employed to the texturization of PDMS triboelectric layers.

2.4.1.2 Chemical modification

Chemical modification can be achieved through surface functionalization, surface treatment or chemical doping.[116] Functionalization with -withdrawing groups is typically done using compounds rich in electronegative elements (for instance, from the halogen group), resulting in negative triboelectric layers with tunable surface charge density. Shin et al. used this technique to functionalize PET with compounds rich in electron acceptor elements Si, F and Br and obtained different properties from the same staring raw material.[122] M- Xenes, a new class of 2D layer structured materials composed of transition elements combined with C or N can be synthetized using different surface terminations and also presents the possibility to fine-tune electrical and mechanical properties are a great candidate to be used as a negative layer in TENGs.[123] Additionally, nitro groups have been introduced in cellulose fibers[124], and nitrocellulose paper/fibers have also been used to achieve paper based TENGs with high output[125]. Oppositely, electron-donating groups can be used to enhance the electropositively of materials. For instance, CNF aerogels have been modified with amino-rich groups[126][127] and allicin-grafted with sulfoxide groups[128]; methyl groups[124] and acetic acid groups[129] were also used to enhance the TENGs output. A chemical modification also includes surface treatments by ionized air injection and corona charge polarization or radiation and plasma treatment. [116]

Chemical doping consists of introducing particles with different electron repulsion or attraction abilities to improve the triboelectric properties. [116] For instance, doping of PDMS with AlOx[130] or introduction of electrolytes such as $CaCl_2$, H_3PO_4, HCl[131], or LiCl, $ZnCl_2$, $CaCl_2$, $FeCl_3$ and $AlCl_3$[132] on the matrix of PVA resulted in the improvement of triboelectric performances.

2.4.1.3 Dielectric modulation

The use of triboelectric layers with high dielectric or permittivity constants contributes to enhancing surface charge density. Because of the intrinsic nature of molecular bonding, most organic polymers cannot induce electronic and atomic polarization and, therefore, have low permittivity. One strategy to overcome this is the synthesis of polymers whose molecular

chains include elements with high polarizable electrons such as Si, Ge or Sn, like PDMS[133][134][135], which results in an increased permittivity of such polymers no greater than 3- 4.[17] Another alternative strategy is to increase other types of polarization, like dipolar, ionic, and interfacial. For instance, dipolar polarization consists of the reorientation of permanent dipoles on the polymer structure and can be achieved by molecular alignment. The orientation of PVDF trough the β-phase by the simultaneous use of high temperatures and electric fields results in a highly crystalline polymer with increased permittivity and, consequently a higher triboelectric performance.[136][137] Ionic polarization consists of the relative displacement of positively and negatively charged ions and can be introduced by the incorporation of ionic components to the polymeric structure, like NaCl or LiCl that form electrical double layers when subjected to electrical fields.[138][139][140] Interfacial polarization consists of the concentration of charges at interfaces between dielectric composites. It was already demonstrated that using multicomponent dielectric composites and different permittivity can enhance the overall triboelectric performance of TENGs. Incorporating high-k nanoparticles of metal oxides like SiO_2, TiO_2, $BaTiO_3$ and $SrTiO_2$ improves the composite's overall permittivity and induces additional space charge polarization at interfaces of polymer/particles.[141][142] The introduction of conductive metal nanoparticles or carbon nanotubes/ graphene causes the formation of micro-capacitor structures on the polymer matrix that induces charge accumulation at interfaces caused by its difference in conductivity.[16] Both strategies increase the triboelectric layer's surface charge density when homogeneously dispersed in the matrix until a certain loading ratio. [16][143][144] Excess use of additives promotes leakage currents or reduces surface area friction.[16][143][144] Interfacial polarization utilizing heterogeneous dielectric multilayer films, for instance, the addition of lower between higher permittivity layers can promote the formation of uniform and parallel charge polarization in relation to the electrodes and function as charge trapping/storage layer and enhance the charge density. [145][146] Additionally, using ionic polymer gels or solid electrolyte polymers like PVA can substantially increase the power output of TENGs by inducing ionic charge polarization by forming an electrical double layer (EDL). [138][147][148]

2.4.2 Enhancement of Energy Transfer Efficiency

TENGs rely on the conversion of ambient mechanical energy that is frequently of intermittent and irregular nature to induce electrical polarization of electrodes. This results in an AC signal of random amplitude and variable frequency. Such an electrical signal is not proper to power DC electrical devices. To be usable, the random AC signal of TENGs must be stored. In addition, the nature of power conversion of the TENGs itself, its high electrical impedance and low charge induction make it crucial to implement convenient electrical circuits and signal conditioning to enhance the energy transfer.[92] Energy storage using supercapacitors presents some of the common advantages of regular electrolytic capacitors and lithium-based rechargeable batteries, namely a great compromise between the energy storage capability and power density, time of charge and discharge associated with a relatively high number of life cycles and additionally, the possibility to attain customized charge storage and even functional integration with TENGs.[149] Since the mismatch in capacitance is the major problem when transferring energy from a TENG to a capacitor, one method to overcome this issue is to transfer the energy directly through inductors.[150] Automatic switching employing a bridge rectifier and diodes were used to enhance the power transfer through inductor-based circuits further.[151] In the case of high resistance electrodes like in the case of flexible TENGs, a different strategy consisting of a series of capacitors alternatively connected in series for charging and parallel for discharging multiply the electrical current (proportional to the number of capacitors) was proven to be advantageous than energy transfer by inductors, given its resistance independence transfer efficiency.[152]

2.5 Wearable Triboelectric Energy Harvesting Systems

Even if based on a technology thousands of years old, clothes are the ultimate functional wearable. Throughout human history, textiles have played the most vital role in human life. From protecting the elements, and insulation from exterior temperatures to helping to

maintain body heat essential to survival, they are at the same time a proof of social and wealth status, providing humans with both individual and cultural identity. In a broader dimension, clothes are an extension of the self. There is therefore no wonder that Textile industry is historically on of the most significant motor of the economic and technologic innovation. Humans took advantage of the abundance of fiber-based structures on nature (mainly cellulose-based fibers, wool and silk) to create woven structures with applications from baskets, barriers, curtains, carriers, bags, and clothes. Conventional textiles are 2D structures composed of 1D elements - fibers or yarns, combined into a woven or knitted structure, held together by frictional forces. Because of this inherent discontinuous construction, its mechanical properties excel compact sheets or films of equivalent materials in terms of flexibility, elasticity, malleability, moisture permeability, breathability and thus, thermal comfort and softness.

With the advances in science and technology, properties like UV protection, water and oil repellency and fire prevention have been adding increased functionality to textiles.[153] In the era of computation, information and artificial intelligence (AI), smart textiles with innovative functionalities like human-machine interfacing with sensing and automatic actuation abilities or energy harvesting, brought life to a new class of functional textiles.

Textile TENGs can be created using two primary approaches: one involves fabricating devices using conventional textiles as the material support, and the other entails constructing devices with fiber or yarn geometries that are subsequently used to build textiles with both supporting and functional capabilities. In the first case, functional layers can be deposited by printing, electrospinning, blow spinning or conventional coating techniques. However, this type of construction degrades the initial mechanical properties of the textile, decreasing its flexibility, bendability, and elasticity, turning it into a bulky stiff material.[154] Alternatively, the fabrication of 1D fiber or yarn TENGs and its posterior incorporated in 2D textile structures by weaving or knitting techniques often result in devices with increased properties over the prior method, like breathability, deformability, biomechanical compatibility, breathability and freedom of design by the possibility of playing with different weave patterns.[154] The following -subsection describes the state of art on 1D fiber/yarn shaped TENGs that can be used as the basic building block for integrating textile weaved structures.

2.5.1 1D Fiber/Yarn Shaped Triboelectric Generators

Fiber/yarn TENGs consist of 1D core-sheath structures of a conductive fiber core coated or wrapped with a triboelectric insolating frictional layer sheath (Figure 2.8 a) and b)), or core-sheath coaxial structures with two electrodes and two triboelectric layers ((Figure 2.8 c)) .The most widely used form of fiber/yarn TENG is the Single Electrode (SE) configuration owing to its simplicity, easy preparation methods and good performance. A device with this structure can function either in single electrode mode (Figure 2.8 a)), in which case an external frictional layer approaching and coming into contact will promote the induction of charges or in contact-separation mode when two similar devices composed of different triboelectric materials are combined by an external circuit and the friction between each other will generate triboelectric charges and the consequent flow of electric charge on the electrodes and through the circuit (Figure 2.8 b)).

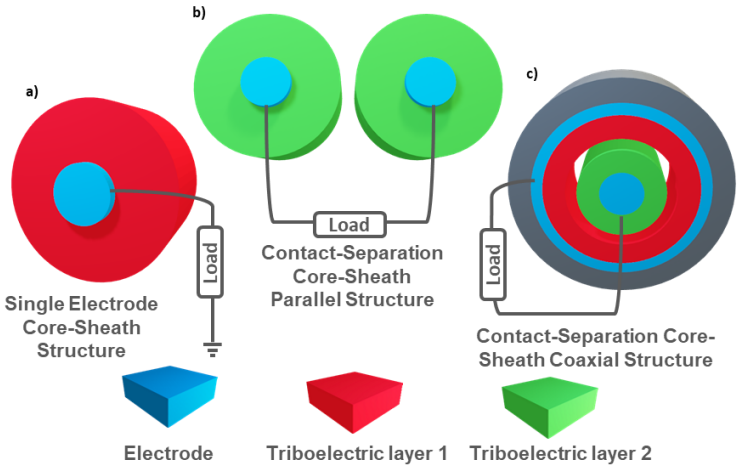

Figure 2.8 – Schematic representation of several structures of fiber/yarn shaped 1D TENGs: a) Single electrode core-sheath. b) Contact-separation Core-Sheath parallel. c) Contact-separation core-sheath coaxial structure.

SE yarn TENGs can be obtained by wrapping triboelectric fibers around conductive fibers/yarns. Yu et al. [155] used conventional textile fiber materials (cotton, silk, nylon) wrapped around conductive fiber core. Busolo et al.[156] developed a core-shell yarn TENGs structure by modifying an electrospinning technique to spin PVDF around CNT yarns using a rotative collector. Alternatively, Ma et al.[157] obtained a more stable yarn structure by using

two electrospinning devices simultaneously to coat conductive core fibers with PVDF and PAN nanofibers. Lai et al.[158] produced SE yarn TENGs by coating stainless steel fiber with a silicone elastomer (Ecoflex), resulting in an output of 15 V and 7 μA. Dong et al.[159] used plied and twisted conductive fibers coated with PDMS and observed that an increased number of conducive fiber strands improved the triboelectric output performance up to 150 W m^{-1}, which should be owed to both the increase in electrical conductivity of the electrodes and the additional surficial area of contact between the conductive fibers and PDMS.

2.5.1.1 Conductive Yarn/Fiber Shaped Electrodes

Conductive electrodes in the form of threads, yarns or fibers are necessary to construct 1D TENGs. Yarns or threads are composed of several fiber filaments that can be short (most natural fibers) or continuous (most man-made fibers). They can be composed of a single thread or multiple ply's twisted around each other for increased thickness and strength. Since it is on electrodes that electrical induction will take place, electrical properties like conductivity, carrier density and carrier mobility can determine the efficiency of this process.

Metallic mono or multifilaments obtained by extrusion like silver, gold, copper, and stainless steel have high conductivity (ranging between $1.3 - 62 \times 10^6\ S/m$) and can be used bare or combined with conventional synthetic yarns. However, they have limited application on wearables because of their relatively high price, high weight, low flexibility, stiffness, and low compatibility with other polymeric materials and textile weaving processes. They are prone to progressive oxide corrosion at the surface and under ambient conditions resulting in degraded electrical properties.[160] Alternatively, metals can be deposited on the surface of conventional polymeric textile materials (mostly Polyester and Polyamide) by vacuum deposition or electroplating, resulting in yarns with similar electrical properties as pure metals and good mechanical properties but still relatively expensive and coupled with environmental issues. Additionally, high weight, poor chemical resistance, frequent adhesion problems and poor corrosion resistance are drawbacks of this type of conductive yarn. Metal particles or other conductive particles like carbon allotropes (carbon black, graphene, graphite, CNTs,

MWCNTs, CFs) can also be combined with conventional polymeric textile materials precursors mixed into the polymeric matrix and melt spun, forming in conductive fibers or filaments. The resulting mechanical and electrical properties are limited and depend mostly on each component's concentration composition, which must be tuned to achieve a good compromise between the two. [160]

Conductive polymers like polyaniline (PANI), polypyrrole (PPy), polythiophene (PT), and poly(3,4-ethylenedioxythiophene) (PEDOT) are an interesting new class of materials counting on their relatively high conductivity (ranging between 10^{-8} and 10^{5} S/cm), low weight and low environmental impact however, its poor mechanical strength, low production rate brittleness, complex processing and high cost still limits their industrial applications. Its use its currently limited to blending with other materials and application as coatings, which deteriorates its electrical properties. [160]

CF s exhibit high strength and stiffness, low weight, excellent thermal stability and high electrical conductivity (from 10^{4} and 10^{6} S/cm) in the length direction due to the orientation of the graphitic structure along the fiber. CF s are mainly produced from extruded Polyacrylonitrile (PAN) fibers subjected to a process of carbonization at elevated temperatures. Its industrial processing is well established, however, due to health-related issues, high cost, high energy consumption upon manufacturing, environmental impact, waste treatment-related issues, stiffness and brittleness limits its use in textiles. [160] Nevertheless, its excellent combination of electrical and mechanical properties makes it a remarkably interesting material for application as electrodes in TENGs.

2.5.1.2 Triboelectric Yarn/Fiber Shaped TENGs materials

According to the triboelectric series, the human skin have a tendency to become positively charged when contacting with most polymers.[161] Because of this, and since many fiber/yarn TENGs have single electrode configurations and use the human skin as an external triboelectric layer, the construction of such devices are normally done using negative triboelectric materials. Owing to its superior charge generation ability, most of these are silicone

elastomers like PDMS and Ecoflex, or fluoropolymers like polytetrafluoroethylene (PTFE), fluorinated ethylene propylene (FEP) and polyvinylidene fluoride (PVDF). However, fluoropolymers inherent properties like lack of flexibility and strong water repellency results in poor breathability and low wearing comfort. On the other hand, rubbery silicone elastomers are flexible, stretchable, biocompatible and relatively easy to modify. For this reason two component silicone elastomers are one of the most used materials for the preparing of these devices.[154]

2.5.2 State of art for fiber/yarn-based silicone elastomer TENGs

Table 2.2 gathers relevant information about the properties of silicone-based fiber/yarn TENGs, like structure, materials, technologies, and electrical output characteristics.

Table 2.2 – State of art relative to fiber/yarn shaped TENGs (SE = Single Electrode, CS = Contact Separation, CxS = Coaxial Structure).

Year	Group	Structure	Description (materials, methods and relevant information)	Voc, Isc	V, I and P	Ref.
2016	Zhong Lin Wang	SE	Silicone-rubber-coated (**Ecoflex** 00-10) stainless-steel thread, cured at RT for 4 h inside a tube as mold. Tested using copper-attached acrylic plate.as external triboelectric material.	200 V, 200 μA	14 mW (100 MΩ)	[158]
2017	Huisheng Peng	CxS	Aligned carbon nanotube sheets as inner and outer electrodes and porous structures in triboelectric polymers of **PDMS** and polymethyl methacrylate.	5 V, 240 nA (25 N)	-	[162]
2017	Hongzhi Wang	CxS	300% stretchable coaxial device containing as core a nylon yarn twined around a metal conductive fiber, and the sheath consisting of a **PDMS** tube in which the interior is coated with bamboo fibers impregnated with AgNWs	-	1.3 mW/m² (500 MΩ) [tensile strain of 100%. 0.5 Hz]	[163]
2017	Chenyang Xue	SE	Ni-coated polyester conductive textile coated and non-coated with **PDMS**, tailed into belts and weaved into a textile structure	540 V, 140 μA	0.892 mW/cm² (10 MΩ)	[164]
2017	Zhong Lin Wang	SE	**Ecoflex** coated 3-ply twisted stainless steel/polyester fiber blended yarn (cured using molds)	150 V (11 N, 3 Hz) and 2.9 μA(5 Hz)	85 mW/cm² (100 MΩ)	[11]
2017	Zhong Lin Wang	SE	**PDMS** coated 3-ply-twisted stainless steel/polyester fiber blended yarn (cured using molds)	45 V, 1.8 μA (5 Hz)	263.36 mW/m² (132 MΩ)	[12]
2018	Shuit-Tong Lee	SE	Liquid metal-based triboelectric nanogenerator. Galinstan as the electrode and silicone rubber (**Ecoflex** 00-30)) as the triboelectric and encapsulation layer. Tested using hogskin as external triboelectric material.	354.5 V, 15.6 μA (6 N, 3 Hz)	8.43 mW/m² (1 GΩ, 3 Hz)	[165]
2018	Zhong Lin Wang	CxS	Coaxial structure (6 mm ∅) composed of an internal core tube of **Ecoflex 0050** obtained by curing inside a circular plastic tube for 4 h at room temperature, then spirally winding a silver-coated nylon yarn; and an external sheath tube composed of a medium rubber tube, spirally winded silver coated yarn and encapsulated with another layer of silicone rubber solution	19 V, 0.43 μA (20 N, 5 Hz)	11 W/m³ (3 Hz, 700 MΩ)	[166]
2018	Xuhui Sun	CxS	Hybrid TENG and supercapacitor structure in a coaxial sucture. TENG itself is a SE and part of the sheath structure, using carbon fiber bundle winding as electrode and coated using **Ecoflex** 00-10. Nylon was used as external triboelectric material.	42.9 V, 0.51 μA (2.5 Hz)	1.12 μW (100 MΩ)	[167]
2019	Xuhui Sun	SE	Stainless steel spring wire electrode coated with **Ecoflex** 00-30 (cured using using acrylic molds), tested using hogskin as external triboelectric material	59.7 V, 2.67 μA (2.5 Hz)	2.13 W (100 MΩ)	[168]

2019	Hongzhi Wang	SE	Stainless steel core yarn and elastic **silicone rubber** tube as sheath prepared by a modified melt-spinning process. Built-in elasticity on stainless steel yarns obtained by blow-molding silicone rubber and the application of traction on the silicon rubber.	-	12.5 μW/m (20 MΩ)	[169]
2020	Zhong Lin Wang	CS	Three-dimensional five-directional braided TENG obtained by multiaxial winding of **PDMS**-coated silver-plated nylon yarn.	90 V (20 N, 3 Hz)	26 W/m^3 (2 GΩ)	[159]
2020	Jianfeng Ping	SE	Elastic fibre coated with MXene ink, followed by spontaneous growth of Ag nanoparticles and consecutively coating the conductive fiber with **PDMS**. 100% strectchable.	7.7 V (3 cm)	-	[170]
2020	Blake Johnson	SE	3D-printed elastomeric metal-core silicone-copper fiber (**Silicone** (SI 595 CL) from Loctite)	5.75 V, 0.38 μA (50 N, 8 Hz)	31.39 W/cm^2 (20 MΩ)	[171]
2021	Yujue Yang	CS	Conductive core-spun yarns with silver-plated nylon yarn as core and insulating cotton fibers as shell. Multiple core-spun yarns coated with nylon and $BaTiO_3$ doped **PDMS** (applied using a continuous coating machine) are used as positive and negative triboelectric materials to realize hierarchical CSCY-TENGs by braiding technology.	135 V, 5.1 μA (50 N, 4 Hz)	174 V, 275 mW/cm^2 (50 MΩ) (70 N, 5 Hz)	[172]
2021	Yujue Yang	SE	Parallel association of stretchable gel electrode organogel prepared inside a continuous silicone hollow fiber. Tested using Kapton as external triboelectric material.	2.2 V, 0.52 μA (20 N)	-	[173]
2021	Junyi Zhai	SE	Flexible and stretchable coaxial TENG yarn fabricated by using coil spring as the inner support layer and mechanoluminescent ZnS:Cu/**PDMS** composite as the outer friction layer.	21 V, 0.1 μA	-	[174]
2021	Meiqi Li	CS	Fiber-based TENG in which conductive Ag-Cot yarn as the core was wrapped by silk staple fibers as the sheath and coated by **PDMS** or TPU	117 V, 2.3 μA (200 N, 3.3 Hz)	213 mW/m^2 (50 MΩ)	[175]
2021	Hudie Yuan	SE	SE mode TENG composed of conductive liquid sealed inside a trichloro (1H, 1H, 2H, 2H-perfluorooctyl) silane (FOTS)-modified silicone rubber (**PDMS**) tube, and using a copper wire for electrical connection	8–60 V, 0.3–2.3 μA (4 Hz)	90 mW/m^2	[176]

3

DEVICES FABRICATION AND CHARACTERIZATION TECHNIQUES

This chapter aims to present a description of some general fabrication procedures or characterization techniques involved generally in all the following chapters. The new in-situ curing technique is described as part of the production process of the Seys-TENG. While the main structure for the energy harvesting Seys-TENG device was kept constant, a few modifications were employed to this basic structure to study different influences on the device's mechanical to electrical conversion but are specified in the respective chapter. A description of the construction and functioning principle of the automatic mechanical force applicator systems that were developed specifically within this project, as well as the development of a rotating machine dedicated to assist in the electrophoretic deposition process when using 1D fiber or yarn shaped substates is included in this chapter.

3.1 Development of Seys-TENGs

The triboelectric energy harvesters developed in this thesis have a single electrode structure. They consist of an inner conductive yarn composed of multiple filaments of CFs, coated by a PDMS silicone elastomer layer. A new technique to deposit PDMS around conductive fiber was developed and is described in detail in the following sub-section.

Modifications to the CFs surface with piezoelectric ZnO NRs, additional layers of CNCs or doping of PDMS were performed prior to this step and are described in the following chapters where the influence of these modifications is studied in detail. The deposition of a layer of PDMS is always the final process of production of Seys-TENGs and, for the simpler devices, sometimes addressed as reference devices through this document, it's the first and only step of production.

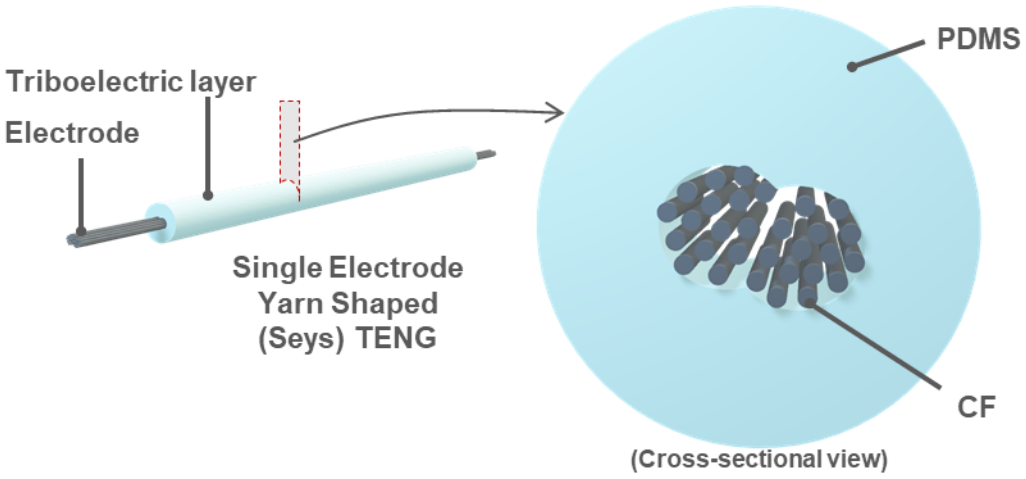

Figure 3.9 – Schematic 3D model of a Seys-TENGs (not to scale).

3.1.1 Development of the in-situ curing technique

In-situ curing of PDMS is a technique developed to simplify the process of depositing and curing PDMS layers around conductive CF yarns. This process involves passing an electric current through the CF yarn, which is submerged on the uncured PDMS slurry. The heat generated by the Joule effect gradually hardens the PDMS from the inside out, and the rate of hardening depends on the injected current. After initial experimentation, a current value of 0.2 A was selected as the optimal compromise between curing time and controllability of results. To ensure consistency in the study, several parameters were held constant unless explicitly mentioned throughout the document:

- Electrical current (I = 0.2 A).
- Electrically conductive fiber (CF yarn).
- Volume of PDMS (2 mL).
- Container shape with PDMS (half a cylinder with 6.5 mm diameter and 6.5 cm length).
- Length of CF yarn inside PDMS (6.5 cm).
- Ambient temperature and humidity.

The container used to hold a fixed amount of uncured PDMS while coating the CF yarns was designed using a 3D modelling software (tinkercad from Autodesk™, designed displayed in Figure 3.10 a) and 3D printed in ABS using a UltiMaker^{2+}. ABS is a widely available, relatively high melting point filament that can endure the final steps of preparation of the container and post curing process that will be mentioned later in the sub-section. The container is composed of 5 half cylinders with 6.5 cm of length and 6.5 mm of diameter and a capacity to hold 2 mL of volume (Figure 3.10 b). The final steps of preparation of the container meant to seal the laterals (Figure 3.10 c) and give it tightness (Figure 3.10 d): the container is held vertically, a foil of PP plastic is wrapped around one lateral and PDMS if poured until about 1 cm heigh and let to cure in the hoven at 70 °C for two hours. After this, the plastic foil is removed, the container is turned upside down, and the process is repeated on the opposite side.

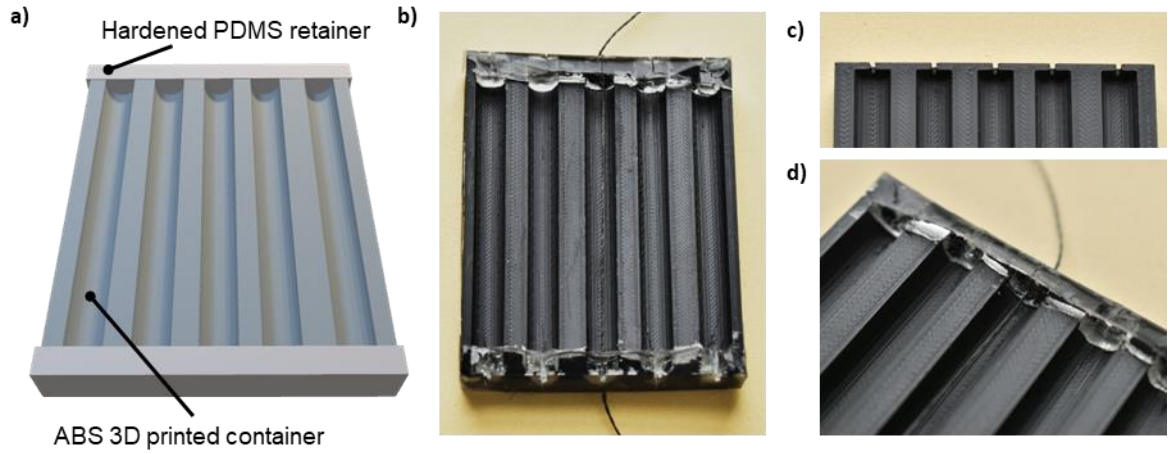

Figure 3.10 – a) 3D model design of the container used for the in-situ deposition. b) photo of the container .c) detail of container before adding PDMS hardened retainer. d) detail of container with PDMS hardened retainer and a CF yarn stuck in place.

Since temperature has a major influence on the hardening progress, whenever possible the in situ curing process of PDMS was performed under a controlled ambient temperature of 25 °C. The PDMS and curing agent (SYLGARD™ 184 Silicone Elastomer from Dow Corning) were used in a fixed weight ratio of 10 to 1. The mixture was prepared by vigorous mixing, degassed for 30 min and used right away. In the meantime, CF yarns were placed on the 3D printed container, stuck between a recess on the hardened PDMS placed previously at both ends of the piece. Two metallic plane crocodiles were attached at both ends of CF yarns.

About 2mL of the as-prepared PDMS mixture was poured into one of the cavities of the container, completely submerging the CF yarns. A power supply (Zhaoxin, PS-303D-II) was used to inject a current of 0.2 A on the CF yarn during a period ranging between 1 and 5 minutes. After the curing, the coated CF yarn was removed from the container and the excess uncured PDMS wiped away, then hung vertically for a final curing step at 70 °C for 15 min in the furnace to remove tackiness of the uncured PDMS residue. A schematic representation of the entire process is presented in Figure 3.11.

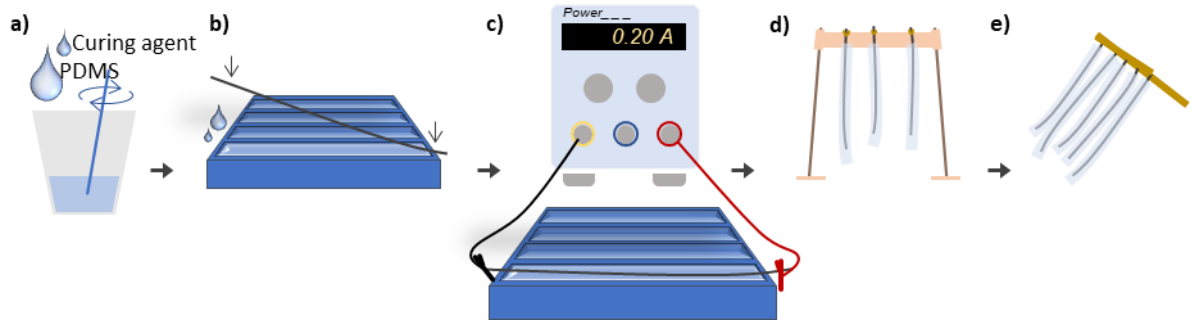

Figure 3.11 – Schematic representation of the in-situ curing process: a) preparation of PDMS mixture; b) pouring PDMS and CF yarns in the container; c) Injection of a current through the CF yarns; d) final curing of PMDS to remove tackiness; e) a set of five Seys-TENGs connected in parallel.

3.1.2 Development of a system for electrophoretic deposition of fiber-shaped electrodes

The electrophoretic deposition (EPD) method involves the electrochemical attraction of charged particles or suspended polymers in a solution toward an oppositely charged electrode. However, there is a natural tendency for the particles to accumulate under the influence of gravity. In the case of fiber-shaped electrodes such as CF yarns, as discovered during this work, this can result in asymmetrical coverage of the yarn. The upper part remains completely uncovered while the bottom accumulates an excessive amount of material. To address this issue and achieve yarns covered with symmetrical and uniform CNC films, a rotative system was designed. The system set up for EPD while the CF yarn electrode is rotating is described in this subsection.

The system for rotating the CF yarn was designed using an 3D modeling software, specifically Tinkercad from Autodesk™. It was then 3D printed in PLA using an Anet A8, and the model is depicted in Figure 3.12 b). The stepper motor drives an 8mm threaded rod with two large gears at a predetermined and programmable speed (1 rotation per second). Smaller coupled gears rotate in the opposite direction, thereby spinning the electrically conductive rods and the plastic-covered crocodile clips to which the yarn is attached. The 3D design for the

rotary system presented in Figure 3.12 b) and the STL files made were available online[1] for a free to download and reproduction of the system with the scientific community.

The container was also specially designed to hold the CNC suspension and printed in PLA. It allows to submerge the CF yarn inside the liquid while rotating. For this, two bumps were designed 7 cm apart (Figure 3.12 e)) in one of the container walls, allowing the yarn to make an angle and leave both ends out of the solution. The CF yarn ends were then connected to the plastic covered alligator clips for electrical connection and to rotate the yarn (Figure 3.12 f)). The other wall of the container holds a support for the static cathode electrode that it fixed to a plastic piece (Figure 3.12 g)). Such features assures that both electrodes are always at the same distance of 8 mm during the EPD process (Figure 3.12 h)).

[1] https://www.thingiverse.com/thing:6261778

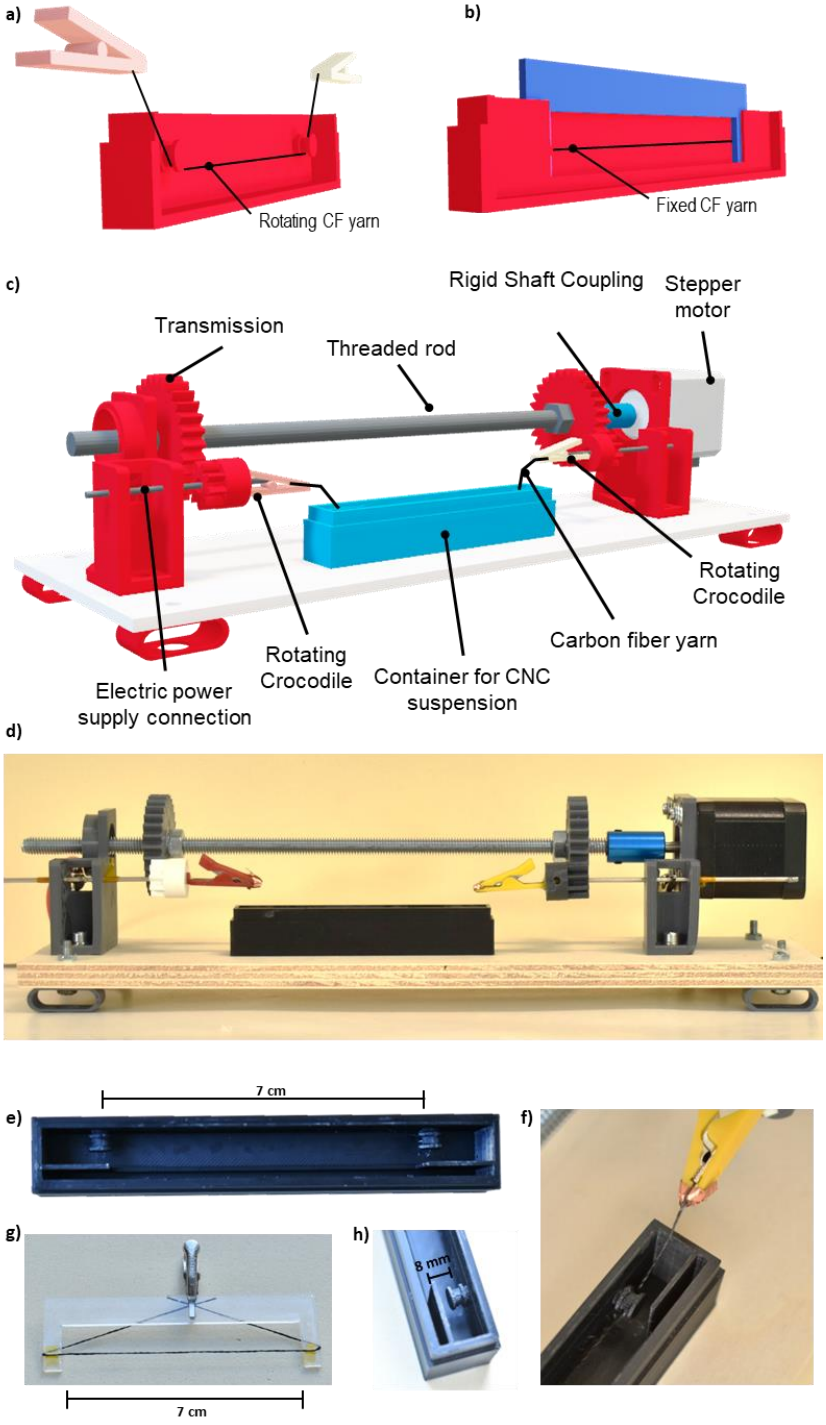

Figure 3.12 – 3D model of the different configurations used for electrophoretic deposition a) assisted by rotation and b) conventional. c) 3D model design of the system developed to rotate the CF yarn during the electrophoretic deposition process. During the process, the power supply is connected to the electrically conductive rod connected to the rotative CF yarn. d) Photograph of the system developed to rotate the CF yarn during the electrophoretic deposition. e) 3D printed container with special features to hold f) the CF yarn main electrode, and g) the CF yarn counter electrode secured in a

plastic support and electrically connected with a metallic clamp. h) The electrodes were placed at a fixed distance of 8 mm.

3.2 Characterization of Seys-TENGs

3.2.1 Development of automatic systems for mechanical load simulation

Given the nature of mechanical-to-electrical conversion, the electrical output's intensity strongly depends on the type and intensity of mechanical stimuli. To properly study and compare the performance of distinct types of devices, it is imperative to provide a constant type of mechanical stimuli. Additionally, control over the magnitude and the period of the mechanical stimuli is also of great interest, so a relation between the intensity of input and output can be drawn. The ideal automatic mechanical load applicator has the following characteristics:

- Reproducible
- Measurable
- Controllable force
- Controllable frequency

This section describes the constructing process of 2 different custom-made models idealized for such mechanical load applicator machines, and a discussion of the results obtained with both is then presented in chapter 3.

3.2.1.1 GFAM - Gravitational Force Actuator Machine

A straightforward way to obtain a reproducible impact with a constant force is by using an object of a certain mass free falling from a certain fixed height. The model of a simple mechanical machine that periodically lifts a certain weight and then drops it from a certain heigh

was developed using a 3D modelling software (tinkercad from Autodesk™) and it's presented in Figure 3.13.

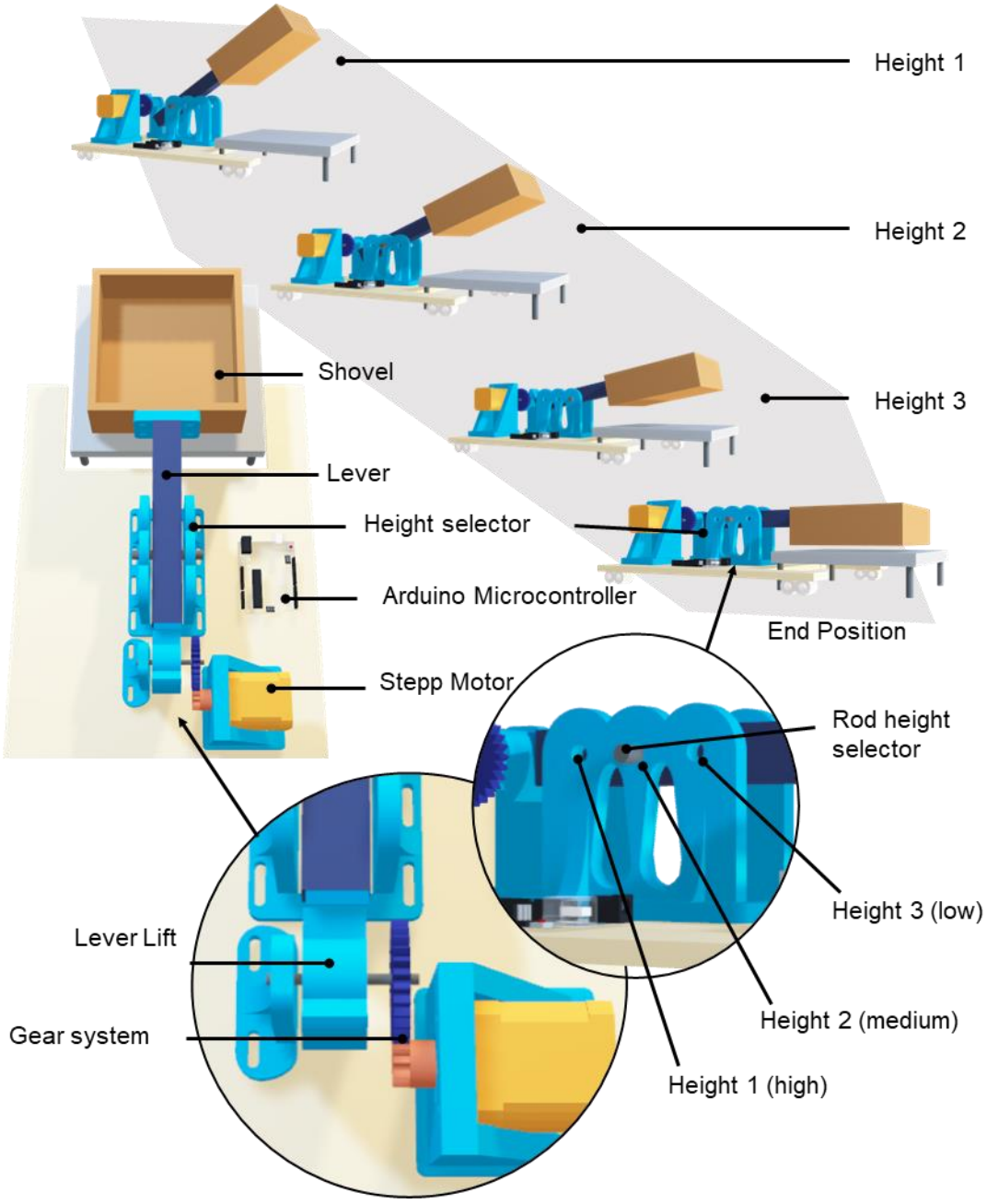

Figure 3.13 – Three-dimensional model of the Gravitational Force Actuated Machine (GFAM).

The 3D designed parts were printed using PET (1.75 mm filament from Velleman) using an Anet A8 3D printer, and other pieces were fabricated using pine wood or chipboard (hammers that hit the samples), medium-density fiberboard (MDF) base, stainless steel (rod axis selector for changing the height) and aluminum (square tube lever). The pieces were

assembled using 8 mm M5 screws and matching bolts on top of the MDF base, and adjustable feet were attached to the board for level and height correction of the platform. The nema 17 stepper motor is controlled by an Arduino UNO. The STL files developed for 3D printing this project were published online[2] for a free reproduction of the system, and the Arduino code used to program the machine is presented in appendix A.1. Figure 3.14 shows a picture of the GFAM machine and Table 3.3 resume the forces registered while varying the weight and the height of the hammer.

Table 3.3 – Resume of the interchange characteristics of the gravitational force actuator machine that allows to vary the force applied to the sample.

	Height 1	**Height 2**	**Height 3**
Hammer 1 (478.53 g)	250 N	400 N	600 N
Hammer 2 (216.86 g)	50 N	-	-

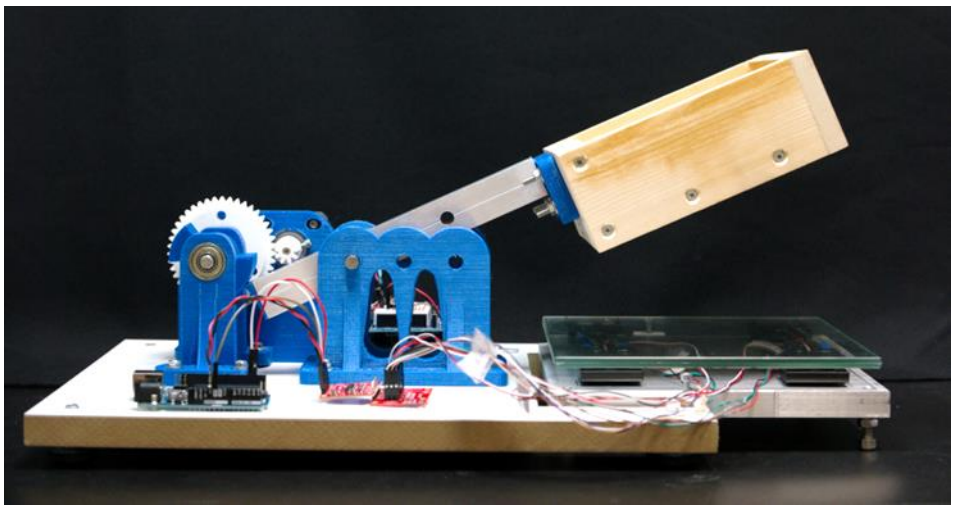

Figure 3.14 – The gravitational force actuator machine (GFAM).

The GFAM has the following characteristics:

- Adjustable force of impact (about 50, 250, 400 and 600 N)
- Adjustable frequency (maximum of 2 Hz)

[2] https://www.thingiverse.com/thing:5488841

To adjust the force of impact, the height at which the lever raises the hammer can be selected from 3 different levels, and the hammers are interchangeable with different weights (478.53 and 216.86 g). The frequency is programable from infinitely slow to a maximum of 2 Hz due to the mechanical constraints of the machine. The impact force was measured using a strain gauge cell connected to an analogue amplifier and a DigiVision button cell (Burster), acquiring 1200 values per second.

3.2.1.2 PFAM - Pneumatic Force Actuator Machine

Certain limitations of the gravitational force actuator machine encouraged the construction of another model of the machine. The new machine was also designed using a 3D modelling software (tinkercad from AutodeskTM). Instead of gravitational force, it is pneumatic actuated by a 50 mm stroke and 6 mm diameter cylinder (Chiser^{R}) using pressurized air. The cylinder is controlled by 2 position /5 ways pneumatic electrovalve (Heschen^{TM}) and powered by a Groove 30 V relay controlled by an Arduino UNO. A schematic representation of how the mechanism works is presented in Figure 3.15. Briefly, the Arduino sends an electrical signal to the relay that opens or shuts the passage of electrical current to the electrovalve. These electrovalves are constituted by two solenoids acting alternatively or one solenoid combined with a spring, attracting the piston towards the active magnet. The piston movement from one side to another in the valve allows the pressurized fluid to pass from the inlet to one of the outlets, which are directly connected to the cylinder actuator that lifts or lowers the piston. The stroke in the cylinder is screwed to a (6x4.5) cm^2 piece of a bamboo board (BB) so the samples contact a plain surface.

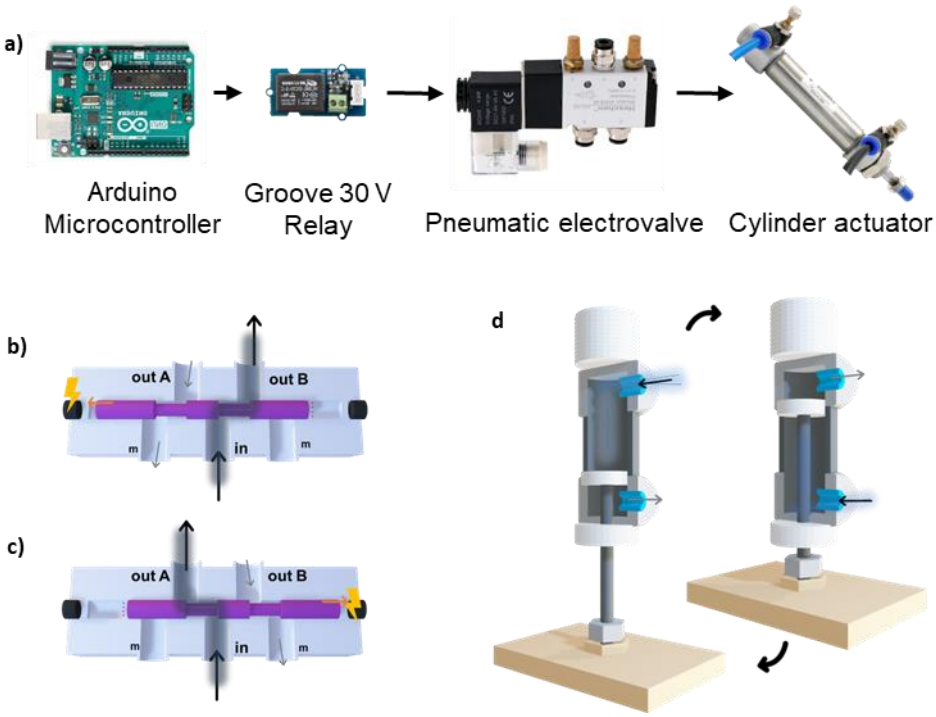

Figure 3.15 – a) Schematic of the components used to assemble the pneumatic actuator ordered by a logic order of control. b) Functioning principle of a 5/2 way pneumatic electrovalve the electromagnet on left side in actioned and the piston moves towards it, allowing the pressurized fluid (in) to pass through outlet B. c) when the electromagnet on the opposite side is actioned, the piston moves right, the passage between pressurized fluid (in) and outlet A is open. The remaining fluid from outlet B vial can escape though muffler. d) cyclic actuation and retraction of the cylinder stroke attached to a wood plate.

Several pieces of V-slot were mounted together to create a structure to hold the actuation mechanism as well as a support for the sample to be tested. The cylinder and the electrical components were fixed to the structure by specially designed 3D supports printed with 1.75 mm PLA filament (Tucab Fil3D) using an Anet A8. The 3D model of the machine is shown in Figure 3.16.

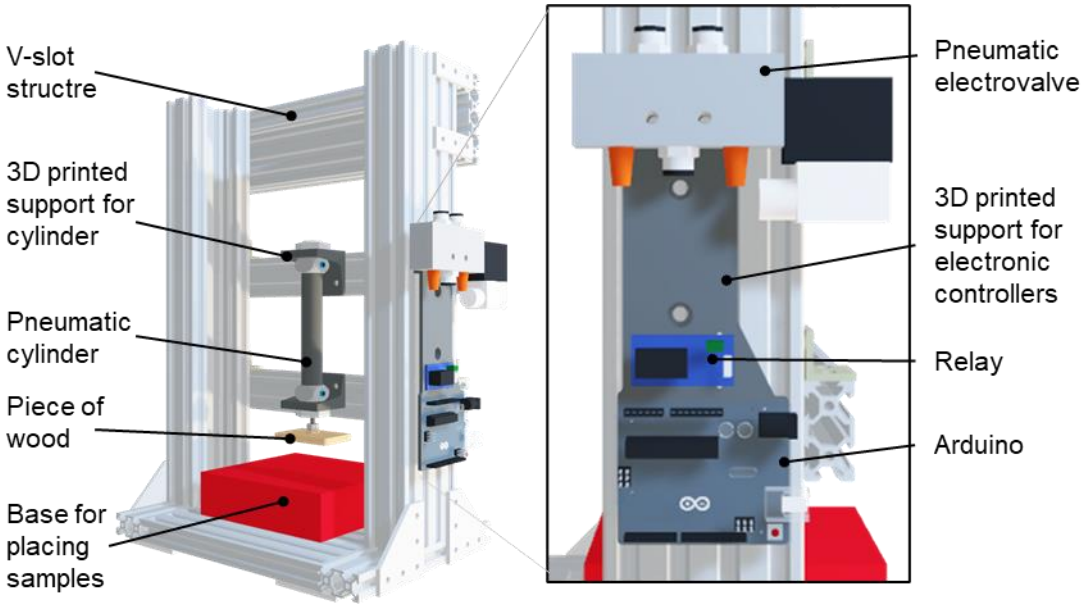

Figure 3.16 – 3D model of set up used to assemble the pneumatic actuated machine with a detail of electrical components. The tubes connecting the in and outlets of pneumatic valve and cylinder are not shown.

The force the cylinder applies depends on the bore diameter and is linearly dependent on the pressure of the fluid. A 16 mm cylinder within its minimum and maximum working pressures (1.5 and 7 bar, respectively) can deliver a force from 30 to 140 N. However, the maximum force used was 60 N.

The following characteristics are a summary of the capability of the pneumatically actuated load machine:

- Adjustable speed of impact /retraction
- Adjustable force of impact (fine control from 30 N to more than 60 N)
- Adjustable frequency (maximum of 3 Hz)

The pneumatically actuated load machine is depicted in Figure 3.17 and the source Arduino code developed to run the electrovalves is present in Appendix A.2. After testing the machine, the electronic controls were removed from the machine structure and placed in a separate structure since they emitted electromagnetic noise that would be captured by the oscilloscope and interfere with the electronic measurement.

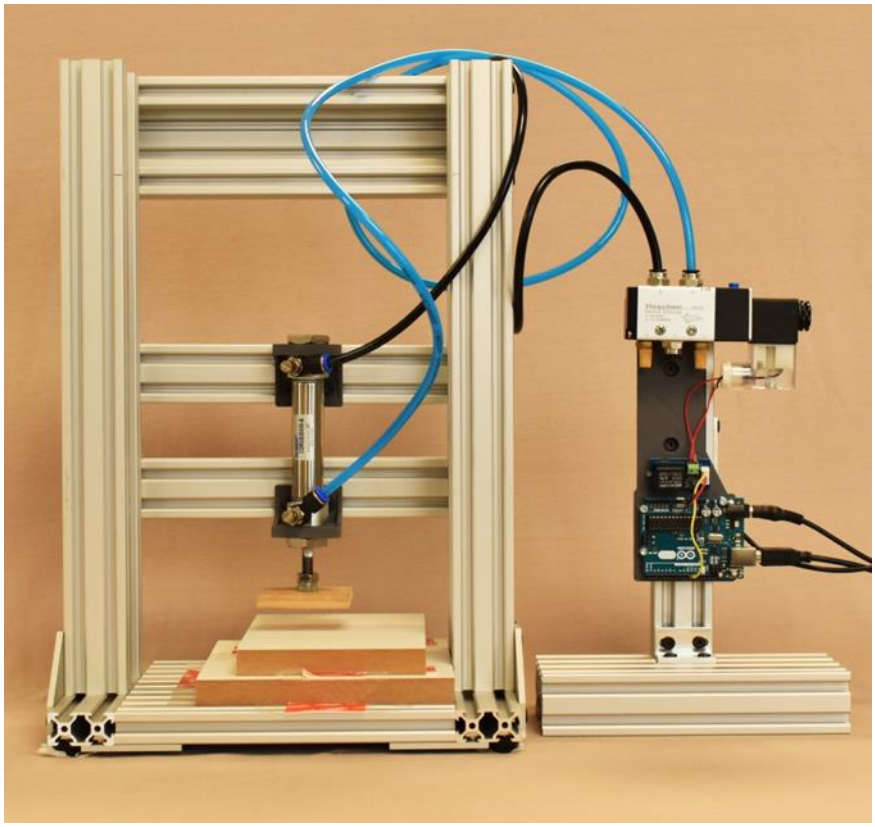

Figure 3.17 – Photograph of the pneumatic actuated machine. The electronic components (Arduino, relay and pneumatic electrovalve) are attached to a separate structure to avoid electrostatic interferences while performing electric measurements.

3.2.1.3 Comparison of performance between GFAM and PFAM

Besides the parameters related to force and frequency that can be adjusted differently in both machines, the way they deliver force to the sample is also different, resulting in a slightly different output when testing the samples using one or other machines. A comparison between the force profiles delivered from GFAM and PFAM and the resulting voltage output is schematized in Figure 3.18.

Because nature of GFAM is the force of gravity, when the free-falling shovel hit the sample/ a surface, the elastic properties will determine the nature of the semi-elastic collision and the most probable thing to happen it the bouncing of the shovel back and forth until losing all potential energy. The force profile is depicted in the force vs. time graphs in Figure 3.18 a). It is characterized by rapid contact between the shovel and the sample, followed by the removal

of contact during the first bounce. Subsequent collisions with decreasing intensity occur after the first bounce until the shovel momentarily rests on the sample. Then, the shovel is lifted again for the next cycle. This results in Seys-TENG outputting of a voltage profile shown above, where the negative peak follows positive peaks, characteristics of triboelectric energy conversion.

On the other hand, PFAM uses the force of a pressurized gas to move the cylinder stroke up and down, allowing much more control on both the moment of contact and lifting as can be seen in the force profile of Figure 3.18 b). Following the impact, the stroke remains in contact with the sample for some time. It is only after that the stroke is finally lifted. This force profile leads to the development of a corresponding positive peak, which is separated in time from the negative triboelectric peak.

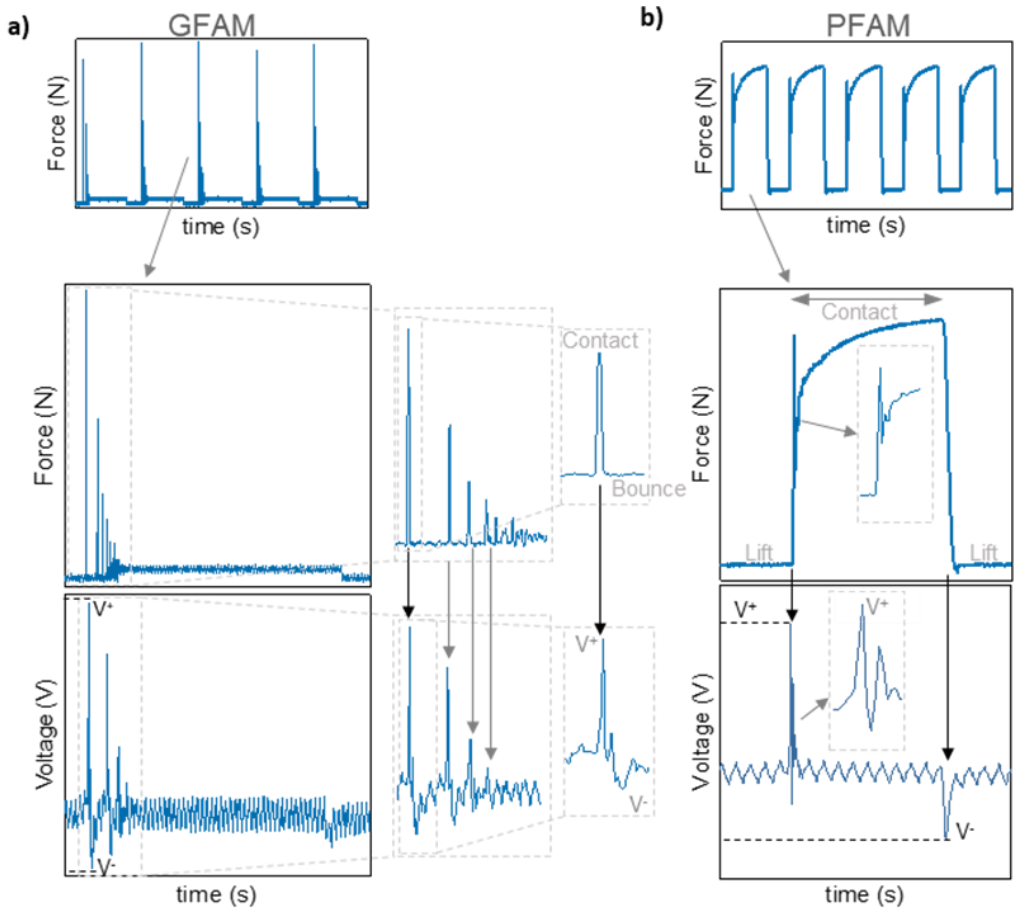

Figure 3.18 - Characteristic force profile and correspondent output voltage peak generated by a set of 4 Seys-TENG connected in parallel when using the a) GFAM and the b) PFAM.

3.2.2 Electrical characterization of Seys-TENGs

3.2.2.1 Voltage and current output

Open-circuit voltage and short-circuit current of TENGs generated by the TENGs were evaluated while delivering a controlled vertical mechanical stimulus using one of the machines described in sub-section 3.2.1. Four TENGs were connected in parallel using conductive and flexible cupper tape, positioned on the sample holder, and fixed using scotch-tape to keep them from moving during the measurements.

Given the single electrode nature of the Seys-TENGs, all electrical measurements were performed using the CF yarn electrode as the positive electrode and taking the ground as the negative electrode. Usually, the ground connection was established by connecting a big piece of metal in the machine structure or the ground from a power socket.

In the case of open-circuit voltage measurements, a 100 MHz bandwidth Tektronix oscilloscope (TBS 1102C) was combined with a 10 MΩ impedance probe connected to the Seys-TENG sets. The short-circuit measurements were measured using either solely a Gamry 600 Potentiostat (at a fixed acquisition rate of 50 μs^{-1}) or a Keithley 485 autoranging picoammeter in combination with the oscilloscope.

The Seys-TENGs were subjected to different forces under different frequencies and using one of two different developed machines. While the specific conditions of the study are detailed in each sub-subsection in the results chapters, typically, a set of four Seys-TENGs connected in parallel using cupper tape were subjected to 1 to 5 minutes of loading according to parameter in the study to obtain the stabilized output powers. The data was acquired by manually saving the voltage peaks displayed in the oscilloscope to an external recording unit (USB pen) and later analyzed by running a script in MATLAB which displayed the data and resumed the value of the positive and negative peaks. The average peak-to-peak values (Vpp and Ipp) were always calculated as an average of five different peaks.

3.2.2.2 Power and normalized power

The maximum power transfer between circuits is achieved by matching the impedance from the output circuit (in this case the TENGs) to the impedance of the input circuit (in this case the measuring circuit). The tunning was made using an empirical method, by combining several load resistors with different resistance values, to the output TENG circuit to match the resistance of both circuits. To calculate the power density, voltage and current were measured from a parallel association of four Seys TENGs using copper tape, connected to load resistances with different values in parallel or series, respectively, as depicted in Figure 3.19.

The voltage and current average values were calculated from five different measurements, and the power was then calculated using the formula bellow:

$$P(R_{Load}) = V_{R_{Load}} \times I_{R_{Load}}$$

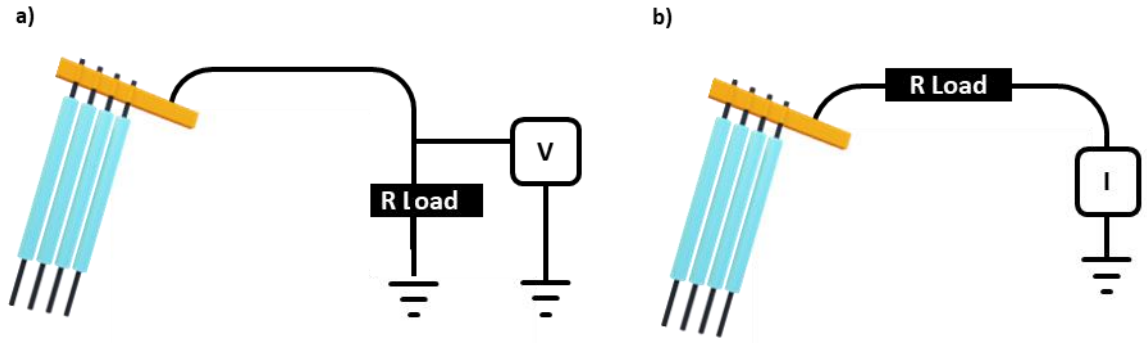

Figure 3.19 - Schematic representation of the circuit used to measure the voltage and current generated while using a load resistance.

Given the absence of a universally accepted standard for normalizing electric power output, three distinct methods to enable meaningful comparisons with other studies we're employed: the power per length unit (P_{max} / L, [$\mu W/m$]), the power per unit of area (P_{max} / A, [$\mu W/cm^2$]) and the power density (P_{max} / V, [$\mu W/cm^3$]). The length unit is the total length of the fours Seys-TENGs ($4 \times 6.5\ cm$), in the case of power per unit of area, the area considered is the minimum area obtained when Seys-TENGs are incorporated into a textile structure, which is given by the product of diameter of the four fibers by its length($4 \times D \times 6.5\ cm^2$); and in the case of power density the volume is calculated based on the dimensions of the four Seys-TENGs ($4 \times r^2 \times \pi \times 6.5\ cm^3$). A summary of this information is presented in Table 3.4.

Table 3.4 – Summary of the power uniformizations used in this work, corresponding equations, and units where l is the length and D the diameter of the Seys-TENG and P_{max} the maximum power achieved with a certain load resistor (R_{Load}).

Uniformized power	Equation	Units
P_{max} / L	$4 \times l$	$[\mu W/m]$
P_{max} / A	$4 \times D\ l$	$[\mu W/cm^2]$
P_{max} / V	$4 \times r^2 \pi\ l$	$[\mu W/cm^3]$

Additionally, the power per unit of area is also the approximate area of contact between the BB and the Seys-TENGs.

3.3 Characterization techniques

3.3.1 Scanning Electron Microscopy (SEM)

Scanning electron microscopy (SEM) is a powerful imaging tool that allows to obtain morphological and chemical information from the surface of a sample with resolution features in the nanometer range. The operation principle consists of focusing a highly energetic beam of electrons on the sample to test. The electrons can be absorbed, reflected (primary or backscattered electrons), result in the emission of secondary electrons or emit electromagnetic radiation. Different information can be extracted from the interaction of the incident beam with the sample. Most commonly, backscattered electrons are utilized to obtain information about the chemical nature of the sample's surface since contrast is related to the atomic number of specimens present in the sample, while the analysis of secondary electrons can access topographic information.

The SEM images present in this work were obtained using several equipment's existent in Cenimat facilities, according to the systems availability and features to be analyzed:

- SEM-FIB Cross-Beam Auriga system (Carl Zeiss)
- Hitachi TM 3030Plus
- SEM Hitachi Regulus SU8220

And,an equipment existent in the facilities of Fraunhofer IKTS, in Dresden:

- Zeiss NVision 40.

In this work, SEM was used to characterize the surface of CF yarns, to visualize the cross-sectional structure of Seys-TENGs, study the morphology, density, and alignment of ZnO NRs on the CF surface, study the degradation of ZnO NRs after stressing the Seys-TENGs and how they are located after the curing of PDMS around them and to study the ordered structure of the EPD CNC films.

3.3.2 X-Ray Diffraction Spectroscopy (XRD)

XRD is a nondestructive characterization technique that allows to study the structure of materials and perceive the presence of amorphous or crystalline phases, chemical composition, crystal structure, crystallite size, lattice strain, preferred orientation and layer thickness. When an incident X-ray beam strikes a sample, the presence of periodic atomic arrangements can promote constructive or destructive interferences that result in the beam diffraction, described as the Braggs Law:

$$n_i\lambda = 2d\sin\theta$$

Where n_i is the diffraction order, λ is the radiation wavelength, d is the distance between atomic layers and θ is the angle on incidence. A diffractogram is obtained when varying the incident angle and tracing the intensity of the constructive interferences.

In this work, XRD was used to characterize the structure of the CF yarns, ZnO NRs and CNCs.

3.3.3 Electrical Impedance Spectroscopy (EIS)

Electrical Impedance Spectroscopy (EIS) is an electrical characterization technique that allows to study the polarization response of liquid and solid materials when subjected to small amplitude AC signal, in a broad range of frequencies. For liquid materials a sealed container with electrodes is necessary but, in the case of solid materials, the sample can be simply mounted between two conductive parallel discs (typically stainless steel or gold electrodes),

just like shown in Figure 3.21 a). In this work, EIS measurements were performed using a Gamry 6oo potentiostat (Figure 2.20).

Figure 2.20 – Gamry reference 600 potentiostat used to perform EIS measurements in this work.

The measure consists on a small sinusoidal excitation potential (Equation 3.13) applied to the material in study, which results in an AC current passing through the cell (Equation 3.14), with a certain amplitude, the same frequency, and a phase shift - ϕ (Figure 3.21 b)) that can be measure by the equipment. The relation between the applied and resulting signal, like the Ohm's law, is the impedance - Z (Equation 3.15). The real and imaginary parts of Z can be representer using a phasor diagram (Figure 3.21 c)), but when studying the impedance values in a certain range of frequencies its most commonly represented using a Bode plot (Figure 3.21 d)) and a Nyquist plot (Figure 3.21 e)).

$$E = E_0 \sin(\omega t) \quad \text{Equation 3.13}$$

$$I = I_0 \sin(\omega t + \phi) \quad \text{Equation 3.14}$$

$$Z = \frac{E}{I} = \frac{E_0 \sin(\omega t)}{I_0 \sin(\omega t + \phi)} = A \frac{\sin(\omega t)}{\sin(\omega t + \phi)} \quad \text{Equation 3.15}$$

Where E is the applied voltage signal, E_0 the voltage amplitude, ω is the angular frequency ($\omega = 2\pi f$), I is the measured current signal, I_0 is the amplitude of the current and ϕ is the phase shift between applied voltage and measure current signals.

While null ϕ values correspond to a linear system consisting of purely resistive elements, positive ϕ values indicate the presence of a material with inductive characteristics whilst negative ϕ values point to a capacitive behavior.

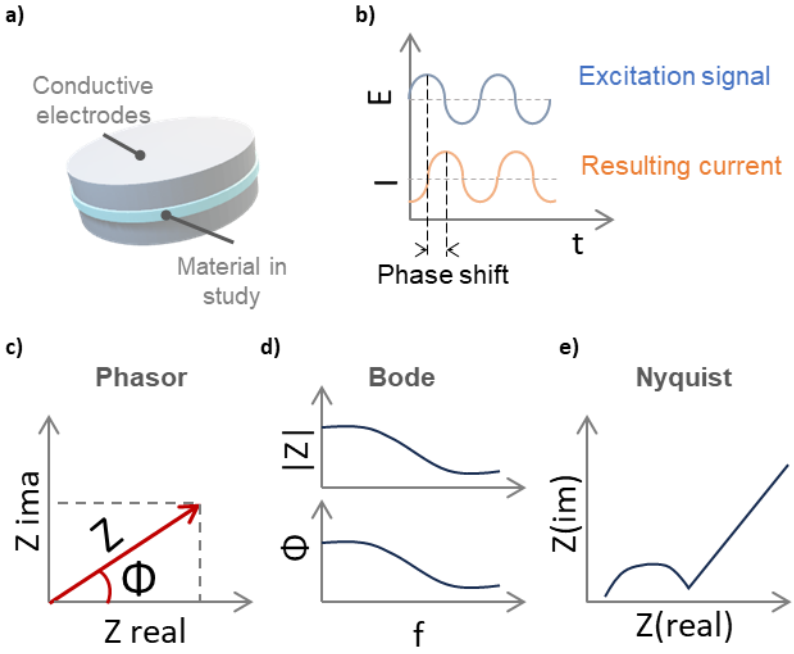

Figure 3.21 – a) Schematic representation of the electrochemical cell mount. b) Relation between the sinusoidal wave applied to the sample and the resulting current signal. c) Representation of the impedance in the phasor diagram. d) Bode and e) Nyquist plot.

4

DEVELOPMENT OF SEYS-TENGS BY IN-SITU CURING OF PDMS

In this chapter, the materials, and the newly developed method of directly curing PDMS by in-situ curing to produce the Seys-TENGs are described. An optimization of the process parameters was performed and the advantages and disadvantages of using this technique and materials are discussed. The possibility of creating a porous morphology of PDMS using this technique was also discussed, and finally the performance of converters obtained from these two different morphologies – smooth and porous, is compared.

4.1 Carbon Fiber Yarn: a 1D current collector

The first known use of CFs was as incandescent light bulb filament, an experiment performed in 1879 by Thomas Edison.[177] Since then, investigation of this materials properties demonstrated remarkable properties as high stiffness, high tensile strength, low weight, high chemical resistance, high temperature tolerance, high electrical conductivity and low thermal expansion.[178] They are used mainly in producing fiber-reinforced resin matrix composites with applications from aerospace industry (aircraft, space systems and aerospace military), turbine blades, construction, light weight cylinders and pressure vessels, medical, automobile, sporting goods and others.[178]

Table 4.5 – Some mechanical properties of carbon fibers (adopted from [179][180]). (CTE = coefficient of thermal expansion)

Parameter	Value	Ref
Density ($\boldsymbol{\rho}$)	1.75–1.93 g/cm3	[179]
Tensile Modulus	220 – 550 GPa	[180]
Tensile Strength	1.8 – 3.5 GPa	[180]
Tensile Elongation	0.3 – 1.4	[180]
Toughness	3 – 30 MPa	[180]
Electrical Resistivity	6 – 18 μΩ/m	[180]
Longitudinal CTE	-0.5 - -0.9 (10)mm^{-1} K^{-1}	[180]

The fabrication of CFs is an energy intensive production process (286 MJ/Kg, which is 8 times higher than that of steel) [181] and it was estimated that waste related to this product end of life will be close to 1million tons by 2050.[181] Recycling of CFs promotes energy savings (10% of that of virgin CF production), though it result in a loss of mechanical properties by increased oxidation processes. [181] However, the remarkable combination of electrical and mechanical properties makes this material highly desirable for use as a current collector in wearable applications. Its lightweight, flexibility, and chemical resistance surpasses those of metallic fibers, metallic-coated fibers, conductive polymers, or any other carbon allotrope composite. This is why it was selected as the charge collector for Seys-TENGs.

4.1.1 Morphological and structural characterization of CF yarns

Stretch broken CF yarns (CF yarns) were obtained from SGL Carbon Portugal (former FISIPE) in the form of 10 000 meter bobbins (Figure 4.22 a)). Its production process consists of a sequence of transformative steps using Polyacrylonitrile (PAN) yarn as source material. The yarn itself results from the intertwining of two strands of non-continuous PAN filaments of 35 tex each, originating a 2-ply of 230 twist per meter in the Z direction. Then, the precursor yarn undergoes an oxidative stage at 200 - 300 °C followed by carbonization at 1200 to 1400°C. The last step of the process consists of the application of a styrene-butadiene rubber coating.

The morphology of CF yarns was studied using a Zeiss Auriga SEM-FIB. Without any compression or extension, CF yarns have an approximate diameter of 420 μm (Figure 4.22 b)). The transversal cutting of the yarn promotes an unraveling at the forefront (Figure 4.22 c)).

The filaments are bean shaped (Figure 4.22 d), with diameters of approximately 5-8 μm. Since the filaments are discontinuous, this fact influences the quality of electrical conduction. The manufacturer does not report the average length of each filament through the yarn.

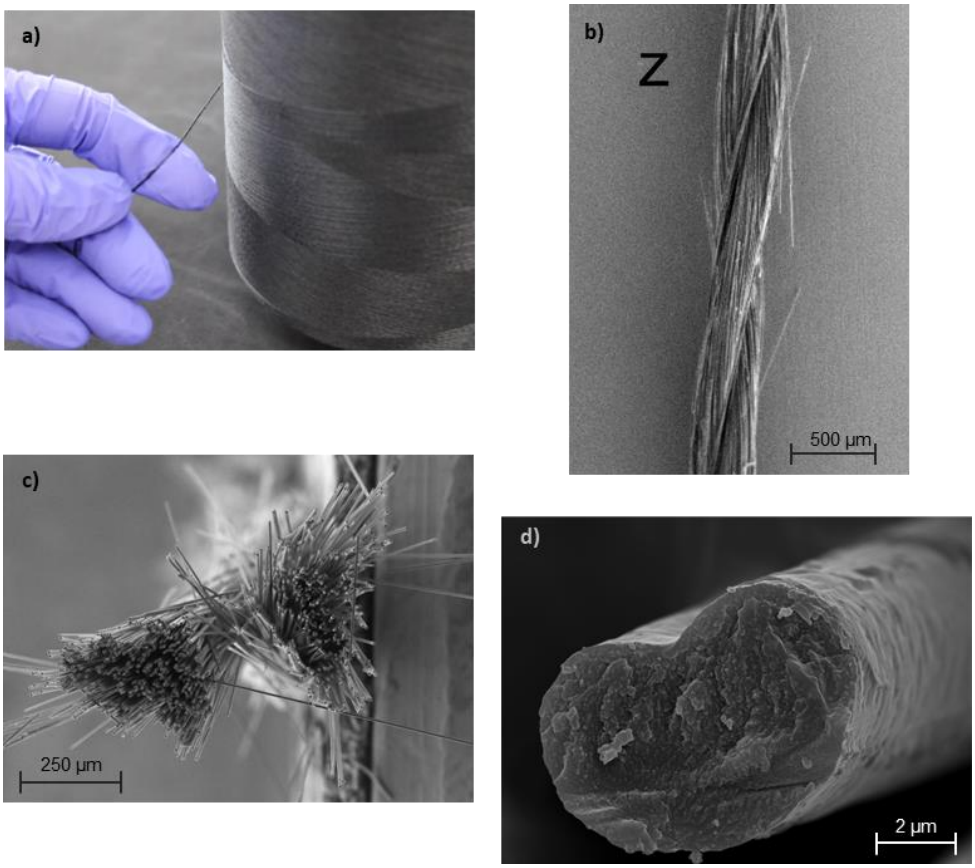

Figure 4.22 – a) Photograph of the CF yarn bobbin. b) SEM image of CF yarn with focus on its characteristic Z - twist. c) cross-sectional image of the CF yarn. When cut, the carbon filaments (CFs) tend to unravel. c) detail of the cross sectional cut of the CF yarn with an individual carbon filament with a bean shape.

An estimation of the number of CFs in each yarn was made by manually counting the CFs from cross-sectional SEM images of four yarns, using ImageJ. The manual counting from four different cuts along the yarn (four different cross-sectional images in Appendix A3) revealed a number of filaments from 773 to 895, which is inferior to the 1000 filaments reported by the manufacturer. Even if these counting methodologies can promote errors that lead to variation (counting two very close fibers as only one, missing fibers due to unravelling or due to shading, for instance), the substantial variation in the count suggests a notable disparity in

the number of fibers within the yarn, which directly impacts the electrical resistance along the yarn. This suspicion is confirmed by the direct observation along several meters of the yarn where it is possible to spot with bare eyes certain regions where the yarn looks particularly thin and fragile. More details regarding this subject and its influence on electrical conductivity will be further discussed in Sub-chapter 4.1.2.

A structural analysis of CFs, used to determine the crystallographic structure of the CFs, was performed using a PANalytical's X' Pert PRO M RD X- ray diffractometer using a monochromatic Cu Kα radiation source (wavelength 1.540598 Å) from 20° to 60° (2θ) with a scanning step size of 0.016 °. The XRD diffractogram reveals an intense and broad peak for 2θ around 25.0 °(Figure 4.23), typical of the well-known mixed crystalline and amorphous components within the CF structure, which corresponds to a (002) hexagonal carbon graphitic plane [182][183][184]. A broader peak near 2θ=44 ° is associated to the (100) plane of graphitic layers.[181][177] According to the manufacturer, the CF is stable until the range of 700-1000 °C. The integrity of the crystalline structure of a yarn annealed at 400 °C under air atmosphere for 15 minutes is confirmed by the XRD diffractogram.

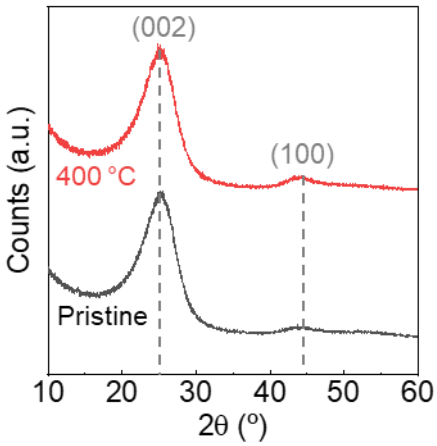

Figure 4.23 – X-Ray Diffractogram of CF yarns in its pristine form and after subjected to an annealing at 400 °C for 15 minutes.

As mentioned initially, a coating on the base of styrene butadiene rubber (SBR) was applied to the surface of CFs. Similarly to most of commercialized CFs, the treatment with a sizing compound means, among others, to promote fiber stabilization, fiber alignment and handling, improve wettability and more importantly, to promote a good adhesion between the fibers and the polymer matrix.[185][186] For this work, its presence cannot be disregarded

since it can have some influence on triboelectrification phenomena, that will be discussed later in more detail.

Effectively eliminating the rubber-based coating is not a straightforward process, as the solvents employed can induce swelling without effectively diluting or eradicating the rubber from its surface. In an attempt to promote its removal, the CF yarns were left to stir for four days and four nights inside methyl ethyl ketone (MEK). A thermogravimetric analysis (TGA) was performed on both raw and washed yarns to study the degradation of materials with temperature (Figure 4.24) using a 449 F3 Jupiter Simultaneous Thermal Analyzer, from room temperature (RT) to 550 °C at a heating rate of 10 °C/min. Under ambient conditions, an initial increase on mass content was registered for both raw and MEK washed yarns. This is attributed to the thermo oxidative decomposition (oxidation) of materials.[187] A slightly higher total mass gain was verified for the yarn washed in MEK (0.15 % difference). In the absence of oxygen, under the purge of an inert gas environment like nitrogen, this mass gain is replaced by a weight loss related to a purely thermal decomposition (pyrolysis). [187] A total 2.83 % of mass loss was registered for the raw yarn, a higher value than the one registered for the washed yarn where a lower decrease of 2.08 % was measured. This suggests some difference in the initial content of the SBR coating, meaning the MEK promoted some rubber degradation. However, the extent of this degradation/removal is still unknown since the manufacturer does not specify the sizing content.

Because washing with MEK introduces a certain degree of degradation but the extent to which SBR is removed remains uncertain, thermal degradation of the coating at 400 °C emerged as a more practical way to modify the surface composition of the fibers.

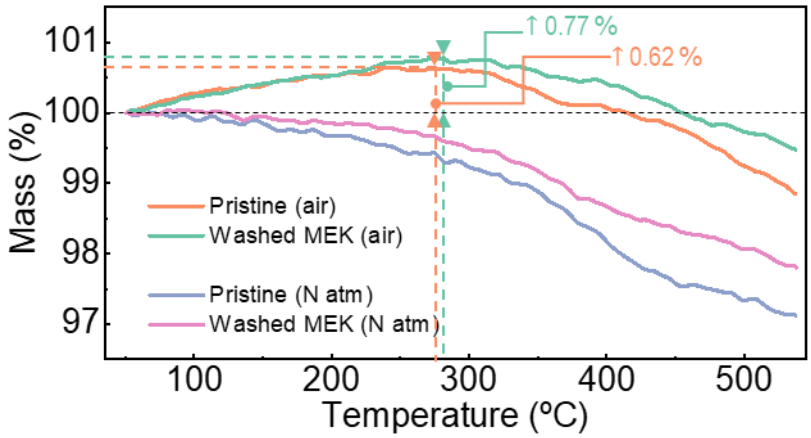

Figure 4.24 – Comparison between the thermographic analysis (TGA) of pristine and washed CF yarns under ambient conditions and using a nitrogen environment.

The surface of the carbon filaments was analyzed through XPS measurements. Pristine CF reveals a relative content of about 75 % Carbon and 25 % Oxygen (Table 4.6). The surface of carbon filaments subjected to an annealing at 400 °C for 15 minutes under air presents a quantitative difference in the elemental composition, specifically a decrease in the O 1s peak intensity and an increase of the C 1s peak. The change in composition after the heat treatment was expected since according to literature, the degradation of SBR starts lower than 300 °C[188]. Additionally, oxidation of the CFs and thermal degradation of the coating after such thermal treatment was verified earlier in the TGA experiments. Following the annealing of the CF yarns, a visible increase in hydrophobicity was observed. This phenomenon serves as an additional corroborative sign that the surface carbonization process has indeed occurred.

Table 4.6 - XPS elemental analysis of a carbon filament in its pristine form and after annealing at 400 °C.

	O 1s		C 1s	
	BE (eV)	**At (%)**	**BE (eV)**	**At (%)**
Pristine carbon filament	532.4	25.15	284.8	74.85
400 °C treated carbon filament	533.7	18.34	286.	81.66

In summary, even if the structure of the carbon is stable at these temperatures, some composition changes at the surface can influence its properties. This will be investigated further by comparing the performance of raw and burned CFs to the performance of Seys-TENGs.

In an effort to replicate the annealing conditions described in the subsequent sub-chapters, a DSC-TGA analysis was conducted on an untreated CF yarn under standard atmospheric conditions. This involved rapidly elevating the temperature to 400 °C and monitoring the mass changes over a 30-minute period, as illustrated in Figure 3.24.

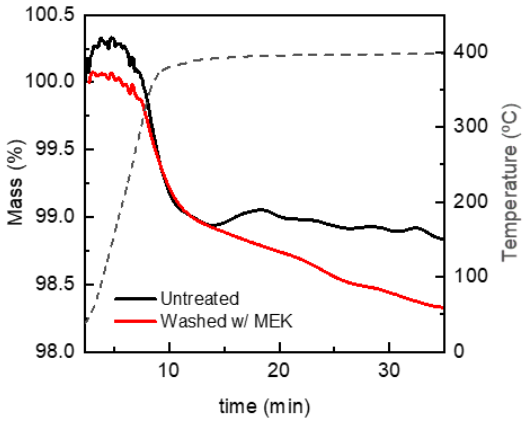

Figure 4.25 – DSC-TGA of untreated and washed CF yarns (using MEK) performed under atmospheric conditions.

The initial mass gain occurs due to oxidation, as previously observed. The rapid mass loss of approximately 1.15% corresponds to the degradation of most of the SBR-based sizing in the initial minutes, particularly when the temperature exceeds 300 °C. In the subsequent minutes, upon reaching a constant temperature of 400 °C, the sizing undergoes further degradation but at a significantly slower rate. In the case of the fiber washed using MEK, a smaller initial mass gain and a steady mass decrease after reaching a constant temperature of 400 °C emphasize the initial presumption of a reduced amount or degraded sizing agent.

4.1.2 Electrical characterization of CF yarns

The electrical conductivity of the CF yarn was evaluated using several different methods and the resistance along the yarn was measured using an ISO-TECH IDM93N multimeter. Resistance values were registered upon stabilization, some seconds after connecting the probes and the conductive yarn. The average results were taken from 15 measurements using each method and then normalized to meter units:

- Method A: a section of 20 cm of tensioned yarn using a weight of 22 g. Electrical connection was established through a conductive rod supporting the yarn.
- Method B: Using the multimeter point probe and squeezing the yarn against the table, through a 20 cm section.
- Method C: Measuring through cupper tape used to sandwich the conductive yarn in a 10 cm section.
- Method D: Using an adaptation of an international norm (DIN EN 16812), tensioning the yarn using a 10 g weight and electrically connecting the yarn though an electrically conductive flat alligator clip.

CF yarns manufacturer (SIGRAFIL - Stretch broken CF yarns) announces an electrical resistance of 490 Ω/m. However, measurements performed at the lab using different techniques reveal different values. Method A is adopted from Guo et al.[160], and consists of tensioning the CF yarns with a weight of 22 g while measuring the resistance between two points of the fiber 20 cm apart using two metallic bobbins that also hold the fiber straight. Method B measured the resistance between 20 cm of the CF yarns using a multimeter probe squeezing the CFs against a substrate. Method C measured the resistance between 10 cm using cupper tape as an intermediate. The CF yarns were sandwiched between the cupper tape and squeezed to improve the electrical contact. Method D is the method described by the international norm DIN EN 16812 and the resistance is measured using two clamps clipped on a 10 cm section of the CF yarn while being tensioned by a 10 g weight. The average resistance values are shown in Figure 4.26.

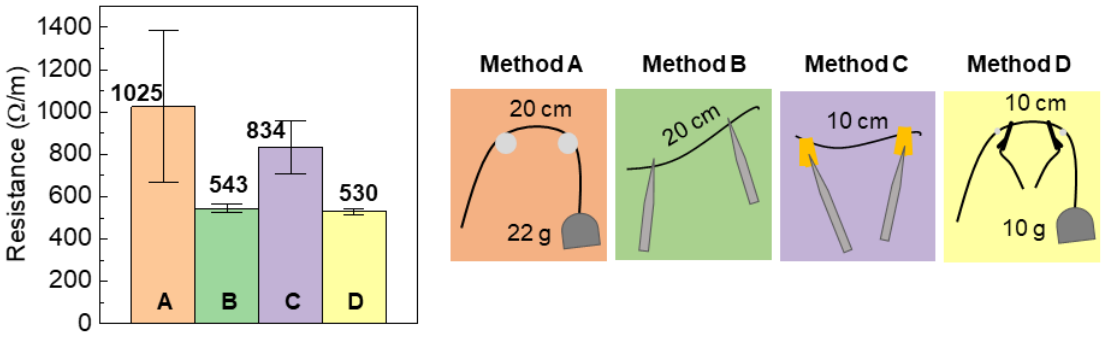

Figure 4.26 -Normalized resistance values obtained by measuring the CF yarns using methods A, B, C and D.

Not surprisingly, the higher value of 1025 Ω/m was obtained for method A and the lower ones for method B and D. Particularly, method D with a linear resistance of 543 Ω/m presents the closer value to the one announced by the manufacturer. This is because for an improved electrical conduction on multifilament yarns, individual fibers must be in close contact, which happens when pressed using the metallic probes or the alligator flat clips. In method A, the tensioning of the yarn using 22 g promotes an even tensioning along the CF yarn section in study but does not push the fibers remarkably close. This also justifies the considerably larger standard deviation using this method since the fibers are leaning freely. Method C has an intermediate value of 834 Ω/m since the fibers are sandwiched between cupper tape and compressed against each other, but not as much as in the case of method B and D. It was considered relevant to measure the resistance using this method since multiple devices are connected in parallel with each other using cupper tape that acts as a connector and as a medium of measuring a more stable value than pressing the CF yarn directly with the probe or the flat alligator clip with the risk of possibly damaging the fibers irreversibly and increasing the contact resistance.

The measured resistance value of the CF yarn is influenced by the measurement technique employed. Therefore, it is imperative to choose a method that closely approximates the actual resistance value relevant to the specific application in question. It is worth noting that this variability in measurement techniques poses a challenge when implementing CF yarns as electrical conductors in real-world applications. Connecting the CF yarn to the circuit can affect the measured resistance value. Method D, for instance, may represent a potentially lower resistance value achievable with this material. However, in practical applications, it is more

likely that the circuit will experience resistance analogous to that measured using Method C, as it mimics the way the CF yarns were connected to the measuring system.

4.2 Optimization of the in-situ curing of PDMS method

Joule heating, also called ohmic or resistive heating, or joule effect, is a well-known physical phenomenon discovered by James Prescott Joule in 1843. It is described by the power dissipation in the form of heat when electrical current passes through a conductor[189]. This physical phenomenon finds practical application on electric heaters, furnaces, fuses, and incandescent light bulbs. The amount of current (I) through a conductor is describe by Ohm's Law:

$$R = \frac{V}{I}$$ Equation 4.16

Where V is the voltage, and R is the electrical resistance. The power dissipation (P) can be obtained by the expression:

$$P = R\,I^2$$ Equation 4.17

And the amount of heat (Q) dissipated is dependent on the intrinsic electrical resistance of the conductor and the current passing through it and is given by the expression:

$$Q = P\,t = R\,I^2\,t$$ Equation 4.18

Polydimethylsiloxane (PDMS) is a biocompatible, non-toxic, chemically inert, thermally stable silicon elastomer[190]. It is also permeable to gases and conformable to submicron features, finding applications on soft lithography[191], microfluidics[192], nano imprint[193], biomedical devices[194][195], and even used as food additive (E900)[196]. Owing to its flexibility and high electronegativity, as well as easy modification using molds or soft lithography methods, it has been one of the most used materials as a negative friction layer on triboelectric nanogenerators.

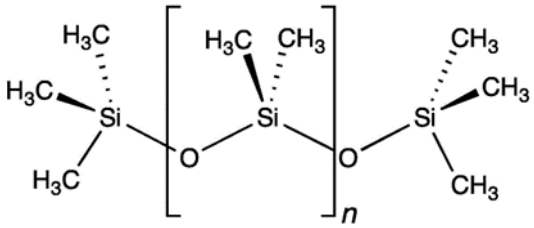

Figure 4.27 – Chemical structure of PDMS.

As a thermosetting polymer, PDMS undergoes irreversible curing or polymerization with temperature. Its chemical structure is shown in Figure 4.27. Elevated temperatures significantly accelerate its curing process, reducing this time from 48 hours at room temperature to just 10 minutes at 150 °C. However, the exact curing time also depends on the dimensions of the piece since heat diffusion occurs throughout its volume.

In the conventional preparation method, PDMS is cast into a mold and then placed in an oven at a specific temperature. Heat primarily propagates from the outer surfaces towards the center of the piece, causing curing to take place near the piece's edges. In contrast, the in-situ curing method involves the transfer of heat from the inside out, starting from the CF yarn located within the PDMS slurry and radiating outwards. Curing initiates near the CF yarn and progresses as the surrounding material gradually receives heat, as illustrated in Figure 4.28 a).

The coating of CF yarns by PDMS using the in-situ curing process is detailed in sub- section 3.1.1. Briefly, 2 mL of previously degassed uncured slurry of 10:1 of SYLGARD™ 184 silicone elastomer to curing agent was poured on one of the wells of the specially designed 3D container detailed in Sub-section 2.1.1. Then, a 12 cm long CF yarn was cut and placed in the container leaving a 6.5 cm segment submerged in the PDMS slurry and the remaining portion left exposed and used to inject a current using a Zhaoxin, PS-303D-II power supply.

4.2.1 Temperature and current of the in-situ curing process

Various current levels were tested to induce Joule heating of the CF yarn. It was observed that when using low current values (0.1 A), the curing process extended significantly, taking several tens of minutes. This extended curing time undermined the advantages of a quicker

PDMS deposition method. Conversely, higher electrical power values (0.3 A) led to overly rapid curing of PDMS, making it challenging to control the thickness effectively. Therefore, a current value of 0.2 A was selected as the optimal compromise between speed and precision for controlling thickness within the range of interest, which was investigated in detail from 1 minute to 5 minutes.

To investigate the temperature achieved by the PDMS when applying a 0.2 A current through the CF yarn, a thermocouple was inserted into the uncured PDMS slurry as close to the yarn as possible, as schematized in Figure 4.28 a). Prior to this, the thermocouple junction was protected by wrapping it with Kapton tape. Temperature measurements were recorded from the initial room temperature and continued for 10 minutes after the current application began. This measurement process was repeated 10 times, and the average resulting values are shown in Figure 4.28 b).

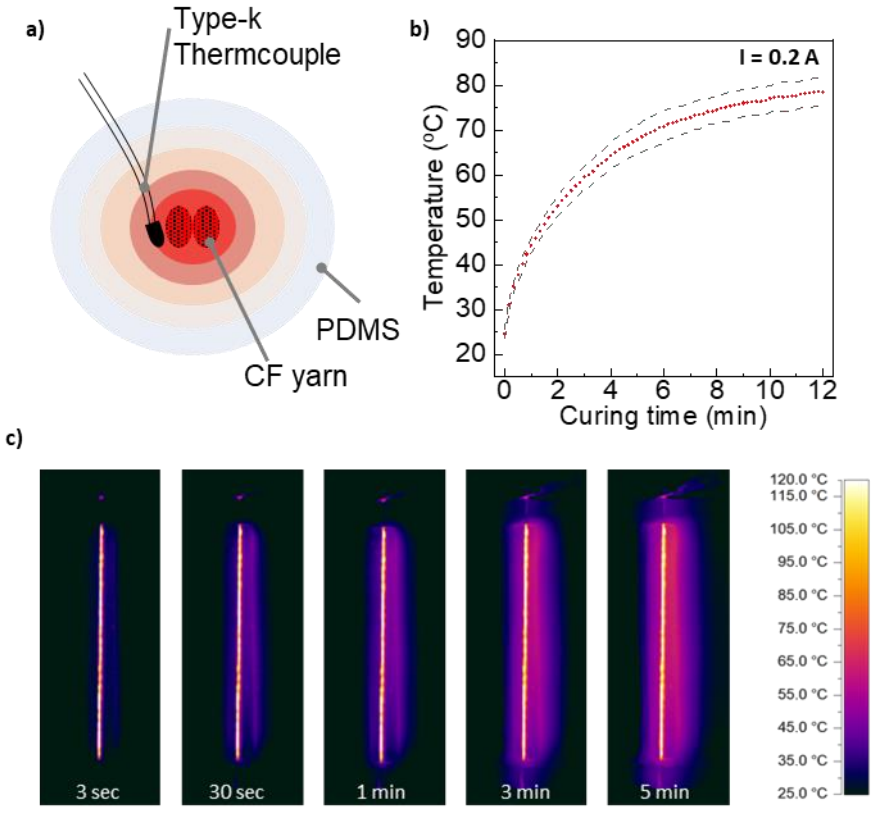

Figure 4.28 – a) Schematic representation of how the thermocouple was placed to monitor the temperature of the PDMS close to the CF yarn. b) Average temperature of 10 measurements performed on PDMS close to the CF yarn injecting a current of 0.2 A as a function of the time, using a type-K

thermocouple. c)Thermographic images while applying an electrical current 0.2 A through 6.5 cm of a CF yarn.

During the initial few minutes, the temperature of PDMS near the yarn rises quickly. However, as the current application continues for several minutes the temperature increase starts to soothe. The highest heat transfer rate occurs during the initial minutes, after which it stabilizes as the temperatures of the yarn and PDMS approach closer alignment. After 12 minutes, the temperature around the yarn gradually stabilizes near 80 °C.

To determine the temperature achieved by the yarn during in-situ curing, a PYROVIEW 380 Lc thermographic camera from DIAS Infrared Systems was used. The camera was securely positioned in a vertical orientation, directed downward, and allowed to warm up for 30 minutes. Subsequently, a CF yarn was positioned on the 3D holder, and a current of 0.2 A was applied through the yarn while temperature measurements were registered during a 5-minutes interval. According to the thermographic images of Figure 4.28 c)., the CF yarn reached a temperature of approximately 120 °C a mere 3 seconds after applying of a 0.2 A electrical current. Subsequently, heat dissipated gradually into the surrounding air medium. It is noteworthy that the maximum temperature recorded corresponds to the limit of detection of the infrared camera, implying that the actual temperature attained by the yarn is probably higher but impossible to precisely quantify using this tool.

4.2.2 Diameters obtained from the in-situ curing PDMS coatings

A closer examination of the first 5 minutes of current application reveals an approximately linear increase in temperature (Figure 4.29 c)). To access the extent of cured PDMS around the CF yarns, the curing process was stopped after 1, 2, 3, 4, and 5 minutes. The excess uncured PDMS was gently removed and the PDMS coated yarns placed inside an oven for 15 minutes while suspended vertically. After this period, the tackiness of PDMS coatings was gone and the diameters were measured using a Mitutoyo digital micrometer. The average of five measures at three distant locations were taken and are presented in Figure 4.29 a). Cross sectional images of these samples were taken using a SEM - Hitachi TM 3030Plus Tabletop

and are shown in Figure 4.30 and a summary of the registered temperature at specific times of curing and correspondent obtained PDMS diameters are presented in Table 4.7.

In the range of 1 to 5 minutes of current application, the temperature increase of PDMS around the yarn is approximately linear (Figure 4.29 c)). The PDMS diameters cured around the CF yarns also present an approximately linear increasing with time, during this period (Figure 4.29b)).

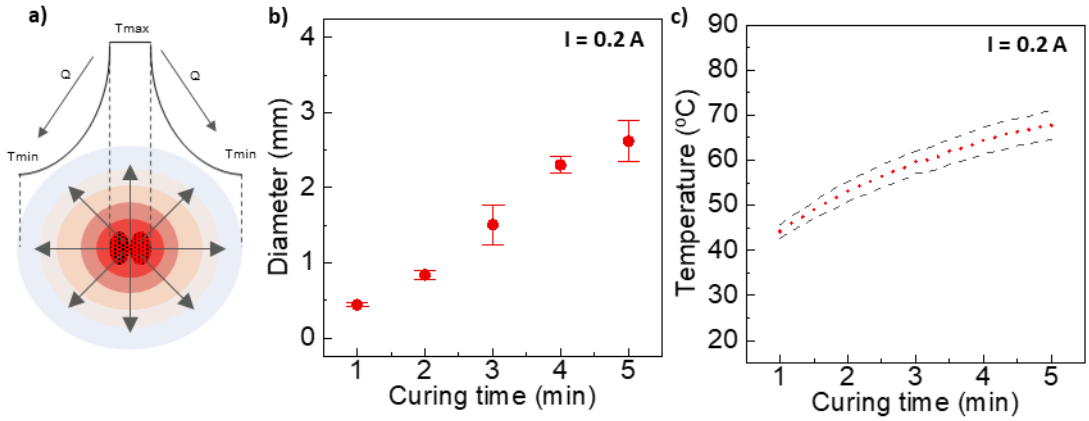

Figure 4.29 - a) Schematic representation of the heat conduction from the CF yarn to the PDMS (radially outwards) in the direction of the minimum temperature gradient. b) Diameters obtained by in-situ curing of PDMS around conductive CF yarns as a function of current application time from 1 to 5 min. c) Detail of the temperature of PDMS near the CF yarn as a function of time until 5 min of current application.

One minute after current application, the temperature of PDMS around the CF yarn is 44 °C. The corresponding cross sectional image of PDMS coating for 1 min shown in Figure 4.30 a) and f). At this stage, the residual PDMS coating around the yarn is minimal, and its solidification is not a result of direct curing induced by the internal heating of the yarn. This outcome is obtained when the yarn is simply dipped into the uncured PDMS slurry without heat application and subsequently placed into the oven. The coated yarn appears very thin, with some CFs exposed, a fact that can be confirmed when assessing its electrical conductivity.

After 2 min of current application, the temperature increased to 53 °C which results in a substantial layer of PDMS cured around the CF yarns. The PDMS coating totally isolates the CF yarn resulting in diameters close to 837.97 μm. This was found to be the least amount of

time to effectively cure PDMS using around the CF yarn promoted by Joule effect when using current of 0.2 A.

After 3, 4 and 5 min of current application, the temperature of PDMS around the CF yarn is 59.6, 64.4 and 67.8 °C respectively, and the layer of PDMS cured around the yarn increases in an approximately linear proportion., reaching a maximum diameter of 2617.83 μm.

During the deposition trials, it was noted that the PDMS slurry's initial temperature and the ambient temperature are two extremely important parameters. Different results were evident when using this technique in winter or summer in rooms without controlled temperature. Minor variations in the starting temperature of PDMS influence the dispersion of results in terms of the final diameter of the resulting coatings.

Table 4.7 –Temperature of PDMS measured around the CF yarn at specific times of the current application and the resultant diameter of the PDMS coating obtained.

Time of current application (min)	**Average temperature around CF yarn (°C)**	**Average diameter of PDMS (μm)**
1	44.0	440.12
2	53.0	837.97
3	59.6	1507.75
4	64.4	2303.42
5	67.8	2617.83

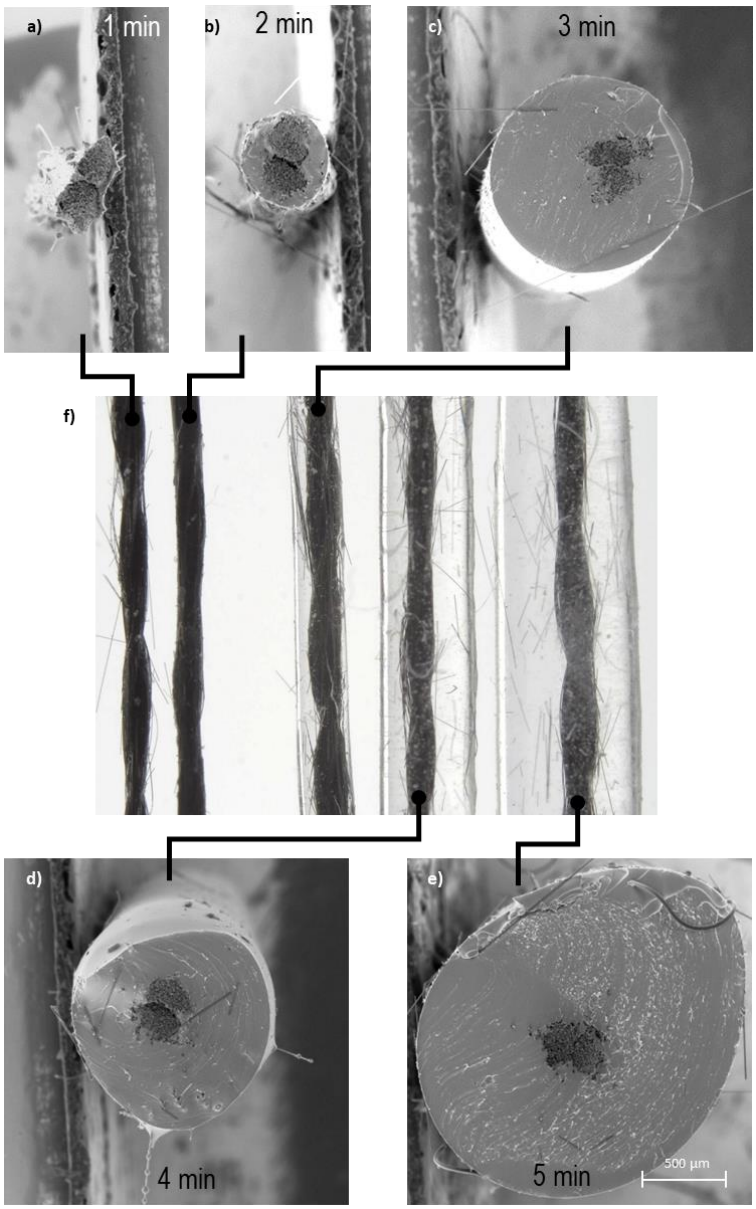

Figure 4.30 – Cross-sectional SEM images of the Seys-TENGs obtained by in-situ curing of PDMS around conductive CF yarns during the period of a)1 min, b) 2 min, c) 3 min, d) 4 min and e) 5 min. The scale bar is common to all images. f) Photograph of PDMS cured around the CF yarns by in-situ curing for 1 to 5 minutes, from left to right.

4.2.3 Compatibility of the in-situ curing process with other conductive yarns and silicone elastomers

In theory, the in-situ curing of PDMS can be applied using any conductive yarn or fiber. In this regard, this technique was employed using a commercial silver-plated nylon 6,6 yarn given by the name of Shieldex® 117/17 dtex, a 2 ply Z twisted yarn, each strand composed of 17 filaments, gently offered by Textile Research Institute Thuringia-Vogtland – (TITV). A SEM Hitachi TM 3030Plus Tabletop was used to study the morphology of the yarn (Figure 4.31). A detailed analysis of the yarn surface revealed several locations where the silver coating was damaged, and the polyamide core yarn was exposed which can compromise its electrical properties.

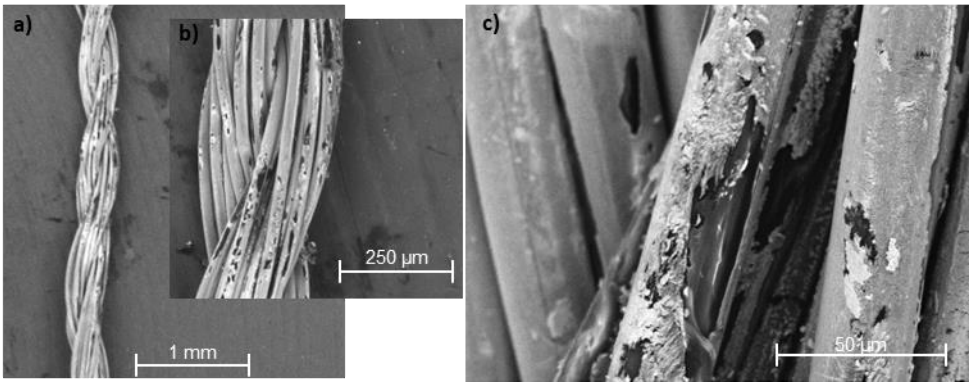

Figure 4.31 – a) SEM image of the silver coated Shieldex yarn with b) detail of the Z twist and c) detail of some region where the silver coating is destroyed.

Electrical conductivity was accessed by securing a section of the conductive yarn using scotch tape (Figure 4.32 a). Electrical contact was made by pressing the yarn using two standard probes and electrical resistance was measured using a ISO-TECH IDM93N multimeter. A total of 10 measures were taken in different sections of 1 cm of the yarn, resulted in an average linear resistance value of 226 $\pm$ 14 Ω/m, which is in line with the value indicated by the manufacturer (<300 Ω/m).

In-situ curing of PDMS around Shieldex yarn was performed using raw yarn as received. Similarly to the previous procedure, the yarn was placed in the 3D printed container and 2 mL of the previously degassed and uncured PDMS slurry was cast leaving 6.5 cm of the yarn submerged into the slurry. The application of 0.2 A electrical current through the silver shielded yarn resulted in many abrupt failures in the initial minutes of current application. Mots trials

resulted in the electrical conduction ceasing unexpectedly. During the process of injecting current through a yarn exposed to air, the polyamide component experienced melting, leading to the disruption of the yarn (as seen in Figure 4.33 a). The cause of this failure became obvious upon inspection with an infrared camera (as shown in Figure 4.32 b). The distribution of heat along the yarn is uneven, with certain areas showing signs of overheating. The reason for these hot spots its related to variations in resistivity along the conducting yarn, derived from imperfections in the silver coating already spotted previously upon inspecting using SEM.

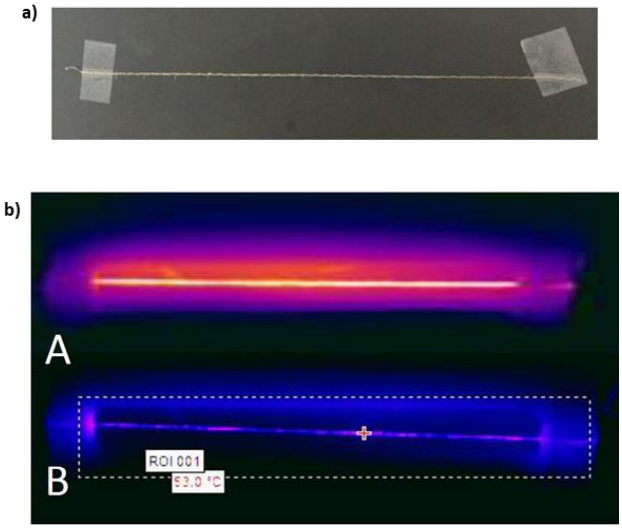

Figure 4.32 – a) A section of Shieldex® yarn secured using scotch tape for accessing the electrical resistance. b) Thermal images of a CF yarns (A) and a Shieldex® yarn (B) when injecting a current of 0.2 A.

Since the overall resistance of this silver coated yarn is lower than that of CF yarns, applying an identical current of 0.2 A promotes a lower heating, as can be verified from Equation 4.18. The resultant PDMS coatings are not very uniform, because of the uneven curing temperature along the yarn (Figure 4.33 b)). A cross-section of a PDMS coated Shieldex® yarn is shown in Figure 4.33 c) and d).

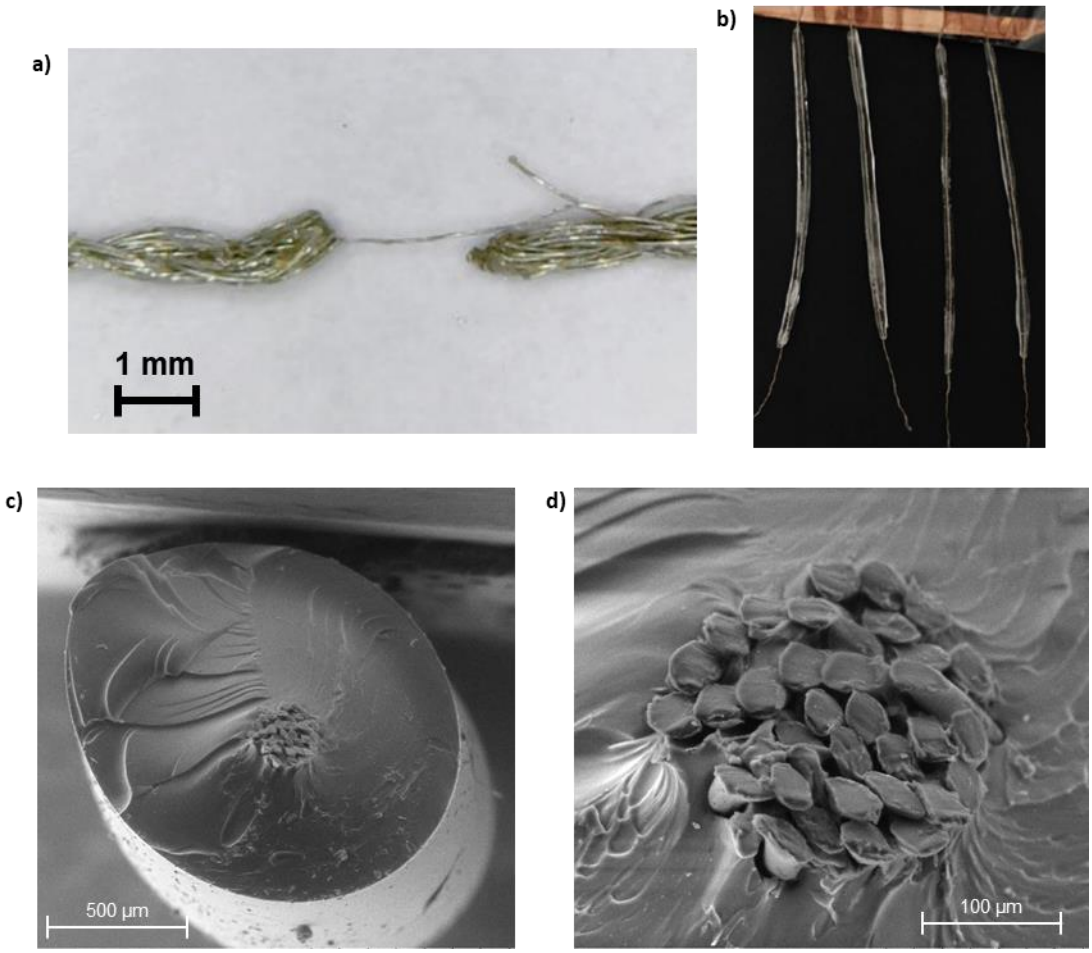

Figure 4.33 – a) Disruption of a Shieldex® yarn upon heating through Joule effect; b) in-situ PDMS coated shieldex® yarn; c) SEM cross sectional images of the coated yarns with a d) detail of the yarn.

The in-situ curing process was also tested using other thermosetting elastomer Ecoflex™ 00-30 commercialized by Smooth-On. The preparation method of this elastomer consists of mixing part A and B in the proportion of 1:1 and the degassing step was skipped since after mixing, the working time is limited to a maximum of 40 minutes after what it is already to hardened. That also implies that the preparation of one batch of the slurry should be planned, as low variations on time spent after mixing have a greater effect on the cumulative curing process than in the case of PDMS where the working window is up to 48 hours. A cross-sectional image and a picture of the Seys-TENG are shown in Figure 4.34.When applying the current of 0.2 A on a CF yarn submerged in uncured elastomer during of 1:30 min, the average diameter obtained was 2.08 mm ($\pm$0.30 mm).

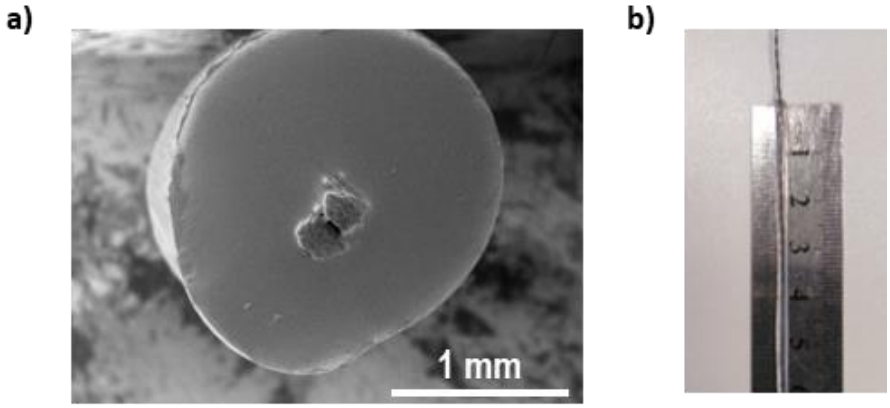

Figure 4.34 – a) cross-sectional SEM image and b) a picture of a Seys-TENG produced by in-situ curing Ecoflex™ 00-30 over a CF yarn.

The results regarding the power output of both Seys-TENGs devices produced using a different electrode yarn and a different elastomer are shown in the following sub-section.

4.3 Porous PDMS coating using in-situ curing

While performing the in-situ curing in a relatively high humid environment, some Seys-TENGs ended with a porous structure resembling air bubbles in the PDMS structure. After some trials, it was concluded that the high humid environment was responsible for the adsorption of water molecules in the CF yarns and the evaporation of water particles promoted by the elevated temperatures while in-situ curing the PDMS leaving behind a porous structure. This phenomenon was then intentionally reproduced and even enhanced by dipping the CF yarns on a water vessel before curing. A picture comparing the resulting PDMS coatings with a smooth and porous structure are shown in Figure 4.35 a) and b), respectively.

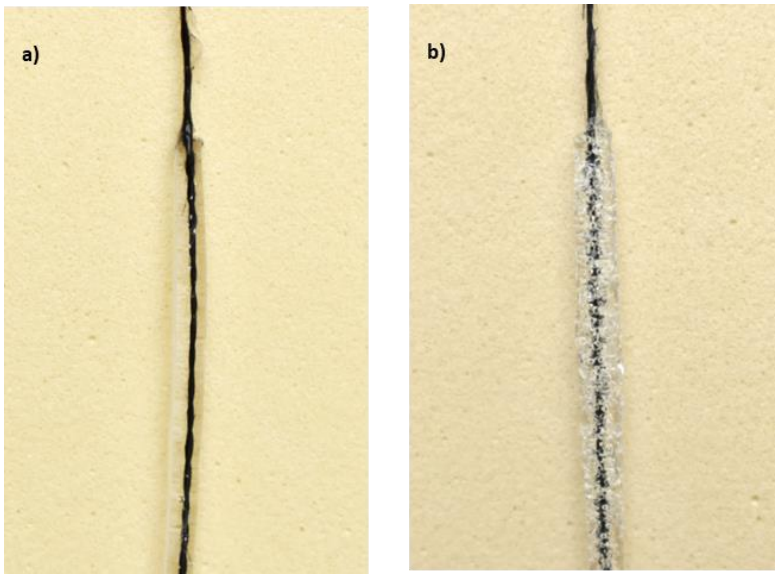

Figure 4.35 -. Photographs of a) smooth and b) porous PDMS deposited by in-situ curing on a CF yarn.

Moisturizing CFs prior to the in-situ PDMS results in porous PDMS structures and in slightly higher PDMS diameters for higher curing times, when compared with non-moisturized counterparts, which present smooth PDMS coatings. This is caused by the expansion and evaporation of water inside the structure that developed at a greater extent for longer curing times, thus creating larger bubbles/voids that result in the porous structure that can be observed in the cross-sectional SEM images of Figure 4.37.

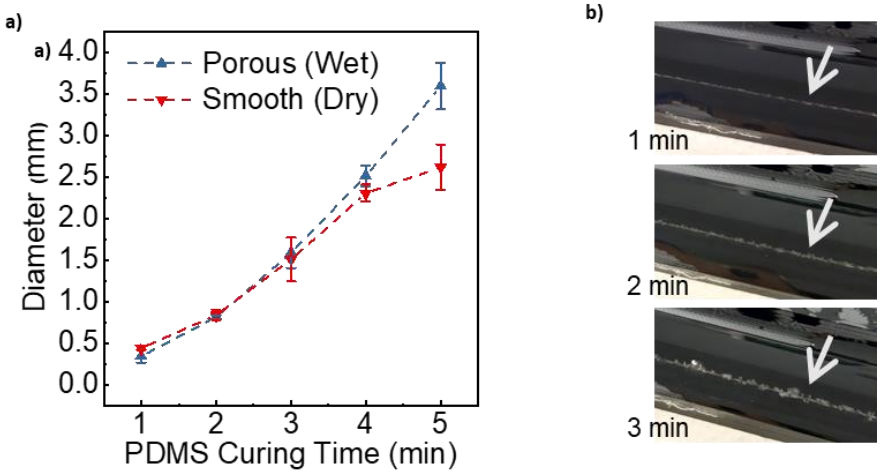

Figure 4.36 – a) Comparison between the diameters of smooth and porous Seys-TENGs obtained by in-situ curing of PDMS around conductive CF yarns for 1 to 5 min. b) Evolution of the formation of bubbles inside the PDMS structure near the CF yarns for periods ranging from 1 to 3 min.

To access the extent of porosities incorporated in the Porous Seys-TENGs structure, the weight of two sets of smooth and porous Seys-TENGs were measured and the obtained values are registered in Table 4.8. It was found that, while having similar diameters, the sets show a difference of 0.135 g which corresponds to a decrease of 13.5 % in mass. If considering similar lengths of the core CF yarns and identical weights of the cupper tape connector, this percentage indicates the difference in PDMS mass that was substituted by porosities. When converted to volume, it corresponds to a total of 0.139 cm^3 of free space inside the devices.

Table 4.8 – Difference in the weight of two sets of Smooth and Porous Seys-TENGs (4 Seys-TENGs connected in parallel).

Smooth (4′curing)	Porous (4′min curing)
1.303 g	1.168 g

Morphological cross-sectional imaging of the Seys-TENGs was done using both a Zeiss Auriga SEM-FIB, a Hitachi Regulus 8220, and a Dual Beam SEM-FIB system (NVision 40, Carl Zeiss AG). The cross-section of samples was prepared by transversely cutting the Seys-TENGs using a surgical blade. By observing the Seys-TENGs cross-section on SEM, other interesting features become visible. In Figure 4.37, the smaller ampliations show the differences in the PDMS structure for both smooth and porous samples. The last one contains several hollow bubbles randomly dispersed transversally in the PDMS structure that can contribute to an increased deformation of the structure when subject to mechanical load. On the other hand, a smooth sample presents a compact PDMS structure around the CF yarn. When observing the samples using higher ampliations, it becomes evident that PDMS also penetrates within the fibers differently, whether they are dry or wet. Smooth Seys-TENGs present PDMS all around the fibers. There are still some small gaps between the CFs, and some patterns that resemble the flow of liquid PDMS that are probably due to the small amount of time the PDMS has to penetrate between fibers before it gets hardened, which may take less than 2 minutes (according to progressive curing time cross-section SEM images in Figure 4.30). When examining the cross-sectional SEM image of the Porous Seys-TENG, a distinctly different situation becomes apparent. There are no indications of PDMS permeating the fibers at the core of the yarn. Consequently, this polymer does not cover the fibers individually, and there's a clear demarcation where the PDMS layer terminates and the fibers along with the hollow space commence. The

distinctive structural variation near the fibers in the Porous Seys-TENG is attributed to the presence of water molecules within the CF yarns. PDMS, being hydrophobic, encounters an obstruction in the form of water, preventing the seamless flow of the liquid PDMS through the structure. This, along with localized heating during evaporation, contributes to forming a bubbly and porous structure.

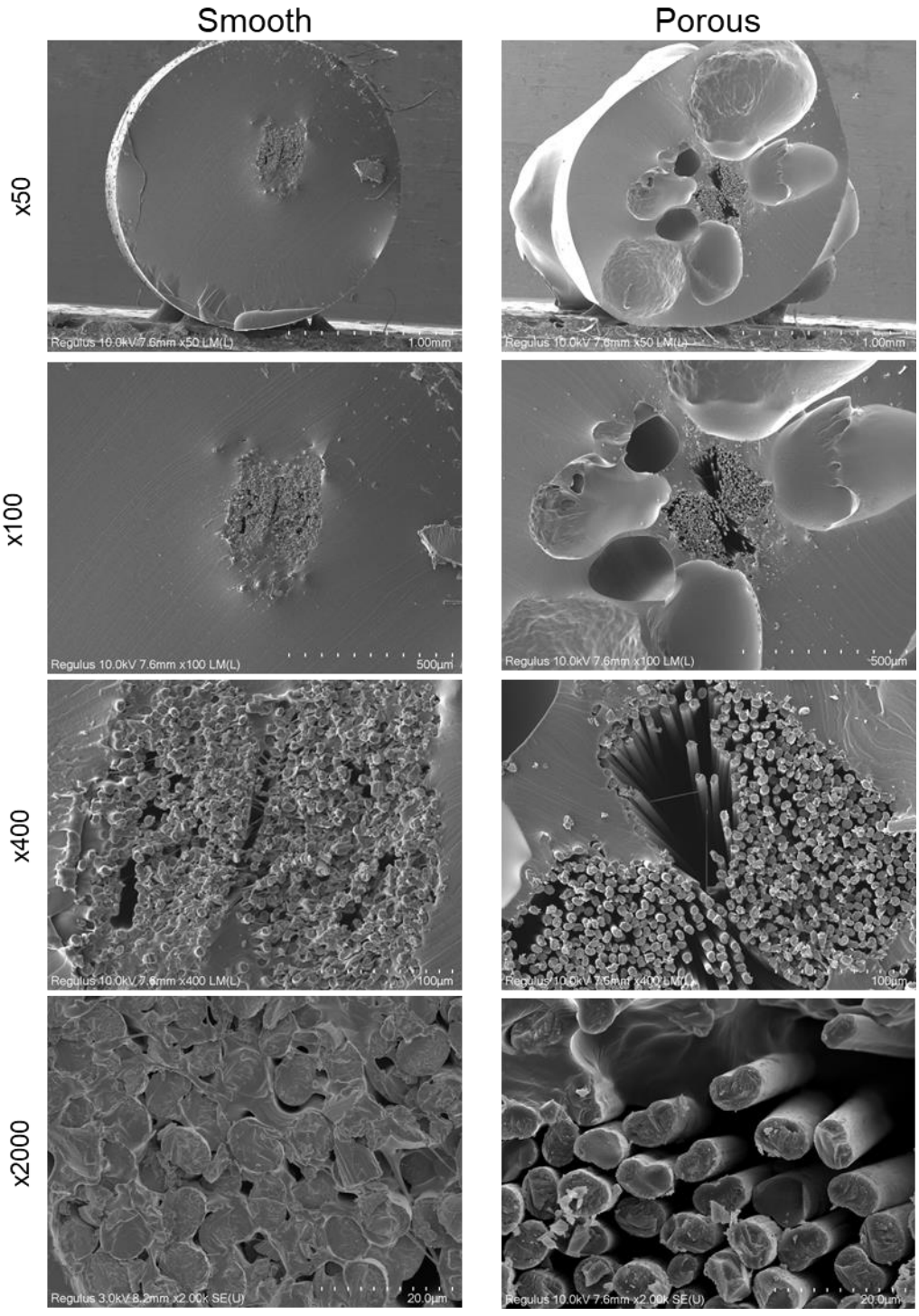

Figure 4.37 – Cross-sectional SEM images of a) smooth and b) porous PDMS deposited by in-situ curing on a CF yarn.

To study the extent of limited flowing time liquid PDMS must penetrate the fibers in the yarns, a reference sample was prepared by simply placing a CF yarn inside an uncured PDMS mixture. No current was applied to the fiber, and no heat was used to speed the curing of the elastomer. The PDMS was allowed to harden naturally at room temperature for several days, and then a cross-section SEM image of the resulting structure was taken and is shown in Figure 4.38. In this sample, once again, small air gaps are visible in the PDMS matrix between the fibers. With multiple hours allowed for PDMS flowing through the fibers, unlike previously stated, it seems that time constraint is not the responsible for the small gaps between the PDMS and fibers. Since PDMS is well known by its ability to easily penetrate small features, often used for mold making and replication of patterns of complex structures on the nanometer range, the presence of this gaps in the matrix close to the fibers is an interesting issue. Two scenarios may explain the presence of these small gaps: Firstly, they could result from the cutting process itself. When the sample is cut with a sharp blade, it can disturb the PDMS as the harder CFs are pulled through the soft polymer during cutting. Alternatively, the small gaps might stem from inadequate adhesion between the rubber-based CF yarn coating and the PDMS silicone elastomer.

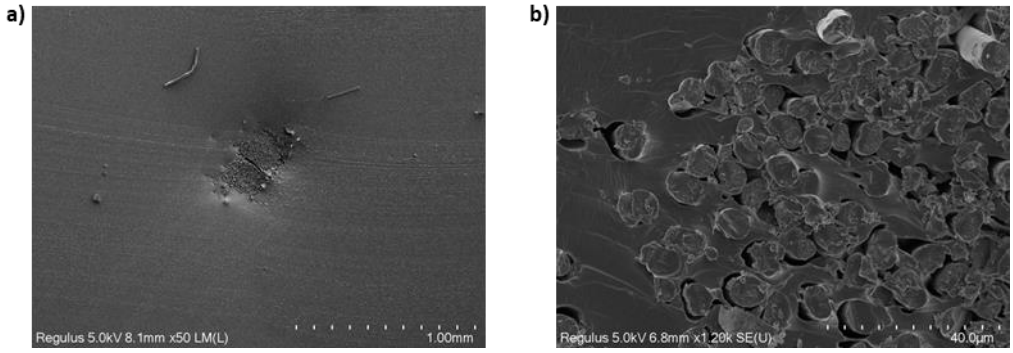

Figure 4.38 – a) Cross sectional SEM image of naturally hardened PDMS at room temperature and b) detail of the CF yarn.

4.4 Electrical characterization of Seys-TENGs

This section reveals the results regarding mechanical to electrical conversion characteristics of the Smooth and Porous Seys-TENGs. Unless otherwise stated, all electrical analyses were made with four Seys-TENGs connected in parallel by cupper tape like shown in Figure 4.39.

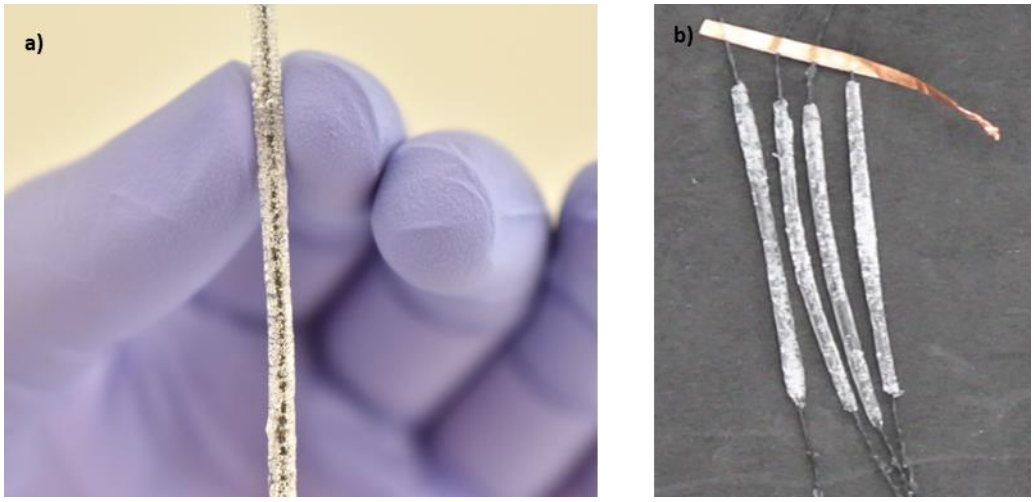

Figure 4.39 - Photograph of a) a Porous Seys-TENG and b) four Seys-TENGs connected in parallel via cupper taper.

Initially, the electrical characterization of set of Seys-TENGs was made using the application of mechanical load by the GFAM machine described in sub subsection 2.2.1.1. The open-circuit voltage measurements, a 100 MHz bandwidth Tektronix oscilloscope (TBS 1102C) was combined with a 10 MΩ of impedance probe connected to the Seys-TENG sets. The short-circuit measurements were measured using a Gamry 600 Potentiostat (at a fixed acquisition rate of 50 μs^{-1}).

The voltage-versus-time graph exhibits an initial prominent positive peak followed immediately by a negative peak and succeeded by at least three subsequent sets of progressively diminishing peak replicas. Eventually, these peaks become indistinguishable within the noisy background signal recorded by the oscilloscope. This phenomenon arises due to the nature of the elastic collision between PDMS and the lever. When the lever delivering the mechanical load strikes the sample, it bounces up and then falls back down until all the energy is dissipated (as illustrated in Figure 4.40 a)). Consequently, multiple mechanical load inputs are delivered to the Seys-TENGs, each converting varying amounts of energy, leading to a sequence

of increasingly smaller voltage peaks for each impact (as seen in Figure 4.41 e). Accordingly, the voltage output signal consisting of one positive peak followed by a negative peak has the typical shape of a piezo/ triboelectric signal. [9][197][198][199]. For the calculation of peak-to-peak voltage or current, only the initial and larger set of peaks is taken into consideration. These peaks are clearly visible in the detailed view of Figure 4.40 b). Following the primary impact and subsequent rebounds, the lever remains in contact with the sample for a brief period, the duration of which depends on the frequency being employed. A short while after, a minor negative bump is observed, signifying the moment when the lever is lifted from the sample to initiate the next mechanical loading cycle.

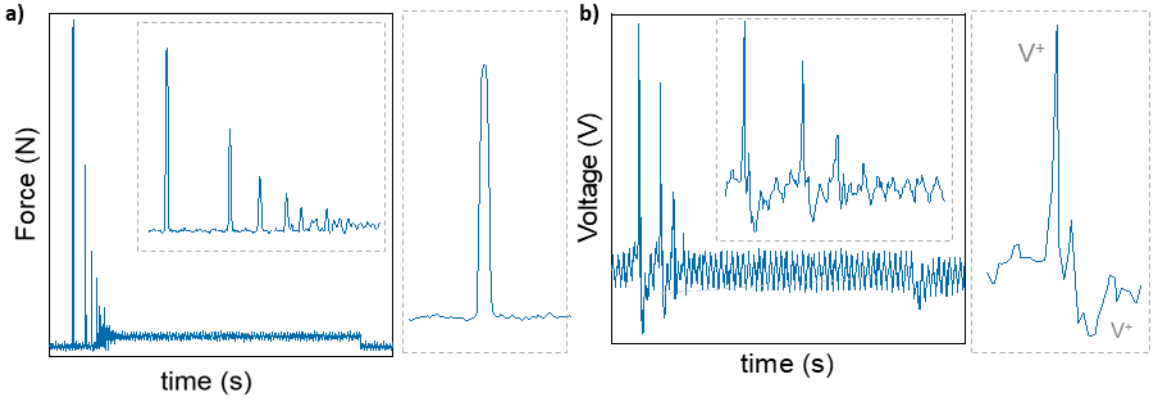

Figure 4.40 - a) Force profile obtained when using the GFAM actuating on a force sensor with details on bouncing and on the form of principal peak. b) Correspondent voltage output profile obtained from a Seys-TENG when mechanically actuated using the GFAM, with detail on the positive and negative triboelectric peaks.

The proposed energy conversion mechanism for the Smooth and Porous Seys-TENGs are schematically illustrated in Figure 4.41 b) and c), respectively. Initially, the shovel is at a high distance from the set of Seys-TENGs and the system is at a relative equilibrium. When the shovel is freed and starts descending (free falling), it comes to a point where the distance from the PDMS surface is such that the relative moving charges at both surfaces induce an electrical current at the electrodes. When in contact, the system stays once more at a relative equilibrium. When the shovel starts the ascending movement, two phenomena coincide: the triboelectrification of the surfaces of the shovel and PDMS that were once in contact; and the induction of an electrical current on the electrodes promoted by the relative movement of charges. Since PDMS is a widely known negative triboelectric material, and wood is in a

positive position relative to PDMS in the triboelectric series, PDMS will have an excess of electrons that will confer a negatively charged surface, whilst the wood will have a lack of electrons and develop a complementary positively charged surface. Even if electron transfer is the more accepted model of charge transference and widely accepted by the scientific community until recently, new scientific findings revealed that mass change is an important mechanism taking part in triboelectrification. These findings suggest that the strong surface adhesion and low cohesive bulk cohesion of PDMS facilitates the covalent bond breakage and material transfer and are responsible for a high surface charge density. The material transfer occurs in both directions but naturally mostly directed from the softer to the harder material. During the mechanical testing of PDMS, heterolytic cleavage of the polymeric chains (-Si $(CH_3)_2O$-) creates the formation of anions (-$(CH_3)_2SiO$-) at the surface.[200][92][101]

The shovel comes up, and this time there are additional charges at both surfaces, promoted by triboelectrification of surfaces after coming into contact. The cycle repeats, and there is accumulation of charges at both surfaces by triboelectrification phenomenon until a certain point, once the amplitude of voltage (and current) rises until eventually reaching a maximum on the surface charge density at both surfaces. In the case of the set of Porous generators, two different structures present in this device account for additional sources of triboelectrification contributing of the overall enhancement on the power conversion. The presence of porosities within the PDMS structure, and the lack of PDMS surrounding the CF electrodes creates possible additional sources of triboelectrification. The comparison of both these structures are shown on the cross- sectional SEM images from Smooth and Porous Seys-TENGs of Figure 4.37. Additional triboelectrification occurs upon contact/separation of PDMS with CFs and at the PDMS/PDMS interface when porosities are squeezed upon contact/compression. The porosities inside PDMS can also contribute to an enhancement of power conversion by increasing the overall capacity through the PDMS layer (charging at PDMS/air interfaces). Finally, a softer structure is obtained in the case of porous PDMS, that allow for a stronger compression and results in increased area of contact between the external surface on PDMS and the surface of the wooden shovel, gaining the ability of generating more charges upon contact.

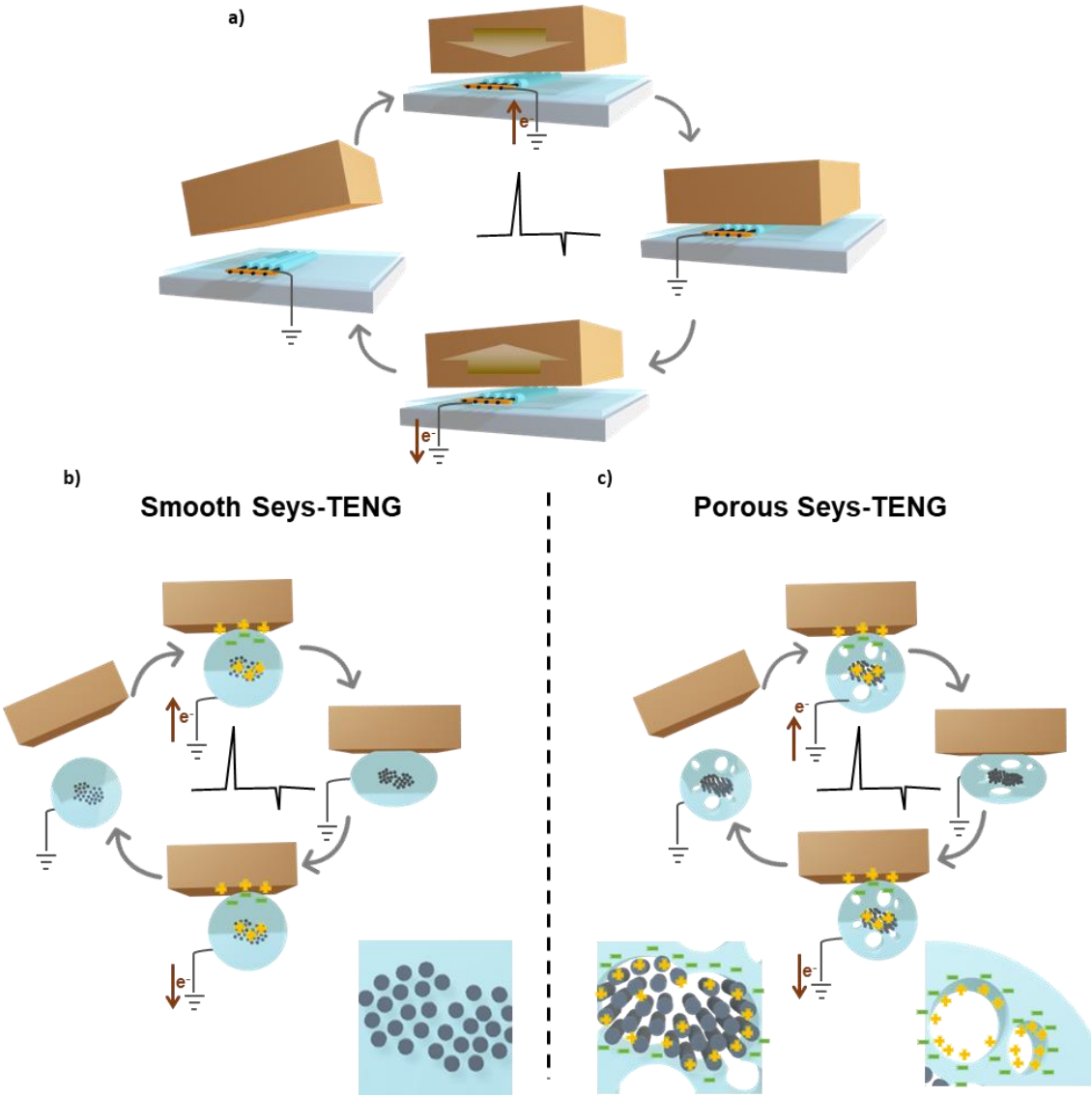

Figure 4.41 – a) Schematic representation of the cyclic mechanical tapping on Seys-TENGs using the GFAM machine. Representation of the power conversion mechanisms on b) Smooth and c) Porous Seys-TENGs, with a detail of additional mechanism contributing for the enhancement of power conversion.

The average of five different voltage and current peak values were obtained from smooth and porous sets of Seys-TENGs under a mechanical load stimulus of 50 N at a frequency of 1 Hz and results are shown in Figure 4.42 a) and c). Both sets present a general tendency of increased peak-to-peak voltage and current as a function of curing time/ PDMS thickness, reaching a plateau for samples with more than 4 min of curing. As the friction layer, PDMS is responsible for generating charges through the triboelectric effect and the surface

charge density directly affects the charge induction at the electrodes. The thicker the PDMS layer, the less probability of charge lost by recombination with the electrode and thus, more charge can accumulate at the surface.[145] Additionally, a ticker film directly affects the diameter of the TENG and the area available for charge generation. However, an excessively thick PDMS film may impair the electrostatic induction effect. A thicker PDMS film may force the electric field to propagate a longer distance until reaching the interface between the PDMS film and the electrode, thus reducing its strength and resulting in lower current and voltage outputs [145][201][202]. A compromise between these phenomenon's is required for optimal effect and can justify the existence of a plateau for samples with more than 4 min of curing.

Mainly when testing the samples using higher mechanical loading (using 600 N of force in Figure 4.42 b) and d)), the Porous sets result in higher voltage and current outputs when compared with the smooth counterparts. Bubbles/voids formation inside the PDMS, next to the CF core, allows the PDMS to deform more efficiently and create an effective higher contact surface (considering the inner surface of the bubbles), which increases the capability of this film to generate charge under a compressive force[203]. The bubbles/voids may also increase the separation between PDMS and the conductive yarn, further enhancing the triboelectric effect. The phenomenon of charging between the PDMS/air voids interface contributes to the overall increase in the permittivity of the material, resulting in a higher amount of charging of the electrodes.

Nevertheless, sets of yarns lacking the PDMS coating continue to generate voltage (Figure 4.42 b). The former effect is assigned to the existence of the SBR rubber-based sizing covering the conducting fibers, which serves as a triboelectrification layer. These results are in accordance with the relative position of the materials in the triboelectric series. Since wood and SBR are less distanced than wood and PDMS, the generation of charges by friction of the first pair is expected to be lower.[204][205]

Another strategy developed to estimate the contribution of the SBR coating to the overall power generation was done by placing the CF yarns on a heating plate at 400 °C for 15 minutes. At this temperature, the SBR coating is degraded: black fumes and a rubber burning odor from its carbonization were perceived, and when rubbing the yarns, black residues suggest the carbonization of the coating which is in accordance with the temperature for thermal degradation

of this compound [188]. This procedure didn't remove the coating. By promoting its carbonization, the residues remain on the surface of the CF yarns. Interestingly, when the CF yarns are annealed at 400 °C, they yield an even greater output than the untreated ones (Figure 4.42 b)). This effect can be assigned to the residual particles on the CFs' produced during the burning process of the sizing. This enhancement may additionally occur by promoting additional charging via mass transfer of these particles.

When covering the burned yarns with PDMS, the amount of force applied results in different outcomes. It was found that for lower impact forces, the output of burned-Seys-TENGs is quite similar to Smooth and Porous sets. However, the same set behaves quite differently when the impact force is increased to 600 N, exhibiting an especially higher voltage generation capacity for sets of PDMS deposited during 4 min. This demonstrates that this interface can also contribute to the charge generation in Seys-TENGs, and this potentiality is explored further in the next chapter.

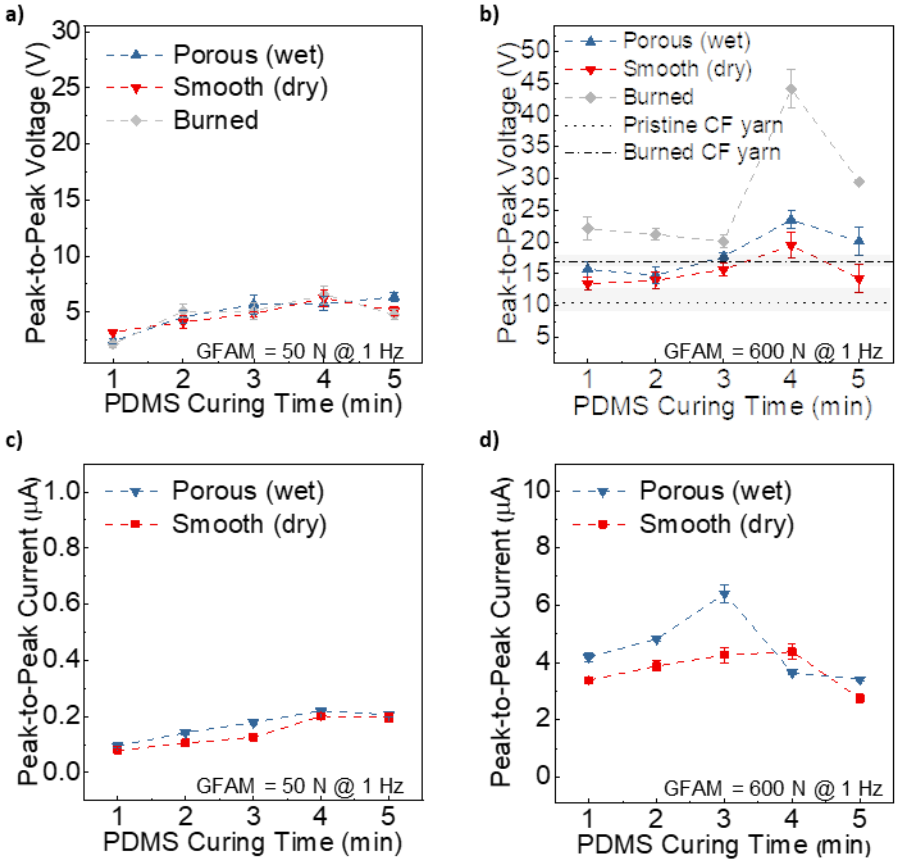

Figure 4.42 - a) The peak-to-peak open circuit voltage and c) short-circuit current for a loading of 50 N at a frequency of 1Hz; b) The peak-to-peak open circuit voltage and d) the peak-to-peak short-circuit current for a loading of 600 N at a frequency of 1 Hz.

The open-circuit voltage and short-circuit current were measured after about 2 years of production, this time using PFAM instead of GFAM. In the case of open-circuit voltage measurements, a 100 MHz bandwidth Tektronix oscilloscope (TBS 1102C) was combined with a 10 MΩ of impedance probe connected to the Seys-TENG sets. The short-circuit current was measured using a Keithley 485 autoranging picoammeter in combination with the oscilloscope. Since testing methodology (type of impact delivered and force of GFAM and PFAM are different – see sub-sub section 2.2.1.3 and Figure 3.18) was changed, it is impossible to truly compare the evolution of the performance of the devices over this period. The schematic representation of Figure 4.43 a) demonstrates how the set of Seys-TENGs was tested, and schematics of Figure 4.43 b) and c) represent the mechanisms of power conversion that are essentially similar to the model proposed when cycling using the GFAM (see Figure 4.41 a), b) and c))

The different impact profile delivered by PFAM and corresponding output triboelectric voltage generated upon impact is shown in Figure 4.43 d) and e).

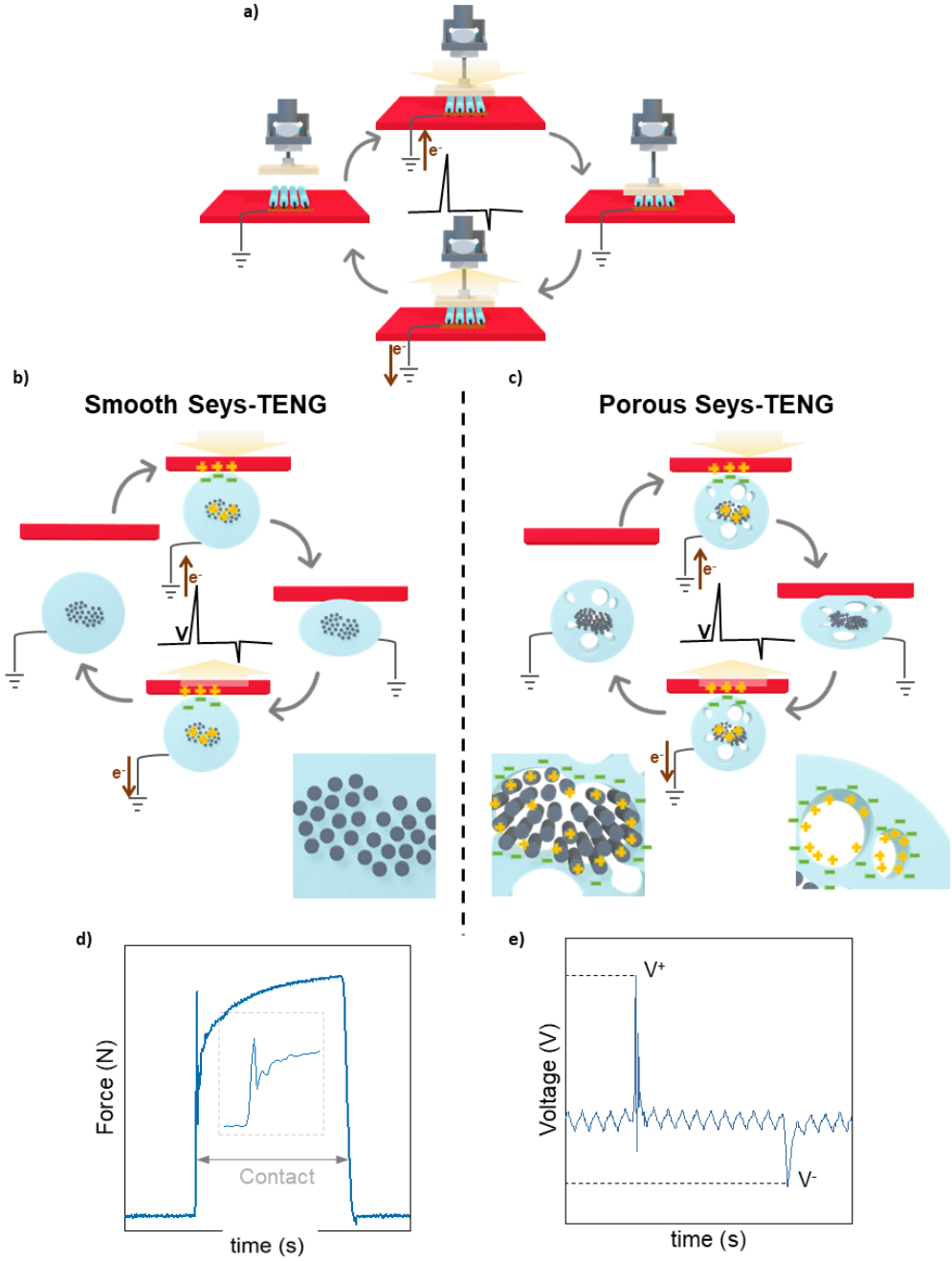

Figure 4.43 - a) Schematic representation of the cyclic mechanical tapping on Seys-TENGs using the PFAM machine. Representation of the power conversion mechanisms on b) Smooth and c) Porous Seys-TENGs, with a detail of additional mechanism contributing for the enhancement of power

conversion. d) force profile obtained using the GFAM actuating on a force sensor and e) correspondent voltage output profile obtained from a Seys-TENG when mechanically actuated using the PFAM.

The samples were kept wrapped in aluminum foil and inside a zip bag. The devices are still functional, reaching maximum open-circuit voltage and short-circuit current values of 38 V and 6.7 μA, respectively, for the Seys-TENG Porous set with a curing time of 4 min. Interestingly, when using higher forces of impact to test the Smooth 4' and Porous 4' set of generators, significantly higher values are obtained, with a maximum voltage of 61.28 Vpp for 50 N, and peak-to-peak current of 10.49 μA whilst applying 60 N of force. Also interesting is the fact that power values generated from Smooth and Porous counterparts over this period seem to converge, with no unambiguous evidence of advantage by using a porous PDMS structure.

Several factors can explain this difference in behavior, starting with the methodology to test the samples that changed from using GFAM to PFAM, as previously explained. Additionally, even if kept in a zip bag closed in aluminum foil to protect it from UV light, degradation of the silicone polymer in contact with air moisture might have occurred to some unknown extent during this period. The hydrolysis of PDMS into DMS monomers is reported in the literature as a general degradation process occurring in the presence of atmospheric humidity and catalyzed in the presence of basic or acid species, minerals and cations (including Al^{3+}) on the environment.[206] It is expected that this kind of degradation can occur at a higher rate in the case of porous PDMS since more surface area can promote hydrolysis at a higher extent. Additional degradation processes can occur through decomposition into volatile elements[206], eventually related to the observed characteristic rubbery smell developed over time. In addition, PDMS have a sticky surface that easily holds small dust particles on its surface that accumulate over time and usage, altering the surficial charge of the generator chemically and changing its overall triboelectric characteristics. Contrary to what one could expect, the degradation on power conversion capability was not proven. However, the performance of the porous set did not exceed much of the Smooth set counterpart.

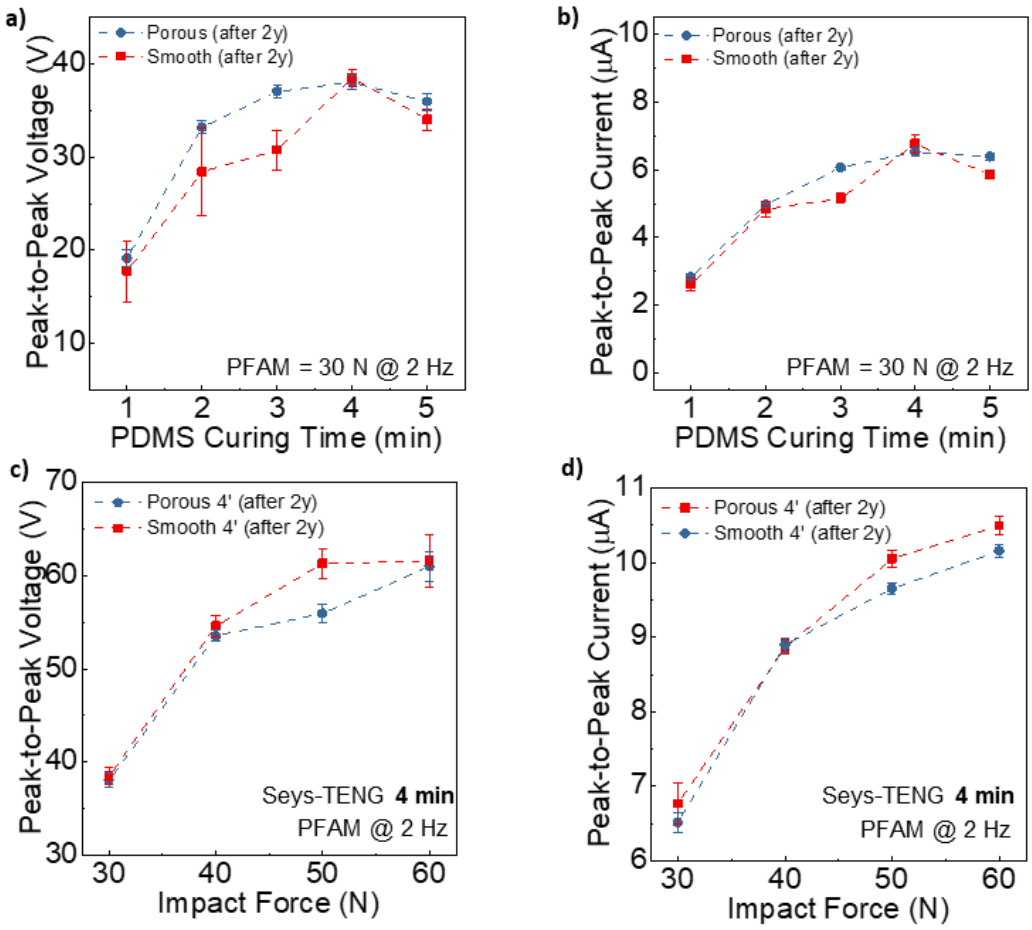

Figure 4.44 – a) The peak-to-peak open circuit voltage and b) short-circuit current for a loading of 30 N at a frequency of 2 Hz using PFAM, obtained for the Seys-TENGs 2 years after being fabricated.

A new set of Smooth and Porous Seys-TENG samples was fabricated, employing the optimal condition of a 4-minute curing time. Their performance was compared to samples aged for two years, as illustrated in Figure 4.45. V_{OC} (Figure 4.45 a)) and I_{SC} measurements (Figure 4.45 b)) were conducted, varying the impact force within the range of 30 to 60 N while maintaining a constant frequency of 2 Hz using the PFAM.

The performance of both the new and old samples demonstrates some similarity, with the older samples slightly outperforming the new ones for all forces except at 60 N. In the freshly prepared samples, it is possible to discern the varying performance between the Smooth and Porous sets. The Porous sets consistently outperform their Smooth counterparts, corroborating the findings initially observed in older samples. Most importantly, the consistent results suggest reproducibility of results.

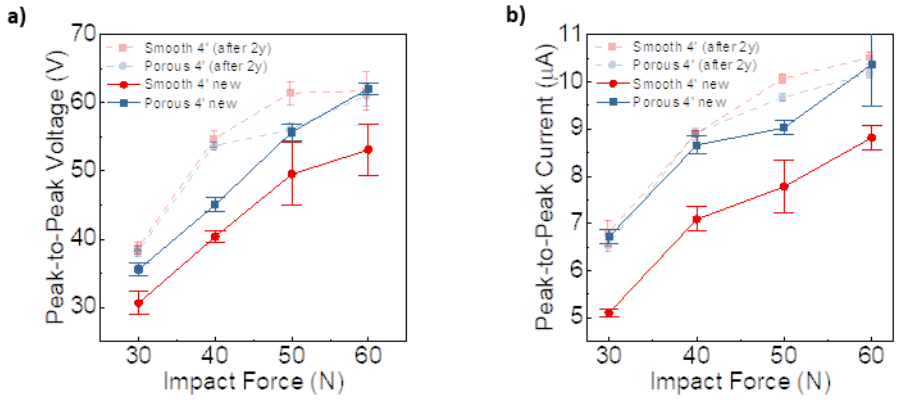

Figure 4.45 – a) V_{OC} and b) I_{SC} of new and old (2 years old) samples of 4' Smooth and Porous Seys-TENGs as a function of impact force, at 2Hz using PFAM.

The influence of the external material in the output voltage of Smooth and Porous Seys-TENGs was studied by testing the energy converters on PFAM using different materials such as Glass, Bamboo board (BB) and Teflon. The resulting output voltages are shown in Figure 4.46. While using glass, the voltage output of both sets diminishes slightly when compared to BB, which may seem counter intuitive when this material is ranked as highly positive in the triboelectric series while wood is considered in a more modest position.[204] However, it should be noted that unlike regular wood, BB are essentially composed of bamboo laminates hold together by glue or resins like melamine-formaldehyde-resin (up to 20% in-take)[207][208]. Studies showed that butylated melamine formaldehyde can become more positively charged than nylon, one of the highly positive materials in the triboelectric series.[209] The composition of the BB used for the tests is unknown, but this facts points to an enhancement of surface charge density that can explain its ability to produce slightly higher voltage output than glass. On the other hand, the position of Teflon in the triboelectric series means it's one of the materials most propense to become negatively charged, even more than PDMS which is considered as a negative material. [204] which is in line with the results obtained. When testing the sets using Teflon, the direction of the voltage peak was inverted, meaning that the surface of PDMS becomes positively charged, as Teflon is more electronegative than PDMS.

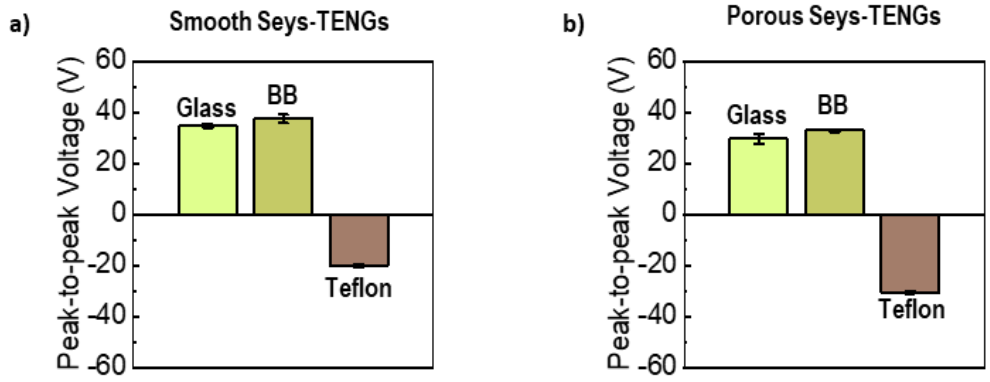

Figure 4.46 – The influence of the external material in the output voltage of a) Smooth and b) Porous Seys-TENGs.

With characteristic high voltages and low current values, matching the high impedance is essential for minimizing the loss of energy during power transmission. The voltage and current of Smooth and Porous new sets were evaluated when connecting load resistors from 100 kΩ to 200 MΩ in parallel or series, respectively, to the measuring instrument. While voltage increases directly with the value of the load resistors, the current decreases and the power was calculated by the product of the two. Both sets find its maximum values for load resistors of 50 MΩ. Smooth and Porous sets presents a maximum power value of 180.67 and 239.79 μW, respectively, which corresponds to a linear power output of 694.89 and 922.27 μW /m. This represents an increase of 33 % by uniquely changing the PDMS structure.

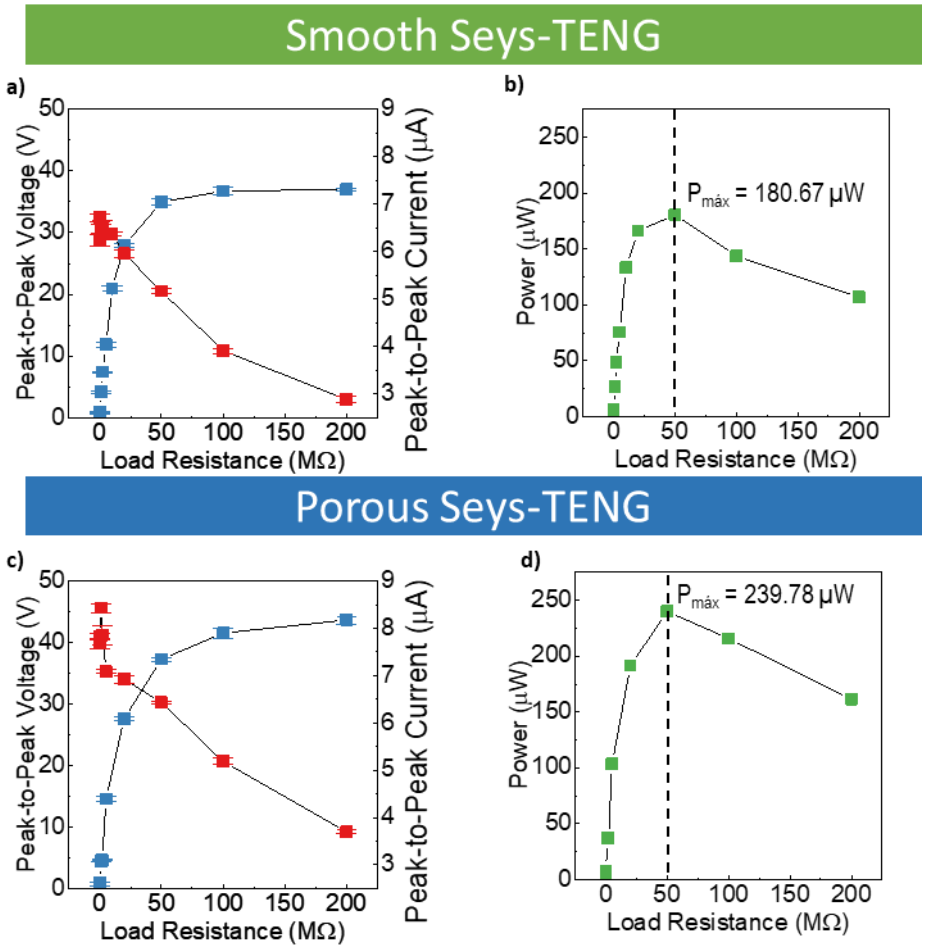

Figure 4.47 – a) Smooth and c) Porous Seys-TENGs voltage and current measured as a function of load resistance and b) and c) calculated power, respectively.

A summary of the electrical output results obtained for Smooth and Porous Seys-TENGs is shown on Table 4.9.

Table 4.9 – Summary of the electrical output results obtained for Smooth and Porous Seys-TENGs sets using PFAM with an impact force of 30 N at 2 Hz.

	V_{OC} [V]	I_{SC} [μA]	R_{LOAD} [MΩ]	V_{RLOAD} [V]	I_{RLOAD} [μA]	D (mm)	P_{max} [μW]	P_{max}/l [μW/m]	P_{max}/A [μW/m²]	P_{max}/V [μW/m³]
Smooth	30.64	5.10	50	34.96	5.17	2.05	180.67	694.88	33.90	210.53
Porous	35.56	6.72	50	37.28	6.43	2.26	239.79	922.27	40.81	229.91

The Seys-TENGs built using varied materials were tested using PFAM and the electric results are shown in Figure 4.48.

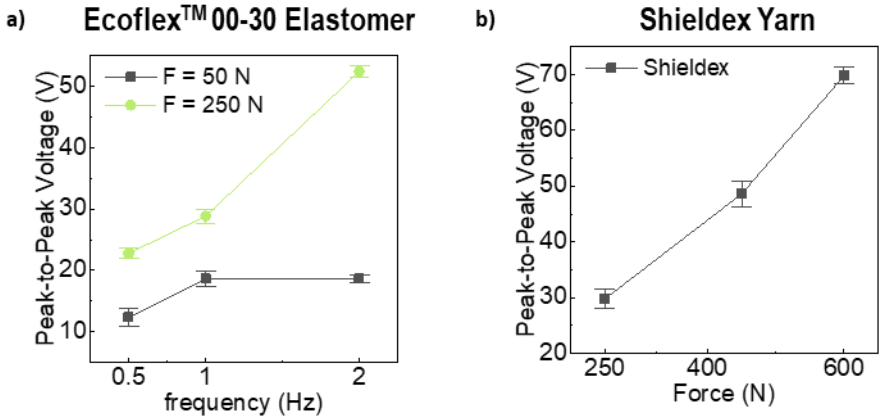

Figure 4.48 – Voltage output of Seys-TENGs a) using Ecoflex™ 00-30 as triboelectric layer and b) Shieldex yarn as electrode. The samples were tested using GFAM.

The use of Ecoflex as triboelectric layer results in the generation of more surface charges owing to the higher elasticity compared to PDMS, which promotes a higher area of contact upon impact. The Seys-TENG using silver as electrode presents a higher voltage than the initial using CF yarn as charge collector.

4.5 Conclusions

In this chapter, the new in-situ curing technique of PDMS was explored and used to produce single-electrode yarn-shaped triboelectric energy generators (Seys-TENGs). CF yarns (CF yarns) with a linear resistance of 530 Ω/m were used as the single electrode charge collector. The degradation of the inherent SBR based sizing on the surface of the CF yarns was studied by TGA, and an annealing procedure of 400 °C for 15 minutes was established to promote its thermal decomposition.

The in-situ curing technique consists of the local curing of PDMS around the conductive CF yarn from inside out by injecting a 0.2 A current through the conductive yarn that promotes heating by joule effect and accelerates the local curing of PDMS. Curing time was studied to control the thickness of the PDMS layer, which increases approximately at a linear rate with increasing curing time from 1 to 5 min when using a fixed current of 0.2 A. Using this current, the CF yarn can achieve a temperature over 120 °C almost immediately, while the temperature of PDMS close to the CF yarn slowly increases towards 80 °C after 12 minutes. PDMS starts curing after 2 minutes of curing application (53 °C), corresponding to an average diameter of 837.97 μm, and after 5 minutes and a measured temperature of 67.8 °C, resulting in diameters of 2617.83 μm.

In-situ curing of PDMS was tested using silver coated polyamide yarn. The presence of defects on the silver coating led to non-uniform curing of PDMS over the length of the yarn and promoted the formation of hot spots that locally melted the polyamide yarn. While the possibility of using this type of yarn was proved, the success rate is low and CF yarns were considered as a better construction choice for the in-situ curing of PDMS.

Porous PDMS structures were achieved by previously wetting the CF yarns with ultrapure water prior to curing PDMS using the in-situ curing technique. While Smooth Seys-TENGs presents a dense PDMS structure with only small gaps between the CF yarns, Porous Seys-TENGs on the other hand presents a porous structure and a defined frontier between PDMS and the CF yarn where large air gaps are imprisoned.

The Seys-TENGs convert mechanical to electrical energy by triboelectric effect and electrical induction at electrodes. When an external material (wood/BB) and the Seys-TENG suffers friction, the surface of PDMS becomes negatively charged by electronic and mass transfer phenomena. The relative moment of the charged surfaces induces an electrical current at CF yarn charge collectors. The presence of a porous PDMS structure promotes additional charging between the interfaces of PDMS/air and enhances the surface charge generation and therefore, the overall power conversion.

Initially, sets of four Smooth and Porous Seys-TENGs were connected in parallel and characterized using GFAM. Sets of Porous Seys-TENGs presented a higher mechanical to-electrical power conversion than its smooth counterparts. The higher results were achieved by the set of Porous Seys-TENGs cured for 4 or 3 min, with a maximum peak-to-peak open circuit voltage of 23.48 V and short-circuit current of 6.40 μA, respectively.

After two years of fabrication the devices were characterized using PFAM and found functional, although the difference in performance between Smooth and Porous sets became reduced. New sets of Smooth and Porous Seys-TENGs (4 minutes of curing time) were produced for comparison between freshly made devices and the previous ones. Interestingly, the older samples slightly outperform the freshly made sets. The new sets show a clear distinct performance between Smooth and Porous, with the Porous ones clearly showing a better performance over Smooth sets. The best results were obtained for the Porous sets with a value of 35.56 V and 6.72 μA of V_{OC} and I_{SC} respectively, and a maximum linear power output of 922.27 μW/m, an increase of 33 % over the Smooth Seys-TENGs.

5

ENHANCING SEYS-TENGS POWER CONVERSION: ZNO NANORODS AND COPPED CFS

This chapter describes the fabrication of Seys-TENGs using two distinct enhancement techniques: The first part is dedicated to the study of the introduction of ZnO NRs, grown hydrothermally in the surface of CF yarns; the second part describes the loading of PDMS matrix with cCFs. The fabrication process details, morphological and electrical characterization are also discussed, and the influence of these particles on the enhancement of mechanical to electrical power conversion is debated.

5.1 ZnO NRs functionalized CF yarns Seys-TENGs

ZnO is a wide direct band gap (3.37 eV) semiconductor, with large excitation emission at room temperature due to large exciton bonding energy (60 MeV), nontoxic, with high chemical and thermal stability, biocompatibility, high electron mobility and dielectric properties. [210] ZnO crystals are composed of alternating positive (Zn^{+}) and negative (O^{-}) planes along the c-axys, arranged in a hexagonal wurtzite structure (Figure 5.49). and its non-centrosymmetric arrangement in combination with a large electromechanical coupling are responsible for its great piezoelectric properties. [211][212] The possibility to grow a plethora of nanostructures using simple solvothermal or hydrothermal synthesis methods have drawn much

attention to this material as a green alternative and lead-free piezoelectric material. In 2006, a Piezoelectric Nanogenerator (PENG) based on vertically grown Zinc Oxide NR arrays marked the beginning of an extensive exploration of this subject.[57] The combination of hybrid triboelectric and piezoelectric phenomenon's on the same generator is also a strategy aiming to enhance the power conversion efficiency.

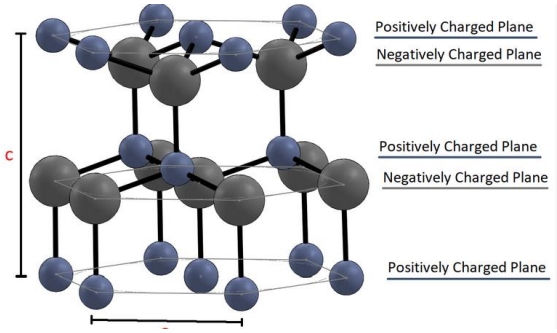

Figure 5.49 – ZnO hexagonal crystalline structure featuring its lattice constituted by alternating positive and negative planes (reproduced with permission from [212]).

In this section, the functionalization of CF surface with ZnO NR structures grown by hydrothermal synthesis and its application the development of Seys-TENG and influence in the overall mechanic to electrical conversion is discussed.

5.1.1 Hydrothermal growth of aligned ZnO nanorods over carbon fibers

ZnO rods can be easily grown on a plethora of different substrates using solvothermal processes. To increase both the coverage and alignment of the rods, a seed layer that promotes crystallographic growth in a certain direction is frequently used before the synthesis. For this work, a comparison between alignment and density of ZnO rods with and without the assistance of a pre-deposited seed layer was made.

The seed solution was set up by dissolving 0.05 M of Zinc Acetate Dihydrate ($Zn(CH_3COO)_2 \cdot 2H_2O$, CAS: 5970-45-6, 98% from Sigma Aldrich) in Ethanol (95% v/v from Fischer). The mixture was vigorously stirred for about 48 hours and then used right away.

Typically, several CF yarns were held in multiple support by clips and dipped simultaneously for 2 minutes in the solution. After that, CF yarns were transferred to a hot plate at 400 °C for 15 minutes. This process was repeated for a minimum of 1 to a maximum of 4 times, and later a correlation between the number of seed layers and the morphology and alignment of ZnO rods was established.

A 3D cap was specially designed using a 3D modelling software (tinkercad from Autodesk™) and 3D printed in ABS using an Anet A8 to fit a 200 mL glass beaker (Figure 5.50). The CF yarns previously treated to a seed layer were fixed vertically in the 3D printed cap using Kapton tape. Then, two separate solutions of 130 mL of 25 mM of Zinc Nitrate Hexahydrate and Hexamethylenetetramine using deionized water (Milipore) and stirred for a few minutes until complete dissolution. The two solutions were then combined in a 200 mL glass beaker and stirred for a couple additional minutes before the stirrers were removed from the solution. Finally, the 3D printed cap holding the CF yarns was placed on top of the beaker so that the yarns were kept immersed in the solution. The solution was heated to a setpoint of 90 °C with a ramp of 30 minutes and kept at this temperature for a total of 4 h inside the chamber of a Nabertherm furnace, where at last it was allowed to cool down naturally slowly. The ZnO NRs formed by growing anchored to the seed layer previously deposited on the surface of CF yarns in the following steps[213]:

(1) $(CH_2)_6N_4 + 6H_2O \leftrightarrow 6HCHO + 4NH_3$

(2) $NH_3 + H_2O \leftrightarrow NH_4^+ + OH^-$

(3) $2OH^- + Zn^{2+} \rightarrow ZnO(s) + H_2O$

Lastly, the CF yarns were removed from the solution, washed by dipping in deionized water and hot with a deionized water jet to release any barely attached bundle of ZnO NRs. Then, hanged vertically and dried in the oven at 60 ◦C.

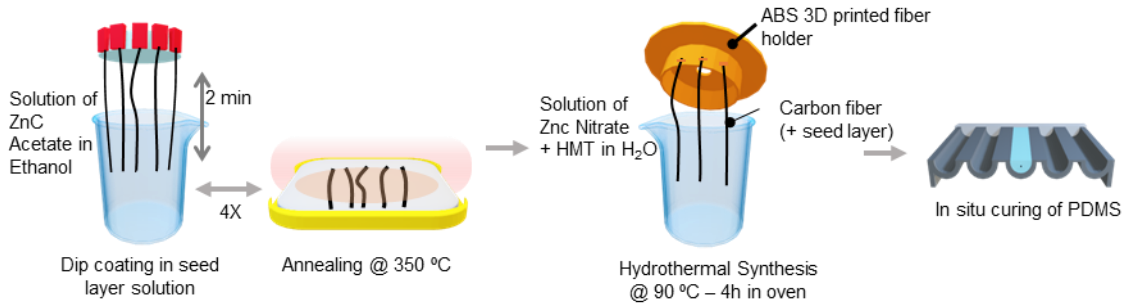

Figure 5.50 – Schematic representation of the procedure to produce ZnO functionalized Seys-TENGs.

The resulting surface of functionalized CF yarns was studied using a Zeiss Auriga Cross-Beam Scanning Electron Microscopy. While analyzing the resulting images in Figure 5.51 it became clear that ZnO NRs hydrothermally grown on the surface of CFs without any special preparation where not particularly well covered. The surface of the CF was not uniformly covered and the ZnO rods were of different dimensions and several orientations, not exactly perpendicular to the surface of CFs. CF yarns treated with a seed layer deposited prior to the ZnO rods growth dramatically increased the extension of the coverage of CFs surface with pillars with a reduced size, more uniform dimensions and orientation. These qualities were improved with the increase in the number of layers deposited prior to the hydrothermal synthesis. After depositing a fourfold of seed layers by dipping the CF yarn in a Zinc Acetate solution followed by annealing at 400 °C, the hydrothermal synthesis resulted in excellent coverage of the surface with ZnO rods dimensions ranging from 300 to 1000 nm of length and from 50 to 100 nm diameter. The alignment direction of the rods is not precisely perpendicular to the CF surface. Still, it is a better alignment than the one obtained for a lower number of seed layers.

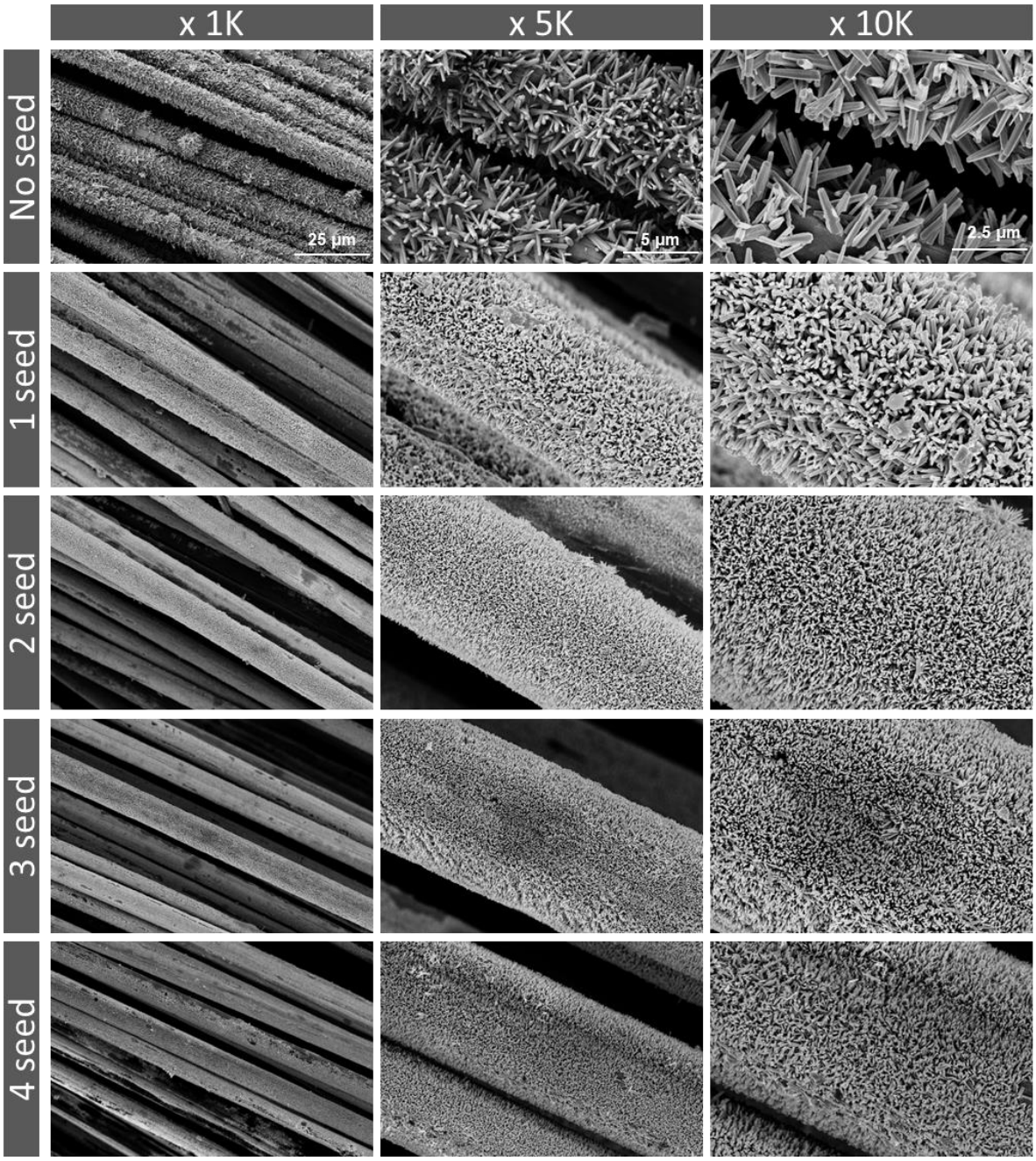

Figure 5.51 -SEM images obtained from the surface of CF yarns functionalized with ZnO rods grown by hydrothermal method, comparing the effect on the number of seed layers (and no seed layer) deposited before the synthesis on the alignment of ZnO rods and overall coverage of the CFs surface.

A PANalytical's X' Pert PRO M RD X-ray diffractometer using a monochromatic Cu Kα radiation source (wavelength 1.540598 Å) from 20° to 60° (2θ) with a scanning step size of 0.016°was used to determine the crystallographic structure of ZnO NRs. Figure 5.52 shows the X-ray diffractogram (XRD) of a pristine CF yarn, a functionalized CF yarns with ZnO rods grown on its surface, and ZnO rods collected from the bottom of the beaker used in the

hydrothermal synthesis. In the CF yarn diffractogram, a broad peak for 2 theta around 25 ° accounts for the well-known mixed crystalline and amorphous components within the CF structure, the former corresponding to (002) hexagonal carbon graphitic plane [182][183][184]. After growing ZnO rods on the CF yarn surface, additional peaks appear at 31.9, 34.6, 36.4, 47.6 and 56.6 °, corresponding to the (100), (002), (101), (102) and (110) planes assigned to the ZnO hexagonal wurtzite structure.[13] Said peaks match the ones of the white powder ZnO precipitates found at the bottom of the growth solution beaker. Additionally, the structure of the CFs remains unchanged after heating at 400 °C for 15 min (during the annealing of the ZnO seed layer), as previously seen in the results of the previous chapter.

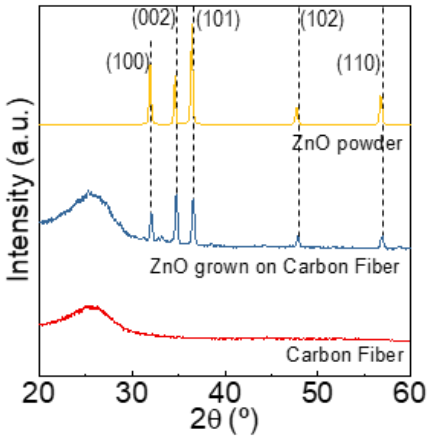

Figure 5.52 - XRD of a CF yarn before (red) and after (blue) growing ZnO rods, and the ZnO rod powder precipitate collected from the bottom of the solution vessel (yellow).

The same procedure described earlier was used to grow ZnO NRs over the surface of Shieldex yarn, with the only difference on the annealing temperature after depositing the seed layer was adjusted to 80 °C to prevent the melting of the polyamide yarn. After the deposition followed by annealing four times, the ZnO NRs were grown using the same process described before. The surface of the yarns was examined using SEM (Figure 5.51), revealing a satisfactory coverage and alignment of the NRs. However, upon closer examination, it becomes evident that the Ag coating has undergone some degradation. This suggests that metallic-coated yarns may not be the most suitable choice for this type of chemical synthesis due to potential damage to the coating.

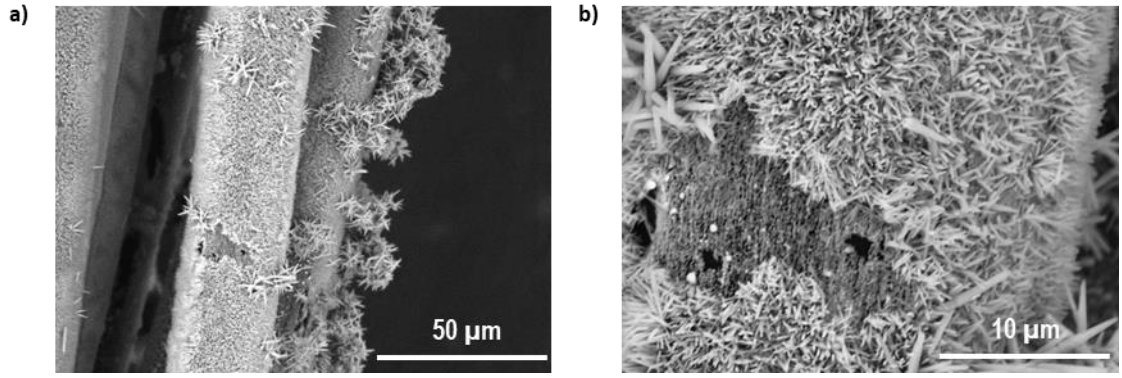

Figure 5.53 - SEM images of the a) ZnO NRs grown on the surface of Shieldex with b) a detail of some defects on the silver coating.

5.1.2 In-situ curing of PDMS around ZnO nanorods functionalized CF yarns

Smooth and porous PDMS structures were cured around the functionalized CF yarns using the in-situ curing method. PDMS mixture was prepared according to the standard procedure of 10:1 of PDMS to curing agent (SYLGARD™ 184 Silicone Elastomer from Dow Corning) and the same method used in the previous chapter. A current of 0.2 A was injected in the CF yarn through a power supply (Zhaoxin, PS-303D-II) during periods ranging between 1 and 5 min, which promoted the curing of PDMS from inside out around the CF yarn and resulting in different diameters depending on the duration of the curing. The diameters of Seys-TENGs were measured using a Mitutoyo digital micrometer. Five measures at three separate locations were taken, and the final diameter is the average of these values.

The resulting Seys-TENG diameters correspondent to each curing time are shown in Figure 5.54. As in the case of pristine CF yarns, the diameter of PDMS increases linearly with curing time for both smooth and porous PDMS structures. Unavoidable variation on initial room temperature and variance in resistance of each CF yarn are responsible for the diameter values dispersion. A slightly thicker PDMS layer was deposited around ZnO dry samples rather than on pristine dry samples. The variation of PDMS thickness between pristine and

functionalized yarns can also be related to the thermal properties of these materials. Typical thermal conductivity values for ZnO in the wurtzite crystalline structure found in the literature are around 50 W m^{-1} K^{-1} [214]. Since this value is higher than that of PDMS (~ 0.15 W m^{-1} K^{-1} [215]), the presence of ZnO rods as an intermediate layer can enhance the thermal exchange from the CF yarns to the PDMS, allowing a faster curing process and, consequently, increasing the final thickness of PDMS. Additionally, a ZnO rod interlayer increases the overall contact area between the CF yarns and the PDMS, which can further contribute to an enhanced thermal exchange.

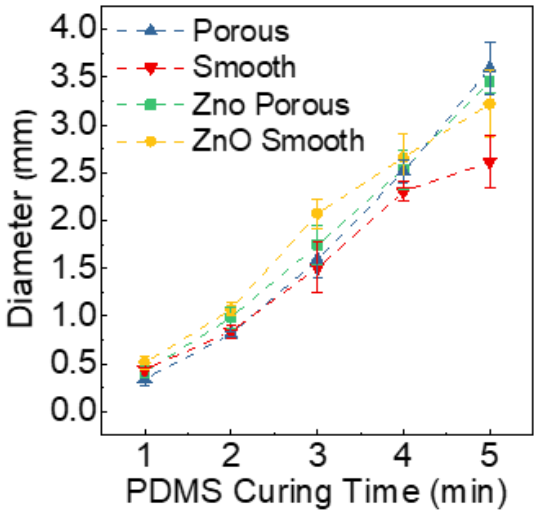

Figure 5.54 - The diameters of Seys-TENGs obtained by in-situ curing of PDMS around ZnO NRs functionalized CF yarns for 1 to 5 min.

Cross-sectional images of ZnO NR functionalized Smooth Seys-TENGs were obtain using a Zeiss NVision 40 SEM. The cross-section of samples was prepared by transversely cutting the Seys-TENGs using a surgical blade. A dense and continuous PDMS structure is visible from Figure 5.55 a). Interestingly, a detailed image near the CFs shows a detachment from the PDMS with a gap between them (Figure 5.55 b)). The ZnO NR forest is detached from the CF yarns and anchored on a surface that resembles a layer peeled off from the fiber (Figure 5.55 c)). This interesting anchoring layer in its turn, presents several cracks, and some stretch marks are also visible in the interior of the layer, facing the fiber (Figure 5.55 d)). From the observation of these cross-sectional images, one hypothesis regarding the nature of this detached layer was made. To begin with, the detached layer can be either a surficial carbon layer or the butene styrene-based rubber coating the fibers. Its detachment from the core fiber is related to the

simultaneous expansion of the CF when heated and to the shrinkage of PDMS while curing and upon cooling to room temperature, followed by a subsequent contraction of the CF when returning to room temperature. Several authors report a shrinkage of PDMS in a broad range of values, from 0.7 % at 80 C to 3 % at 60 °C.[216][217][218] Madsen et al. (2014)[219], reported an average of (1.92 ± 0.07) % shrinkage in both directions while curing a mixture of PDMS in the proportion of 10:1 (to curing agent) at 80 °C which are parameters very close to the ones experienced by the PDMS in Seys-TENGs. On the other hand, PAN based CFs transversal constant of thermal expansion (CTE) were reported ranging from 3.8 to 5.6 $\times 10^{-6}$ K^{-1} [220][221]. Although the transversal CTE of CFs is considered of a low value (compared to other types of metallic fibers), the combination with the PDMS shrinkage factor and the great surficial area between interstitial PDMS that completely penetrated between ZnO NRs can cause contraction forces that should be able to rip of the rods along with the anchoring layer. Additionally, during the deposition of the seed layer, prior to the hydrothermal growth of the ZnO rods, the fibers suffered a total of 1 hour of annealing at 400 °C (combination of the four-fold seed layer deposition and subsequent annealing for 15 minutes). This led to the thermal decomposition of the SBR sizing that weakened the bonds between this layer and the CF surface.

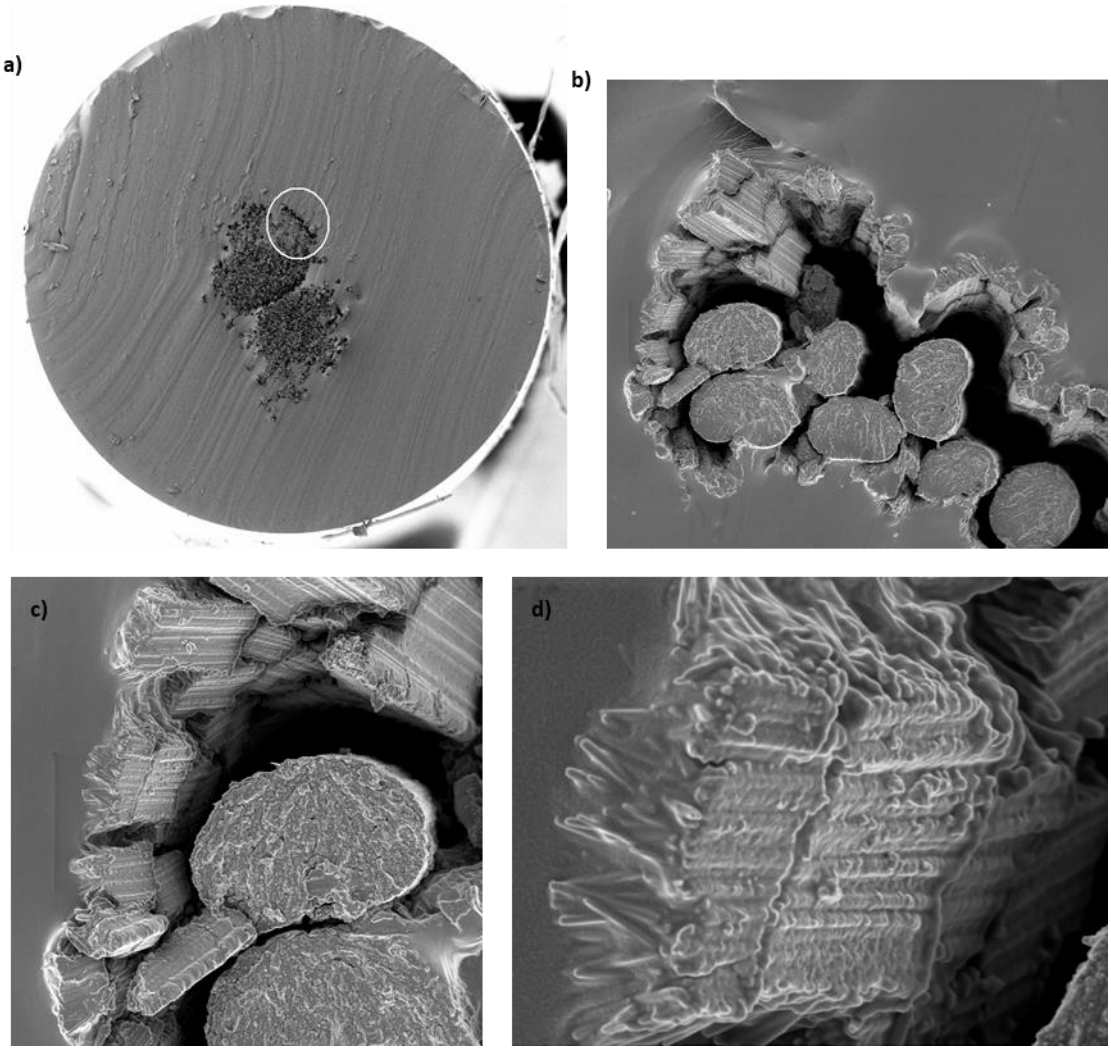

Figure 5.55 –SEM cross-sectional images of as prepared ZnO NR functionalized Seys-TENGs.

Additionally, the ZnO NR-functionalized Shieldex yarns were utilized for the in-situ curing of PDMS by applying a current of 0.2 A over a 4-minute duration. The increased number of defects resulting from the hydrothermal synthesis led to the sudden failure of a greater quantity of yarns than their raw form.

5.1.3 Electrical characterization of ZnO nanorod functionalized Seys-TENGs

This sub-subsection reveals the mechanical to electrical conversion characteristics of the ZnO NR functionalized Smooth and Porous Seys-TENGs and compares it with previously resulting data obtained from non-functionalized Seys-TENGs for reference. Unless otherwise stated, all electrical analyses were made with four Seys-TENGs connected in parallel by cupper tape. Initially, the open-circuit voltage and short-circuit current generated by the sets were evaluated while delivering a controlled vertical mechanical stimulus using the Gravitational Force Actuator machine (GFAM) described previously in sub-subsection 2.2.2.1. In the case of open-circuit voltage measurements, 100 MHz bandwidth Tektronix oscilloscope (TBS 1102C) was combined with a 10 MΩ of impedance probe connected to the sets. The short-circuit measurements were measured using a Gamry 600 Potentiostat (at a fixed acquisition rate of 50 μs^{-1}). The following parameters were used during the open-circuit voltage and short-circuit current measurements:

- Force of impact: 50, 250, 400 and 600 N.
- Frequency: 0.5, 1 and 2 Hz.

The sets were subjected to 1 to 5 minutes of loading for each of the mechanical load parameters in study to obtain a stabilized output value. The average peak-to-peak values (Vpp and Ipp) were calculated from five different peaks obtained for all sets.

As described in the previous chapter, because the applied load bounces forth and back after hitting the sample, it results in several bumps of continually reduced force. The first load has the highest amount of force and, when delivered o a set of Seys-TENGs, results in a voltage output signal consisting of one positive peak followed by a negative peak with the typical shape of a piezo/ triboelectric signal [9][197][198][199]. The first and larger set of main peaks are those considered in calculating the peak-to-peak voltage and current.

The proposed energy conversion mechanism for the ZnO functionalized Smooth and Porous Seys-TENGs are schematically illustrated in Figure 5.56 a) and b), respectively. Initially, the shovel is at a high distance from the set of Seys-TENGs, and the system is at a relative equilibrium. When the shovel starts descending (falling), it comes to a point where the distance

from the PDMS surface is such that the relative movement of charges at both surfaces of the shovel and PDMS induce an electrical current at the electrodes. Since PDMS is a widely known negative triboelectric material, and wood is on the positive side relative to PDMS in the triboelectric series, PDMS will have an excess of electrons that will confer a negatively charged surface, whilst the shovel will have a lack of electrons and develop a complementary positively charged surface. Upon pressure, the system is compressed, and the ZnO NRs located in the inner surface of PDMS are pushed against the CFs, contributing to the induction of more charges at electrodes. Additionally, the mechanical deformation of ZnO NRs can induce a piezoelectric current. While compressed, the system is at equilibrium with no relative movement of charges and, consequently, no current flows through the circuit. Once the pressure from the shovel is released and the ZnO rods return to their original unbent state, a new piezoelectric current arises in the opposite direction. The shovel produces additional charges at both surfaces, promoted by triboelectrification of surfaces after coming into contact. As the shovel interface moves away from the PDMS surface, the relative movement of charges. induces a current in the electrodes. Once the shovel reaches enough distance from the PDMS surface, the system returns to equilibrium and no current flows through the circuit. The cycle repeats with an accumulation of charges at both surfaces by triboelectrification. The amplitude of voltage (and current) keeps rising until eventually reaching the maximum charge density at both surfaces.

A similar mechanism is proposed in the case of ZnO NRs functionalized Porous sets, with the addition that the generation of charge induction is further enhanced by the presence of porosities inside the PDMS matrix. The interfacial charging between PDMS and air from porosities increases the system's capacity. As discussed previously, the porosities also create a softer PDMS with extended deformation, promoting the creation of a higher contact surface [203].

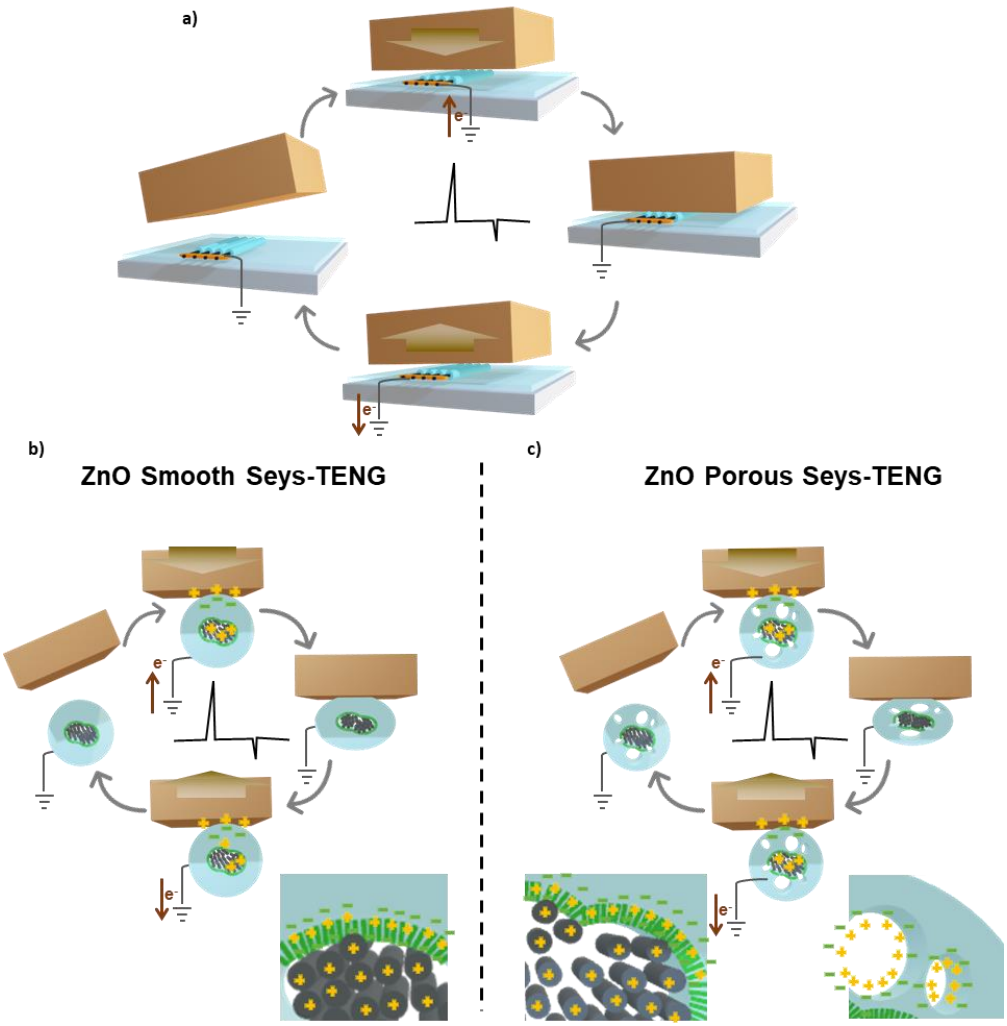

Figure 5.56 - a) Schematic representation of the cyclic mechanical tapping on Seys-TENGs using the GFAM machine. Representation of the power conversion mechanisms on ZnO NR functionalized b) Smooth and c) Porous Seys-TENGs, featuring additional mechanism contributing for the enhancement of power conversion.

The average of five different voltage and current peak values obtained under a mechanical load stimulus of 50 N at a frequency of 1 Hz is shown in Figure 5.57 a) and c). ZnO functionalized Smooth and Porous sets present a general tendency of increased peak-to-peak voltage and current as a function of curing time/ PDMS thickness, reaching a plateau for samples with more than 4 min of curing. Similarly to what was discussed in the previous chapter, the presence of PDMS enhances the performance of the harvester due to its ability to generate charges through the triboelectric effect and an increase in the PDMS diameter increases the surface area generating a higher number of charges. But the presence of a plateau it appears that an excessively thick PDMS film may force the electric field to propagate a longer distance

until reaching the interface between the PDMS film and the electrode, thus reducing its strength and resulting in lower current and voltage outputs [201][202]. ZnO NR functionalized Porous sets deliver a higher peak-to-peak voltage output than the remaining samples, achieving its maximum value for the set corresponding to a PDMS in-situ curing time of 4 min. When testing the samples using a higher mechanical loading of 600 N, output values from ZnO NR functionalized and non-functionalized sets follow significantly different tendencies. Smooth and Porous sets of ZnO functionalized Seys-TENGs develop a higher peak-to-peak voltage and current than its non-functionalized counterparts. A maximum value of 72.2 V and 10.4 μA is achieved for the ZnO NRs functionalized Porous set for a curing time of 3 min. After reaching its maximum value, the voltage and current output decrease significantly for higher curing times. It is reasonable to assume that the presence of ZnO NRs somehow contributes to a significant enhancement of Seys-TENGs power conversion.

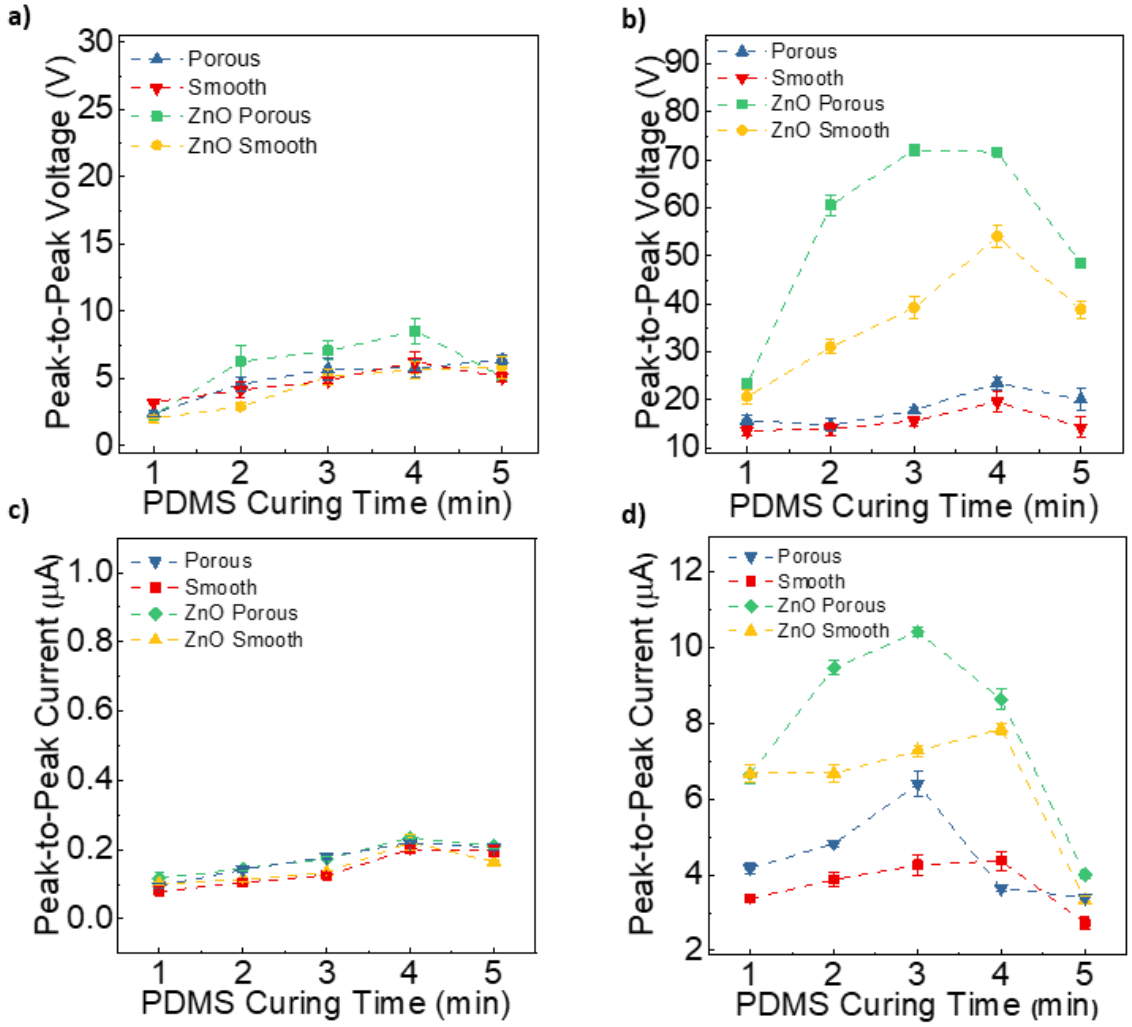

Figure 5.57 – a) Average values of open circuit peak-to-peak voltage output obtained for sets of sets using 50 N and b) 600 N of mechanical load. c) Average values of short-circuit peak-to-peak current output obtained for sets using 50 N and d) 600 N of mechanical load.

The power generation capacity of a TENG is intricately tied to the electrical characteristics of its dielectric material. The presence of ZnO NRs impregnated at the surface of the PDMS matrix promotes additional electron charging at interfaces between the insulating PDMS matrix and particles (Figure 5.58Figure 5.77).

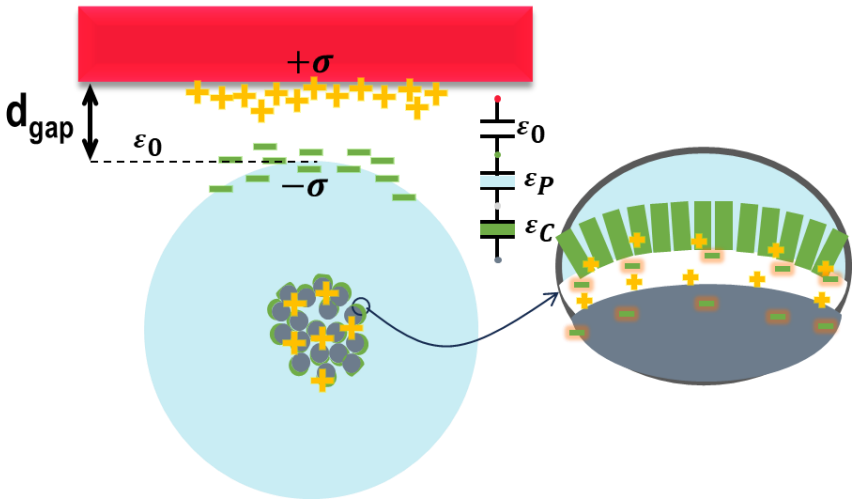

Figure 5.58 – Schematic representation of the charging mechanism of the Seys-TENGs functionalized with ZnO NRs.

Equation 2.6 describes how the Voc of a generator is directly dependent on the surface charge density. In its turn, the surface charge density (σ) dependence on the dielectric properties of the triboelectric material is described in Equation 5.20, where ε_0, d_{gap} and $\varepsilon_{composite}$ are the permittivity of free space, the gap dimensions and the relative permittivity of the composite (the PDMS and the ZnO NRs), and σ_0 and $d_{composite}$ are the initial surface charge density and the thickness of the PDMS composite, respectively. [222]

$$\sigma = \frac{\sigma_0 d_{gap}}{d_{gap} + \frac{d_{composite}}{\varepsilon_{composite}}} \qquad \text{Equation 5.19}$$

Deformation of Seys-TENGs is a critical factor for the charge generation process. The time of in situ curing as well as final PDMS thickness, the porous or smooth nature of the elastomer, the random disposition of voids inside the porous structure, and the extent of the flow of PDMS through the fibers of the CF yarn electrode all form a complex combination of parameters that can influence the mechanical properties of the Seys-TENGs. Compressive mechanical tests were performed to better understand how the different nature of structures can play a role in the overall electrical performance on the devices. A static-dynamic miniature testing machine inspekt micro LC 100N from Hegewald & Peschke with a velocity of 100 mm/min and a maximum load of 40 N was used to perform the compressive mechanical characterization of TENGs. The calculated Young's modulus is resumed in Table 5.10. In general,

Seys-TENGs with higher curing times have higher Young's moduli, indicating a higher resistance towards compressive forces. The extra time required for increasing the TENGs final diameter also contributes to forming a stiffer region of PDMS near the core of the fiber that can be related to the decrease in the performance observed for the higher curing times. It is also possible to see that Seys-TENGs presenting porous structures tend to have lower Young's moduli than their smooth counterparts. Thus, an increased amount of deformation occurring on these samples, based on their softer structure, can be partially responsible for an enhancement in the charge generation.

Table 5.10 - Young's modulus of different Seys-TENGs.

	3 min		**5 min**	
	Young's modulus (MPa)	**Std D. (MPa)**	**Young's modulus (MPa)**	**Std D. (MPa)**
ZnO Porous	0.214	0.099	0.985	0.301
ZnO Smooth	0.567	0.087	0.454	0.133
Porous	0.047	0.031	0.818	0.188
Smooth	0.146	0.099	0.863	0.507

ZnO NRs piezoelectric properties may be responsible for such enhancement of electrical conversion. To estimate the individual contribution of triboelectric and piezoelectric phenomena for the overall output of the generators, a brief analysis was performed based on the results obtained for the several types of Seys-TENGs under a stimulus of 600 N (1 Hz). Bar height in Figure 5.59 represents the maximum values of open-circuit voltage and short-circuit current obtained for 3 min in-situ cured sets. The increased voltage and current percentage, relative to the Smooth non-functionalized set (used as reference), are indicated over each bar. The value inside the bars, over the shadowed area corresponds to the percentage that may be attributed to the presence of ZnO NRs.

The best output values obtained for Smooth non-functionalized Seys-TENGs are 19.52 V and 4.38 μA. Based on previous studies [223] that confirm that PDMS is not a piezoelectric material, the mechanism of power conversion, in this case, can be exclusively assigned to the triboelectric effect. When introducing air bubbles/voids on the PDMS layer and interface of

Porous Seys-TENGs, the voltage and current increased by 20.3% and 46.3%, respectively, due to purely triboelectric charge generation. When introducing vertically aligned well-known semiconductor and piezoelectric ZnO NRs between the PDMS layer and the CF electrodes, the voltage and current increased by 177.0% and 79.3%, respectively. Many groups have reported that the presence of solvothermal grown and vertically aligned ZnO NR structures can contribute to the piezoelectric response of a generator [224][225][226]. According to the calculated values, a theoretical maximum of 63.9% and 44.2% of voltage and current, respectively, could be attributed to piezoelectric origin. Additionally, ZnO NR functionalized Porous Seys-TENGs have an increase of 269.7% and 138% in voltage and current, respectively. In this case, a maximum of 67.5% and 38.5% voltage and current would be ascribed as of piezoelectric origin. However, according to other authors [227][228], ZnO NRs can also contribute to charge generation by means of triboelectrification. Such high improvement on voltage values while operating at low frequencies (1 Hz) suggests that triboelectrification phenomenon might indeed occur in charge generation at some unknown extent, possibly lowering the real value percentage of piezoelectric input. The presence of ZnO NRs that are not attached to the CFs and undergoes contact/separation as well as the PDMS surface makes this a likely possibility.

It should be emphasized that the values in the shadowed areas of the bars correspond to the theoretical maximum contributions of ZnO NRs, either of piezo or triboelectric origin. Further studies on this topic are necessary to understand the exact contribution of each phenomenon clearly.

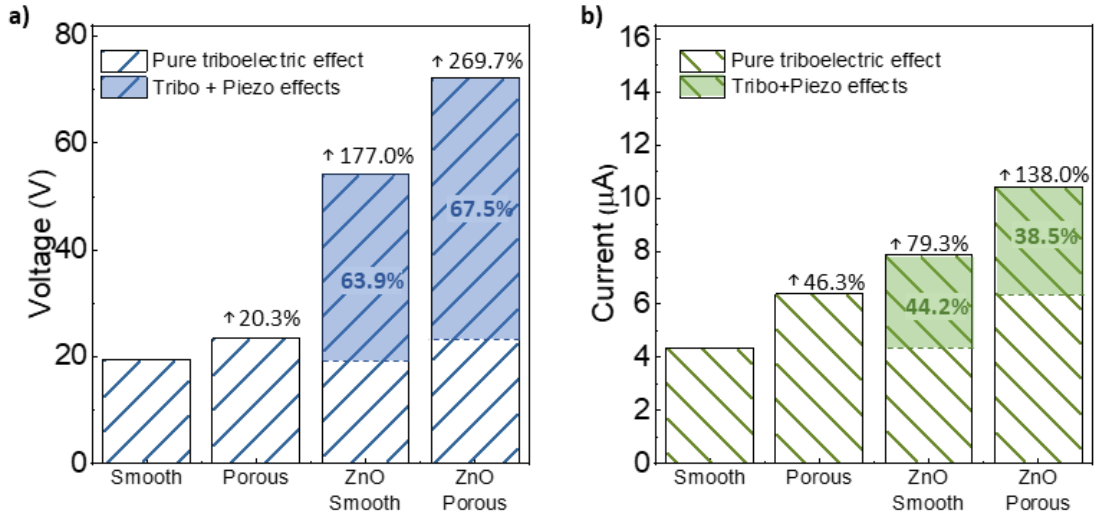

Figure 5.59 – Overall a) voltage and b) current enhancement of Seys-TENGs promoted by introducing porous PDMS structure and functionalization using ZnO NRs. The values inside the shadowed areas represent the maximum possible theoretical contribution of piezoelectric effect, although most probably it corresponds to mixed mechanism of piezo and triboelectric phenomena.

The best set of Seys-TENGs was chosen to proceed with further electrical tests. In this case, the set of ZnO functionalized Porous sets in-situ cured for 3 min. The power density was obtained by measuring the voltage and current generated by the set when connected to different load resistors. The current density was calculated by establishing the effective area of charge transfer as a gross estimation of the external area of the yarn. Briefly, the yarn was approximated to a cylinder, and the lateral area was calculated. Power density was obtained from the voltage and current density, and all three parameters are present in Figure 5.60 a). A maximum value of power density was 74.1 μW/cm^2, obtained while using a load resistor of 20 MΩ.

Open-circuit voltage and short-circuit current increase for mechanical loading of higher forces and frequencies (Figure 5.60 b) and c)), respectively. The Porous set was subjected to an endurance of 10 000 mechanical loading cycles at a force of 600 N (at 1 Hz) while monitoring the open-circuit voltage and short-circuit current (Figure 5.60 d)). Both electrical parameters increased, particularly for the first 1000 cycles. This effect is related to the charge accumulation and retention in the PDMS surface. Charges generated in this layer take a particular time to dissipate through the conductive CF electrodes. This phenomenon can enhance the electrical output by promoting the accumulation of a large quantity of charges, which results in a larger

induction current in the CF yarn electrodes when mechanically stimulating the devices. This phenomenon was confirmed by measuring the charge flowing through the carbon electrodes for a certain period. The experiment involved a repeated mechanical loading of a Porous set using a human hand for a period of 60 sec. The monitoring of charge flow through the CF yarn electrodes (Figure 5.60 e)) showed an initial linear increase of charge flow (while tapping the set), promoted by the charge accumulation, followed by a subsequent slow exponential decay that was measured for a couple of hours.

The performance of the Porous set was evaluated while subject to different degrees of bending intensity as shown in Figure 5.60 f). There is some degradation on the open-circuit voltage, particularly when increasing the bending intensity. In the extreme case of forcing the Seys-TENG into an "S" shape curve, the voltage degrades to about half its initial value. On the other hand, the current values remain unaltered under the bending situations. These results highlight this TENG's capability to perform under demanding physical situations.

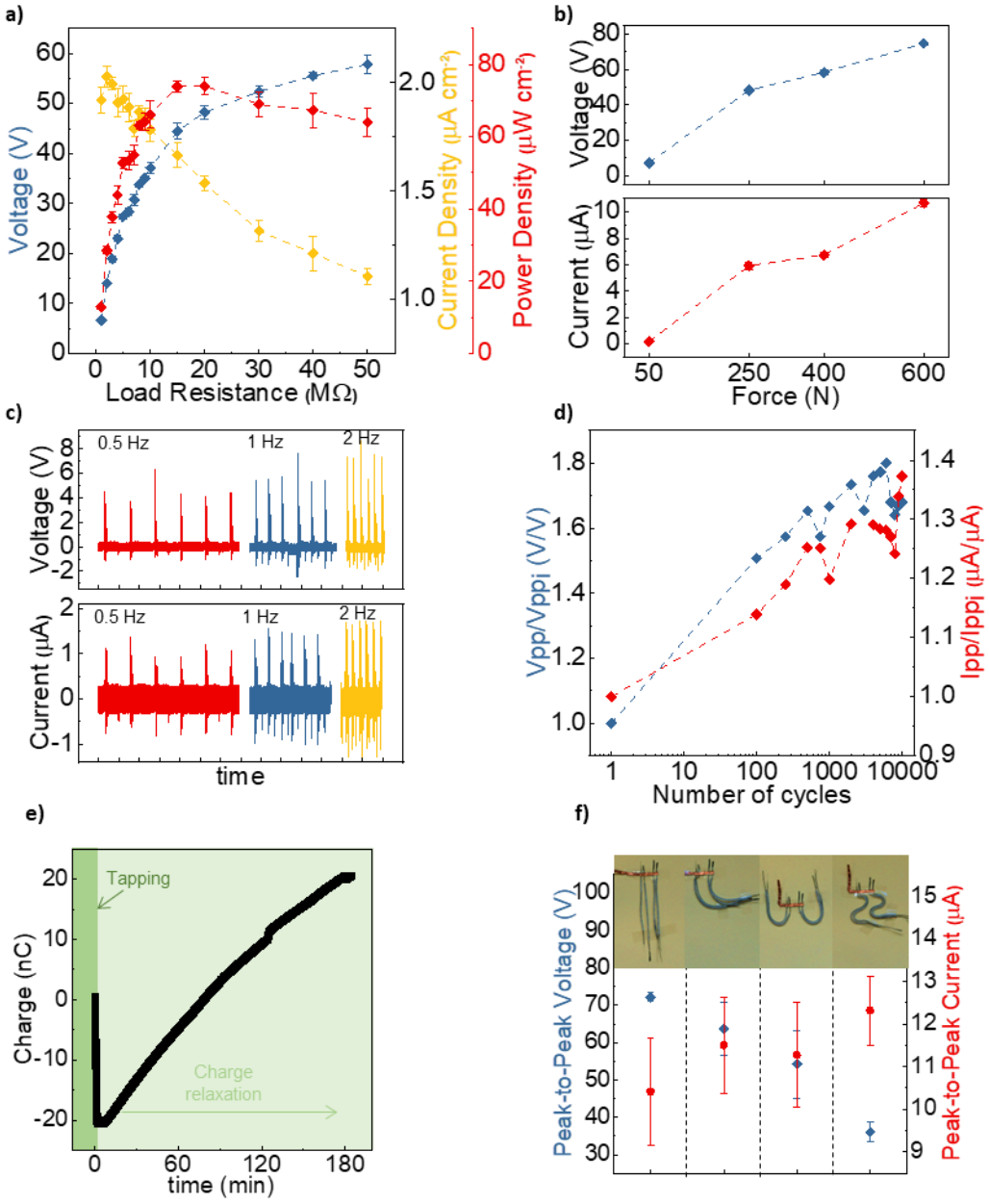

Figure 5.60 – a) Peak-to-peak voltage, current density obtained and calculated power density for a set of ZnO Porous - 3min compressed using a mechanical load of 600 N at 1 Hz as a function of different load resistance values. b) open circuit peak-to-peak voltage and short-circuit peak-to-peak current values obtained for a set of ZnO NR functionalized Porous sets-3min as a function of mechanical loads ranging from 50 to 600 N applied at a fixed frequency of 1 Hz c) Electrical signal obtained from ZnO NR functionalized Porous sets-3min while subjected to a mechanical load of 600 N applied at frequencies varying from 0.5 to 2 Hz. d) open circuit peak-to-peak voltage and short-circuit peak-to-peak current values obtained for a set of ZnO NR functionalized Porous sets-3min compressed from 1 to 10 000 cycles using a mechanical load of 600 N at 1 Hz. e) Charge relaxation measured from a set of ZnO NR functionalized Porous sets. f) Open-circuit voltage and short-circuit current output values obtained for

a force of 600 N while bending the set of ZnO NR functionalized Porous sets in different configurations.

The open-circuit voltage and short-circuit current were measured after about 2 years of production using PFAM. As described in the last section, the samples were wrapped in aluminum foil and inside a zip bag. The devices are still functional, reaching maximum open-circuit voltage and short-circuit current values of 42.16 V and 6.8 μA, respectively for the ZnO functionalized Seys-TENG Porous set with a curing time of 3 and 4 min, respectively, when tested using a force of 30 N at a frequency of 2 Hz (Figure 5.61 a) and b)). However, when using higher forces of impact to test all sets cured for 4 minutes (Smooth, Porous, ZnO Smooth and ZnO Porous), the sets functionalized with ZnO NRs do not perform better than its non-functionalized counterparts (Figure 5.61 c) and d)). Although a different force and type of impact is being used for these tests, this suggests a shift in the initial tendency of the sets, where initially the functionalization ones would grant a significant advantage in enhancing power conversion efficiency. As described previously in subsection 3.2.4., water and specific catalysts can enhance the hydrolysis of PDMS[206]. All samples were kept wrapped in Al foil, which may act as a catalyst for this reaction in the exterior part of the device. ZnO is hygroscopic and can contribute to increasing the moistening in the internal part of the device. At the same time, its presence contributes to an increased area of contact and gap between the CF electrodes and PDMS like is possible to observe in SEM images from Figure 5.63 d). This can indicate that a faster deterioration of PDMS occurs in the presence of ZnO NRs. While hydrolysis of PDMS in the exterior shell does not seem to impact the overall ability of power conversion (like in the case of non-functionalized Smooth and Porous sets), hydrolysis taking place in the internal structure, specifically in the interface between PDMS and the CFs, points to a deterioration of electrical qualities to the point where the presence of ZnO NRs in the structure is no longer advantageous.

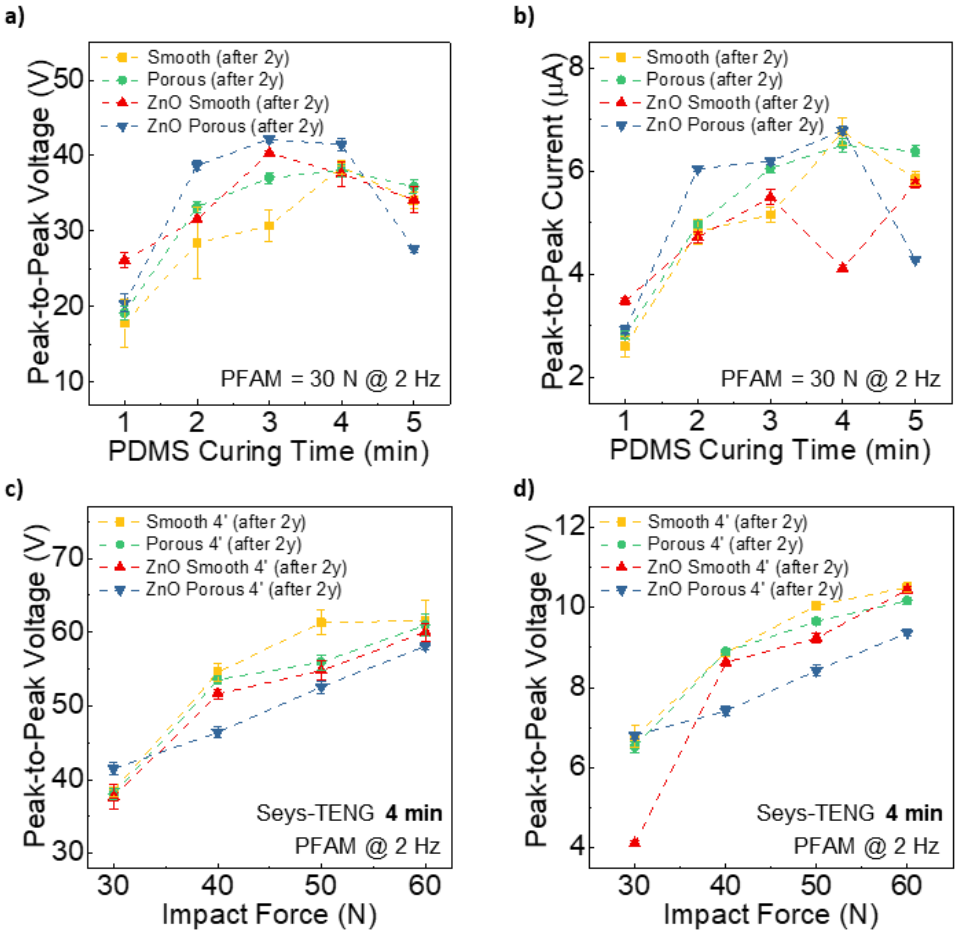

Figure 5.61 – Electrical measurements performed on ZnO functionalized Smooth and Porous Seys-TENGs after 2 years of fabrication using PFAM: a) open circuit voltage and b) short-circuit current for a force of 30 N at 2 Hz and c) open-circuit voltage and d) short-circuit current produced by the ZnO Smooth and Porous obtained after 4 min of curing time using forces from 30 to 60 N.

Since the testing methodology (type of impact delivered and force of GFAM and PFAM are different, as well as the testing material – see sub-sub section 2.2.1.3 and Figure 3.18) was changed, it is impossible to truly compare the evolution of the performance of the devices over this period. A new set of Smooth and Porous Seys-TENG samples was fabricated, employing the optimal condition of a 4-minute curing time. Their performance was compared to samples aged for two years, as illustrated in Figure 5.62. V_{OC} (Figure 5.62 a)) and I_{SC} measurements (Figure 5.62 b)) were conducted, varying the impact force within the range of 30 to 60 N while maintaining a constant frequency of 2 Hz using the PFAM.

The new samples clearly distinguish between Smooth and Porous sets output values, with Porous sets consistently outperforming the Smooth ones for the several forces employed

in the study corroborating the findings initially observed in older samples. Oppositely, it is an interesting fact that the older samples present remarkably similar output values for both the Smooth and Porous sets, and Smooth sets even outperform the Porous ones by forces higher than 30 N. This inversion in behavior suggests a potential faster degradation of deterioration to a higher extent taking place on the ZnO functionalized Porous Seys-TENGs. These findings are like to the previously non-functionalized sets where the same tendency for higher degradation on Porous sets was also noted.

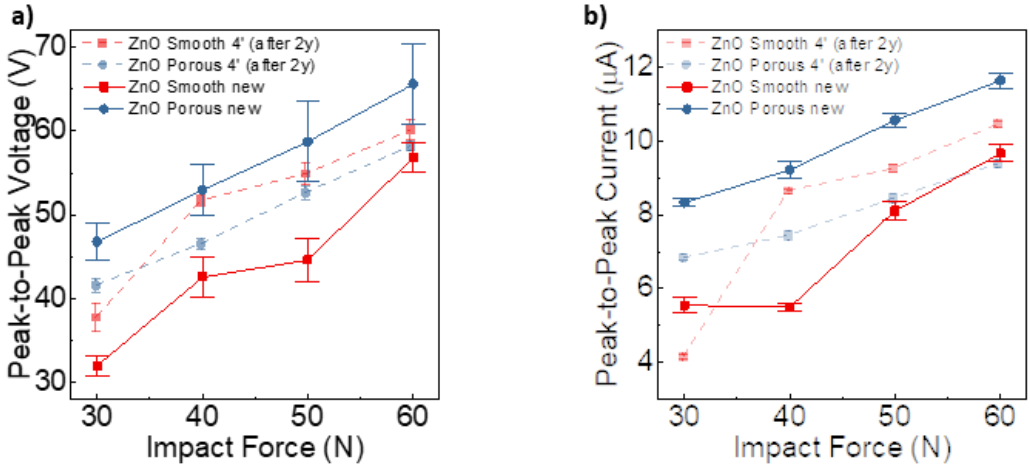

Figure 5.62 – a) V_{OC} and b) I_{SC} of new and old (2 years old) samples of 4' ZnO functionalized Smooth and Porous Seys-TENGs as a function of impact force, at 2Hz using PFAM.

Cross-sectional SEM images were taken from one ZnO Porous Seys-TENG after being subjected to 10,000 cycles of 60 N mechanical loads (at 1 Hz). The anchoring layer of rods show slight deterioration, while ZnO NRs themself appear to remain surprisingly intact (Figure 5.63).

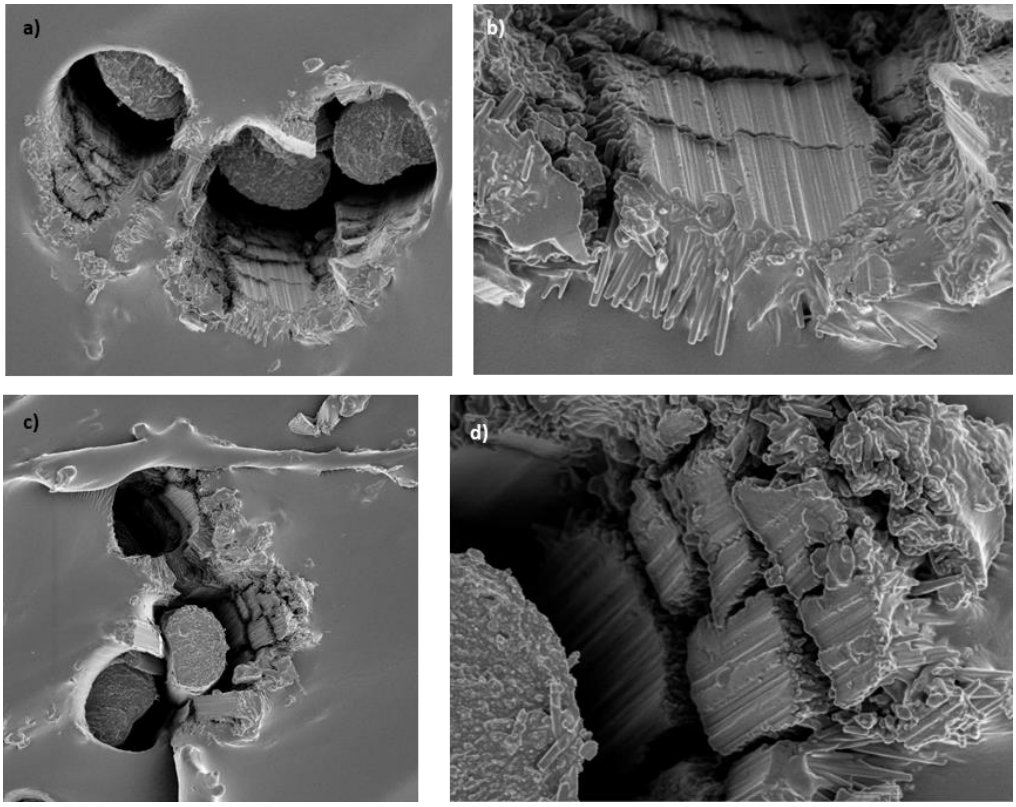

Figure 5.63 – SEM cross-sectional images of Smooth ZnO NR functionalized Seys-TENGs after 10 000 stress cycles using 60 N force.

The influence of the external material in the output voltage of Smooth and Porous Seys-TENGs was studied by testing the energy converters on PFAM using different materials such as Glass, Bamboo board (BB) and Teflon. The resulting output voltages are shown in Figure 5.64. The results obtained are like the ones in the previous section: the loading using glass slightly lowers the voltage outputs, while using Teflon inverts the signal obtained since this material in more electronegative than PDMS, promoting the accumulation of positive charges at its surface.

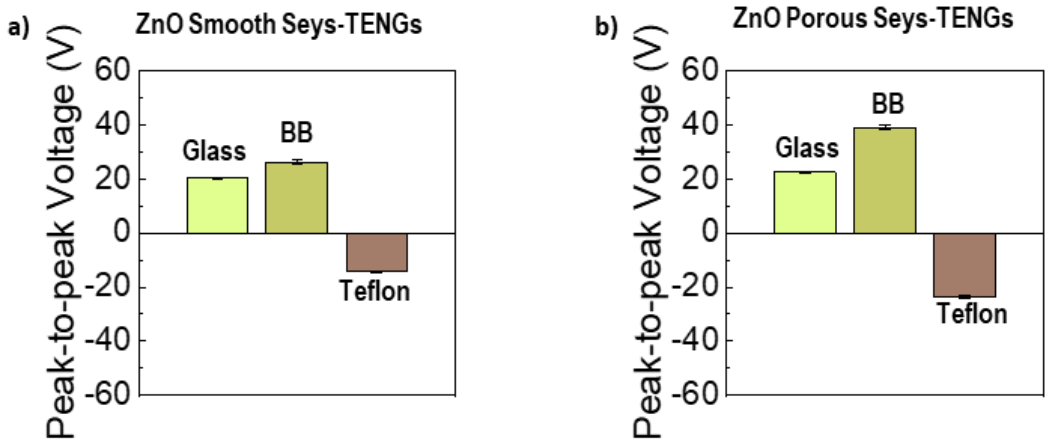

Figure 5.64 - The influence of the external material in the output voltage of a) Smooth and b) ZnO NR functionalized Porous Seys-TENGs.

For the sake of uniformization and a better comparison between the several Seys-TENGs produced in this work, the power as a function of loading was measured using the new produced samples and the using PFAM delivering a constant force of 30 N at a frequency of 2 Hz. The voltage and current of Smooth (Figure 5.65 a)) and Porous (Figure 5.65 c)) new sets were evaluated when connecting load resistors from 100 kΩ to 200 MΩ in parallel or series, respectively, to the measuring instrument. While voltage increases directly with the value of the load resistors, the current decreases and the power was calculated by the product of the two. Both sets find its maximum values for load resistors of 50 MΩ ((Figure 5.65 b) and d)). ZnO functionalized Smooth and Porous sets presents a maximum voltage value of 98.56 and 187.2 μW, respectively, which corresponds to a linear power density of 379.08 and 720.15 μW /m, equivalent to an increase of 4 % in the case of ZnO functionalized Porous Seys-TENGs. The lower value obtained for the measurement of ZnO Smooth Seys-TENG seems to contradict the initial results which foresaw a higher potential power generation. One highly likely explanation for this is the possible contamination of the BB with glue, used to fix the Teflon and glass that were used in the characterization before these measurements.

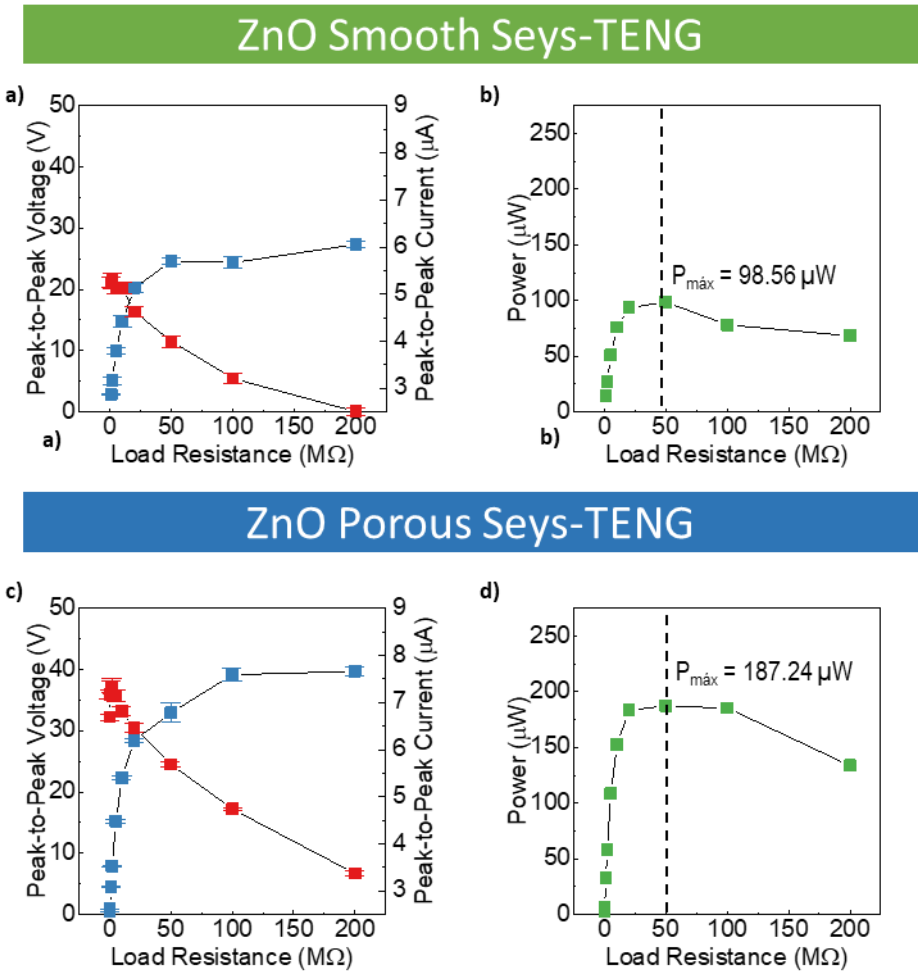

Figure 5.65 – Voltage and current of ZnO functionalized a) Smooth and c) Porous Seys-TENGs measured as a function of load resistance and b) and c) are the calculated power, respectively.

A summary of the electrical output results obtained for Smooth and Porous Seys-TENGs is shown on Table 5.11

Table 5.11 - Summary of the electrical output results obtained for ZnO functionalized Smooth and Porous Seys-TENGs sets using PFAM with an impact force of 30 N at 2 Hz.

	V_{OC} [V]	I_{SC} [μA]	R_{LOAD} [MΩ]	V_{RLOAD} [V]	I_{RLOAD} [μA]	D (mm)	P_{max} [μW]	P_{max}/l [μW/m]	P_{max}/A [μW/m²]	P_{max}/V [μW/m³]
ZnO Smooth	32.00	5.55	50	24.64	4.00	2.55	98.56	379.08	14.87	74.23
ZnO Porous	46.80	8.34	50	32.92	5.69	2.54	187.24	720.00	28.35	142.12

The results regarding the Seys-TENG prepared using Shieldex as electrode are shown in Figure 5.66. It was found that when ZnO NRs are grown at the surface of the Shieldex yarn using hydrothermal growth, the silver conductive films become very damaged which may explain its low performance compared to the Seys-TENGs using the raw Shieldex yarn.

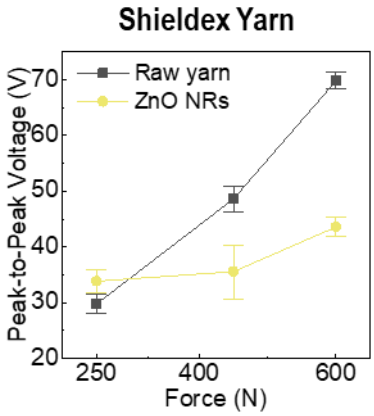

Figure 5.66 - Voltage output of raw and ZnO NR functionalized Seys-TENGs using Shieldex as electrode. The samples were tested using GFAM.

5.1.4 Proof of concept and prototype

The best set of Seys-TENG was further tested in the context of a practical application. In the first moment, the output of the set of ZnO NR functionalized Porous Seys-TENG was connected to a simple electrical circuit (Figure 3.19) with a diode bridge rectifier and a 10 μF capacitor. The set was subjected to mechanical loadings of 600 N (1 Hz) for about 15 minutes using GFAM, and the energy converted was used to charge the capacitor in the circuit. After that period, the capacitor was directly connected to the terminals of a hygrometer, and it was possible to briefly switching ON of the device by the LCD lighting (Figure 5.67 b)). The same procedure was repeated, this time in power a thermometer, and a similar result was obtained: the device was able to briefly switch ON given the lighting of the LCD (Figure 5.67 b)). Another similar experiment was made, using the capacitor previously charged by the set of Seys-TENGs to light a single LED. The LED could stay switched ON for more than 100 sec after connecting the capacitor (Figure 5.67 c)).

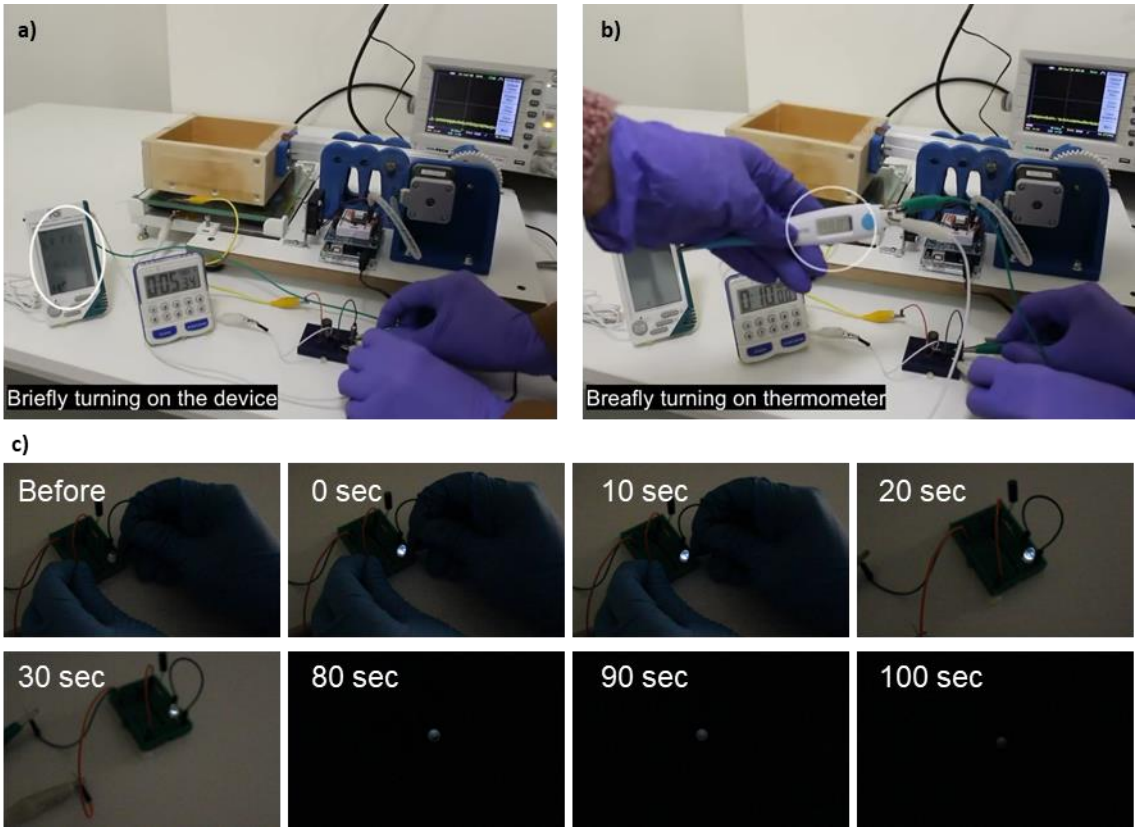

Figure 5.67 – Demonstration of using a) turning ON a hygrometer, b) turning ON a thermometer and c) lightening one LED for more than 100 sec, by using a capacitor charged by the set of ZnO NR functionalized Porous sets 3 min using the force of GFAM for some minutes.

In another experiment, the set of Seys-TENGs was used directly to power LED devices by converting the mechanical loading of a human hand to electrical energy (Figure 5.68 a)). The set could light at least 28 LEDs connected in series with the direct conversion of mechanical energy from the tapping of a hand (Figure 5.68 b)). The LEDs would switch ON each time the Seys-TENGs were pushed.

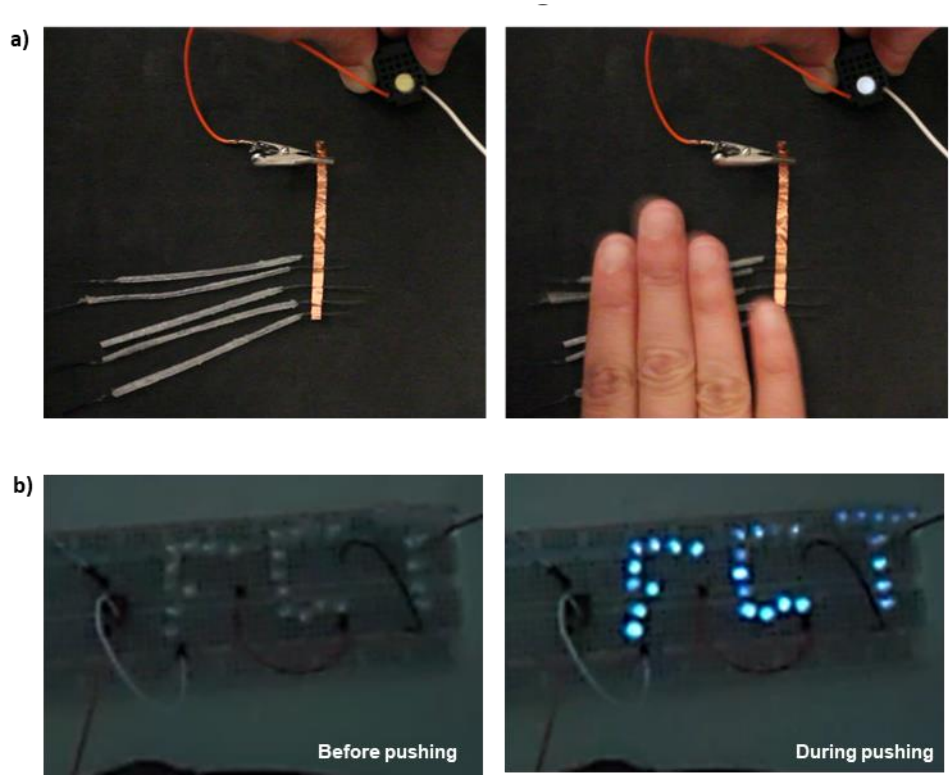

Figure 5.68 – Demonstrating the switching of a) a single LED and b) 28 LEDs connected in series by directly converting the mechanical energy delivered to the set of ZnO NR functionalized Porous - 3 min using the force of a hand.

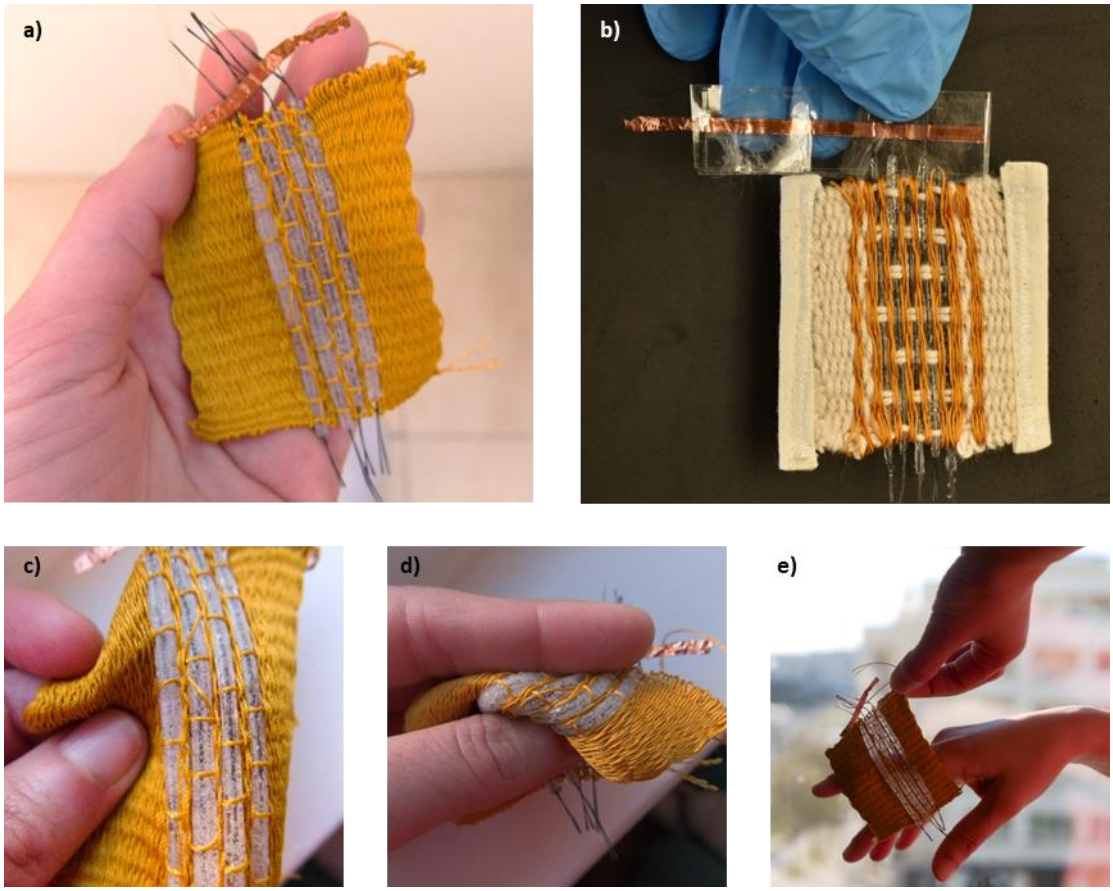

Figure 5.69 -a) A prototype consisting of incorporating a set of Seys-TENGs into the structure of a textile piece. b) Another similar prototype with a different design. c) demonstration of the flexibility of the textile part of the prototype and b) the flexibility of the Seys-TENGs while incorporated in the textile structure. e) A demonstration of the translucent nature of the Seys-TENGs while incorporated in the textile prototype.

5.2 Seys-TENGs loaded with chopped CFs

The presence of conductive particles in the polymer matrix increases the interfacial polarization and enhances the overall capacity of the system. For this reason, conductive particles have been employed in the triboelectric matrix of TENGs for enhancing its surface charge density. Conductive carbon-based particles, such as graphene, graphene oxide, CNTs, and MWCNTs, have been explored as alternatives to metal nanoparticles. [229] Alternatively, cCFs are micro-sized conductive particles with diverse industrial applications. One common use is blending them with polymer resin, which allows for greater design flexibility compared to large tows of fibers. The random orientation of these particles imparts isotropic mechanical reinforcement to composites, enhancing their overall mechanical properties. However, to the best of the author's knowledge, cCFs have never been utilized in this context. Herein, this subchapter describes the development of cCFs loaded Seys-TENGs.

5.2.1 Preparation of chopped CF loaded PDMS mixture

cCFs were obtained from SGL Carbon (former Fisipe) and are manufactured using the same process employed for CF yarns, resulting in a significant structural resemblance between the two. After the sizing with SBR, the fibers are chopped to the desired length instead or being winded in a bobbin, resulting in a powder like material like shown in Figure 5.70 a). The structural analysis of cCFs was performed by PANalytical's X' Pert PRO M RD X-ray diffractometer using a monochromatic Cu Kα radiation source (wavelength 1.540598 Å) from 20° to 60° (2θ) with a scanning step size of 0.016°. Similar to its yarn form, its crystallographic structure presents a broad peak for 2θ around 25.0 ° signifying the existence of a hexagonal carbon graphitic plane oriented along the (002) plane[182][183][184] and a broader peak near 44 ° associated to the (100) plane of graphitic layers.[181][177] (Figure 5.70 b)).

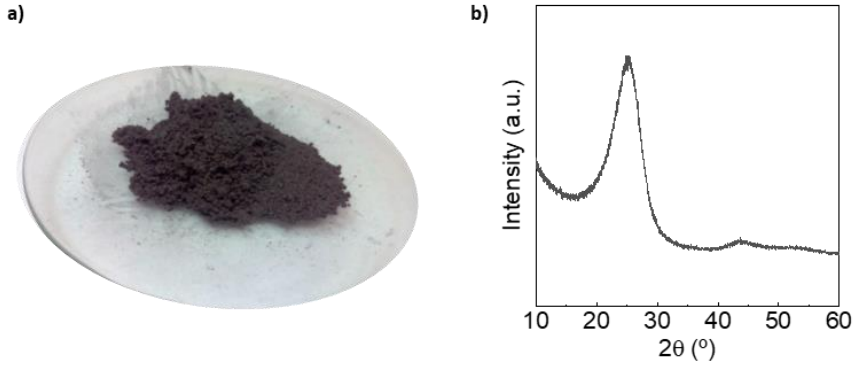

Figure 5.70 – a) The cCF powder and b) its characteristic XRD pattern.

SEM images of the cCFs revealed fiber particles of various dimensions, with diameters ranging from 1 to 8 μm and a broad length distribution (Figure 5.71 a)). By performing length measurements on 132 fibers, a range of values between 10.16 and 179.43 μm was encountered. The size distribution of the counting was plotted on a histogram (Figure 5.71 b)) and the Gaussian fitting revealed a mean length value of 40.58 μm.

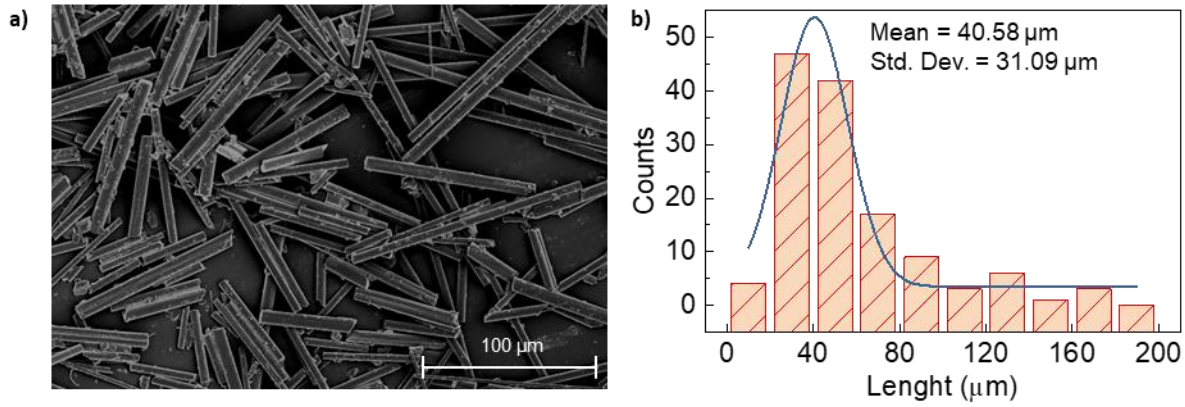

Figure 5.71 – a) SEM image from cCFs. B) Non-linear gaussian fit on the cCFs length distribution-

The cCF loaded Seys-TENGs were obtained by combining PDMS with different proportions of cCFs. Before combination with the curing agent, the PDMS elastomer was thoroughly mixed with cCFs using proportions from 0.1 to 30 % wt. The mixture was thoroughly blended by hand for at least 5 minutes until a uniform dispersion of cCFs was obtained. At this point, the curing agent was added in the standard proportions of 1:10 to the mixture, thoroughly blended, and then degassed for 30 minutes in a vacuum chamber and used immediately.

5.2.2 In-situ curing of cCF loaded PDMS around CF yarns

About 2 mL of the mixture preparation described above was poured inside one of the wells of a specially designed 3D container detailed in sub-section 3.1.1. Then, sections of CF yarn with about 12 cm were cut and placed directly inside the PDMS mixture filed container. A current of around 0.2 A was injected in the CF yarn through a power supply (Zhaoxin, PS-303D-II) during 4 min, which promoted the curing of loaded PDMS from inside out around the CF yarn. After this period, the fiber and PDMS coating were removed from the container, the excess uncured PDMS removed using a soft sponge, hung vertically and placed inside the oven for 15 minutes until residual uncured PDMS is fully cured.

5.2.3 Morphological and electrical characterization of cCFs loaded Seys-TENGs

Optical images of the cCF-Seys-TENGs were taken using an optical stereo microscope Leica M80 (Figure 5.72). Whilst rising the loading content, Seys-TENGs quickly lost its transparency while gaining an increasingly black shade.

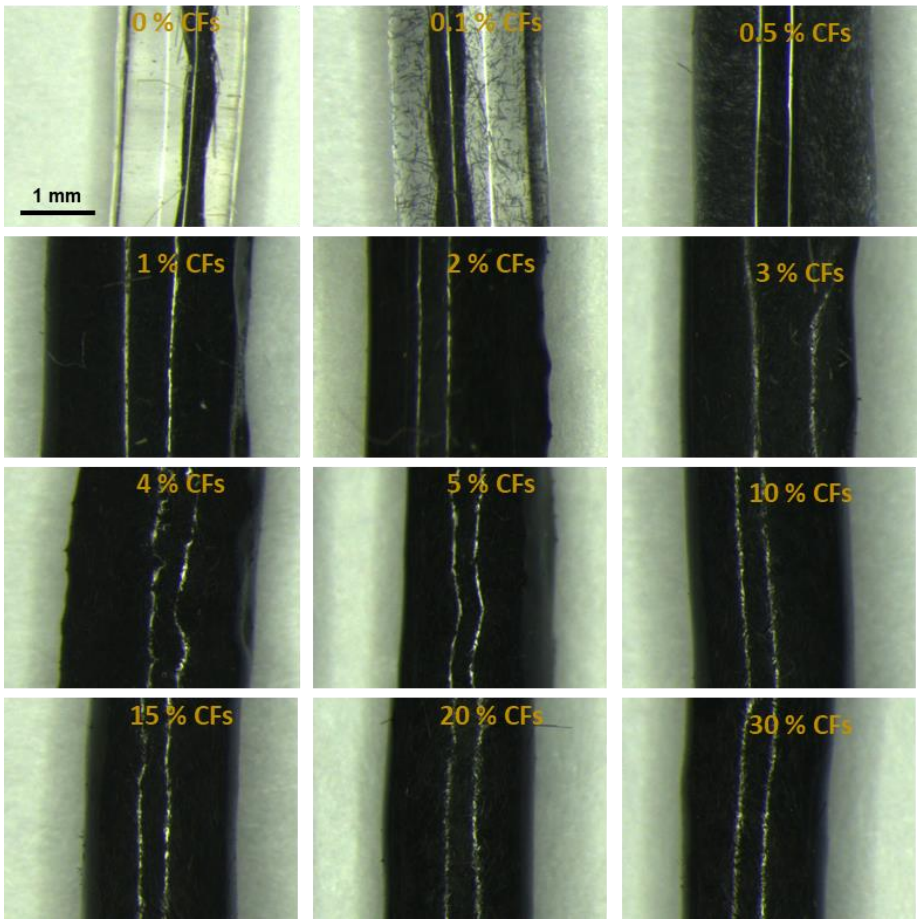

Figure 5.72 – Set of optical microscopic images of the cCFs Seys-TENG with different loading ratios specified in every image.

While increasing the loading ratio of cCFs within the PDMS, the thermal properties of this composite are being altered. While PDMS is a good thermal insulator, CFs are known for their good thermal conductivity, contributing to an increase of the overall thermal conductivity of the composite. This was evident while performing the in-situ curing of PDMS slurry, when the same curing time resulted in lower diameters, and the current was adjusted accordingly to maintain consistent dimensions through the study. However, other parameters affect the progress of the curing process, for instance and most importantly, the initial temperature of the PDMS slurry, which can be difficult to control depending on the external temperature. Hence some dispersion on the resulting diameters was obtained. The diameters of cCFs loaded Seys-TENGs were measured directly from the optical images. The average of five measures at three separate locations were taken and a summary of this values are presented in Figure 5.73.

Higher discrepancies registered for lower loading ratios were related to a lower ambient temperature.

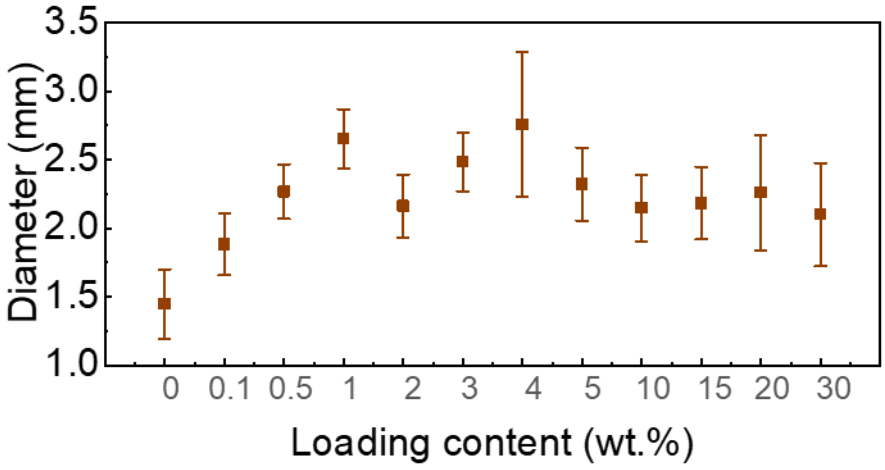

Figure 5.73 – Diameter of cCFs loaded Seys-TENGs using different loadings of cCFs, for a 4 min in-situ curing.

The mechanical to electrical energy conversion characteristics of the cCFs loaded Seys-TENGs was assessed by connecting four devices in parallel using conductive and flexible cupper tape. The set was then positioned on a piece of paper foil to facilitate the positioning, fixed using scotch-tape to keep them from moving during the measurements (Figure 5.74).

Figure 5.74 - Four cCF-Seys-TENGs connected in parallel.

Open-circuit voltage and short-circuit current generated by the sets were evaluated while delivering a controlled vertical mechanical stimulus using the Pneumatic Fore Actuator Machine (PFAM) described previously in sub-subsection 3.2.1.2. In the case of open-circuit voltage measurements, a 100 MHz bandwidth Tektronix oscilloscope (TBS 1102C) at a horizontal scale of 40 ms was combined with a 10 MΩ of impedance probe connected to the sets. The short-circuit current measurements were measured using a Keithley 485 autoranging picoammeter in combination with the oscilloscope. The sets were subjected to 5 minutes of

loading to obtain a stabilized output value. The data was acquired by manually saving the voltage peaks displayed in the oscilloscope to an external recording unit (USB pen) and later analyzed by running a script in MATLAB. The resulting voltage is a characteristic positive followed by a negative peak, resultant from the excess electrons in the PDMS surface after contact with the BB (Figure 5.75). Apart from a difference in the voltage peak amplitude, the presence of cCFs embedded within the PDMS matrix does not change its characteristic voltage pattern, as shown in the graph of Figure 5.75 where the voltage peaks generated by cCF-Seys-TENGs of different loading ratios are shown.

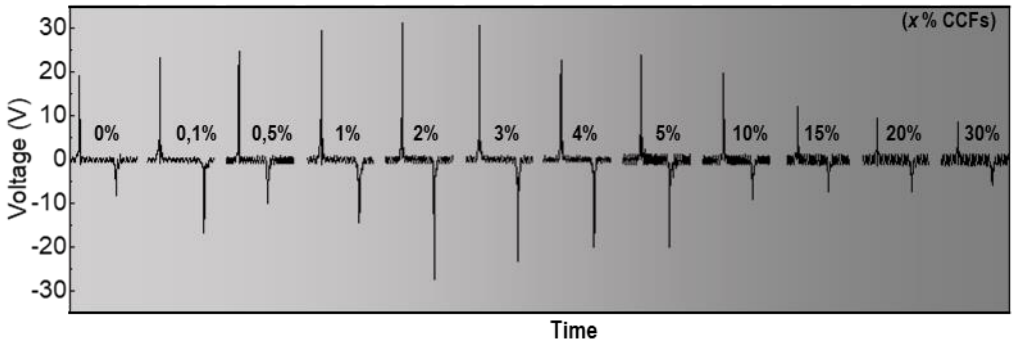

Figure 5.75 – Voltage peaks generated by cCF-Seys-TENGs of different cCF loading ratios.

The average value of five different peak-to-peak voltage and current peak values (Vpp and Ipp) generated by cCF-Seys-TENGs of different loading ratios were taken. Resulting values are shown in Figure 5.76 a) and b), respectively. It is possible to observe that with the increase of the cCFs loading ratio, both voltage and current exhibit a noticeable rise, reaching its maximum value at the 2% loading mark, where a V_{OC} and I_{SC} output of 58.16 V and 9.46 μA is achieved, respectively. Further escalation in loading ratios appears to compromise the power generation capability of the generators, since the voltage and current starts to decline, until reaching its lowest value at the 30 % wt. mark.

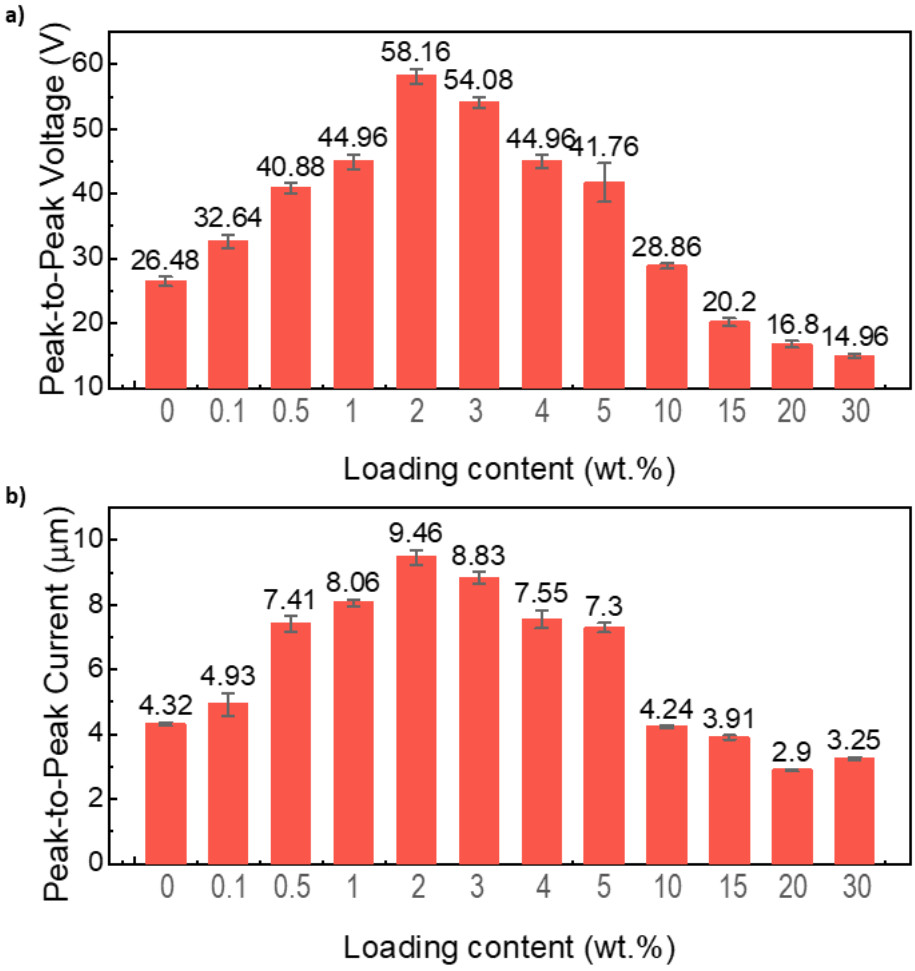

Figure 5.76 – a) Peak-to-peak open-circuit voltage and b) short-circuit current for cCFs loaded Seys-TENGs with a different cCFs loading content, obtained using PFAM and a mechanical loading force of 30 N and 2 Hz.

The proposed energy conversion mechanism is like the one used previously for Seys-TENGs. Upon impact, the surface of PDMS gains electrons and becomes negatively charged, while the surface of the external material (BB) loses electrons and becomes positively charged. The formation of charges induces a current in the external electric circuit. The cycle repeats with an accumulation of charges at both surfaces until reaching the maximum charge density at both surfaces.

The power generation capacity of a TENG is intricately tied to the electrical characteristics of the dielectric material, which undergo modifications as the loading of cCFs is increased. The presence of conductive particles randomly dispersed in the PDMS matrix promotes electron charging at interfaces between the insulating PDMS matrix and conductive filler (Figure 5.77). This method has been used as an effective method of improving the permittivity on microelectronic devices and capacitors. [230][229] Specifically, using conductive fillers rather than high-k dielectric particles results in an abrupt rise of permittivity near the percolation threshold.[229] The presence of conductive particles embedded in the polymer matrix act as micro-capacitor structures[16][231][232] that undergoes electronic polarization in the presence of an electric field.

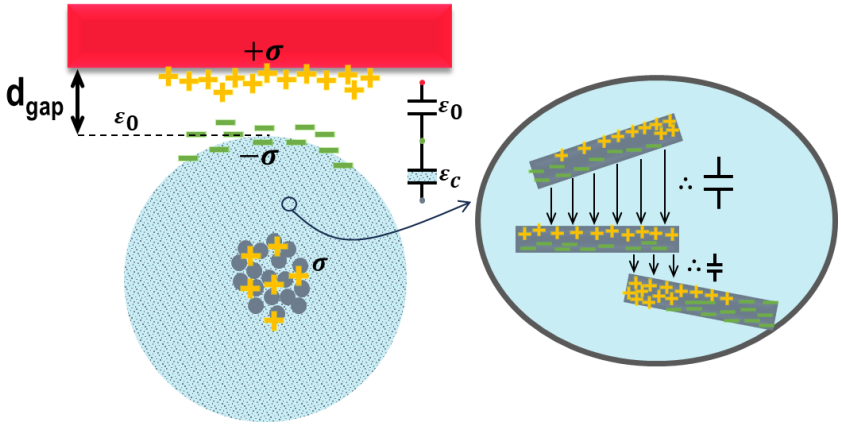

Figure 5.77 - Schematic representation of the charging mechanism on the cCFs dispersed in the PDMS matrix.

Equation 2.6 describes how the V_{OC} of a generator is directly dependent on the surface charge density. In its turn, the surface charge density (σ) dependence on the dielectric properties of the triboelectric material is described in Equation 5.20, where ε_0, d_{gap} and $\varepsilon_{composite}$ are the permittivity of free space, the gap dimensions and the relative permittivity of the composite, and σ_0 and $d_{composite}$ are the initial surface charge density and the thickness of the PDMS composite, respectively. [222]

$$\sigma = \frac{\sigma_0 d_{gap}}{d_{gap} + \frac{d_{composite}}{\varepsilon_{composite}}} \qquad \text{Equation 5.20}$$

To gain deeper insights into the dielectric attributes that drive the mechanic to electrical conversion behavior observed, impedance spectroscopy was conducted on PDMS films possessing the same loading content proportion as their Seys-TENG counterparts.

Films with 0.1 to 30 % cCFs were prepared by running a blade over a small amount of the uncured slurry on top of a glass substrate, using spacers of 450 μm. Films were placed horizontally in the oven and cured at 70 °C for 30 minutes. The cured films were peeled off the glass substrate and placed between two stainless steel discs on a parallel plate capacitor configuration. Impedance spectroscopy measurements were performed using an Agilent 4294A Precision Impedance analyzer connected to an Agilent 42941A Impedance Probe. Capacitance was measured by applying 500 mV in a frequency range of 40 Hz to 100 GHz.

While it has been taken into account the notion that cCFs possess an essentially random orientation during deposition around CF yarns through in-situ curing, it's conceivable that the fluid dynamics present during casting from a syringe into a tube-like shape – where minimal lateral spreading of the fluid occurs – could potentially lead to some form of preferential orientation in the overall arrangement of cCFs. Such orientation might diverge from that achieved when films are produced via blade casting. This aspect could introduce a certain degree of limitation to the analogy, the extent of which remains uncertain. While analyzing the results, it's prudent to consider this potential limitation. For the time being, we commence with the assumption that the films bear adequate semblance to simulate the electric and dielectric properties of cCF-based Seys-TENGs.

The mechanical stimulation of the Seys-TENGs was executed at frequencies of 2 Hz, generating peaks widths of approximately 3.7×10^{-4} seconds, spaced at a distance of roughly 4.9×10^{-3} seconds (from positive to negative peaks), as illustrated in Figure 5.78. Given that this voltage represents an oscillating signal, one can consider these time intervals as part of its characteristic wavelength, allowing for conversion into equivalent frequencies, yielding values of 252 Hz and 1.3 kHz.

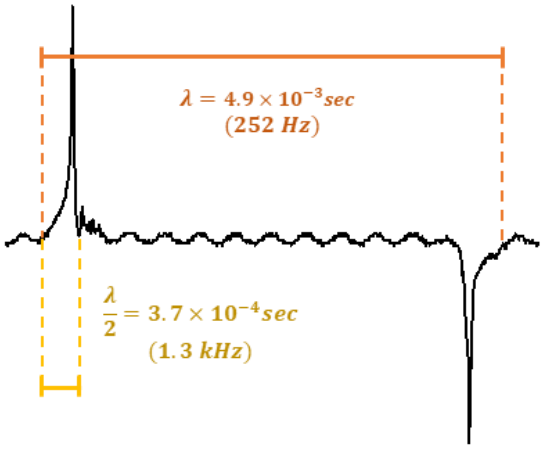

Figure 5.78 – Voltage peak generated by the 2 % wt. cCF Seys-TENG.

Dielectric properties are dependent upon the frequency of electrical stimulation. EIS sweeps the samples in a broad frequency range, starting at 40 Hz. A pertinent question arises concerning the appropriate frequency to consider for simulating the operational conditions of the generators. From the previous peak analysis, it seems that 100 and 1000 Hz are two good options to represent the progression of electric parameters as the loading content is incrementally increased to be analyzed in more detail. In all scenarios, it's important to note that this method does not constitute an ideal simulation of the actual polarization processes occurring during the nanogenerator operation, primarily because the signal applied during the EIS measurement consists of a perfectly sinusoidal wave. Nonetheless, even under these conditions, it can yield valuable insights into the underlying mechanisms that undergo transformation when the PDMS matrix is loaded with more conductive particles.

Figure 5.79 resume how the loading of cCFs within the PDMS matrix influence the dielectric characteristics of the composites. Initially, at low cCF concentrations the films present a -90° phase evidencing the presence of a capacitive domain. The films lack conductivity due to an insufficient presence of conductive particles, electrical properties of PDMS are dominant and result in notably high impedance.

When the cCFs reach a certain critical loading concentration – the percolation threshold, some continuous paths begin to form and allow the electrical conduction through the films, hence the composite properties change drastically. This pivotal point can be identified as a loading ratio of 10% wt. As the loading exceeds this critical point, an abrupt phase shift from

-90° to 0° occurs. This shift is a clear indicator of the transition from a purely capacitive state to an electrically conductive regime (resistive state). The presence of a mixed domain is narrow and exists anywhere between the 10 % and 15 % loading ratio.

The percolation threshold depends on several parameters of the filling particles as the quality of the dispersion, shape, dimensions, aspect ratio and density of the filler particles.[233] Typical composites that incorporate metal nanoparticles as fillers often exhibit higher percolation threshold.[230] [234] This is partly attributed to the greater density of metallic nanoparticles, and it's also influenced by their predominantly spherical shapes [234]. CFs have a density of 1.80 g/cm^3, which is lower than that of metallic nanoparticles[230]. Other carbon-based nanoparticles composites present density values close to that of CFs (1.7-2.26 g/cm^3 for particles including carbon nanotubes (CNTs) and multiwalled carbon nanotubes (MWCNTs), graphene, graphene oxide (GO) and reduced graphene oxide (rGO), graphite and carbon black). [235] [236] [237] Given the dimensions of the cCFs aforementioned in sub-section 5.2.1, the aspect ratio of the cCFs is approximately 1:5. Similarly, cCFs, CNTs and MWCNTs possess high aspect ratios. Its dimensions are, however, typically much lower, in the nanometer range. Composites using CNTs or MWCNTs often presents reduced percolation thresholds, typically between 0.1-1% wt.[238], lower than the value observed int this work. This is due to a certain weight of nanoparticle sized material corresponding to a higher number of particles than the same weight of micro/macro-sized material, in principle with a much more uniform distribution. Additionally, in this case the low homogeneity of particle distribution was attributed to the obtainment of higher percolation threshold. [238] Considering the deposition of the PDMS mixture via blade casting, the dispersion of the cCFs can exhibit a preferential orientation in one direction, aligning with the movement of the blade, and this factor can also contribute to the attainment of such value.

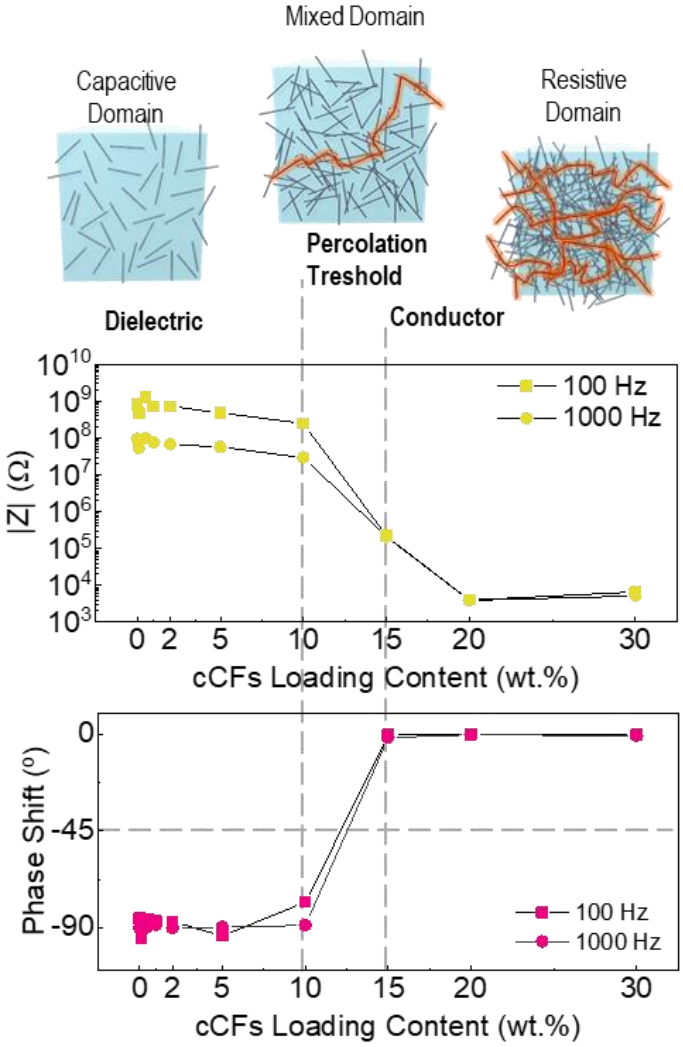

Figure 5.79 - Impedance and phase shift as a function of the cCFs loading content (measured at a frequency of 100 Hz). Schematic of the formation of percolation paths by increasing the cCFs load content.

As previously mentioned, the loading with cCFs enhances the power conversion capacity of Seys-TENGs by improving the charge storage capacity. However, the critical concentration upon which the polymer becomes electrically conductive restricts the maximum loading to 10% wt. When the polymer becomes electrically conductive, the charges formed at the PDMS surface are easily dissipated from the bulk composite into the electrodes and thus the power conversion is diminished. The observation that the maximum power conversion is achieved with a 2 %wt. of cCFs can be attributed to the fact that this critical concentration decreases when the composite undergoes compression. Under a compression force of 30 N, the probability of percolation increases because conductive particles can more easily form

conductive paths. The higher the loading content, the stiffer the composite will become, offering increased resistance to compression and diminishing the contact area between PDMS surface and the BB, meaning that triboelectrification phenomenon can be reduced.

The capacitance measured from films with loading proportions of 0.1 to 30 % is shown in Figure 5.80 a). However, from the point of view of the resistive regime that is dominant from loading ratios of 10 %wt., the capacitance values for 10 % and above makes little sense from a physical perspective. The permittivity k can be obtained using the following equation:

$$C = \frac{k\ \varepsilon_0 A}{d} \qquad \text{Equation 5.21}$$

Where C is the Capacitance, ε_0 is the permittivity of free space, d is the film thickness and A is the area of the electrode. The values from 0 to 30 %wt. of cCFs loading ratios were calculated using the previous equation and the resulting values are shown in Figure 5.80 b) as a function of loading ratio.

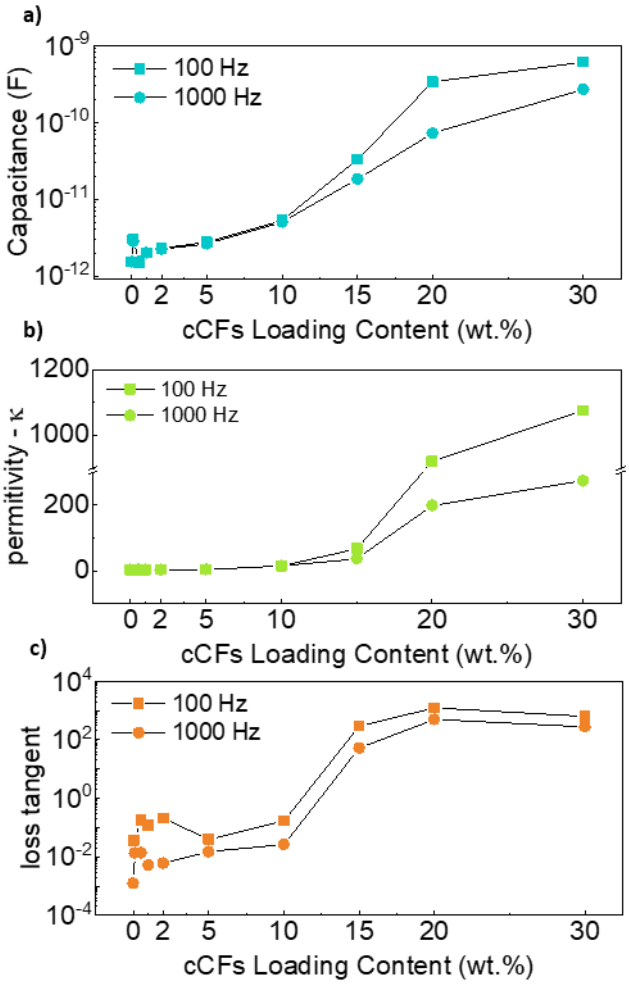

Figure 5.80 - a) Capacitance as a function of loading ratio and b) the corresponding permittivity and c) dielectric loss tangent.

The best set with 2 % wt. loading was chosen to perform extended electrical characterization. The influence of force applied on the resulting electrical output and its frequency dependency on peak-to-peak open-circuit voltage and short-circuit current are shown in Figure 5.81 a) and b). In general, higher forces and frequencies result in higher voltage and current values. The higher V_{OC} and I_{SC} values were obtained while applying 60 N of vertical mechanical loading at a frequency of 2 Hz and was 84.96 V and 12.94 μA, respectively. More gradually, the voltage (Figure 5.81 c)) and current (Figure 5.81 d)) output also increases as a function of frequency applied, with the higher results attained for a frequency of 3 Hz.

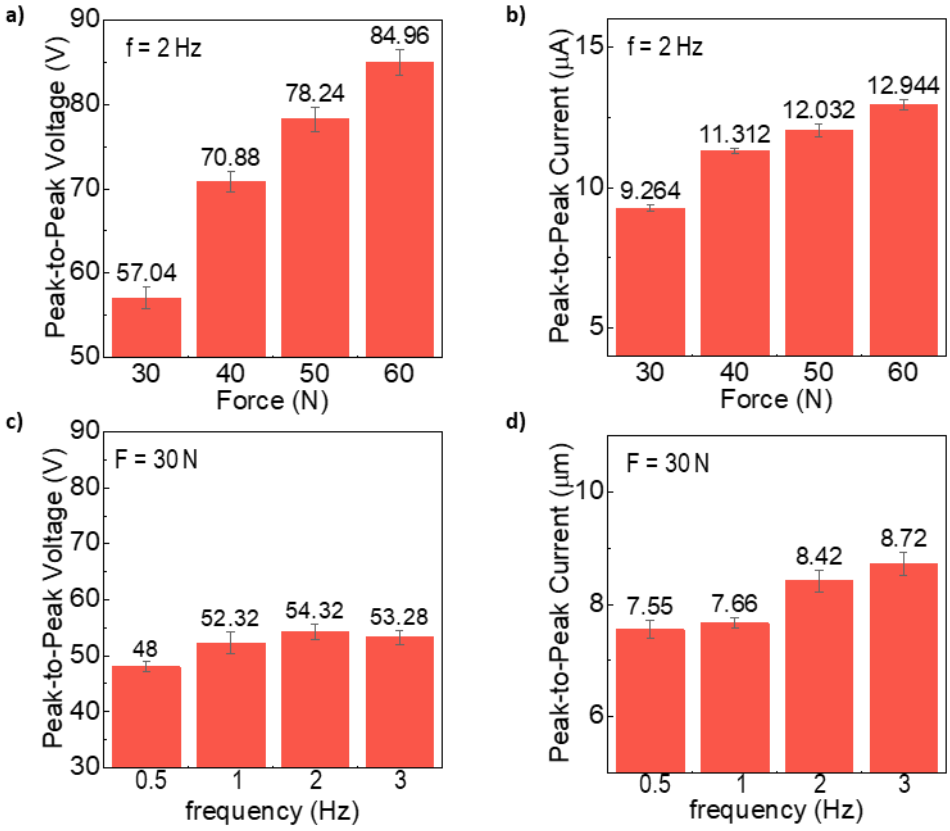

Figure 5.81 – a) Peak-to-peak open circuit voltage and b) short circuit current for 2 %wt. cCF Seys-TENGs using a fixed frequency of 2 Hz and variating the force from 30 to 60 N. c) Peak-to-peak open circuit voltage and d) short circuit current for 2 %wt. cCFs Seys-TENG using a fixed force of 30 N and variating the frequency from 0.5 to 3 Hz.

The maximum power of 2%wt. cCFs Seys-TENG was calculated after measuring the voltage and current when connecting load resistors from 100 kΩ to 200 MΩ in parallel or series, respectively, to the measuring instrument. While voltage increases directly with the value of the load resistors, the current decreases and the power was calculated by the product of the two. The maximum value was found when using a 20 MΩ load resistor. Interestingly, this load resistor value is inferior to that obtained for Smooth, Porous or ZnO functionalized Seys-TENGs. The reduction of 50 to 20 MΩ is related to the increased conductivity of the PDMS loaded composite. The maximum power value obtained, 276.44 μW corresponds to a linear power density of 1063.23 μW/m, equivalent to an increase of 53 % compared with the Smooth Seys-TENG.

The set stability was tested by measuring V_{OC} while applying repeated impacts using PFAM at 30 N and 2 Hz during slightly more than 90 minutes. The voltage increased rapidly

during the initial minutes as the charges accumulated at the PDMS surface, stabilized around 40 V and the output was still stable after being subjected to a total of 10 000 impact cycles.

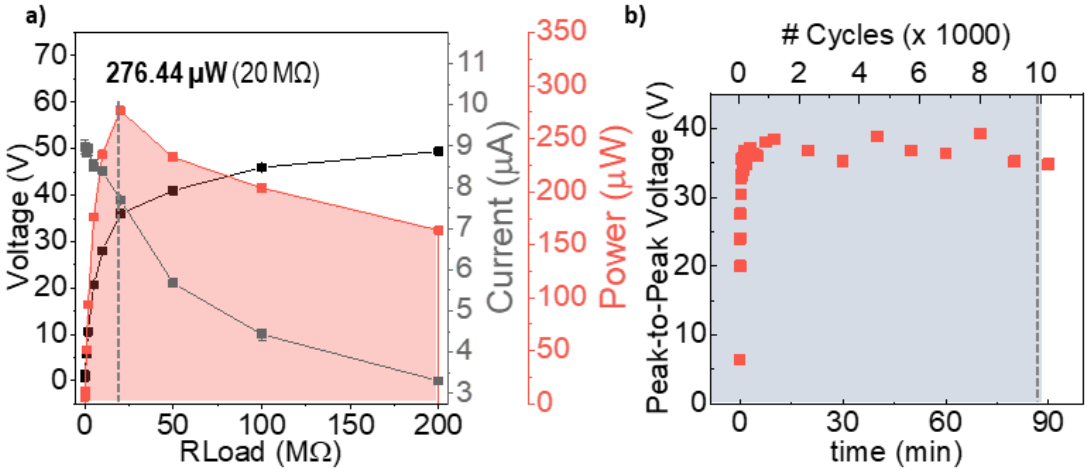

Figure 5.82 – a) Voltage, current and power generation as a function of the load resistor and b) voltage output as a function of the number of cycles. All measurements were performed using PFAM using 30 N of force at 2 Hz.

The influence of the external material in the output voltage of the 2 % wt. cCF Seys-TENGs was studied by testing the energy converters on PFAM using different materials such as Glass, Bamboo board (BB) and Teflon. The resulting output voltages are shown in Figure 5.83. Results are similar to those obtained for Seys-TENGs tested in the previous chapters and sections. The use of glass, a slightly less positive material[204][207][208] [209] diminishes the output voltage, while when using Teflon, an even more electronegative material than PDMS[204], the voltage peak is inverted.

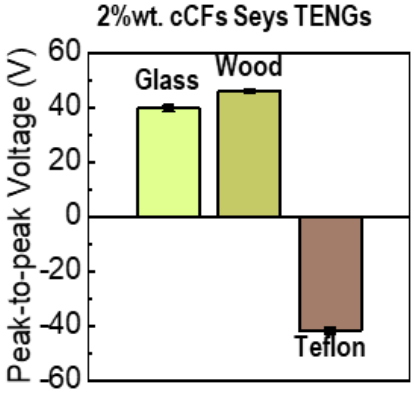

Figure 5.83 - The influence of the external material in the output voltage on the set of 2 % cCFs Seys TENGs.

A summary of the electrical output results obtained for the 2 %wt. cCFs Seys-TENGs is shown on Table 5.12.

Table 5.12 - Summary of the electrical output results obtained for the 2 %wt. cCFs Seys-TENGs sets using PFAM with an impact force of 30 N at 2 Hz.

	V_{OC} [V]	I_{SC} [μA]	R_{LOAD} [MΩ]	V_{RLOAD} [V]	I_{RLOAD} [μA]	D (mm)	P_{max} [μW]	P_{max}/l [μW/m]	P_{max}/A [μW/m²]	P_{max}/V [μW/m³]
2 % wt. cCF	58.16	9.46	20	35.92	7.70	2.16	276.44	1063.23	49.22	290.16

A simple prototype was prepared by incorporating a set of 2 % wt. cCFs Seys-TENGs within a weaved structure composed of polyester yarns as warp and polyester ribbon as weft (Figure 5.84 a)). The textile sample was produced using a custom-made loom, and the 2 % wt. cCFs Seys-TENGs were incorporated in the warp while weaving.

To assess the influence of the textile structure surrounding the energy converters, the set was characterized using PFAM at 30 N and 2 Hz, both before ((Figure 5.84 b)) and after (Figure 5.84 c)) weaving. It was observed that when the set was tested within the woven structure (Figure 5.84 d)), there was a reduction of 38% in output voltage and 28% in output current. This decrease can be attributed partially to a reduced contact area between the sets and the base material, as well as the presence of additional material that may dampen the impact force.

In this context, it's important to consider the diameter of the yarns used when implementing the sets in textile structures. Thin and lightweight yarns should be preferred to minimize the adverse impact on the power conversion efficiency of the converters.

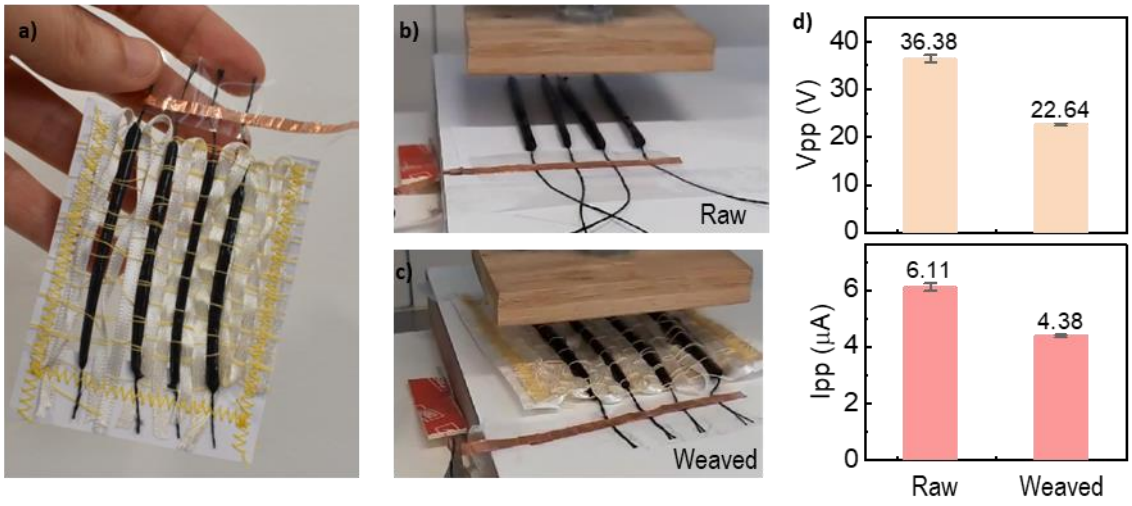

Figure 5.84 -a) A set of 2 % wt. cCFs Seys-TENGs weaved into a textile structure. The set in a b) raw state and c) after weaved while being tested on PFAM. d) Vpp and Ipp of the set before and after weaved.

A prototype of a plantar foot sensor was prepared by sewing four individual strands of 2 % wt. cCFs Seys-TENGs on strategic locations of a sock – the heel, forefoot and arch of the foot, as shown in Figure 5.85 a). The prototype was used to monitor the gait pattern of a volunteer while walking. The gait pattern was registered by measuring the individual signals from each Seys-TENG using two oscilloscopes and the results are shown in Figure 5.85 b). The positive peak indicates a touch on the ground and the signal generated is intended to be qualitative. A impact phase of normal gait when walking begins with the heel landing on the ground, followed by the forefoot. [239] When measuring the signal generated by the volunteer on the impact phase of walking, sensor A located on the heel was initially triggered, and a few microseconds after, sensors C and D located on the forefoot were triggered almost simultaneously. Sensor B would only been triggered by a fallen arch, which is not the case of a normal healthy feet.

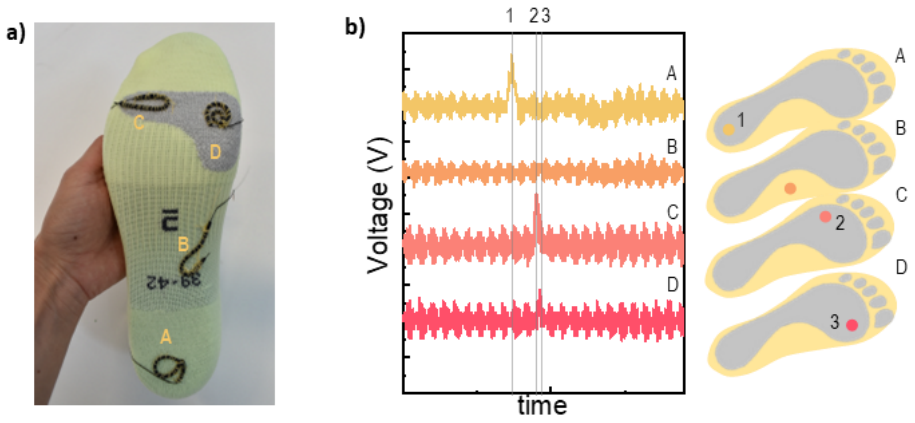

Figure 5.85 – a) Plantar foot sensing prototype produced using the 2 % wt. cCFs Seys-TENGs as sensors sewed to a sock. b) gait pattern of a volunteer when walking, registered using the plantar foot sensing sock.

5.3 Conclusions

In this chapter, two different methods were employed to enhance the power conversion capability of the Seys-TENGs. The first strategy consisted of functionalizing the CF yarn with vertically aligned ZnO NRs. The ZnO NRs were produced by hydrothermal synthesis based on Zinc Nitrate and Hexamethylenetetramine as precursors, after the density and alignment over the fibers been optimized for a 4-fold of seed layer deposited using Zinc Acetate solution. Dense forests of vertically aligned NRs with a size range between 300 to 1000 nm of length and from 50 to 100 nm in diameter were obtained. ZnO NR functionalized Seys-TENGs were obtained by in-situ curing smooth and porous PDMS using a current of 0.2 A and curing times ranging from 1 to 5 minutes. It was found that the presence of ZnO NRs, combined with the Smooth or the porous PDMS structures enhanced the power conversion ability of the generators. The power enhancement was attributed to the higher permittivity of ZnO NRs and mixed phenomenon of charge generation at the NR interfaces promoted by piezoelectric effect and triboelectrification, in combination with additional charge generation and consequent polarization at interfaces of porosities in the PDMS matrix. SEM analysis revealed that after in-situ curing PDMS, the ZnO NR would become detached from the fiber surface and impregnated into the PDMS matrix, leaving a small gap between the two. The best results were achieved for the ZnO NR functionalized Seys-TENGs with 3 minutes curing, resulting in a peak-to-peak voltage of 72.2 V and a peak-to-peak short-circuit current of 10.4 μA when testing using GFAM at 600 N and 1 Hz. A maximum power density of 74.1 μW^{-1} was achieved using a load resistance of 20 MΩ. The ZnO NR functionalized Porous Seys-TENGs were still functional after 10 000 cycles of mechanical solicitation at 600 N with no degradation of its conversion capability and ZnO NR are still found intact after the tests. The set can also function while being bent in different directions. The set was tested in a real context. It was successfully used to directly light 28 LEDs by using the mechanical energy of a tapping human hand and charge a supercapacitor and light a single LED for a period longer than 100 sec. The set was also successfully integrated into a textile weaving structure, contributing towards the development of

basic building blocks to power the future generation of wearables. After two years the sets were still functional. New sets of ZnO NR functionalized Seys-TENGs were produced to uniformize the electrical characterization procedure. It was found that new and 2-year-old sets produce comparable results when tested using PFAM, with slight degradation of the Porous sets. The best results were obtained for the new set of ZnO NR functionalized Porous Seys-TENGs after a curing of 4 minutes (corresponding to a diameter 2.26 mm), with V_{OC} and I_{SC} values of 35.56 V and 6.72 μA of respectively, and a maximum linear power output of 720.15 μW/m, an increase of 4 % over the Smooth Seys-TENGs.

The second strategy consisted of the combination of conductive cCFs onto the PDMS coating of Seys-TENGs. cCFs with dimensions ranging from 1 to 8 μm in diameter and a mean length size of 40.58 μm were introduced in the PDMS mixture before curing and then used to coat the CF yarns using the in-situ curing technique and a fixed curing time of 4 min. A study concerning optimizing the loading content of these conductive particles impregnated in the PDMS structure ranged from 0.1 to 30 %wt. The presence of cCFs in the PDMS matrix resulted in an enhancement of the mechanical to electrical energy conversion until reaching the maximum results at the 2 %wt. mark, from which the presence of higher concentrations would results in a reduced energy conversion. The presence of this particles bellow the percolation threshold (at 10 %wt.) is responsible of promoting additional polarization at the interfaces between the PDMS matrix and the conductive cCFs, enhancing the overall capacitance of the triboelectric composite and contributing towards an enhanced surficial charge density. The permittivity of the PDMS composites was increased from 4.02 to 4.19 when adding 2 %wt. of cCFs. A V_{OC} and I_{SC} of 58.16 V and 9.46 μA respectively, and a maximum linear power density of 1063.23 μW/m while using a 20 MΩ load resistor were achieved using PFAM at 30 N and 2 Hz. This corresponds to an enhancement of 53 % compared with the Smooth Seys-TENG as reference. After 10 000 impact cycles the set was still functional without visible signs of energy conversion degradation. The sets were also tested when incorporated on a weaved textile structure and a 37.77% reduction of output voltage was registered. The application of 2 %wt. cCFs Seys-TENGs as plantar foot sensors for the gait pattern analysis was successfully demonstrated.

6

CNCs AS INTERLAYER IN SEYS-TENGs

Following friction between two triboelectric layers, surface charge decay may come from recombination with opposite charges, ions or particles from air, combined with the induced positive charges on the electrode or intrinsic carriers on the material.[240] This phenomenon has a detrimental effect on the power conversion efficiency as it diminishes the density of surface charge accumulation. To address this issue, a recent exploration strategy involves introducing an additional transition layer between the triboelectric friction layer and the electrode. Charge trapping sites can be formed by amorphous regions, cross linking points, imperfections in the crystal lattice, dangling bonds defects and functional groups in the polymer chain or oxygen vacancies in metal oxides.[241][242] The nonuniform energy levels promoted by the presence of aromatic rings along the main chain of some polymers like polystyrene (PS) and polyimide (PI) also have been found to have many trapping sites. PDMS was found to have even deeper charge traps and a larger trap density than the aromatic polymers.[243] Feng et al.[146] improve the output performance of a planar CS TENG by one order of magnitude by introducing a 25 μm thick polyimide layer between the PVDF friction layer and Cu electrode (and using nylon as second friction layer). Kim et al.[145] obtained a 173-fold increase in power conversion of a high-performance stretchable single-electrode TENG by adding PDMS as an interlayer containing deep charge traps of large trap density between a charge generation layer and an electrode.

Cellulose stands as the most abundant biopolymer on Earth, found in a diverse array of sources including wood, plants, waste agricultural biomass, bacteria and algae, and even found within marine organisms like tunicates. [227][228] The quest for sustainable materials

has led to the fabrication of TENGs using cellulose as triboelectric frictional layer. Wang et al. [244] utilized sulphonated cellulose nanofibers as triboelectric frictional layer in TENGs. He claims that the presence of sulfonated groups increases the hole deep trap density and is responsible for the ultrahigh electrical output performance. Peng et al.[245] obtained a 10-times-enhanced triboelectric performance by combining CNC flakes and PDMS. Compared with its pure PDMS counterpart, CNC-PDMS composite presented higher permittivity.

CNC possesses interesting self-assembly characteristics into chiral nematic structures which find application on optics filters or lenses. Chiral nematic CNC films can be obtained through slow evaporation from cast suspensions of CNC or by electrophoretic deposition. Hamad et al.[246] recently found that protonated sulfate groups on H-CNCs both accept and form H-bonds, promoting the formation of local induced dipoles. He found that adding 3 mM of NaCl was responsible for dramatically enhancing the piezoelectric properties of the H-CNC film.

The presence of sulfate protonated functional groups along the CNCs, the CNC self-assembly ability into layered chiral nematic structures, the existence on many interfacial regions between the CNC and local induced dipoles can potentially promote charge trapping effects. However, to the best of the author's knowledge the use of CNCs as charge trap layer intercalated into a TENG structure has never been studied.

This chapter describes the fabrication process and results regarding Seys-TENGs fabricated using an intermediate layer of CNCs between CF yarns and PDMS. Its influence as a charge trapping layer is discussed. The CNC layer is deposited around the CF yarn electrode charge collector using electrophoretic deposition assisted by rotation and the suspension was altered by substituting H^+ for Na^+ and adding NaCl. A study regarding the influence of thickness, geometrical conformation around the CF yarn and chemical modification in its composition and the influence in the overall power conversion is debated.

6.1 CNC based films

Agricultural or industrial cellulose rich waste are the predominant raw materials for the production of CNCs. [247] Within plant cell walls, cellulose forms microfibrils comprising repeating units of cellobiose, a disaccharide composed of D-glucose molecules linked via β (1, 4) glycosidic bonds. These repeating units combine to form long cellulose polymer chains that are arranged in the form of microfibrils, linked to neighboring chains through robust hydrogen bonds and weaker van der Waals forces [248].

Cellulose fibers encompass regions of both high and low order, known as the crystalline and amorphous regions. Different micro or nano cellulose structures can be obtained from different processing methods. Cellulose nanofibers (CNF) are obtained using mechanical processes and are composed of crystalline and amorphous regions. To obtain CNCs, acid hydrolysis using HCl, H_3PO_4 or H_2SO_4 or enzymatic degradation are employed. This process hydrolysis the amorphous regions and preserves the crystalline ones, resulting in spindle shaped nanoparticles with ordered regions of high crystallinity. [247]

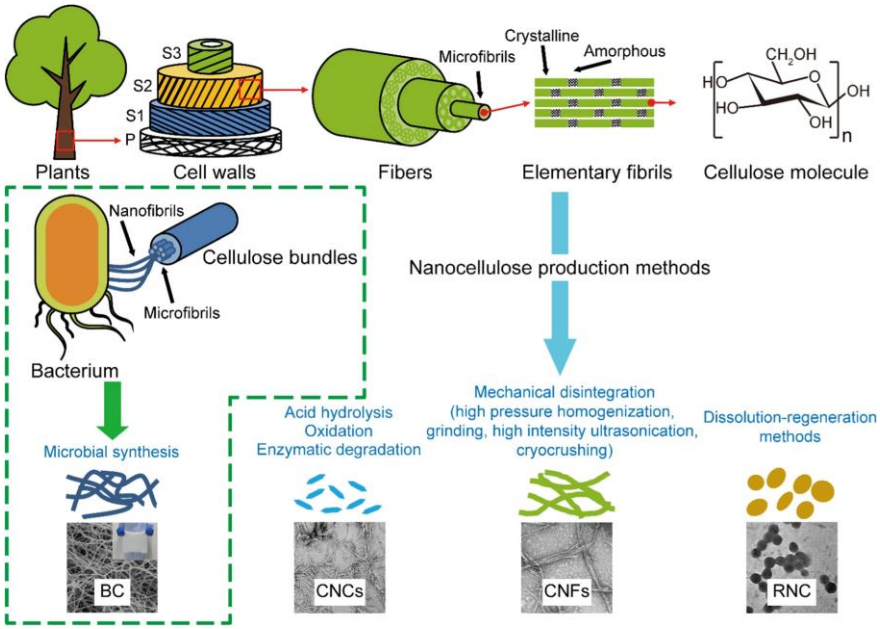

Figure 6.86 –Schematic representation of the hierarchical structure of cellulose molecules and the principal routes to obtain nanostructures cellulose (*Reproduced with permission from* [247] *Springer Nature under the license number 5645351427678*).

This section reports the preparation procedures and characterization of CNC based films/coatings by electrophoretic deposition around CF yarns.

6.1.1 Preparation of CNC based suspensions

Cellulose nanocrystals (CNCs) are insoluble molecules that can be well dispersed and stabilized in aqueous systems. Commercial CelluForce CNCs were used to prepare an aqueous suspension. Those are industrially produced spray dried sodium neutralized CNCs obtained by acid hydrolysis using sulfuric acid (Figure 6.87 a) and b)). The neutralization of CNCs by exchanging the H^+ for Na^+ or other bigger alkali ions leads to an increase in thermal stability in the solid state. [249][250] Ence, they are sulfate half-ester sodium terminated CNCs with the chemical formula of Figure 6.87 c).

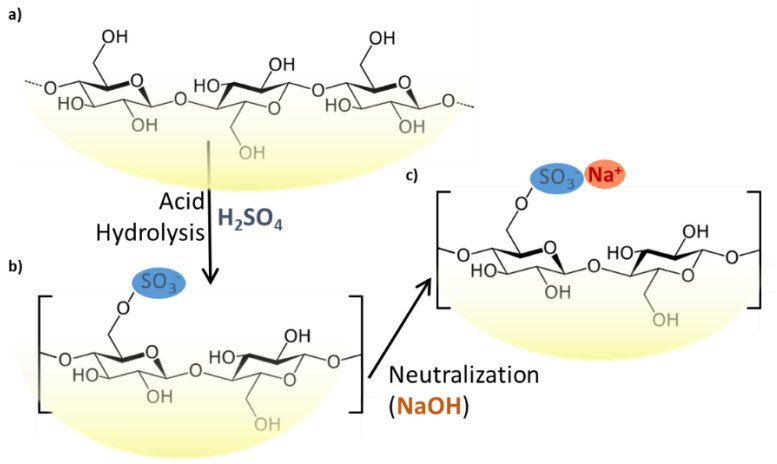

Figure 6.87 –Molecular structure of cellulose a) before and b) after sulfuric acid (H_2SO_4) acid hydrolysis. c) Resulting structure after sodium neutralization.

A suspension containing 2 % wt. CNCs (Celluforce) was prepared following the route from [246]. Slowly, the CNC-Na powder was added to a beaker with 100 mL of deionized (Millipore) water while stirring with a magnetic stirrer to avoid the formation of bundles. The suspension was left to stir for 2 hours, and the viscosity of the solution increased substantially. The solution was then subjected to stirring combined with sonication using a 5 mm tapered microtip working at an amplitude of 60% and programmed for pulses of 1 second ON and 1 second OFF (VCX 500) for 2 hours. After the sonication, the viscosity decreased, and the earlier cloudiness evolved to a clear transparent suspension. Finally, the resulting suspension was

either filtered through a glass fiber filter with 1.6 μm pore diameter or processed further. The resulting suspension was named Na-CNC and was used either as is or after further exchanging the Na^+ counterion. The Na^+ counter ions in the sulphate group were substituted for H^+ by adding roughly 3 times the weight of CNCs of ion exchange beads (SAC – Strong Acid Cation Dowex Marathon C Hydrogen form) to the suspension (about 6 g). The beads had been washed several times with deionized water to remove resin residue. Before the addition of beads to the CNCs suspension the pH was near 6 and at this point it dropped almost immediately to pH 2. The ionic substituted CNCs are addressed as H-CNC. The mixture was vigorously stirred overnight to ensure the total substitution of sulphate groups. After that, the -exchanged beads were removed from the suspension, washed and reserved for further use, while the suspension was filtered through a glass fiber filter with 1.6 μm pore diameter and ready to use. When not used immediately, the suspensions were kept inside a well-tapered opaque flask protected from light and inside the fridge.

The addition of NaCl modified the ionic strength of Na-CNC and H-CNC suspensions. Briefly, aqueous solutions of different concentrations of 1, 3 and 5 mM of NaCl were prepared and 1 μl was added to each 10 mL of the 2 % wt. Na-CNC or H-CNC suspension while stirring. When not used immediately, the suspensions were kept inside a well-tapered opaque flask protected from light and inside the fridge. A brief schematic representation of the procedure involved on the preparation of CNC based suspensions is shown in Figure 6.88 a).

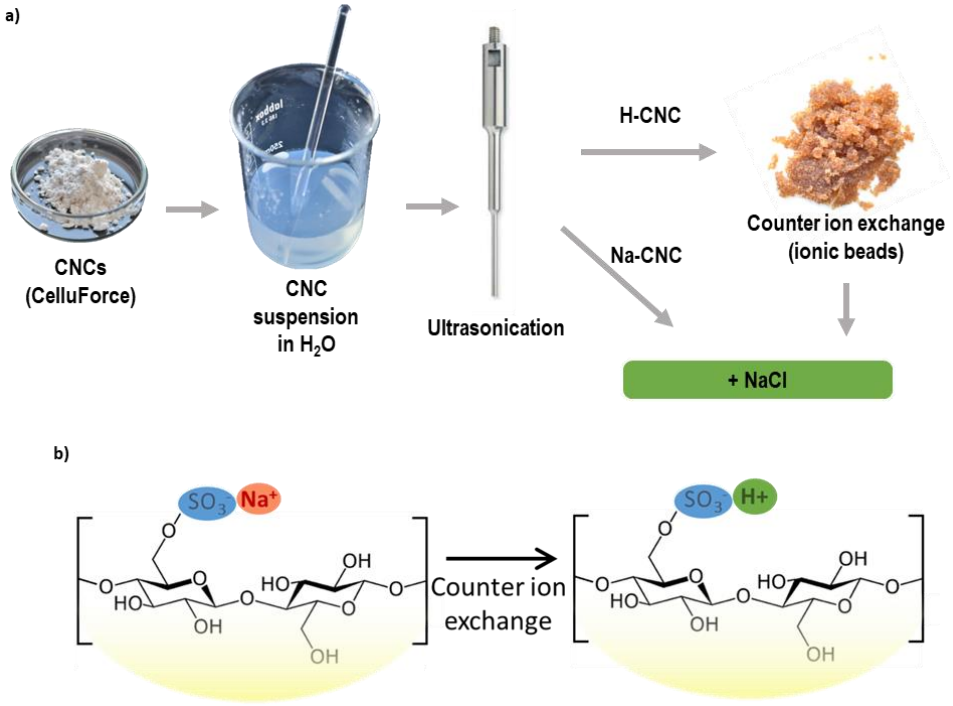

Figure 6.88 – a) Schematic illustration the CNC based suspensions process. b) Molecular structure of CNCs before and after exchanging of the counter ion Na^+ per H^+ using molecular beads.

Table 6.13 summarizes the CNC based suspensions utilized during this study and respective terminology used throughout the document.

Table 6.13 – Summary of the CNC based suspensions used during the electrophoretic deposition and respective attributed nomenclature.

NaCl [mM]	Na-CNC suspension	H-CNC suspension
0	Na-CNC	H-CNC0
1	Na-CNC1	H-CNC1
3	Na-CNC3	H-CNC3
5	Na-CNC5	H-CNC5

6.1.2 Electrophoretic deposition of CNC based suspensions around CF yarns

The one-dimensional (1D) structure of CF yarn electrodes turns deposition processes like coating, which are straightforward in a two-dimensional (2D) geometry, considerably more challenging. In the case of CNC suspensions, the typical method of creating planar CNC-based films involves drop casting followed by solvent evaporation. However, this approach is fundamentally incompatible when a fiber is the substrate. Another deposition method that have been explored to obtain self-assembled CNC films more rapidly is the electrophoretic deposition (EPD).[251] This method consists on the application of an electric potential between two electrodes. CNCs obtained by sulfuric acid hydrolysis are negatively charged based on its surface grafted sulfate half-ester groups. During the application of an electric field, the CNC particles move towards the positive electrode (anode) and form a thick gel that self-assembles in the form of a chiral nematic structure. The use of this technique was already successfully employed to coat of geometrically challenging surfaces like spheric or rod like surfaces using Cellulose Nanofibers (CNF).[252] To the best of the author's knowledge, this technique has never been employed in the deposition of CNC films around fiber/yarn shaped conductive electrodes.

In this sub-section, the possibility of using EPD to obtain CNC coatings around CF yarns was studied. H-CNC suspensions whose preparation is described in the previous sub-section were used. Because of its chemical stability, CF yarns were used simultaneously as the anode and cathode material during the process. Initially, both CF yarns were securely attached to a plastic holder like depicted in Figure 5.89 c). The CF yarns were mounted so that they loop around the holder so that both ends are connected to a parallel plane crocodile to ensure an even distribution of the electric potential applied. The plastic holders were mounted into the specially made container like shown in the schematic of Figure 5.89 b). A top view of the EPD apparatus is shown in Figure 5.89 a), with a distance of 8 mm between the electrodes and an effective section of 7 cm long exposed to the EPD. The volume of H-CNC suspension was fixed at 7 ml. A Uni-Trend UTP3313TFL-II power supply was used to apply a voltage between the electrodes. After some trials, the potential was fixed at a value of 15 V. When applying a 15 V DC voltage, continuous bubble formation was observed around both the cathode and the

anode throughout the process. This phenomenon can be attributed to the applied voltage significantly exceeding the theoretical reported decomposition voltage for water molecules, which stands at 1.48 V.[253] After some seconds of applying the EPD potential, a thick H-CNC gel developed around the anode at +15 V. After vertically drying for a couple of hours, the gel turned into an H-CNC film. It was found that the 1D nature of the CF yarns leads to an accumulation of the deposited material on only one side of the yarn due to gravity, resulting in an uneven film distribution around the yarn. This is visible in the Figure 5.89 d) and in the cross-section SEM image in of 15 V e).

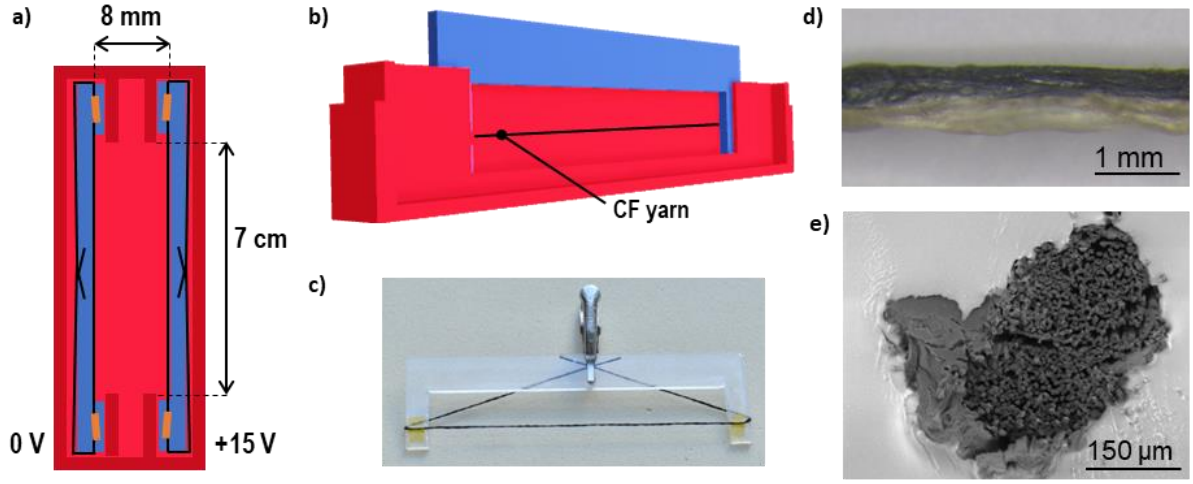

Figure 5.89 – a) Schematic representation of the fixed electrophoretic deposition container set up, b) detail of the plastic yarn holder set in position inside the container here displayed from a cross-section perspective. c) detail of the CF yarn set up on the plastic holder and connected at both ends using a planar alligator clip. d) image and e) cross sectional SEM image of the H-CNC film profile obtained using the fixed deposition set up.

The non-uniform distribution of the H-CNC coating around the CF yarn is not ideal for the application in the Seys-TENG. To solve this issue, a modification to the electrophoretic deposition was conceived: by guaranteeing that the yarn was continuously rotating during deposition, the film can become evenly distributed around the yarn instead of accumulating asymmetrically at the bottom. As such, a motorized system able to promote the rotation of the yarn submerged in the H-CNC suspension at a constant and steady speed while proportioning the ability of applying an electric potential was developed and is explained in detail in the subsection 3.1.2. The EPD assisted by rotation was performed in similar conditions to the conventional EPD. The CF yarn in the anode position was rotated while at the same time the CF yarn in the cathode was kept in a fixed position (Figure 6.90 c). The container was adopted, with

one side unaltered left to hold the plastic holder for the fixed electrode. In contrast, the other side was redesigned with two smooth bump features that allows the effective length of the CF yarn anode to be submerged. At the same time, both ends are guided outside the suspension and attached to rotating planar alligators (Figure 6.90 b). Just enough ease is added to the CF yarn to follow the rotation movement, rotating freely inside the CNC based suspensions and reducing the friction in the angled region. A top view of the modified 3D printed container is shown in Figure 6.90 a), with the distance of 8 mm between electrodes and an effective deposition length of 7 cm left unaltered from the previous conventional EPD system.

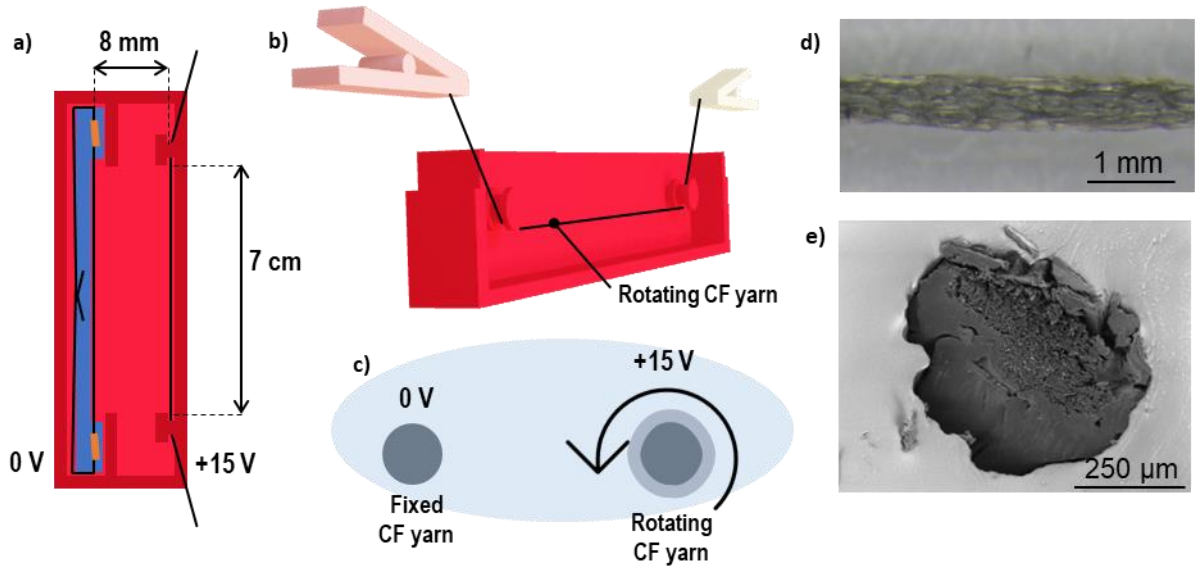

Figure 6.90 - a) Schematic representation of the rotating electrophoretic deposition container and b) detail of the rotating yarn (used as anode) set up inside the container displayed from a cross-section perspective. c) Schematic of a cross sectional view of the fixed (cathode) and rotating yarn (anode) inside the container. d) image and e) cross sectional SEM image of the H-CNC film profile obtained using the deposition set up assisted by rotation.

Images from H-CNC films obtained using the conventional method and the rotating system are presented in Figure 6.90 d). Films obtained from EPD assisted by rotation results in apparent symmetric films deposited with uniform thickness over the length of the yarn. The uniformity of the coating over the diameter of the CF yarn is shown in Figure 6.90 e), although the cross-sectional cutting partially smashed the film. The same images are displayed together in Figure 6.91 to allow for a better comparison. There is a clear difference in the distribution of the H-CNC coating over the yarn. The accumulation effect at the bottom for conventional EPD disappears when using EPD assisted by rotation.

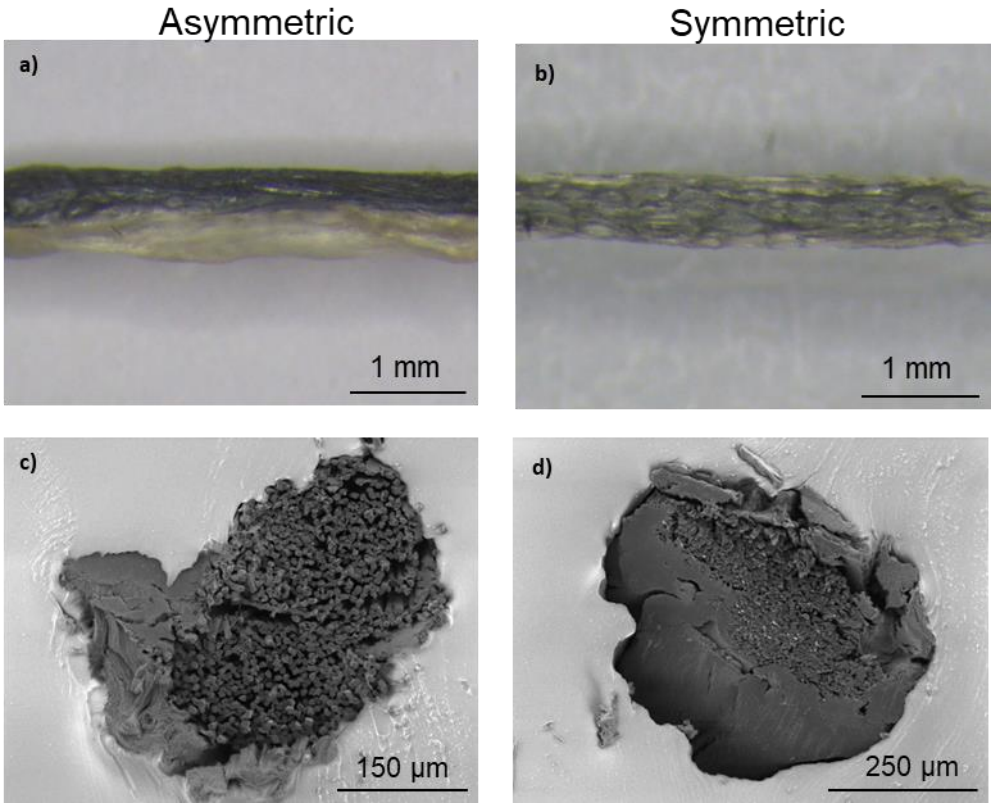

Figure 6.91 –Images of a) asymmetric and b) symmetric films of H-CNC deposited over a CF yarn using by conventional EPD and EPD assisted by rotation, respectively. Cross-sectional SEM images of H-CNC Seys-TENGs produced using c) asymmetric and d) symmetric coated CF yarns.

Conventional EPD and EPD assisted by rotation were used to deposit asymmetric and symmetric H-CNC films, respectively. Deposition times of 60, 90 and 120 seconds were used and diameter at three different locations of four CF yarn coated with H-CNC through conventional EPD and EPD assisted by rotation is presented in graphs of Figure 6.92 a) and b), respectively, as a function of deposition time. The diameters increase linearly as a function of deposition time for both cases. In the case of asymmetric coatings, the diameters tend to be slightly higher. In both cases the dispersion of values can be attributed to the inherent surface roughness of the CF yarn, to the presence of bubbles formed during the EPD and to non-uniform shrinking of the H-CNC gel when drying.

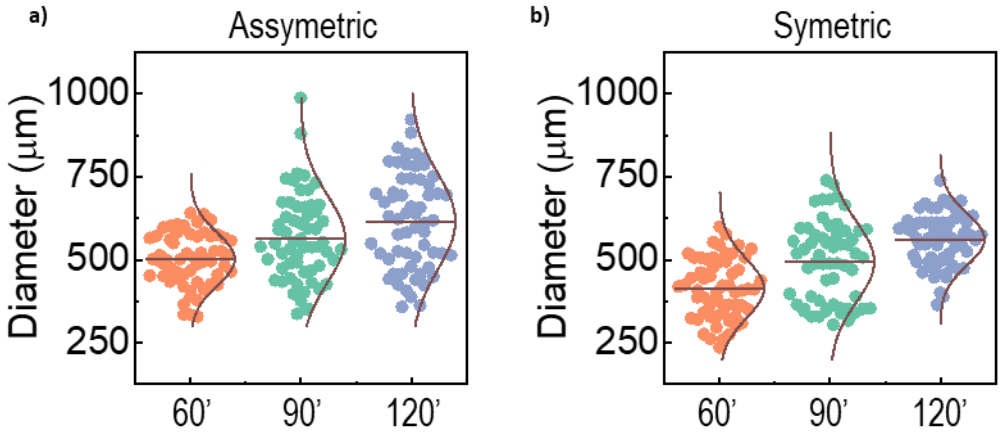

Figure 6.92 - Box plot with the diameters of H-CNC coated CF yarn using a) conventional electrophoretic deposition and b) assisted by rotation.

Even if the influence of using a symmetric and asymmetric coating over the CF yarn in the performance of the Seys-TENGs will be examined in subsequent sub-chapters, the preferred method of NCC based film deposition is for now on the EPD assisted by rotation.

Figure 6.93 a) shows a sequence of images captured during the electrophoretic deposition of H-CNC around a CF yarn using the rotating system and the resulting CF yarn after being coated with the H-CNC and the gels drying hanged vertically with a weight clip attached to keep it from curling is shown in Figure 6.93 b) and in more detail in Figure 6.93 c).

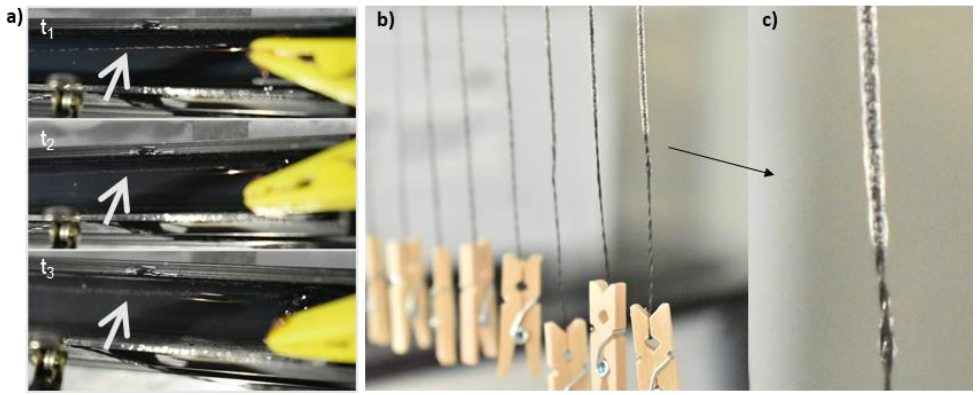

Figure 6.93 – a) Sequence showing the formation of a film of H-CNC that is being deposited by electrophoretic deposition. d) The resulting H-CNC coating the CF yarn electrode. C) Detail of the H-CNC film electrophoretic deposited on CF yarn electrodes.

During the EPD process, there are noticeable bubbles forming, because of the high voltage applied (associated to the decomposition of H_2O). These bubbles become trapped within the H-CNC gel structure that forms subsequently and are visible in Figure 6.93 c). These

bubbles are partially responsible for an increased roughness of the films. As the gel dries, it undergoes contraction and transforms into a thick shell, with certain regions exhibiting a wrinkled or shriveled appearance (Figure 6.94 a)). The surface of the film also presents a sort of wrinkled appearance (Figure 6.94 b)).

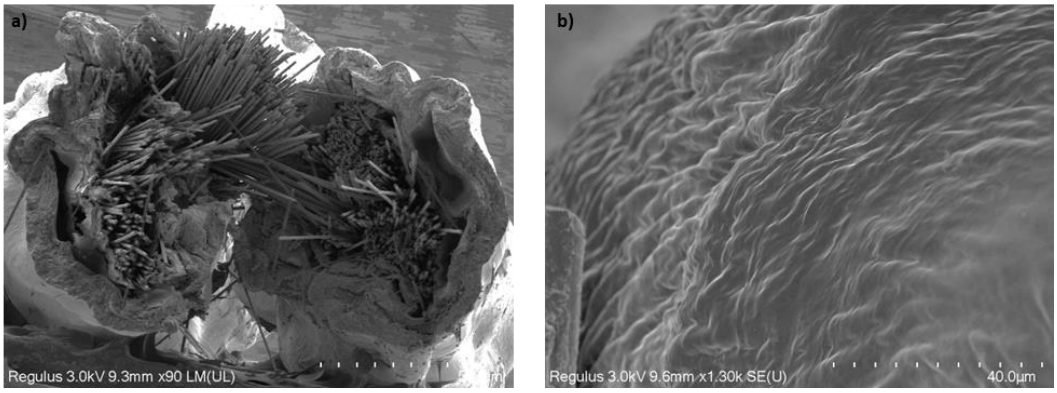

Figure 6.94 – a) Cross-sectional SEM image of a two CF yarns with a H-CNC EPD film. b) detail of the surface of H-CNC films.

A more detailed observation through the cross-section images of the films obtained (Figure 6.95) shows an ordered structure of CNCs arranged in sheets parallel to the direction of the CF yarn. This structure is achieved when CNCs migrate towards the anode, resulting in the formation of a concentration gradient that promotes CNC interactions, leading to their self-assembly.

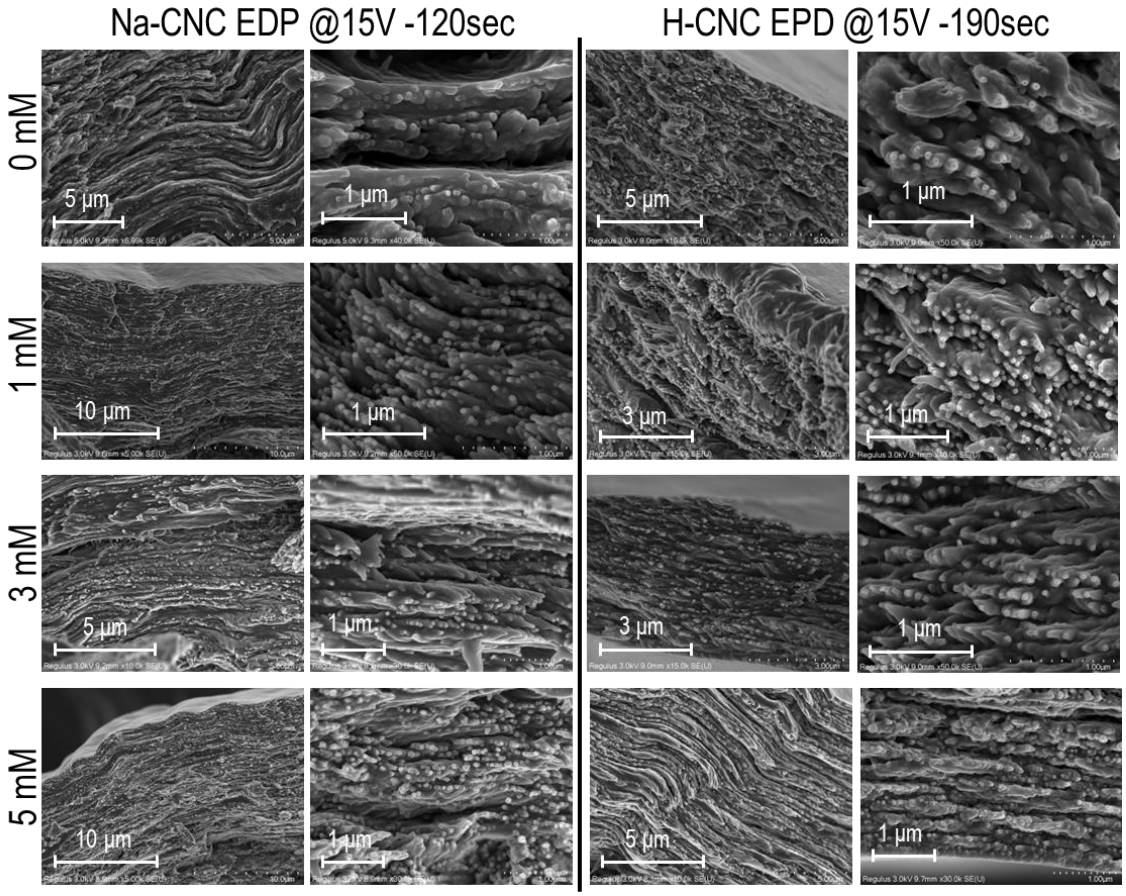

Figure 6.95 – Cross sectional SEM images of Na-NCC and H-NCC films EPD around CF yarns using 15 V during 120 and 190 seconds, respectively.

From the cross-sectional SEM images obtained from the Na-CNC and H-CNC EPD films, it is difficult to tell if there is a chiral nematic ordering in the structure. Partially because the film suffered some degradation when performing the cross-sectional cut.

The surface of the films was observed on the optical microscope in reflectance mode under left and right polarized filters and the results are shown in Figure 6.96. The chiral nematic ordering consists of the staking of CNC into layers and subsequent twisting of the CNCs between each layer in one direction. Films obtained by evaporation induced self-assembly normally present lefthand twisted alignment of CNCs and reflect left circular polarized (LCP) light while transmitting right circular polarized (RCP) light.[251] Accordingly, all the EDP films present some iridescence, mainly when viewed through the left Polarized filter. This confirms that at least locally there is chiral nematic ordering of the structure. The most intense

effect is shown as an inset with higher amplification. The pitch is the distance of a full 360° rotation and is directly connected to the optic properties of the films, shifting the reflected wavelength. Due to the irregularity of the Na-CNC and H-CNC EPD film's surface the light is reflected in many different angles which makes it difficult to perceive the true structural colors since it shifts with the viewing angle.

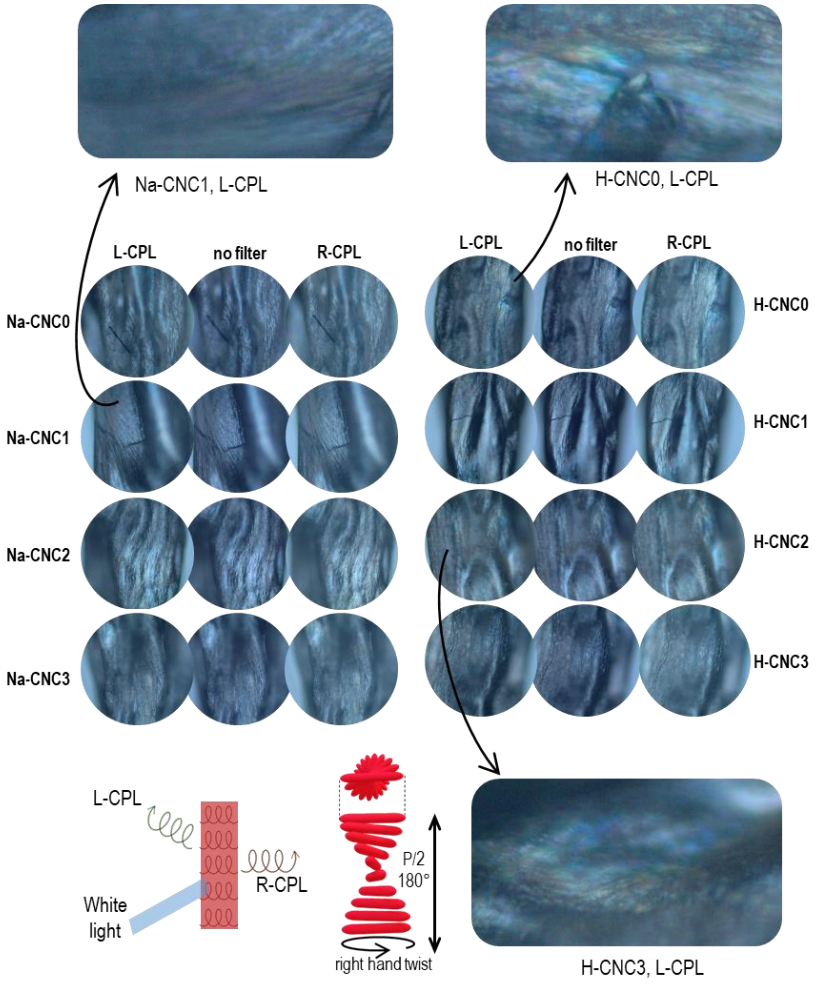

Figure 6.96 –Microscopic images of Na-CNC and H-CNC membranes with different NaCl concentrations. Images were taken in reflection mode using left and right circular polarized filters.

The rate at which the films of Na-CNC and H-CNC are deposited when using EPD was found to be different. To have sets of corresponding dimensions, the deposition times were studied, and it was found that a deposition time of 90 seconds of Na-CNC suspensions corresponds to 120 seconds in the case of H-CNC, resulting in diameters of approximately 525 µm (Figure 6.97 a) and c)). In the case of a deposition of 120 seconds of Na-CNC suspension, the

same diameters can be achieved with 190 seconds of deposition time in the case of H-CNC suspensions (Figure 6.97 b) and d)), which are approximately 730 μm (with some slight variation in this case).

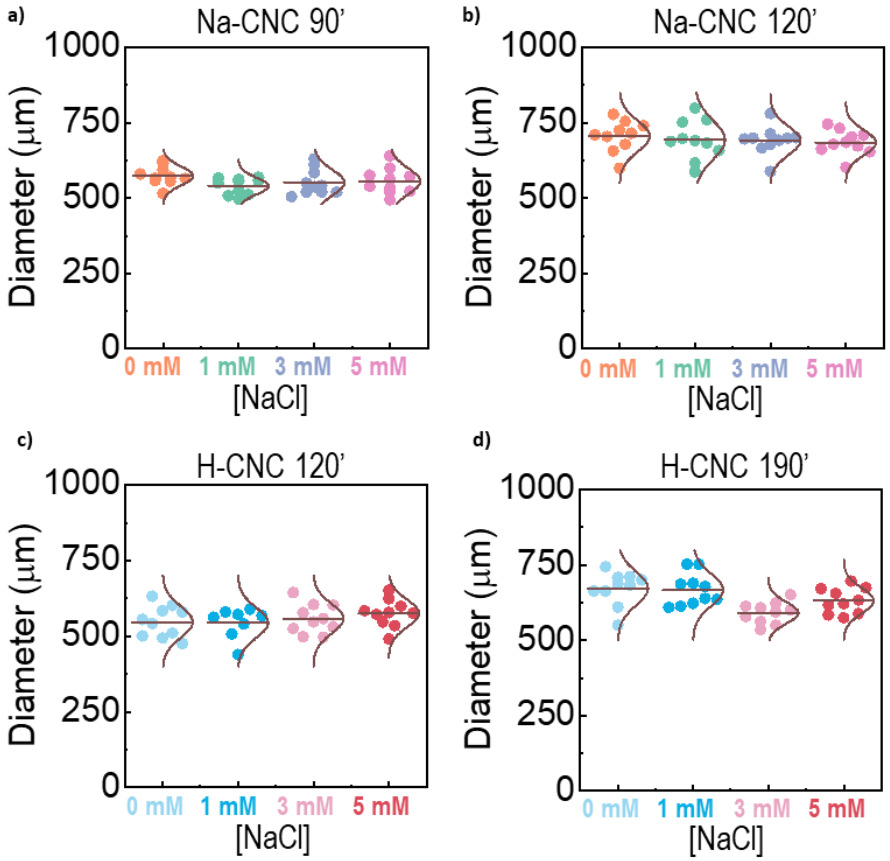

Figure 6.97 – Distribution of diameters obtained for the Na-CNC EPD assisted by rotation during a) 90 and b) 120 seconds and for H-CNC during c) 120 and d) 190 seconds and as a function of salt concentration.

The rate at which Na-CNC films are deposited using EPD is approximately 6.83 μm/sec comparing to only 2.93 μm/sec in the case of H-CNC. The presence of NaCl in various concentrations from 1 to 5 mM does not seem to have a major influence on the deposition rate. To look in further detail for the electrophoresis process regarding the different suspensions, the electrical current during the EPD was manually monitored in 5 sec intervals during the electrodeposition of Na-CNC and H-CNC, while applying 15 V between the two CF yarns in a set up assisted by rotation. The suspensions used during each deposition were always renewed with a fresh suspension after the previous EPD. The average values of a total of 10 different

deposition for each suspension with different concentrations of NaCl as a function of deposition time are shown in Figure 6.98.

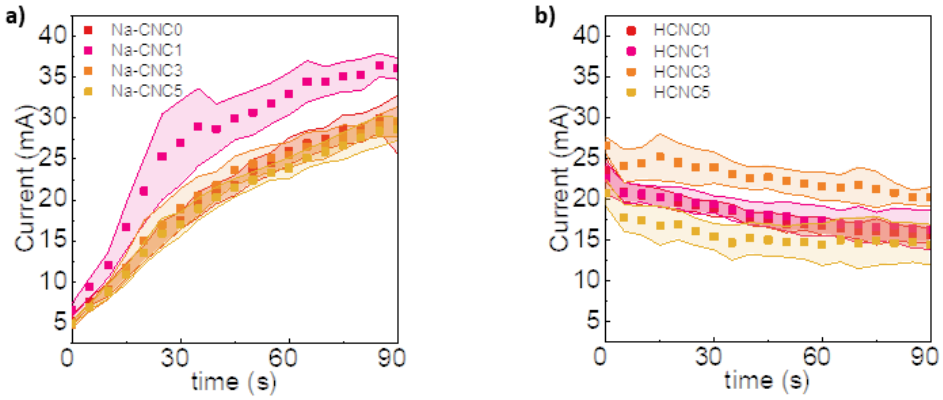

Figure 6.98 – Current as a function of the electrophoretic deposition time for a) Na-CNC and b) H- CNC based suspensions with different NaCl concentrations, using a deposition voltage od 15 V.

In the case of Na-CNC, the suspension with 1 mM of NaCl stands out with a consistently higher current during the entire process. And in the case of H-CNC, suspensions with 3 mM have higher conductivity above the rest, with the suspension of 5 mM presenting a lower current than its counterparts. The presence of NaCl in solution increases the conductivity of liquids due to the total ionic dissociation of Na^+ and Cl^-.[254] However, the difference in current may results in different deposition rates as will be explored in the following subsections.

6.1.3 Dielectric and structural characterization of CNC based films

The tubular-shaped nature of the CNC based films deposited by EPD around CF yarns is hard to characterize based on its geometry especially for the case of EIS. For this reason, planar films were prepared using the same starting suspensions and the same EPD conditions, except for the anode electrode material that was replaced by Aluminum foil. These films were then used to perform EIS, XRD and FTIR measurements. The Aluminum foil electrode was wrapped around one piece of glass, and the back was covered with another glass slide. The cathode was prepared by winding approximately one meter of CF yarn over a glass slide for an increased surface area. Then the back was covered using another glass slide with a piece of aluminum foil sandwiched between the slides to electrically address the CF based electrode more efficiently, like shown in Figure 6.99 a). Both electrodes were submerged into the CNC

based suspensions 1 cm apart, and a potential of 15 V was applied during 30 sec using a Uni-Trend UTP3313TFL-II power supply (Figure 6.99 b)). After this period, the Aluminum foil with the deposited films were left to dry overnight at room temperature. EIS characterization of electrophoretic deposited CNC based membranes was performed using the films sandwiched between two stainless steel electrode discs of 11.6 mm diameter on a typical capacitor structure configuration (Figure 6.99 e)).

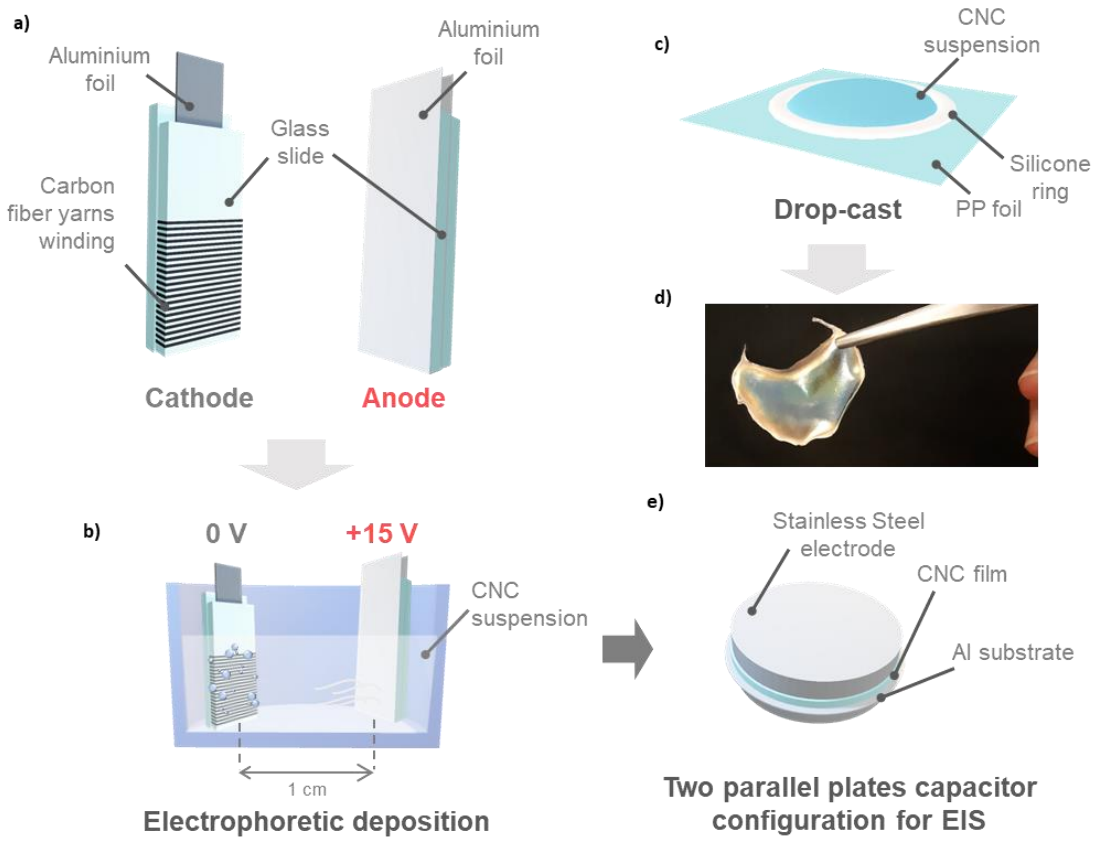

Figure 6.99 – Schematic representation of a) cathode and anode electrodes used for b) electrophoretic deposition of CNC based suspensions and c) drop-cast apparatus. d) resulting free standing drop-cast film. e) schematic representation of the parallel plate capacitor configuration used for characterization of CNC based films by EIS.

A GAMRY Reference 600™ potentiostat was used and potentiostatic EIS measurements were performed by applying a 10 mV AC voltage signal in a frequency range between 0.1 Hz and 1 MHz. The results are shown in Figure 6.100.

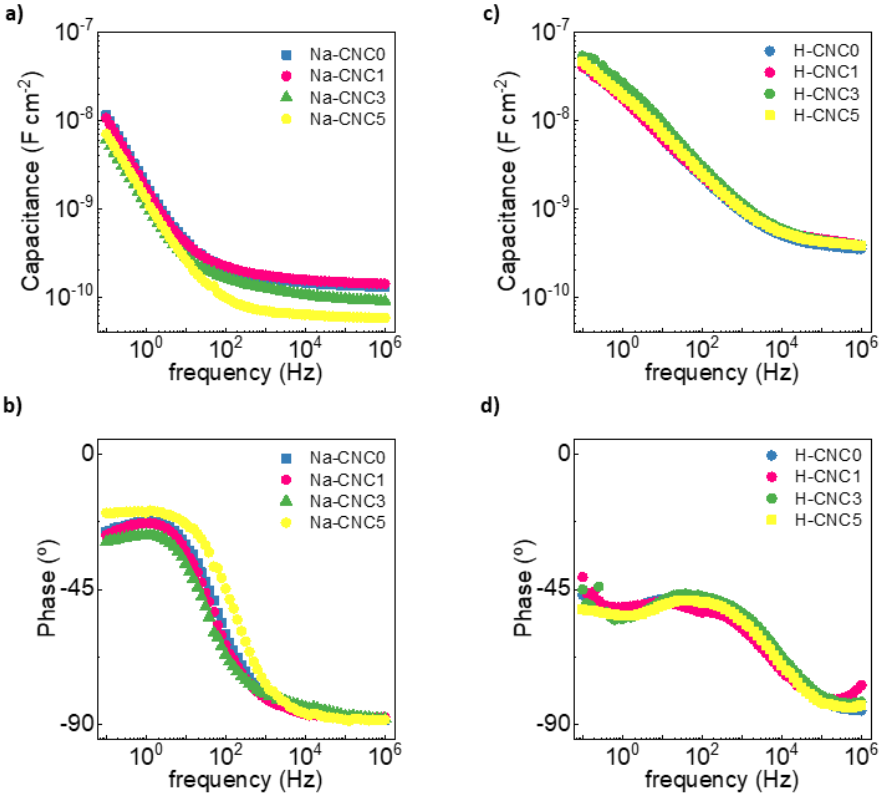

Figure 6.100 – EIS results measured from 10^{-1} to 10^{6} Hz. a) Capacitance and b) phase shift of Na-CNC membranes as a function of frequency. c) Capacitance, e) permittivity and d) phase shift of H- CNC membranes as a function of frequency.

Frequencies above approximately 100 Hz result in a phase angle between voltage and current lower than -45° which suggests the predominance of a capacitive regime. In this high range of frequencies, dipolar relaxation occurs as the prevalent mechanism of polarization. From 100 Hz to 1 MHz (the higher frequency in study) the phase angle decays progressively from – 45 ° until reaching the maximum phase shift at -90 °. Hydroxyl groups on the cellulose chain are responsible for the electronic/atomic polarization. On the other hand, they promote intermolecular H bonding that restricts the polarization and as such, high crystallinity is inversely proportional to polarization.[255]

At frequencies lower than approximately 100 Hz, the phase shift tends to lower its absolute value, in the case of Na-CNCs reaching values higher than -45 ° which indicates the transition to a more resistive regime. The existence of ionic displacement characterizes the lower frequencies domain. Under slower alternating electric fields, ionic species move towards the

interfaces forming an Electrical Double Layer (EDL), responsible for increased capacitance. This ionic species can be Na^+, Cl^- or water molecules. However, the capacitance does not seem to be affected by the presence of NaCl on the Na-CNC nor H-CNC structures. In the case of H-CNC films the phase shift remains lower than -45 °even for lower frequencies.

Fourier transform infrared spectroscopy (FTIR) spectra of CNC based films was acquired at room temperature between 4000 and 550 cm^{-1} using a PerkinElmer Spectrum Two FTIR Spectrometer equipped with a Pike Miracle accessory operating in Universal Attenuated Total Reflectance Accessory (UATR) mode. Free standing membranes were prepared by dop-casting approximately 3 mL of solution on a polypropylene foil demarcated by all-purpose silicone ring as a container (Figure 6.99 c)) and then let to dry at room temperature (~25 °C) for 2 days until ready to peel off (Figure 6.99 d)). The FTIR spectra of a Na-CNC and H-CNC drop casted membranes in shown in Figure 6.101 a). Both spectra's shows identical main peaks at 3332, 2900, 1644, 1426, 1278, 1234, 988-1156, 894, 814 and 594 cm^{-1} assigned to O-H and C-H stretching, O-H (associated to absorbed water molecules), C-H in plane bending, O=S=O asymmetric and symmetric stretching, C- O- H glucopyranose ring stretching, C-O-C from β glycosidic link and S-O from the half-ester groups, respectively.[256][257][258][259] The peak list is shown in greater detail in Figure 6.101 d). Normalized FTIR spectra of drop-casted membranes of Na-CNC and H-CNC with different amounts of NaCl concentration are presented in Figure 6.101 b) and c), respectively. The primary distinction between the spectra lies in the intensities of the O-H and C-H peaks, which are located near 3332 and 2900 cm-1, respectively. In the Na-CNC membranes, the introduction of salt appears to align with a reduction in the intensity of these peaks. Similarly, in the H-CNC membranes, the peak intensities decrease, except in the case of the 5 mM concentration.

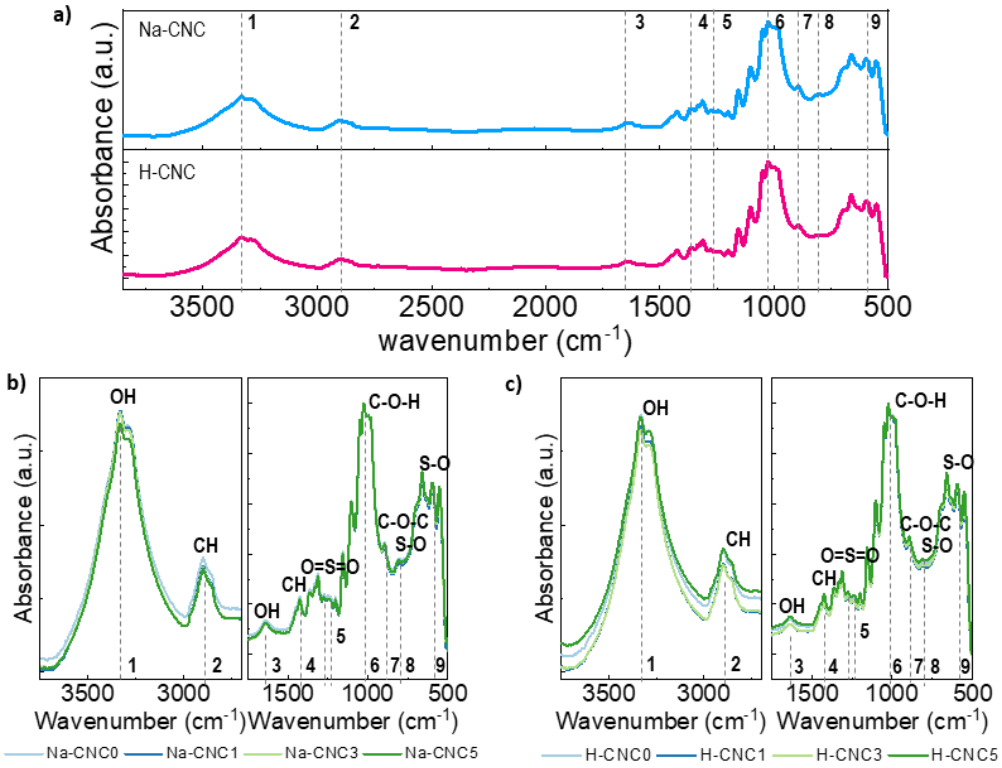

d)

Peak Number	Wavenumber (cm^{-1})	Functional Group
1	3332	O-H (Stretching)
2	2900	C-H (Stretching)
3	1644	O-H Absorbed water (Bending)
4	1426	C-H (in plane Bending)
5	1278, 1234	O=S=O (assymmetric, symmetric stretching)
6	988-1156	C-O-H Glucopyranose ring (Stretching)
7	894	C-O-C (β Glycosidic Linkage)
8	814	S-O (stretching)
9	594	S-O (stretching)

Figure 6.101 – a) FTIR spectra of Na-CNC and H-CNC membranes obtained from drop casting. Comparison between b) Na-CNC and c) H-CNC peaks with different NaCl concentration from 1 to 5 mM. d) List of the principal peaks and corresponding vibrations.

A PANalytical's X' Pert PRO M RD X-ray diffractometer using a monochromatic Cu Kα radiation source (wavelength 1.540598 Å) from 20° to 60° (2θ) with a scanning step size of 0.016° with samples mounted on a rotating stage was used to determine the crystallographic structure of the CNCs. The diffractogram obtained is shown in Figure 6.102.

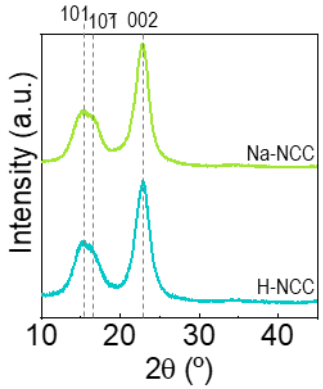

Figure 6.102 – XRD of Na-CNC and H-CNC membranes obtained by drop casting.

Diffraction peaks are visible at 2θ of 15.5°, 16.6° and 22.8°, associated with (101), (10$\bar{1}$) and (002) crystallographic planes, respectively, characteristics of type I Cellulose. Crystallinity index (IC) was estimated using Equation 5.22 proposed by Segal et al.[260][261]:

$$IC = \frac{(I_{002} - I_{min})}{I_{002}} \times 100 \qquad \text{Equation 5.22}$$

Where I_{002} is the 002-peak intensity at 2θ=22.8° and I_{min} is the minimum intensity between the 101 and 002 peaks near 2θ =18.5 ° corresponding to the influence of amorphous regions. A slight increase of the IC from 83 to 86.1 % can be noticed for the protonated H-CNC film. This can be due to protonated sulfate half ester groups, simultaneously accepting and forming H-bonds between the CNC surface and promoting higher ordering of the structure.

Table 6.14 – Crystallinity index of drop-cast Na-CNC and H-CNC films.

	IC
Na-CNC	83.0%
H-CNC	86.1 %

6.2 CNC functionalized Seys-TENGs

The Na-CNC and H-CNC coated CF yarns were used to fabricate Seys-TENGs. PDMS (SYLGARD™ 184 Silicone Elastomer from Dow Corning) was cured around the functionalized CF yarns using the in-situ curing procedure described in sub-section 3.1.1. In short, the PDMS was prepared by mixing with a curing agent in the proportion of 1:10, degassed for 30 min and then 2 mL of the mixture was poured in a specially designed container. The functionalized CF yarns were also placed in the container, submerged in the uncured PDMS slurry, and a current of 0.2 A passed through the CF yarn. The heat generated allowed the curing of the PDMS around the functionalized CF yarn, and the curing time was fixed at 4 min. The following sub-sections are dedicated to the morphological and electrical characterization of the CNC functionalized Seys-TENGs. Two main studies were conducted, namely the comparison between symmetric and asymmetric H-CNC coatings in the overall conversion of Seys-TENGs; and the influence of the presence of CNCs as inter layer of Seys-TENGs as well as the chemical nature of Na-CNC vs H-CNC with different NaCl concentrations and respective thickness on the power conversion.

6.2.1 Morphological characterization of CNC-functionalized Seys-TENGs

6.2.1.1 Symmetric vs Asymmetric H-CNC coatings in Seys-TENGs

The final diameters of the Seys-TENGs were measured by capturing images from three different locations of all four fibers using an optical stereo microscope Leica M80. Five different measures from three distinct locations of the Seys-TENG were acquired and measured through imageJ. A violin plot with all the measures and the average diameter of each set of H- CNC functionalized Seys-TENGs obtained either by conventional EPD or EPD assisted by rotation are presented in Figure 6.103 a) and b), respectively, as a function of the H-CNC layer deposition time. In general, for a fixed PDMS curing time of 4 min, different final diameters were obtained. The average diameter of the sets is dependent on the EPD H-CNC thickness

and increases as a function of the H-CNC thickness. The great amount of dispersion in the diameters of each Seys-TENG is attributed to both variations in ambient temperature and to the rough nature of the H-CNC film.

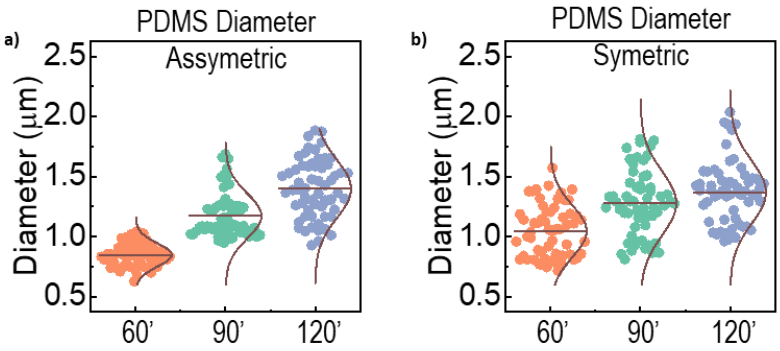

Figure 6.103 – Violin plot featuring the diameters of each H-CNC functionalized Seys-TENG where the H-CNC layer was obtained using a) conventional EPD and b) EPD assisted by rotation, as a function of H-CNC deposition time.

6.2.1.2 Na-CNC vs H-CNC coatings in Seys-TENGs

To optimize the uniformity within the sets of 4 Seys-TENGs, four individual Na-CNC and H-CNC coated CF yarns with similar dimensions were selected and the diameters of each are presented in the violin plots of Figure 6.104.

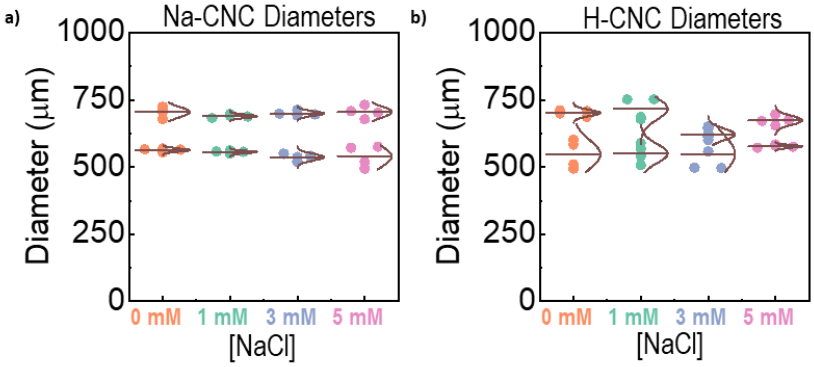

Figure 6.104 – Diameter values of the a) Na-CNC and b) H-CNC coated CF yarns selected to produce the Seys-TENGs sets.

The violin plots in Figure 6.105 display the average diameter values obtained from the in-situ curing of PDMS on the chosen Na-CNC and H-CNC coated CF yarns. Despite efforts to carefully curate the dimensions of the Na-CNC and H-CNC coatings and select similar dimensions, a significant level of dispersion was observed in the PDMS diameters for the fixed in-situ curing time of 4 minutes. Some of this dispersion might be attributed to fluctuations in

ambient temperature. However, it's also evident that non-uniform coating of the CF yarn plays a role. Interestingly, it was observed that whenever there was a crack in the Na-CNC/H-CNC-based coating or a lack of coverage on the CF yarn, the PDMS coverage in those areas would be thinner than other regions.

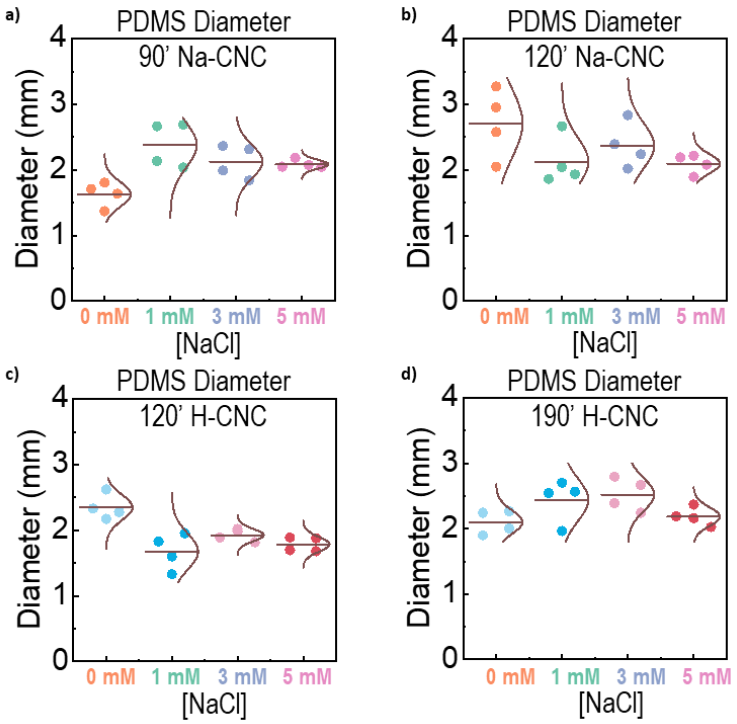

Figure 6.105 – Diameters of the Na-CNC based Seys-TENGs with EPDs of a) 90 and b) 120 seconds, and H-CNC based Seys-TENGs with EPDs of c) 120 and d) 190 seconds.

In subsection 4.2.1, a temperature of approximately 60 °C was noted around the 4-minute mark during the in-situ curing process. It is known from the literature that protonated CNCs (H-CNCs) has less thermal stability than in its neutralized form (Na-CNC). For this, the in-situ curing process can potentially degrade the CNC coating. It has been confirmed through DSC-TGA analysis that at such temperatures, there is no degradation of the H-CNC coating (Figure 6.106). The analysis revealed a mass loss of less than 5%, which is attributed to evaporation of volatile elements present in the structure (water) as indicated by the DSC peak at 71 °C. Evidence of degradation occurs at further higher temperatures, as suggested by the second exothermic peak at 177 °C.

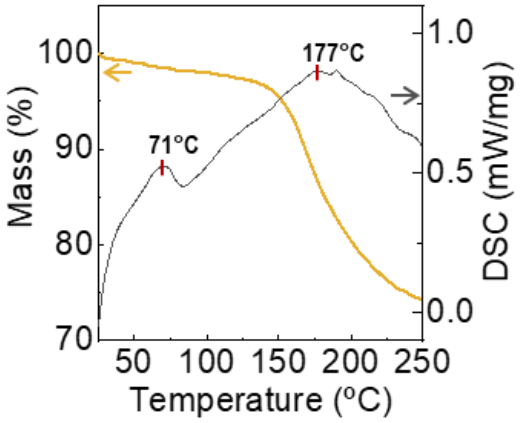

Figure 6.106 – DSC-TGA measurement of a H-CNC coated CF yarn over air atmosphere.

6.2.2 Electrical characterization of CNC - Seys-TENGs

As described in the previous chapters, four devices were connected in parallel using conductive copper tape. The sets were then fixed on a piece of paper sheet using scotch tape and positioned on the sample holder and fixed again using scotch tape to keep it from moving during the measurements. Electrical characterization of the sets was performed by applying vertical mechanical load using PFAM. In general, the proposed mechanism of energy conversion is the same presented in the last chapters. In summary, the cyclic friction of the BB (from PFAM) with the surface of PDMS promotes the transfer of negative charges that accumulate at the surface of PDMS inducing a current at the Seys-TENGs electrodes. The influence of the presence of a CNC layer in the charging mechanism and overall power output is discussed in the following sub-sub sections.

6.2.2.1 Symmetric vs Asymmetric H-CNC coatings in Seys-TENGs

The open circuit peak-to-peak voltage and short-circuit peak-to-peak current obtained for each set of four H-CNC functionalized Seys-TENG connected in parallel is depicted in Figure 6.107 a) and b), respectively.

The presence of thinner layers of either asymmetric or symmetric H-CNC films between the CF yarn and the PDMS layer results in a reduction of mechanical to electrical conversion.

However, Seys-TENGs power conversion seems to increase as a function of the H-CNC thickness and converters constituted by layers with deposition times of 120 sec can generate higher voltage and current than the reference sample without H-CNC layer, whether in the case of asymmetric or symmetric films. The best results for Seys-TENGs functionalized with H-CNC symmetric coatings were obtained using 120 seconds of deposition with a maximum of 34.24 V obtained when testing the set using 30 N of force (using the PFAM). The best current was achieved for the asymmetric set with 120 sec of curing with a maximum of 5.14 μA.

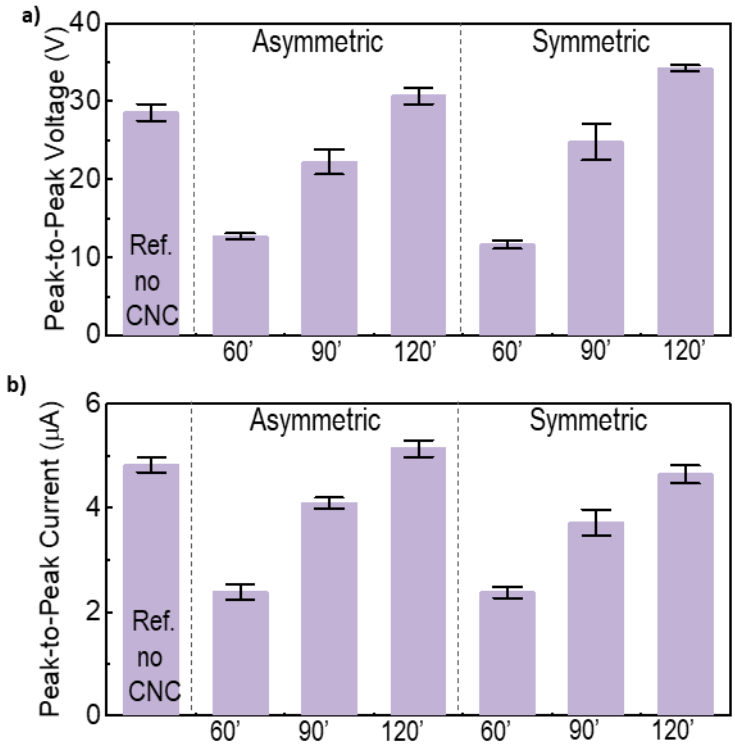

Figure 6.107 – Peak-to-peak a) open-circuit voltage and b) short-circuit current of Seys TENGs intercalated with symmetric and asymmetric H-CNC coatings.

6.2.2.2 Na-CNC vs H-CNC coatings in Seys-TENGs

The output of Seys-TENGs with Na-CNC and H-CNC interlayers of two different thicknesses were studied by applying 30 N of force at 2 Hz using PFAM and compared with a simple Seys-TENG without interlayer, for reference. The results obtained are shown in Figure 6.108

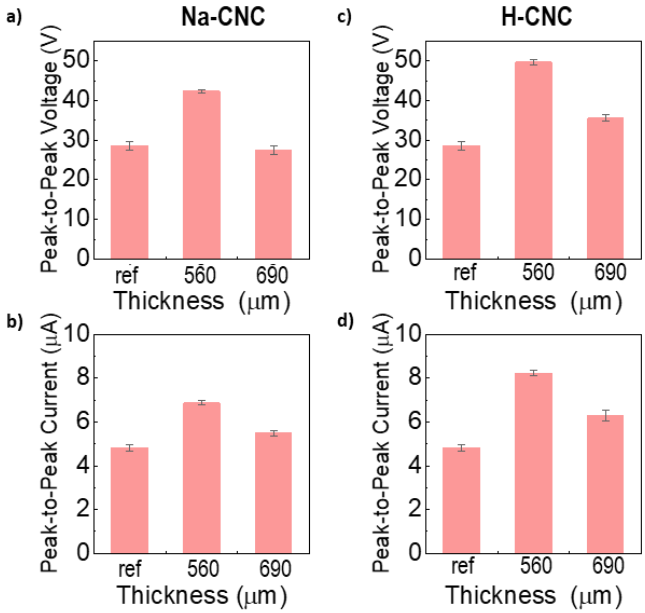

Figure 6.108 – a) Voltage and b) current output of Seys-TENGs as a function of the thickness of Na- CNC interlayer and c) voltage and d) current for a H-CNC interlayer. All measures were taken using PFAM at 30 N and a frequency of 2 Hz.

The introduction of a thinner Na-CNC or H-CNC interlayer results in a substantial increase of voltage and current of the Seys-TENGs, compared to the reference sample that does not have any interlayer. An overall increase of 48.3% and 73.9% of voltage were verified in the case of the presence of a 560 μm thick Na-CNC and H-CNC interlayers, respectively. It was also found that the presence of thicker interlayers of 690 μm reduces the power conversion enhancement. In the case of Na-CNC interlayer, the thicker layer cancels out the previously verified voltage enhancement. In the case of H-CNC, the thicker layer simply reduces the enhancement effect.

The influence of NaCl concentration of the constitution of the Na-CNC and H-CNC interlayers (of both 550 and 690 μm thick) was also studied and the results obtained when testing using PFAM at 30 N and 2 Hz are shown in Figure 6.109.

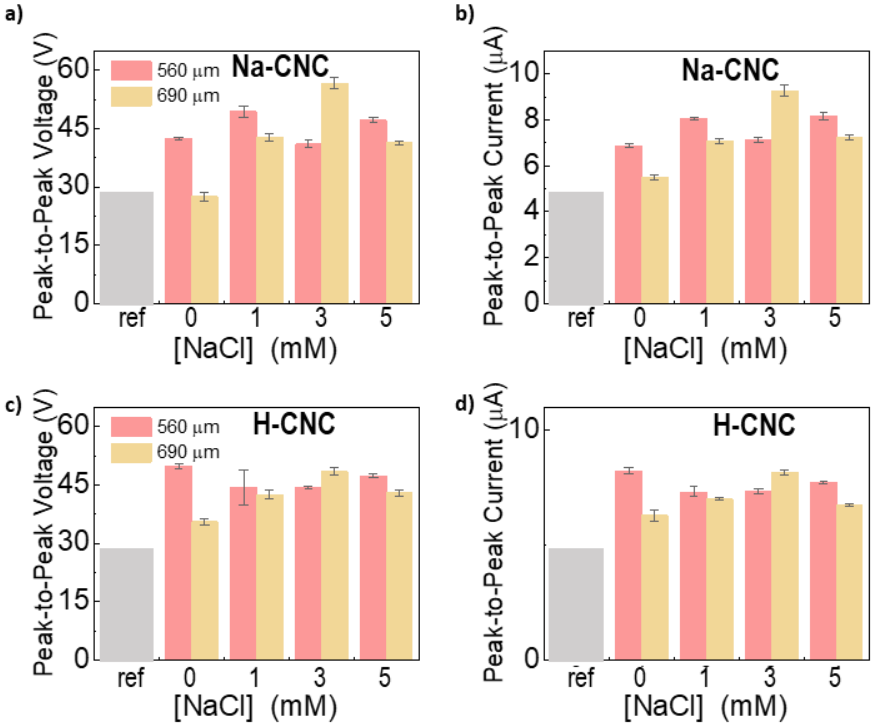

Figure 6.109 – Peak-to-peak a) voltage and b) current of Seys-TENG sets with Na-CNC interlayer and the a) voltage and c) current for H-CNC interlayers, with different thicknesses as a function of NaCl concentration. All measures were taken using PFAM at 30 N and a frequency of 2 Hz.

Several tendencies are verified when comparing the results obtained:

- Firstly, in the case of 560 µm thick Na-CNC interlayers, the addition of NaCl enhances the voltage/current output, and the highest voltage value is obtained when using low concentrations of 1 mM of NaCl.
- The addition of increasing amounts of NaCl to thicker 690 µm Na-CNC interlayers is highly beneficial to the power conversion and a maximum enhancement the voltage is encountered when adding moderate concentrations of 3 mM. This condition results in the higher voltage of all sets, with a value of 56.72 Vpp.
- The addition of NaCl to the thinner 560 µm H-CNC interlayers have barely any effect in the output of Seys-TENGs.
- Finally, adding salt is beneficial in the case of H-CNC thicker interlayers of 690 µm. Increase in NaCl concentration slowly results in the increase of the output voltage and the maximum value is obtained for a concentration of 3 mM.
- The output current follows the same trend as the voltage.

As shown by these results, there is evidence that the presence of Na-CNC or H-CNC interlayers benefits the power conversion. As a rule, thin Na-CNC and H-CNC interlayers alone (without salt addition) promote the enhancement of power conversion of Seys-TENGs, while thicker layers don't. For the last case, the addition of NaCl is beneficial and, in both thick Na-CNC and H-CNC interlayers, 3 mM was found to be the optimal salt concentration. The best results were obtained for the 690 μm thick CNC interlayer doped with 3 mM NaCl with a maximum V_{OC} and I_{SC} of 56.76 V and 9.26 μA, respectively; and for the 560 μm thick H-CNC interlayer without NaCl addition with a maximum V_{OC} and I_{SC} of 49.68 V and 8.24 μA, respectively.

Several mechanisms can be responsible for the enhancement of power conversion. The presence of an interlayer constituted by crystalline nano-structured cellulose rods rich in interfacial regions can promote additional charge induction at interfaces. The existence of sulfonated functional groups attached to the CNC's surface contributes to the dielectric enhancement. The polarization mechanisms of Na-CNC and H-CNC films were demonstrated through EIS measurements on sub-section 6.1.3 that revealed a higher capacitance for lower frequencies caused by ionic displacement and EDL formation and interfaces.

The permittivity of PDMS, Na-CNC and H-CNC membranes was calculated from the Capacitance obtained through EIS using Equation 5.21 and the correspondent value at 1000 Hz can be found in Table 6.15. This values are in accordance with the ones found in literature.[255][262] The permittivity of Na-CNC and H-CNC are superior to the PDMS, which suggests that the enhancement of power conversion may be partially attributed to this effect.

Table 6.15 – Permittivity values for the different materials constituting the Seys-TENGs.

	κ
PDMS	2.00
Na-CNC	2.29
H-CNC	5.28

Several groups have used sulfonated groups grafted to cellulose nanostructures as an additive to polymer composites to enhance the power conversion efficiency of TENGs. Peng et al.[245] obtained a 10-times-enhanced triboelectric performance by combining CNC flakes

and PDMS. Compared with its pure PDMS counterpart, CNC-PDMS composite presented higher permittivity. By grafting allicin (a sulfur rich compound found in garlic juice) onto CNFs, Roy et al.[128] was able to obtain power conversions 41 times greater than that of pure cellulose. The higher surface polarity, electron donating capacity.

The presence of sulfate functional groups on the CNCs surface can additionally promote charge trapping effects. Several authors report that charge trapping sites can be formed in functional groups attached to polymer chains.[241][242] Wang et al. [244] utilized sulphonated cellulose nanofibers as triboelectric frictional layer in TENGs. He claims that the presence of sulfonated groups increases the hole deep trap density and is responsible for the ultrahigh electrical output performance. However, to the best of the author's knowledge, the use of sulfonated CNCs as charge trap layer in TENGS has never been reported. For future work, a good idea would be to perform and compare charge decay tests between Seys-TENGs with and without CNC interlayer.

CNC based suspensions present good stability owing to the negatively charged sulfonated groups on the crystals surface. The presence of NaCl affects the ionic strength of the suspension. From literature, it was observed that adding salt in the mM concentration range reduces the absolute value of zeta potential which compromises the colloidal stability of the suspension, and ion concentrations higher than 10 mM lead to an aggregation of the particles. [263] This happens through the Na^+ counter ion adsorption in the negatively charged CNC surface. Later, the screening effect of Na^+ cations in the negatively charged sulfate groups results in a more densely packed chiral nematic structure of the subsequent films, normally perceived as a blue shifting of its reflected color in EPD films on flat substrates.[251]

Despite optical properties not being relevant to the application of CNC based films in the Seys-TENGs, they potentially provide information about the structural of the coatings. From the cross-sectional SEM images taken from the EPD films around CF yarns presented previously in Figure 6.95 it's not possible to appropriately perceive the pitch nor the distance between consecutive layers of the spindle shaped CNCs. Observing the coatings in reflection mode and using left circular polarized filters shows some iridescence. Still, once again it's hard to compare between samples owing to the irregular and rough surface of the coating.

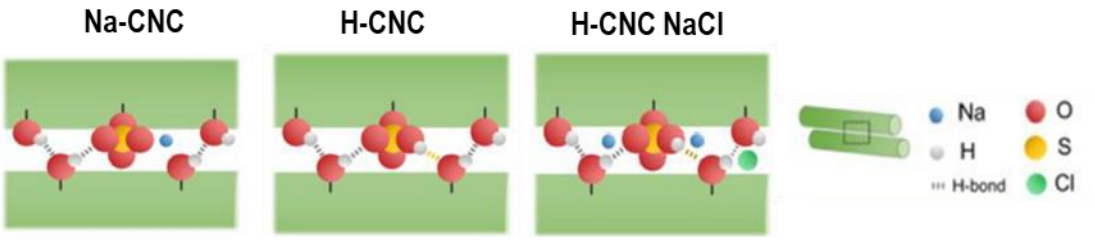

Figure 6.110 – Schematic representation of the hydrogen bonding between surface sulfate and hydroxyl groups in Na-CNC, H-CNC and H-CNC with NaCl films, as proposed by Hamad group [246]. Adapted with permission under license number 5647770171180 from Elsevier from publication [246].

Hamad group[246] reported a big enhancement of piezoelectric coefficient, with is comparable to that of PVDF, of CNC films when protonated (exchange of Na^+ for H^+) and after fine tuning with 3 mM of NaCl. They attribute this behavior to the capacity of protonated sulfate half ester groups to accept and form H-bonds, raising the net polarity and promoting highly aligned locally induced dipoles that contribute to piezoelectricity.

Throughout this project, it was not feasible to confirm the presence of a piezoelectric phenomenon in Na-CNC or H-CNC films coexisting to produce hybrid power conversion. Even if it exists, its direct contribution to enhancing power conversion would be minimal and non-uniform across the devices. This is due to the films being excessively rough, wrinkled, and even shriveled over the electrode, which hinders the alignment between the force application and the piezoelectric axis.

The presence of an ordered chiral nematic assembly in which the CNCs are disposed into layered 2D structures implies that instead of a compact material, the CNC films consist of mesoporous material that imprison amounts of air into its structure. This type of material promotes additional interfacial charge polarization.

Additionally, increased porosities and air bubbles that form during the EPD and become imprisoned inside the CNC interlayer can also contribute with additional interfacial polarization.

A limitation of this study that should be considered is the variation in the PDMS thickness. It was shown in sub-sub section 6.2.1.2 that despite the efforts to maintain this factor as constant as possible and minimize the influence of this parameter in the study, some deviations occurred that may unwillingly contribute to distort some interpretation on the results

shown. A way to avoid this would be to use molds to obtain consistent Seys-TENG diameters or PDMS thicknesses.

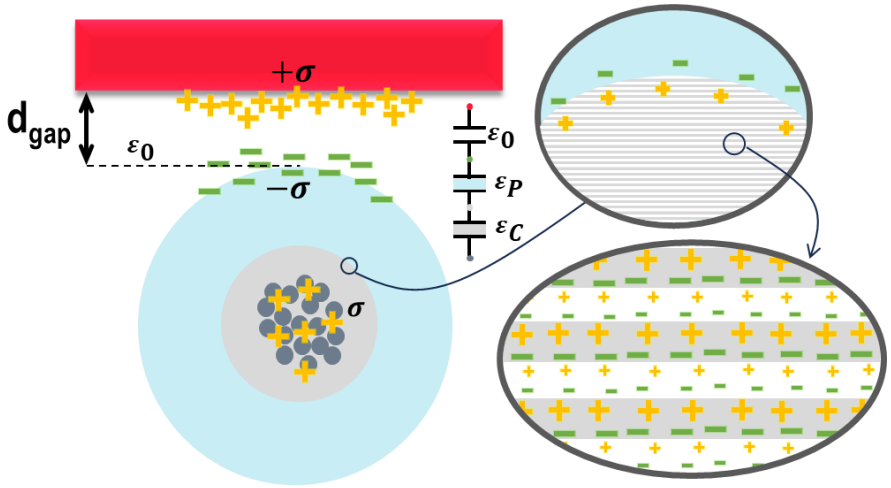

Figure 6.111 - a) Simplistic schematic representation of the cyclic mechanical tapping on Seys-TENGs using PFAM. b) Representation of the power conversion mechanisms on CNC coated Seys-TENGs, with a detail of the ionic polarization occurring on CNC/PDMS interface and CNC interlayers contributing for the enhancement of power conversion.

The best two samples of 690 μm thick Na-CNC interlayer doped with 3 mM NaCl and 560 μm thick H-CNC interlayer without salt addition, for now on addressed as Na-CNC3 and H- CNC0 were selected for additional electrical characterization tests.

The maximum power (Figure 6.112 c) and d)) was calculated after measuring the voltage and current when connecting load resistors from 100 kΩ to 200 MΩ in parallel or series, respectively, to the measuring instrument (Figure 6.112 a) and b)). While voltage increases directly with the value of the load resistors, the current decreases and the power was calculated by the product of the two. The maximum value was found when using a 20 MΩ load resistor. Interestingly, this load resistor value is inferior to that obtained for Smooth, Porous or ZnO functionalized Seys-TENGs and like the one obtained when loading the PDMS structure with 2 % wt. cCFs. The maximum power values obtained for Na-CNC3 and H-CNC0 Seys-TENGs were 276.01 and 198.14 μW, respectively which corresponds to a linear power density of 1061.58 and 762.08 μW/m, equivalent to an increase of 53 % and 10 %, respectively, when comparing with the Smooth Seys-TENGs as reference. The lower value obtained for the measurement of H-CNC0 Seys-TENG seems to contradict the initial results which foresaw a higher potential power generation. One highly likely explanation for this is the possible

contamination of the BB with glue, used to fix the Teflon and glass were used in the characterization before these measurements.

The set stability was tested by measuring V_{OC} while applying repeated impacts using PFAM at 30 N and 2 Hz during slightly more than 90 minutes (Figure 6.112 e) and f)).

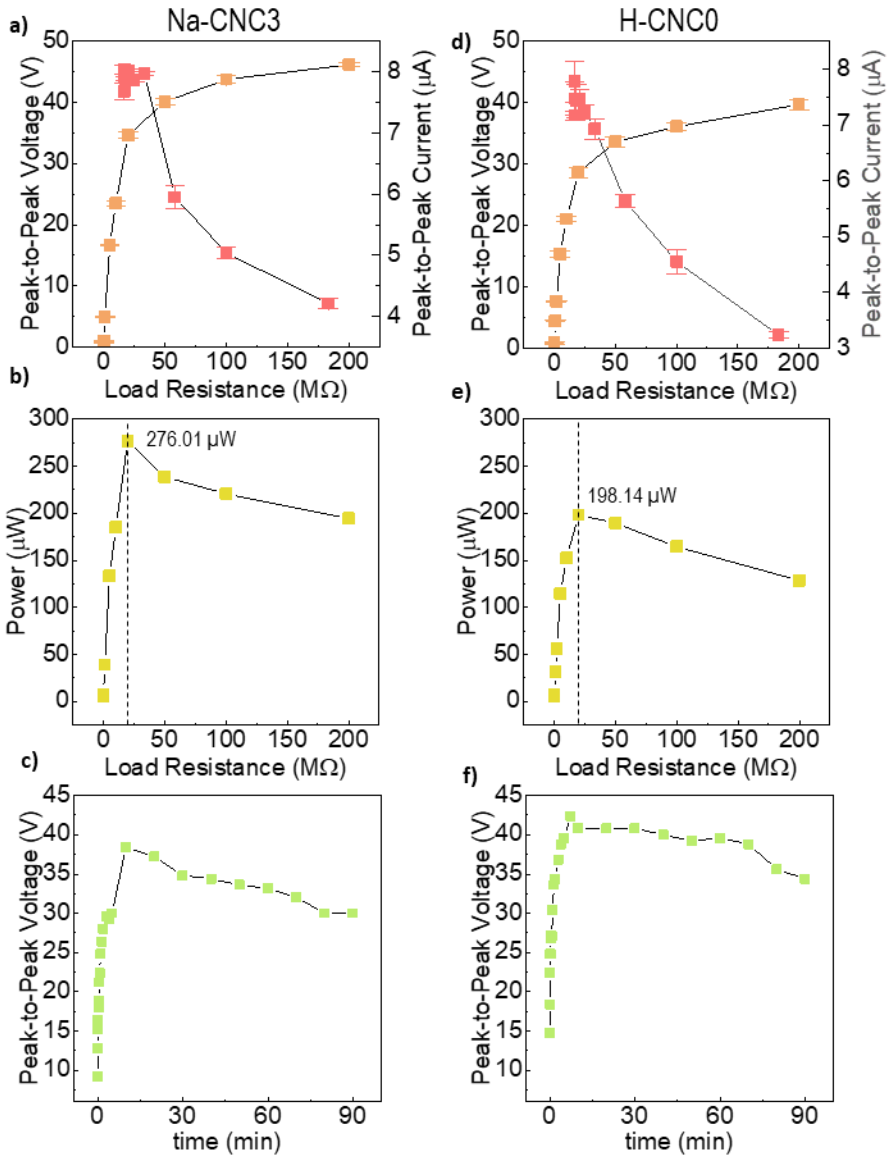

Figure 6.112 – a) Voltage and current and b) Power as a function of load resistance, and c) Voltage as a function of loading cycles of CNC3-Seys-TENG. d) Voltage and current, e) Power as a function of load resistance, and f) Voltage as a function of loading cycles of H - CNC0-Seys-TENG.

The voltage of both sets increased rapidly in the initial minutes until 10 and 7.5 min of continuous 30 N impact at 2 Hz for Na-CNC3 and H-CNC0, respectively reached a peak

voltage at 40 V. After this initial period, a decrease of voltage may be associated with some degradation phenomenon taking place at the structure of the Na-CNC interlayer. In fact, some degradation had already been noticed when the output of H- CNC Seys-TENG decreased from the initial tests while measuring the open circuit voltage and short circuit current to the final tests of the voltage and current as a function of load resistances.

The influence of the external material in the output voltage of Na-CNC3 and H-CNC0 Seys-TENGs was studied by testing the energy converters on PFAM using different materials such as Glass, Bamboo board (BB) and Teflon. The resulting output voltages are shown in Figure 6.113. The results are like those obtained for Seys-TENGs tested in the previous chapters and sections. The use of glass, a slightly less positive material[204][207][208] [209] diminishes the output voltage, while when using Teflon, an even more electronegative material than PDMS[204], the voltage peak is inverted.

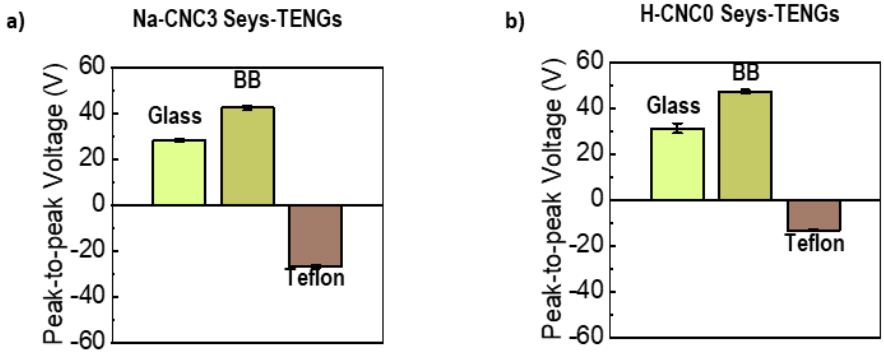

Figure 6.113 - The influence of the external material in the output voltage on the sets of a) Na-CNC3 Seys-TENGs and b) H-CNC0 Seys-TENGs.

A summary of the electrical output results obtained for the 2 %wt. cCFs Seys-TENGs is shown on Table 6.16.

Table 6.16 - Summary of the electrical output results obtained for the Na-CNC3 and H-CNC0 Seys-TENGs sets using PFAM with an impact force of 30 N at 2 Hz.

	V_{OC} [V]	I_{SC} [μA]	R_{LOAD} [MΩ]	V_{RLOAD} [V]	I_{RLOAD} [μA]	D (mm)	P_{max} [μW]	P_{max}/l [μW/m]	P_{max}/A [μW/cm²]	P_{max}/V [μW/cm³]
Na-CNC3	56.72	9.26	20	34.64	7.97	2.37	276.01	1061.58	44.79	240.64
H-CNC0	49.68	8.24	20	28.6	6.93	2.35	198.14	762.08	32.43	175.70

6.3 Conclusions

In this chapter, a CNC intercalation layer was added to the Seys-TENG structure, and its influence on the power conversion efficiency was studied. CNCs were obtained by H_2SO_4 acid hydrolysis of vegetal biomass grafted with sulfate half ester groups and the counter Na^+ ion exchanged by H^+ (Na-CNC to H-CNC). H-CNC interlayers were deposited on the CF yarn electrode using electrophoretic deposition assisted by rotation. EPD has already been used to obtain self-assembled H-CNC ordered structures on planar substrates in shorter amounts of time than the common method of evaporation assisted self-assembly. The technique was successfully adopted to 1D electrodes. The H-CNC films were deposited at the anode, forming a thick gel and then retaining the ordering after drying. It was found that during the conventional EPD the CNC-based gel would accumulate at the bottom of the CF yarn due to gravity, creating asymmetric coatings. Thus, a rotative custom-made system that consisted of rotating the CF yarn anode during the whole duration of the EPD was developed to mitigate this issue. EPD assisted by rotation resulted in symmetric films around the CF yarns anode. Seys-TENGs were prepared by the in-situ curing method using symmetric and asymmetric H – CNC as interlayer. Interestingly, the electrical results obtained from both structures were similar, regardless of the H-CNC films geometry. The EPD assisted by rotation was adopted as the standard deposition method in this work, using a fixed voltage of 15 V and a CF yarn working as the cathode.

Seys-TENs were produced using CNC based as interlayers between the CF yarn electrode and the PDMS layer. Several parameter regarding the nature of the CNC-based interlayer were investigate for their influence on power conversion efficiency, namely the interlayer thickness, the counter ion at the sulfate half-ester group (Na^+ or H^+) and the addition of varying NaCl concentrations. Throughout these studies, the PDMS thickness remained approximately constant due to in-situ curing on top of the CNC interlayer for 4 minutes.

It was discovered that thinner layers of Na-CNC and H-CNC, with a thickness of 560 μm, significantly enhanced V_{OC} and I_{SC} when incorporated into the Seys-TENGs. In contrast, thicker layers measuring 690 μm had barely any effect.

When comparing the influence of different amounts of salt addition, an enhancement on the performance was verified in the case of thicker 690 μm interlayers of both Na-CNC and H- CNC, reaching a maximum at 3 mM of NaCl, but having negligible effect on the case of thinner 560 μm interlayers.

The enhancement of Seys-TENGs power conversion was assigned to introducing Na- CNC and H-CNC as interlayers. The interlayers were responsible for and enhancement of the surface charge density owing to several phenomenon's:

- High capacitances at low frequencies, verified by EIS and promoted by the ionic displacement and formation of an EDL at interfaces.
- A higher permittivity of the interlayers (2.29 and 5.28 for Na-CNC and H-CNC, respectively, against 2 from PDMS).
- Eventually a charge trapping mechanism was promoted by the presence of a substantial number of interfacial surfaces of the Na-CNC/H-CNC and enhanced by the presence of surface functional groups at its surface. Additional charge decay tests should be performed to confirm this theory.
- Porosities between the Na-CNC and H-CNC interlayers and the CF yarn promote additional surface polarization.

Additionally, the protonated sulfate groups of H-CNC contribute with polarization owing to additional hydroxyl groups but simultaneously promote the creation of additional intermolecular hydrogen bonds that hinders this effect. The addition of 3 mM of NaCl promotes the alignment of the crystals in forming permanent dipoles, normal to the z axis of the films. Still, the high roughness, wrinkled and shriveled conformation of the coating around the CF yarn electrode makes it improbable for any piezoelectric contribution effect.

The best results were obtained for the 690 μm thick Na-CNC interlayer doped with 3 mM NaCl with a maximum V_{OC} and I_{SC} of 56.76 V and 9.26 μA, respectively; and for the 560 μm thick H-CNC interlayer without NaCl addition with a maximum V_{OC} and I_{SC} of 49.68 V and 8.24 μA, respectively. The maximum power values obtained for Na-CNC3 and H-CNC0 Seys-TENGs were 276.01 and 198.14 μW, respectively which corresponds to a linear power density of 1061.58 and 762.08 μW/m, equivalent to an increase of 53 % and10 %, respectively, when comparing with the Smooth Seys-TENGs as reference. All the electrical measurements

were performed using PFAM with a force of 30 N and frequency 2 Hz. Both Seys-TENGs withstand 10 000 cycles of stress remaining functional, however they revealed a slight degradation over its electrical performance from the 7.5-10-minute mark.

7

CONCLUSIONS AND FINAL REMARKS

This chapter aims to summarize and reflect on the work developed throughout this PhD project.

The development of 1D shaped TENGs is detrimental for using of these devices on wearable applications and using the mechanical energy of human movements as source for electrical generation. During this project, a type of Single Electrode Yarn Shaped Triboelectric Energy Nanogenerator (Seys-TENG), based on a 1D single electrode structure already existent in literature was recreated by implementing a new manufacturing technique. The Seys-TENG is constituted by a charge collector CF Yarn and a layer of Polydimethylsiloxane acting as triboelectric material for charge generation upon friction with an external material.

The new manufacturing technique consists of using the device electrode itself as the heat source enabling the cure of the thermosetting PDMS around it, by injecting an electric current of 0.2 A during a period of a maximum of 5 minutes. This innovative technique, known as in-situ curing, offers several advantages compared to the standard procedure involving silicon or acrylic molds to create coatings on 1D electrodes. It eliminates the need for custom molds with precise dimensions for the film and significantly reduces the time required to produce these devices while maintaining a reasonable level of reproducibility. The in-situ curing technique was effectively applied over a length of 6.5 cm, and it has the potential for application over longer fiber lengths, allowing for potential upscaling. This advantage places it ahead of the conventional method that employs molds.

When applying 0.2 A of current through the CF yarn submerged in the uncured PDMS slurry, the curing rate shows an approximately linear dependence on time. While the CF yarn itself reaches a temperature of over 120 °C immediately after the current application, the temperature of the PDMS near the CF yarn rises slowly from ambient (~23 °C) until 80 °C after 5 minutes. The minimum of 2 minutes of curing are necessary to electrically insulate the conductive yarn and after 5 minutes a coating with a diameter of around 2617.83 μm is obtained.

One drawback of this technique is the generation of excess waste PDMS. This could be reduced by reproducing the study on a lower volume of PDMS. The in-situ curing technique is a good option for producing faster Seys-TENGs using whole conductive fibers of yarns such as carbon based of metallic fibers. However, it may not be the optimal method for low-melting-point polymer metal-coated electrodes. In such cases, defects in the conductive layers can result in localized high current densities, potentially leading to the melting of the yarn and device failure.

The Seys-TENGs produced using the process described above are referred to as Smooth Seys-TENGs. The diameter of the PDMS layer influences their power generation. The V_{OC} (and I_{SC}) increases with the diameter, peaking at around 3 to 4 minutes of curing before gradually declining. The enhancement is led by increased surface area available for the charge generation. The decrease is due to an excessive distance from the electrode that degrades the power induction.

The electrical characterization performed in this project was uniformized by developing a pneumatic system for consistent vertical force application with adjustable intensity and frequency of impact over the sample, name PFAM. Standard electrical results are presented as the average value of the peak-to-peak voltage / current obtained when delivering an impact of 30 N of force at a frequency of 2 Hz. The Seys-TENGs were tested in sets of four connected in parallel. The external triboelectric material is a piece of Bamboo Board which tends to develop a positive charge, while PDMS develop a negative charge.

The maximum V_{OC} and I_{SC} obtained for the set of Smooth Seys-TENG obtained from an in-situ curing time of 4 minutes were 30.64 V and 5.10 μA, respectively. The maximum power of 180.67 μW was obtained using a load resistor of 50 MΩ, corresponding to a linear density of 694.88 μW/m. The mechanism of triboelectrification occurs at the surface of the PDMS, as

confirmed when switching the external triboelectric layer by Teflon (a more electronegative material than PDMS), which resulted in an inversion on the direction of current. As a comparison, Dong et al.[11] developed a device using a similar structure but using Ecoflex as triboelectric material and a 3-ply twisted stainless steel coated polyester yarn and was able to obtain a power density over one order of magnitude higher than the one obtained in this work.

Another objective of this PhD work was the implementation of diverse strategies to enhance overall power conversion efficiency. As such, number of strategies were developed, all of them aiming to increase the surface charge density, namely:

- The introduction of porosities in the PMDS structure (Porous Seys-TENG).
- The functionalization of the surface of the CFs with vertically aligned ZnO NRs.
- The simultaneously functionalization of the surface of the CFs with vertically aligned ZnO NRs and introduction of porosities in the PMDS structure
- The loading of the PDMS matrix with cCFs.
- The introduction of an additional CNC based layer between the CF yarn and PDMS.

The schematic in Figure 7.114 illustrates the different Seys-TENG developed during this project.

The introduction of porosities on the PDMS structure, also described as part of chapter 4, was done by wetting the CF yarn before the in-situ curing of PDMS, which results in evaporation of the water molecules leaving behind porosities over the PDMS. The presence of these hollow structures also prevents the PDMS from penetrating between the CFs. An overall enhancement of power generation is promoted by charging at PDMS/air interfaces inside the hollow structures that contributes to an increase of capacity of the system and results in a higher surface charge density, and by the promotion of a higher area of contact due to the softer and porous structure. The best results were obtained for the Porous sets obtained by-situ cured during 4 minutes with a value of 35.56 V and 6.72 μA of V_{OC} and I_{SC} respectively, and a maximum linear power output of 922.27 μW/m, an increase of 33 % over the Smooth Seys-TENGs. The Sets were still functioning even after 2 years of fabrication.

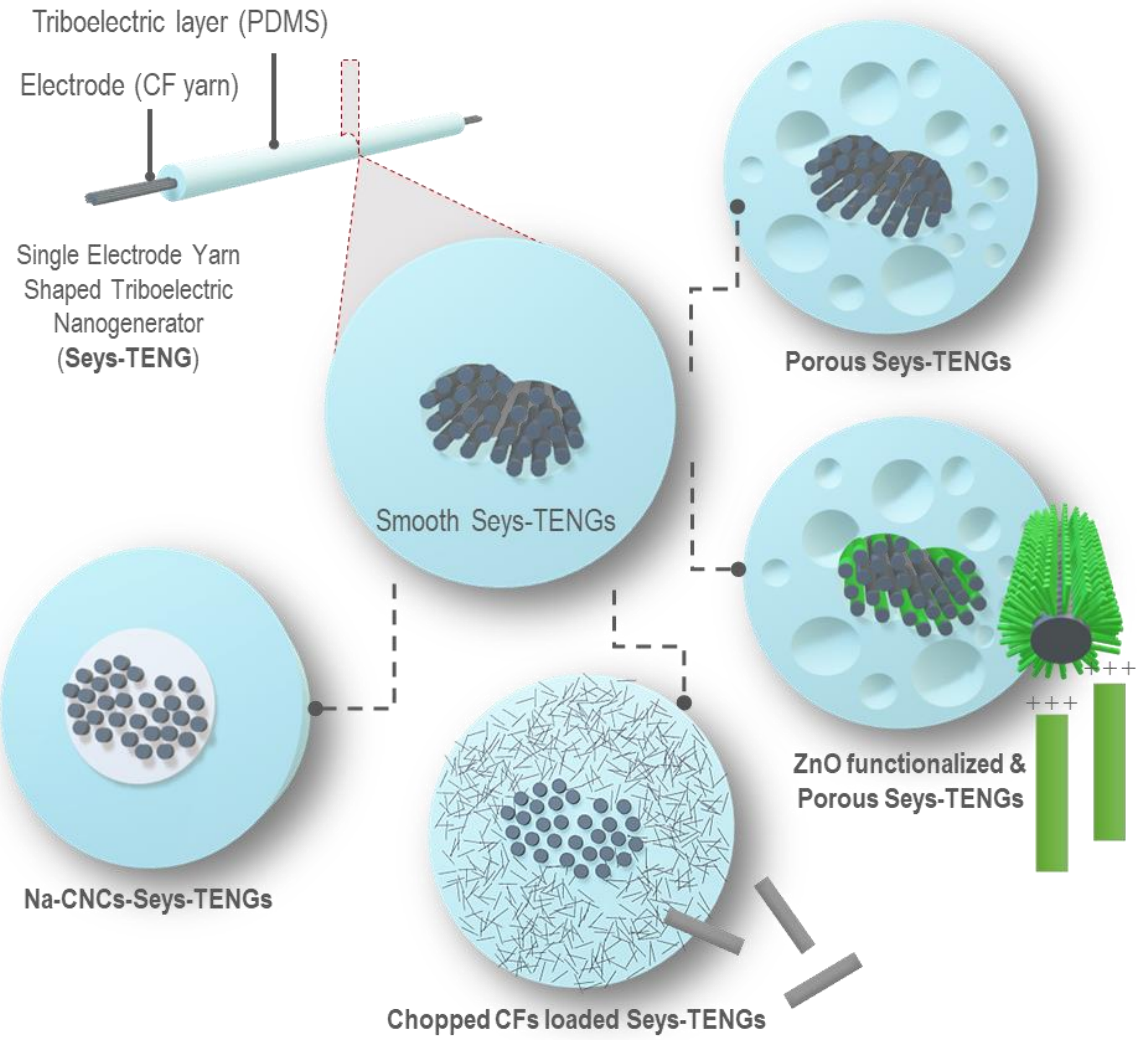

Figure 7.114 – Schematic representation of the different types of Seys-TENGs produces in this work as a summary of all the strategies applied to enhance the power conversion.

The second strategy is the functionalization of CF yarn with vertically aligned ZnO NRs, in the initial part of Chapter 5. The ZnO NRs were grown by hydrothermal synthesis using Zinc Nitrate and Hexamethylenetetramine as precursors, after an optimized 4-fold deposited step of the seed layer consisting of a Zinc Acetate solution. Vertically aligned NRs with a size range between 300 to 1000 nm of length and from 50 to 100 nm in diameter were obtained. In-situ curing of PDMS around the functionalized CF yarns consisted of obtaining a Smooth and a porous PDMS structure. SEM cross sectional images revealed a "peel-off" of the ZnO NRs from the CFs surface, while remaining impregnated into the PDMS structure. The presence of

ZnO NRs contributed to the enhancement of power generation by several factors, namely by triboelectrification of the ZnO surface and piezoelectric induction, all contributing to the increase of the surface charge generation. A maximum V_{OC} and I_{SC} values of 35.56 V and 6.72 μA of respectively were obtained for the set of ZnO NR functionalized Porous Seys-TENGs after an in-situ curing of 4 minutes. A maximum linear power output of 720.15 μW/m was obtained while using a 50 MΩ loading resistance, which corresponds to an increase of 4 % over the Smooth Seys-TENGs. Sets of ZnO NR functionalized Seys-TENGs were still functional after 10 000 cycles of impact at 600 N and after 2 years of without presenting any degradation of its electrical properties. The sets were used to power a total of 28 LEDs simultaneously by tapping with a human hand as well as charging a supercapacitor briefly power two simple electronic devices for a couple seconds.

Other strategies that are integrated in the second part of Chapter 5 consists on the loading of different proportions of cCFs in the PDMS matrix. The optimization of the loading ration was done using proportions in the range of 0.1 to 30 % wt. of PDMS. The presence of this conductive particles in the PDMS matrix results in additional mechanisms of charge induction at the interfaces between the conductive material and the PDMS which contributes towards a higher permittivity of the composite material. The best proportion was found when adding 2 %wt. of cCFs, resulting in Seys-TENGs with a V_{OC} and I_{SC} of 58.16 V and 9.46 μA respectively. Higher loadings resulted in a degradation of the electrical properties derived from the enhanced conductivity of the composite. A maximum linear power density of 1063.23 μW/m was obtained while using a 20 MΩ load resistor, which corresponds to an enhancement of 53 % compared with the Smooth Seys-TENG as reference. After 10 000 impact cycles the set was still functional without visible signs of energy conversion degradation however, when weaved into a textile structure and a 37.77% reduction of output voltage. The application of 2 %wt. cCFs Seys-TENGs as plantar foot sensors for the gait pattern analysis was successfully demonstrated by top stitching individual Seys-TENGs at the bottom of a sportive sock.

The last strategy utilized to enhance the power conversion efficiency of Seys-TENGs was the introduction of a CNC based layer between the CF yarn and the PDMS, described in Chapter 6. The CNC suspensions were deposited by EPD but using a modification to the conventional technique that applies rotation during the deposition and promotes a uniform coating

over the CF yarn, denominated EDP assisted by rotation. The anodic EPD assisted by rotation consisted of the application of 15 V between two CF yarns working as the anode and cathode distanced by 8 mm. Two types of suspensions were used, one consisting of the raw CNC using Na^+ as a counter ion (Na-CNC) and the second consisting of a protonated form in which H+ exchanged the counter ion exchanged the counter ion exchanged the counter ion (H-CNC). Additionally, different NaCl concentrations were added to the suspensions: 1, 3 and 5 mM. The presence of such intercalated CNC based layers can promote the enhancement of the Seys-TENGs power conversion due to the ionic displacement at low frequencies, an enhanced permittivity of this films, charge induction and interfaces of the nanostructured films, charge trapping owing the presence of sulfur half ester groups and to the presence of permanent dipoles in the case of H-CNC at 3 mM. Additional porosities between the Na-CNC and H-CNC interlayers and the CF yarn promote additional surface polarization. The best results were obtained for the 690 μm thick Na-CNC interlayer doped with 3 mM NaCl with a maximum V_{OC} and I_{SC} of 56.76 V and 9.26 μA, respectively; and for the 560 μm thick H-CNC interlayer without NaCl addition with a maximum V_{OC} and I_{SC} of 49.68 V and 8.24 μ, respectively. The maximum power values obtained for Na-CNC3 and H-CNC0 Seys-TENGs were 276.01 and 198.14 μW, respectively which corresponds to linear power densities of 1061.58 and 762.08 μW/m, equivalent to an increase of 53 % and 10 %, respectively, when comparing with the Smooth Seys-TENGs as reference.

A summary of the results obtained using all the different Seys-TENG developed during this project is presented in Table 7.17.

In terms of power conversion, the most effective strategies utilized in this PhD to enhance the electrical properties of the Seys-TENG were the loading of the PDMS matrix with 2 % wt. of chopper CFs as well as the introduction of a Na-CNC + 3 mM NaCl interlayer in the device structure. It is worth noting that while both of these strategies resulted in similar enhancements of the power conversion, the simple fabrication process of loading the matrix with conductive particles, as well as the affordable price of chopped CFs, makes the use of this strategy more advantageous in practical terms. A comparison of the linear power obtained for the different Seys-TENGs developed in this work is presented in Figure 7.115

Table 7.17 – Summary of the parameters obtained for all Seys-TENGs studied in this work including four possible forms to normalize the electrical power output: the power per length unit (P/l - μW/m), the power per unit of area, where A1 is the minimum area when the Seys-TENGs are incorporated into a textile structure and A2 is the effective area of contact with the external load (P/A1/2 - μW/cm2) and the power density (P/V - μW/cm3).

	$P_{máx}$ (μW)	R_{Load} (MΩ)	$V_{máx}(R_{Load})$ (Vpp)	$I_{max}(R_{load})$ (Ipp-μA)	V_{OC} (Vpp)	I_{SC} (Ipp-μA)	P/l (μW/cm)	P/A (μW/cm²)	P/V (μW/cm³)
Smooth	180.67	50	34.96	5.17	30.64	5.10	694.89	33.90	210.53
Porous	239.79	50	37.28	6.43	35.56	6.72	922.27	40.81	229.91
ZnO Smooth	98.56	50	24.64	4.00	32.00	5.55	379.08	14.87	74.23
ZnO Porous	187.24	50	32.92	5.69	46.8	8.34	720.15	28.35	142.12
2 %wt. cCF	276.44	20	35.92	7.70	58.16	9.46	1063.23	49.22	290.16
Na-CNC-3mM	276.01	20	34.64	7.97	56.72	9.26	1061.58	44.79	240.64
H-CNC	198.14	20	28.60	6.93	49.68	8.24	762.08	32.43	175.70

A limitation of this study is the variation in diameter when using the in-situ curing technique to obtain PDMS layers. Although this doesn't pose a problem when creating the devices, it could complicate the interpretation of results when considering other variables. The analyses in this research introduced a single variable for study while assuming all other variables remained constant, including the PDMS diameter. As this is not the case, this could lead to added errors associated with the study.

A particular concern within this study is the possibility that practical errors may have influenced the electric power results obtained for the sets of ZnO NR functionalized Smooth Seys-TENGs and the H-CNC interlayered Seys-TENGs. The error involved the contamination of the bamboo board used as an external triboelectric layer with glue. This occurred while testing the effect of other types of materials (which were fixed using double-sided tape and glue) before measuring the power as a function of loading for those specific samples. This contamination impacted the results, causing them to be lower than expected. This might result in the misinterpretation that adding ZnO NRs degrades the power conversion of the Seys-TENGs which was not what was verified in the same set of samples prepared in the past and tested using GFAM.

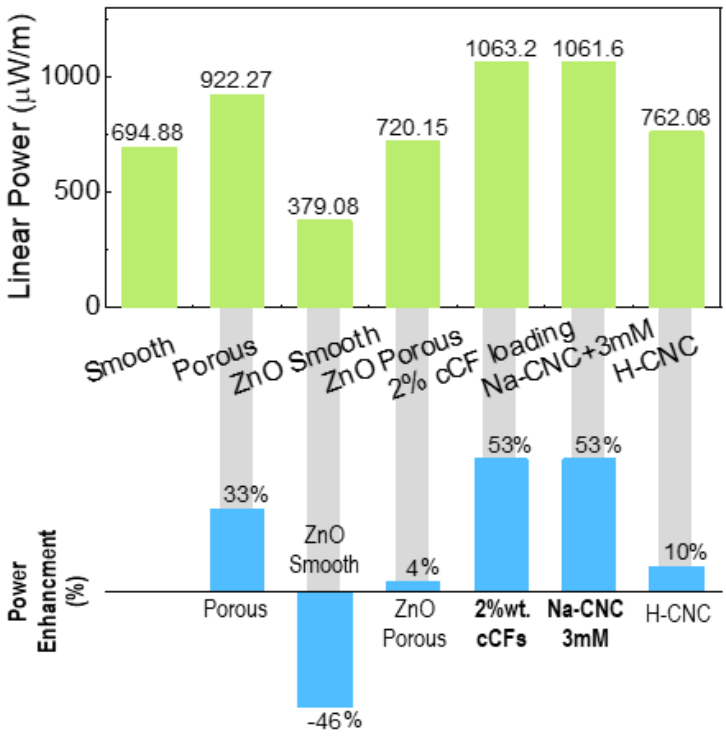

Figure 7.115 – Comparison between the absolute (μW/m) and relative (%) linear output of the different Seys-TENGs developed in this work.

In Figure 7.116 the results obtained from the literature for 1D fiber or yarn shaped TENGs with various structures (SE, CS, or CxS) that incorporate a silicone elastomer (primarily PDMS and Ecoflex) as at least one of their triboelectric layers are presented.

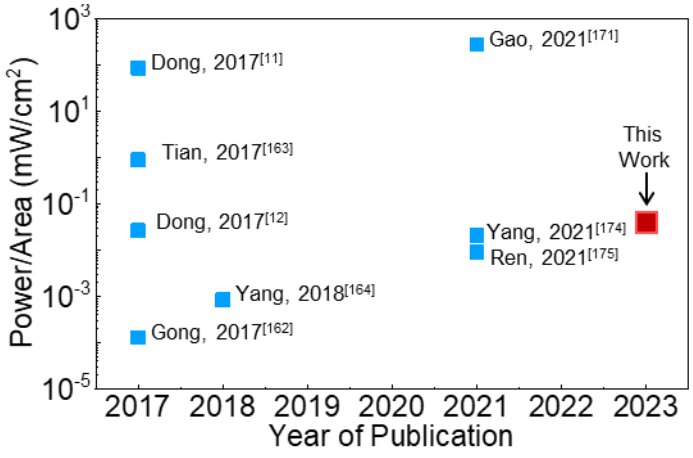

Figure 7.116 – Comparison of power output of several works utilizing yarn or fiber based TENGs and silicone elastomers (mainly PDMS or Ecoflex) as one of the triboelectric layers with the maximum power obtained in the present work with the 2 % wt. cCFs loaded Seys-TENG. [11] [12] [163] [164] [165] [172] [175] [176]

When compared with the state-of-the-art devices, the 2% wt. cCFs loaded Seys-TENG, the best-performing device developed in this study, ranks as the 4th best out of a total of 9 devices. It's worth emphasizing that, in comparison to the top three-ranked devices, this Seys-TENG has certain advantages. It features a simple single electrode structure and uses fewer raw materials.[172] It was tested under a relatively low force of 30 N [172]. It was prepared using a less complex procedure than the traditional method of depositing PDMS around the conductive material using molds [11]. Additionally, it has a lower overall density as it is free from metal and plastic components. [164]

The value of energy efficiency encountered for the best Seys-TENG device dopped with 2 % wt. cCFs was $\boldsymbol{\eta \sim 0.012}$ % (Appendix A.4). However, since the value of mechanical energy utilized is underestimated, the real energy efficacy value should be lower than the one obtained. It is realized that a tremendous amount of energy dissipation is taking place at the system since most of the mechanical energy is not being converted to electric energy. However, it should also be noted that these types of devices are developed for applications where they should utilize "wasted" energy or mechanical energy that is already existing and not being processed. From this point of view, even such low conversion efficiency can be beneficial.

7.1 Future perspectives

Time limitations constrain this PhD project, and as a result, many more experiments and studies could be conducted. The analysis of the results has also raised further questions. Therefore, some suggestions for future research are provided below.

Regarding chapter 4:

- Reproduce the study of in-situ curing of PDMS using a lower volume of PDMS to reduce waste.
- Use stainless steel yarn as electrodes for the in-situ curing of PDMS.
- Compare the performance of the Seys-TENG obtained though the in-situ curing of PDMS with similar devices prepared using molds and cured either at room temperature or at various temperatures and times.
- Test the in-situ curing method over longer fiber lengths as a step towards upscaling.

Regarding chapter 5:

- Study the incorporation of other types of conductive particles with small dimensions in the nanometer range within the PDMS matrix.
- Study the incorporation of semiconducting ZnO NR and high k metal oxides (SiO_2, TiO_2, Al_2O_3, etc.) into the PDMS matrix.
- Combine the incorporation of conductive/semiconducting/high k particles with porosities.
- Utilize a greater number of individual Seys-TENGs for prototyping a gait sensor.

In November 2022, a one-month exchange took place at the Fraunhofer IKTS Institute in Dresden with the aim of conducting measurements on the piezoelectric effects of ZnO NRs. The samples were prepared by depositing a four-fold seed layer solution on a CF yarn, from

which a single CF fiber was removed and fixed to an Au-coated glass substrate (Figure 7.117 a)). The sample was then placed in a glass beaker with a precursor solution to promote the hydrothermal growth of aligned ZnO NRs (Figure 7.117 b)). The measurements were carried out using a Nanomechanical TI 950 Triboindenter from IKTS facilities, along with an electrically conductive CubeCorner tip (Synton-MDP, HST/CUBECORNER/050/EL). Electrical connections were established, with one end of an electrically conductive wire attached to the magnetic sample holder using silver glue, and the other end secured to the lateral side of the nano indenter tip using conductive silver glue (Figure 7.117 c)). A ground connection was set up by attaching one end of an electrical conductive wire to the metallic stage inside the nanoindenter using copper tape, with the other end guided outside the chamber (Figure 7.117 d)). Both ends of the electrical wires outside the chamber were connected to a FLUKE 289 TRUE RMS multimeter with the Ohmic function selected. During an indentation test, an error consistently appeared on the screen during the transducer check routine before the indentation, resulting in the software's abrupt termination.

It was concluded that when the multimeter was connected to the tip in Ohmic measuring mode, an electrical current was being injected through the tip to the transducer, in direct contact with the moving capacitor plate, which should be causing the error. During the brief exchange period, the issue could not be resolved. However, a potential solution was proposed to address this problem. The solution involved using a nonconductive tip instead of a conductive one, with a thin layer of metal sputtered on half of the tip, ensuring no contact with the transducer plates.

An additional suggestion is replacing the FLUKE 289 TRUE RMS multimeter with an alternative measuring unit. The change is suggested because the FLUKE 289's data logging capabilities are limited and event based. Using an instrument capable of seamless data logging may be more effective.

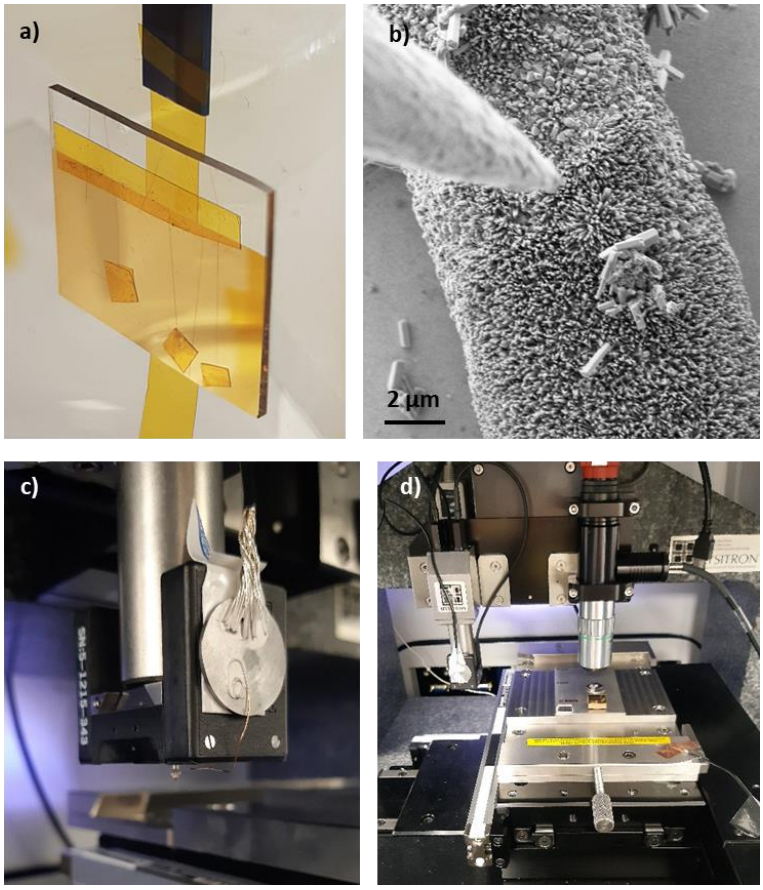

Figure 7.117 – a) Single CFs aligned and fixed to a Au coated glass substrate using kapton tape and b) SEM image of the hydrothermally grown ZnO NRs. c) The electrical connection effectuated at the tip of the nanoindenter and d) overview of the interior of the nanoindenter chamber with the electrical connections on the tip and on the electrically grounded stage and sample mounting.

Regarding chapter 6:

- Use molds to maintain the diameter of PDMS unaltered while studying the influence of other parameters on the performance of Seys-TENGs.
- Preparation of thicker layers of CNC and H-CNC as interlayer in Seys-TENGs and comparison with the existent results.
- Combine the incorporation of the interlayer with incorporation of porosities in the PDMS structure by performing the in-situ curing of the PDMS before drying the gel. Investigate if this procedure would destroy the self-assembly of the CNCs.
- Perform charge retention measurements to investigate the presence of a charge trapping mechanism.

- Perform K-PFM measurements of Na and H-CNC based films to determine the presence of piezoelectric phenomenon.

Some drawbacks from using CF are the vast amounts of energy employed in the CFs manufacturing process, which is also associated with high costs. From this perspective, a pertinent question that arises in a world where climatic urgency is at the top of our society's main interest is this: will this technology ever be carbon neutral, producing more energy than the one spent on the manufacturing process?

The possibility of using recycled CF should be considered for its utilization leads to energy savings. The common drawback concerning degradation of tensile strength may not be an issue in this application since high mechanical performance is not the main goal. The use of CFs in the yarn form would not be possible when fibers are recycled, however, tows would also work if the number of fibers remain somewhat consistent, and this could be an interesting starting point for future investigation. Additionally, the use of CFs originated from renewable sources such as lignin or cellulose could be another interesting possibility. Concerning the best performing device produced in this work used cCFs mixed in the PDMS matrix. Yet, another strategy to reduce environmental impact would be the use of cCFs prevenient of damaged recycled CFs or the production of CFs from textile waste.

In addition to the primary focus of this dissertation, some work unrelated to the main research was conducted during a 3-month internship at the Textile Research Institute of Thuringia-Vogtland (TITV) in Greiz. This work involved the development of functionalized conductive yarns, both at the laboratory scale and on a pilot scale, and their integration into a textile structure through weaving at the Textile Prototyping Lab (TPL) in Berlin. To create these functionalized yarns, CF yarns and silver-coated polyamide yarns (Shieldex) were used as the conductive core elements. They were functionalized through a coating process using Polyacrylonitrile (PAN, from Sigma Aldrich) and Mowiol (a water-soluble hydrocolloid based on poly(vinyl alcohol), also from Sigma Aldrich). PAN was used as the triboelectric negative material, while Mowiol was chosen as the triboelectric positive material, based on their positions in the triboelectric series. These materials were previously dissolved at 7 % wt. in

Dimethylformamide (DMF) and at 15 % wt. in boiling ultrapure water, respectively. The coating process was initiated using a custom-made continuous apparatus developed in collaboration with the chemical lab of TITV, as shown in Figure 7.118 a). This setup was adapted to work with a pilot-scale rotative drying oven. Alternatively, a pilot-scale modular coating unit was employed (Figure 7.118 b)). Approximately 100 meters of yarn were functionalized using this technique. Once functionalized, the yarns were taken to TPL, where they were woven on a Jacquard loom, as depicted in Figure 7.118 c). The weaving was done in a plain weave pattern and various other patterns. However, one challenge encountered during weaving was the brittleness of the functionalized CF yarns, resulting in broken fibers. To address this issue, the best solution was to cut segments of the thread and weave without bending the yarn. The functionalized yarns were laterally rinsed with the appropriate solvent (DMF or water) to expose the conductive yarns and electrically connected using cupper tape (Figure 7.118 g)). Swatches were then tested by sliding one negative triboelectric layer against another positive triboelectric layer. But the output produced was quite low. This was partially attributed to a low surface area caused by the stiffness of the functionalized CF threads. When a stiffer yarn is incorporated into a woven structure, it doesn't experience enough tension to curl and conform. Instead, the adjacent softer threads tend to wrap around it, creating upper and lower layers. These layers will be the ones suffering friction when sliding de swatches. Another problem derived from these stiff functionalized yarns is while handling the yarn it can easily suffer a fracture which compromises the electrical conduction. The stiffness issue was due to the increased number of polymer layers required to electrically insulate the CF yarn, which amounted to six layers.

In the case of the functionalized Shieldex yarn, the yarn was considerably softer and easier to handle. However, assessing the conductive yarns using the rinsing technique was problematic because attempting to remove the functional layer often led to the destruction of both the functional layer and the conductive layer. It became impossible to perform electrical testing.

As a suggestion for future work, it may be more beneficial to utilize CFs in the form of tows rather than yarns, as a smoother surface requires fewer layers and results in less stiffness.

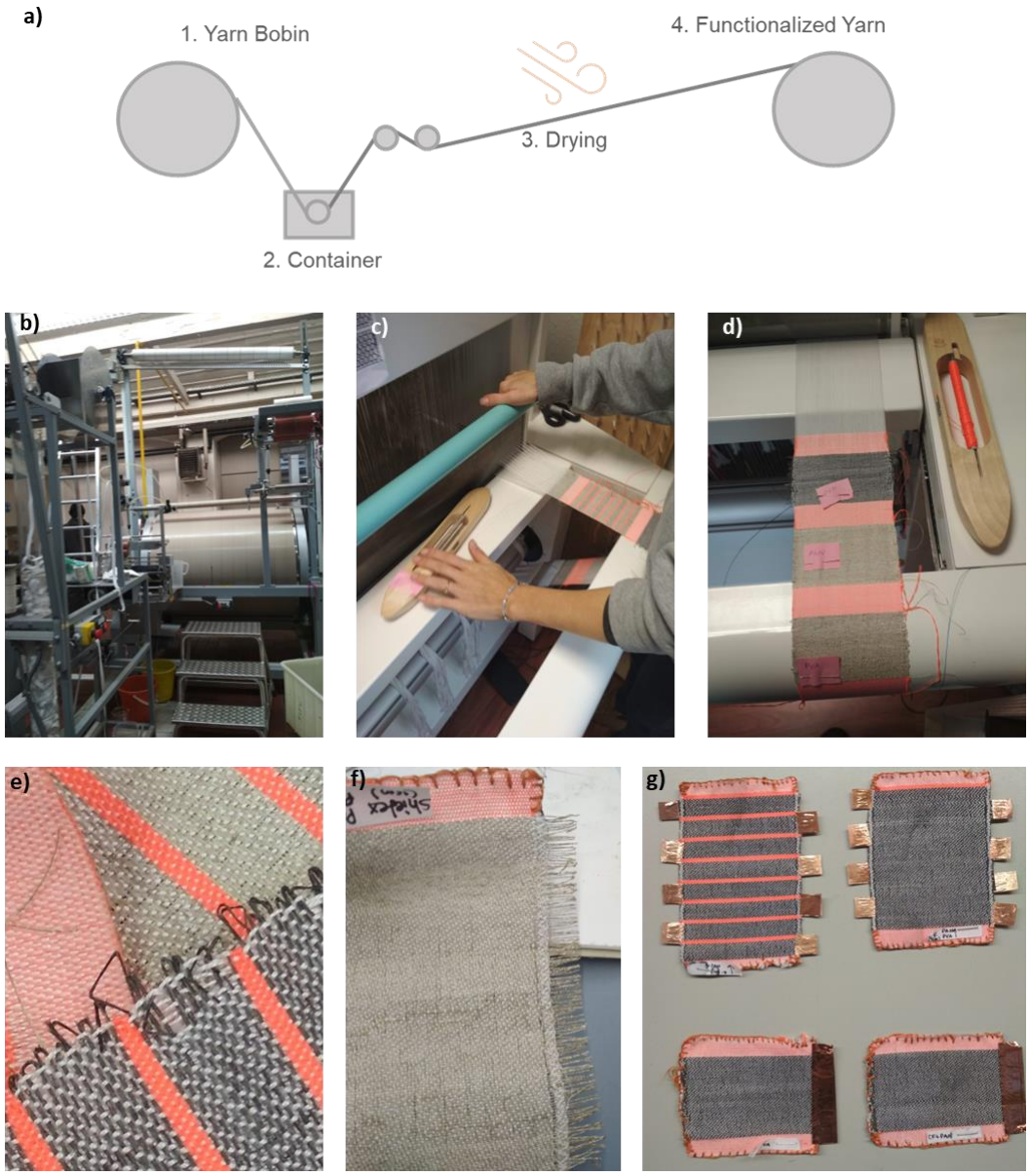

Figure 7.118 – a) Schematic representation of the continuous coating apparatus assembled for the functionalization of yarns and b) pilot scale modular coating unit at TITV used for the functionalization of yarns. c) Weaving the functionalized yarns using the jacquard loom at TPL and d) one swatch of the weaved functionalized textile. e) Detail of brittleness of functionalized CF yarns when weaved and f) Shieldex functionalized yarns. g) Swatches produced using different patterns and electrically connected using cupper tape.

REFERENCES

[1] Precedence Research, "Wearable Technology Market," 2023. https://www.precedenceresearch.com/wearable-technology-market (accessed Feb. 01, 2023).

[2] X. Cui, H. Wu, and R. Wang, "Fibrous triboelectric nanogenerators: fabrication, integration, and application," *J. Mater. Chem. A*, vol. 10, no. 30, pp. 15881–15905, 2022, doi: 10.1039/D2TA03813G.

[3] F.-R. Fan, Z.-Q. Tian, and Z. Lin Wang, "Flexible triboelectric generator," *Nano Energy*, vol. 1, no. 2, pp. 328–334, Mar. 2012, doi: 10.1016/j.nanoen.2012.01.004.

[4] X. Pu, C. Zhang, and Z. L. Wang, "Triboelectric nanogenerators as wearable power sources and self-powered sensors," *Natl. Sci. Rev.*, vol. 10, no. 1, Jan. 2023, doi: 10.1093/nsr/nwac170.

[5] A. dos Santos *et al.*, "E-Skin Pressure Sensors Made by Laser Engraved PDMS Molds," *Proceedings*, vol. 2, no. 13, p. 1039, Nov. 2018, doi: 10.3390/proceedings2131039.

[6] A. Dos Santos *et al.*, "E-skin bimodal sensors for robotics and prosthesis using PDMS molds engraved by laser," *Sensors (Switzerland)*, vol. 19, no. 4, p. 899, Feb. 2019, doi: 10.3390/s19040899.

[7] B. Y. Lee, D. H. Kim, J. Park, K. Il Park, K. J. Lee, and C. K. Jeong, "Modulation of surface physics and chemistry in triboelectric energy harvesting technologies," *Sci. Technol. Adv. Mater.*, vol. 20, no. 1, pp. 758–773, Dec. 2019, doi: 10.1080/14686996.2019.1631716.

[8] S. Jang and J. H. Oh, "Rapid Fabrication of Microporous BaTiO3/PDMS

Nanocomposites for Triboelectric Nanogenerators through One-step Microwave Irradiation," *Sci. Rep.*, vol. 8, no. 1, p. 14287, Dec. 2018, doi: 10.1038/s41598-018-32609-6.

[9] Z. Tian *et al.*, "Core-shell coaxially structured triboelectric nanogenerator for energy harvesting and motion sensing," *RSC Adv.*, vol. 8, no. 6, pp. 2950–2957, 2018, doi: 10.1039/c7ra12739a.

[10] K. Kim, G. Song, C. Park, and K. S. Yun, "Multifunctional woven structure operating as triboelectric energy harvester, capacitive tactile sensor array, and piezoresistive strain sensor array," *Sensors (Switzerland)*, vol. 17, no. 11, p. 2582, Nov. 2017, doi: 10.3390/s17112582.

[11] K. Dong *et al.*, "A Highly Stretchable and Washable All-Yarn-Based Self-Charging Knitting Power Textile Composed of Fiber Triboelectric Nanogenerators and Supercapacitors," *ACS Nano*, vol. 11, no. 9, pp. 9490–9499, Sep. 2017, doi: 10.1021/acsnano.7b05317.

[12] K. Dong *et al.*, "3D Orthogonal Woven Triboelectric Nanogenerator for Effective Biomechanical Energy Harvesting and as Self-Powered Active Motion Sensors," *Adv. Mater.*, vol. 29, no. 38, p. 1702648, Oct. 2017, doi: 10.1002/adma.201702648.

[13] A. Pimentel *et al.*, "Effect of solvents on ZnO nanostructures synthesized by solvothermal method assisted by microwave radiation: a photocatalytic study," *J. Mater. Sci.*, vol. 50, no. 17, pp. 5777–5787, Sep. 2015, doi: 10.1007/s10853-015-9125-7.

[14] S. H. Ferreira *et al.*, "High UV and sunlight photocatalytic performance of porous ZnO nanostructures synthesized by a facile and fast microwave hydrothermal method," *Materials (Basel).*, vol. 14, no. 9, 2021, doi: 10.3390/ma14092385.

[15] D. Kaur, A. Bharti, T. Sharma, and C. Madhu, "Dielectric Properties of ZnO-Based Nanocomposites and Their Potential Applications," *Int. J. Opt.*, vol. 2021, pp. 1–20, Jul. 2021, doi: 10.1155/2021/9950202.

[16] X. Xia *et al.*, "Embedding variable micro-capacitors in polydimethylsiloxane for enhancing output power of triboelectric nanogenerator," *Nano Res.*, vol. 10, no. 1, pp. 320–330, Jan. 2017, doi: 10.1007/s12274-016-1294-4.

[17] M. P. Kim, D.-S. Um, Y.-E. Shin, and H. Ko, "High-Performance Triboelectric Devices via Dielectric Polarization: A Review," *Nanoscale Res. Lett.*, vol. 16, no. 1, p. 35, Dec. 2021, doi: 10.1186/s11671-021-03492-4.

[18] D. Klemm, B. Heublein, H.-P. Fink, and A. Bohn, "Cellulose: Fascinating Biopolymer and Sustainable Raw Material," *Angew. Chemie Int. Ed.*, vol. 44, no. 22, pp. 3358–3393, May 2005, doi: 10.1002/anie.200460587.

[19] N. Anusha, B. P. Kumar, and L. Agarwal, "Study on Recent Trends of Smart Wearable," in *2022 2nd International Conference on Artificial Intelligence and Signal Processing (AISP)*, IEEE, Feb. 2022, pp. 1–5. doi: 10.1109/AISP53593.2022.9760637.

[20] V. Patel, A. Chesmore, C. M. Legner, and S. Pandey, "Trends in Workplace Wearable Technologies and Connected-Worker Solutions for Next-Generation Occupational Safety, Health, and Productivity," *Adv. Intell. Syst.*, vol. 4, no. 1, p. 2100099, Jan. 2022, doi: 10.1002/aisy.202100099.

[21] J. E. Mück, B. Ünal, H. Butt, and A. K. Yetisen, "Market and Patent Analyses of Wearables in Medicine," *Trends Biotechnol.*, vol. 37, no. 6, pp. 563–566, Jun. 2019, doi: 10.1016/j.tibtech.2019.02.001.

[22] H. Akinaga, "Recent advances and future prospects in energy harvesting technologies," *Jpn. J. Appl. Phys.*, vol. 59, no. 11, p. 110201, Nov. 2020, doi: 10.35848/1347-4065/abbfa0.

[23] J. Mandel JS, Bond, "The Effect of Intensive Treatment of Diabetes on the Development and Progression of Long-Term Complications in Insulin-Dependent Diabetes Mellitus," *N. Engl. J. Med.*, vol. 329, no. 14, pp. 977–986, Sep. 1993, doi: 10.1056/NEJM199309303291401.

[24] N. A. ElSayed *et al.*, "7. Diabetes Technology: Standards of Care in Diabetes —

2023," *Diabetes Care*, vol. 46, no. Supplement_1, pp. S111–S127, Jan. 2023, doi: 10.2337/dc23-S007.

[25] "No Title," 2023. https://www.bccresearch.com/market-research/healthcare/continuous-glucose-monitoring-cgm-technology-markets-report.html (accessed Oct. 04, 2023).

[26] A. Mayyas, D. Steward, and M. Mann, "The case for recycling: Overview and challenges in the material supply chain for automotive li-ion batteries," *Sustain. Mater. Technol.*, vol. 19, p. e00087, Apr. 2019, doi: 10.1016/j.susmat.2018.e00087.

[27] E. Comission, "2030 Climate Target Plan." https://climate.ec.europa.eu/eu-action/european-green-deal/2030-climate-target-plan_en

[28] B. E. Murdock, K. E. Toghill, and N. Tapia-Ruiz, "A Perspective on the Sustainability of Cathode Materials used in Lithium-Ion Batteries," *Adv. Energy Mater.*, vol. 11, no. 39, p. 2102028, Oct. 2021, doi: 10.1002/aenm.202102028.

[29] S. Lee and A. Manthiram, "Can Cobalt Be Eliminated from Lithium-Ion Batteries?," *ACS Energy Lett.*, vol. 7, no. 9, pp. 3058–3063, Sep. 2022, doi: 10.1021/acsenergylett.2c01553.

[30] N. J. Boxall, S. King, K. Y. Cheng, Y. Gumulya, W. Bruckard, and A. H. Kaksonen, "Urban mining of lithium-ion batteries in Australia: Current state and future trends," *Miner. Eng.*, vol. 128, no. August, pp. 45–55, Nov. 2018, doi: 10.1016/j.mineng.2018.08.030.

[31] M. Azevedo, N. Campagnol, T. Hagenbruch, K. Hoffman, A. Lala, and O. Ramsbottom, "Lithium and cobalt-a tale of two commodities," *McKinsey&Company Met. Min.*, no. June, pp. p1-25, 2018, [Online]. Available: https://www.mckinsey.com/~/media/mckinsey/industries/metals and mining/our insights/lithium and cobalt a tale of two commodities/lithium-and-cobalt-a-tale-of-two-commodities.ashx

[32] K.-E. Byun, M.-H. Lee, Y. Cho, S.-G. Nam, H.-J. Shin, and S. Park, "Potential role

of motion for enhancing maximum output energy of triboelectric nanogenerator," *APL Mater.*, vol. 5, no. 7, Jul. 2017, doi: 10.1063/1.4979955.

[33] L. Manjakkal, L. Yin, A. Nathan, J. Wang, and R. Dahiya, "Energy Autonomous Sweat-Based Wearable Systems," *Adv. Mater.*, vol. 33, no. 35, Sep. 2021, doi: 10.1002/adma.202100899.

[34] C. Xu, Y. Song, M. Han, and H. Zhang, "Portable and wearable self-powered systems based on emerging energy harvesting technology," *Microsystems Nanoeng.*, vol. 7, no. 1, p. 25, Mar. 2021, doi: 10.1038/s41378-021-00248-z.

[35] J. Figueira *et al.*, "Screen-printed, flexible, and eco-friendly thermoelectric touch sensors based on ethyl cellulose and graphite flakes inks," *Flex. Print. Electron.*, vol. 8, no. 2, p. 025001, Jun. 2023, doi: 10.1088/2058-8585/acc114.

[36] Z. Tabaie and A. Omidvar, "Human body heat-driven thermoelectric generators as a sustainable power supply for wearable electronic devices: Recent advances, challenges, and future perspectives," *Heliyon*, vol. 9, no. 4, p. e14707, Apr. 2023, doi: 10.1016/j.heliyon.2023.e14707.

[37] R. Feng, F. Tang, N. Zhang, and X. Wang, "Flexible, High-Power Density, Wearable Thermoelectric Nanogenerator and Self-Powered Temperature Sensor," *ACS Appl. Mater. Interfaces*, vol. 11, no. 42, pp. 38616–38624, Oct. 2019, doi: 10.1021/acsami.9b11435.

[38] L. Huang, Y. Zheng, L. Xing, and B. Hou, "Recent progress of thermoelectric applications for cooling/heating, power generation, heat flux sensor and potential prospect of their integrated applications," *Therm. Sci. Eng. Prog.*, vol. 45, no. August, p. 102064, Oct. 2023, doi: 10.1016/j.tsep.2023.102064.

[39] Y. Zou, L. Bo, and Z. Li, "Recent progress in human body energy harvesting for smart bioelectronic system," *Fundam. Res.*, vol. 1, no. 3, pp. 364–382, May 2021, doi: 10.1016/j.fmre.2021.05.002.

[40] A. S. Khan and F. U. Khan, "A survey of wearable energy harvesting systems,"

Int. J. Energy Res., vol. 46, no. 3, pp. 2277–2329, Mar. 2022, doi: 10.1002/er.7394.

[41] T. Wu, F. Wu, J.-M. Redoute, and M. R. Yuce, "An Autonomous Wireless Body Area Network Implementation Towards IoT Connected Healthcare Applications," *IEEE Access*, vol. 5, pp. 11413–11422, 2017, doi: 10.1109/ACCESS.2017.2716344.

[42] A. E. Ostfeld and A. C. Arias, "Flexible photovoltaic power systems: integration opportunities, challenges and advances," *Flex. Print. Electron.*, vol. 2, no. 1, p. 013001, Mar. 2017, doi: 10.1088/2058-8585/aa5750.

[43] V. Kartsch, S. Benatti, M. Mancini, M. Magno, and L. Benini, "Smart Wearable Wristband for EMG based Gesture Recognition Powered by Solar Energy Harvester," in *2018 IEEE International Symposium on Circuits and Systems (ISCAS)*, IEEE, May 2018, pp. 1–5. doi: 10.1109/ISCAS.2018.8351727.

[44] Y. Mao, Y. Li, J. Xie, H. Liu, C. Guo, and W. Hu, "Triboelectric nanogenerator/supercapacitor in-one self-powered textile based on PTFE yarn wrapped PDMS/MnO2NW hybrid elastomer," *Nano Energy*, vol. 84, no. December 2020, p. 105918, Jun. 2021, doi: 10.1016/j.nanoen.2021.105918.

[45] K. A. Kim, F. S. Bagci, and K. L. Dorsey, "Design considerations for photovoltaic energy harvesting in wearable devices," *Sci. Rep.*, vol. 12, no. 1, p. 18143, Oct. 2022, doi: 10.1038/s41598-022-22232-x.

[46] X. Huang *et al.*, "Wearable biofuel cells based on the classification of enzyme for high power outputs and lifetimes," *Biosens. Bioelectron.*, vol. 124–125, no. September 2018, pp. 40–52, Jan. 2019, doi: 10.1016/j.bios.2018.09.086.

[47] A. J. Bandodkar *et al.*, "Soft, stretchable, high power density electronic skin-based biofuel cells for scavenging energy from human sweat," *Energy Environ. Sci.*, vol. 10, no. 7, pp. 1581–1589, 2017, doi: 10.1039/C7EE00865A.

[48] S. Choi, "Biofuel Cells and Biobatteries: Misconceptions, Opportunities, and Challenges," *Batteries*, vol. 9, no. 2, p. 119, Feb. 2023, doi:

10.3390/batteries9020119.

[49] T. Starner, "Human-powered wearable computing," *IBM Syst. J.*, vol. 35, no. 3.4, pp. 618–629, 1996, doi: 10.1147/sj.353.0618.

[50] B. Dziadak, Ł. Makowski, M. Kucharek, and A. Jóśko, "Energy Harvesting for Wearable Sensors and Body Area Network Nodes," *Energies*, vol. 16, no. 4, p. 1681, Feb. 2023, doi: 10.3390/en16041681.

[51] V. E. Ogbonna, A. P. I. Popoola, and O. M. Popoola, "Piezoelectric ceramic materials on transducer technology for energy harvesting: A review," *Front. Energy Res.*, vol. 10, no. December, pp. 1–7, Dec. 2022, doi: 10.3389/fenrg.2022.1051081.

[52] J. Feenstra, J. Granstrom, and H. Sodano, "Energy harvesting through a backpack employing a mechanically amplified piezoelectric stack," *Mech. Syst. Signal Process.*, vol. 22, no. 3, pp. 721–734, Apr. 2008, doi: 10.1016/j.ymssp.2007.09.015.

[53] T. Li and P. S. Lee, "Piezoelectric Energy Harvesting Technology: From Materials, Structures, to Applications," *Small Struct.*, vol. 3, no. 3, Mar. 2022, doi: 10.1002/sstr.202100128.

[54] D. Shen *et al.*, "Micromachined PZT cantilever based on SOI structure for low frequency vibration energy harvesting," *Sensors Actuators A Phys.*, vol. 154, no. 1, pp. 103–108, Aug. 2009, doi: 10.1016/j.sna.2009.06.007.

[55] P. Pattanaik and M. Ojha, "Review on challenges in MEMS technology," *Mater. Today Proc.*, vol. 81, no. 2, pp. 224–226, 2023, doi: 10.1016/j.matpr.2021.03.142.

[56] X. Yang and M. Zhang, "Review of flexible microelectromechanical system sensors and devices," *Nanotechnol. Precis. Eng.*, vol. 4, no. 2, p. 025001, Jun. 2021, doi: 10.1063/10.0004301.

[57] Z. L. Wang and J. Song, "Piezoelectric Nanogenerators Based on Zinc Oxide Nanowire Arrays," *Science (80-.).*, vol. 312, no. 5771, pp. 242–246, Apr. 2006, doi:

10.1126/science.1124005.

[58] B. Kumar and S.-W. Kim, "Energy harvesting based on semiconducting piezoelectric ZnO nanostructures," *Nano Energy*, vol. 1, no. 3, pp. 342–355, May 2012, doi: 10.1016/j.nanoen.2012.02.001.

[59] C. Opoku *et al.*, "Fabrication of ZnO Nanowire Based Piezoelectric Generators and Related Structures," *Phys. Procedia*, vol. 70, pp. 858–862, 2015, doi: 10.1016/j.phpro.2015.08.176.

[60] I. Voiculescu, F. Li, G. Kowach, K.-L. Lee, N. Mistou, and R. Kastberg, "Stretchable Piezoelectric Power Generators Based on ZnO Thin Films on Elastic Substrates," *Micromachines*, vol. 10, no. 10, p. 661, Sep. 2019, doi: 10.3390/mi10100661.

[61] A. Rovisco *et al.*, "Piezoelectricity Enhancement of Nanogenerators Based on PDMS and ZnSnO 3 Nanowires through Microstructuration," *ACS Appl. Mater. Interfaces*, vol. 12, no. 16, pp. 18421–18430, Apr. 2020, doi: 10.1021/acsami.9b21636.

[62] N. Soin *et al.*, "High performance triboelectric nanogenerators based on phase-inversion piezoelectric membranes of poly(vinylidene fluoride)-zinc stannate (PVDF-ZnSnO3) and polyamide-6 (PA6)," *Nano Energy*, vol. 30, no. October, pp. 470–480, 2016, doi: 10.1016/j.nanoen.2016.10.040.

[63] D. Meisak *et al.*, "Piezoelectric Nanogenerators Based On BaTiO 3 /PDMS Composites for High-Frequency Applications," *ACS Omega*, vol. 8, no. 15, pp. 13911–13919, Apr. 2023, doi: 10.1021/acsomega.3c00321.

[64] T. Gao *et al.*, "Highly oriented BaTiO 3 film self-assembled using an interfacial strategy and its application as a flexible piezoelectric generator for wind energy harvesting," *J. Mater. Chem. A*, vol. 3, no. 18, pp. 9965–9971, 2015, doi: 10.1039/C5TA01079A.

[65] K.-I. Park *et al.*, "Piezoelectric BaTiO 3 Thin Film Nanogenerator on Plastic

Substrates," *Nano Lett.*, vol. 10, no. 12, pp. 4939–4943, Dec. 2010, doi: 10.1021/nl102959k.

[66] K. Verma and R. Sharma, "A flexible piezoelectric generator based on KNN/PVDF composite films: Role of KNN concentration on the piezoelectric performance of generator," *Chinese J. Phys.*, vol. 84, no. December 2022, pp. 198–215, Aug. 2023, doi: 10.1016/j.cjph.2022.12.007.

[67] K. S. Nair *et al.*, "Synthesis of KNN nanoblocks through surfactant-assisted hot injection method and fabrication of flexible piezoelectric nanogenerator based on KNN-PVDF nanocomposite," *Mater. Today Commun.*, vol. 31, no. February, p. 103291, Jun. 2022, doi: 10.1016/j.mtcomm.2022.103291.

[68] S. Bairagi and S. W. Ali, "A hybrid piezoelectric nanogenerator comprising of KNN/ZnO nanorods incorporated PVDF electrospun nanocomposite webs," *Int. J. Energy Res.*, vol. 44, no. 7, pp. 5545–5563, Jun. 2020, doi: 10.1002/er.5306.

[69] Y. Wang, L. Zhu, and C. Du, "Progress in Piezoelectric Nanogenerators Based on PVDF Composite Films," *Micromachines*, vol. 12, no. 11, p. 1278, Oct. 2021, doi: 10.3390/mi12111278.

[70] S. Ye *et al.*, "High-performance piezoelectric nanogenerator based on microstructured P(VDF-TrFE)/BNNTs composite for energy harvesting and radiation protection in space," *Nano Energy*, vol. 60, no. March, pp. 701–714, Jun. 2019, doi: 10.1016/j.nanoen.2019.03.096.

[71] A. Ali, H. Shaukat, S. Bibi, W. A. Altabey, M. Noori, and S. A. Kouritem, "Recent progress in energy harvesting systems for wearable technology," *Energy Strateg. Rev.*, vol. 49, no. July, p. 101124, Sep. 2023, doi: 10.1016/j.esr.2023.101124.

[72] G. Zhu, B. Peng, J. Chen, Q. Jing, and Z. Lin Wang, "Triboelectric nanogenerators as a new energy technology: From fundamentals, devices, to applications," *Nano Energy*, vol. 14, pp. 126–138, May 2015, doi: 10.1016/j.nanoen.2014.11.050.

[73] S. Niu and Z. L. Wang, "Theoretical systems of triboelectric nanogenerators,"

Nano Energy, vol. 14, pp. 161–192, 2014, doi: 10.1016/j.nanoen.2014.11.034.

[74] B. Saravanakumar, R. Mohan, K. Thiyagarajan, and S.-J. Kim, "Fabrication of a ZnO nanogenerator for eco-friendly biomechanical energy harvesting," *RSC Adv.*, vol. 3, no. 37, p. 16646, 2013, doi: 10.1039/c3ra40447a.

[75] Y. Minami and E. Nakamachi, "Development of enhanced piezoelectric energy harvester induced by human motion," in *2012 Annual International Conference of the IEEE Engineering in Medicine and Biology Society*, IEEE, Aug. 2012, pp. 1627–1630. doi: 10.1109/EMBC.2012.6346257.

[76] M. Yuce, R. Hamid, and A. Mohammadi, "WE-Harvest: A Wearable Piezoelectric-Electromagnetic Energy Harvester," in *Proceedings of the 10th EAI International Conference on Body Area Networks*, ICST, 2015. doi: 10.4108/eai.28-9-2015.2261451.

[77] Q. Brogan, T. O'Connor, and D. S. Ha, "Solar and thermal energy harvesting with a wearable jacket," in *2014 IEEE International Symposium on Circuits and Systems (ISCAS)*, IEEE, Jun. 2014, pp. 1412–1415. doi: 10.1109/ISCAS.2014.6865409.

[78] C. Rodrigues *et al.*, "Hybridizing Triboelectric and Thermomagnetic Effects: A Novel Low-Grade Thermal Energy Harvesting Technology," *Adv. Funct. Mater.*, vol. 32, no. 21, May 2022, doi: 10.1002/adfm.202110288.

[79] X. Tang, X. Wang, R. Cattley, F. Gu, and A. Ball, "Energy Harvesting Technologies for Achieving Self-Powered Wireless Sensor Networks in Machine Condition Monitoring: A Review," *Sensors*, vol. 18, no. 12, p. 4113, Nov. 2018, doi: 10.3390/s18124113.

[80] M. Zhou, M. S. H. Al-Furjan, J. Zou, and W. Liu, "A review on heat and mechanical energy harvesting from human – Principles, prototypes and perspectives," *Renew. Sustain. Energy Rev.*, vol. 82, no. November 2017, pp. 3582–3609, Feb. 2018, doi: 10.1016/j.rser.2017.10.102.

[81] P. F. O'Grady, *Thales of Miletus: The beginnings of western science and philosophy*. 2017. doi: 10.4324/9781315544311.

[82] F. Berna *et al.*, "Microstratigraphic evidence of in situ fire in the Acheulean strata of Wonderwerk Cave, Northern Cape province, South Africa," *Proc. Natl. Acad. Sci. U. S. A.*, vol. 109, no. 20, pp. E1215–E1220, 2012, doi: 10.1073/pnas.1117620109.

[83] A. C. Sorensen, E. Claud, and M. Soressi, "Neandertal fire-making technology inferred from microwear analysis," *Sci. Rep.*, vol. 8, no. 1, pp. 1–16, 2018, doi: 10.1038/s41598-018-28342-9.

[84] F. Spahn and M. Seiß, "Granular matter: Charges dropped," *Nat. Phys.*, vol. 11, no. 9, pp. 709–710, Sep. 2015, doi: 10.1038/nphys3417.

[85] F. Jungmann, T. Steinpilz, J. Teiser, and G. Wurm, "Sticking and restitution in collisions of charged sub-mm dielectric grains," *J. Phys. Commun.*, vol. 2, no. 9, p. 095009, 2018, doi: 10.1088/2399-6528/aad0d2.

[86] S. L. Miller, "A production of amino acids under possible primitive earth conditions," *Science (80-.).*, vol. 117, no. 3046, pp. 528–529, 1953, doi: 10.1126/science.117.3046.528.

[87] A. P. Johnson, H. J. Cleaves, J. P. Dworkin, D. P. Glavin, A. Lazcano, and J. L. Bada, "The Miller volcanic spark discharge experiment," *Science (80-.).*, vol. 322, no. 5900, p. 404, 2008, doi: 10.1126/science.1161527.

[88] D. J. Lacks and R. Mohan Sankaran, "Contact electrification of insulating materials," *J. Phys. D. Appl. Phys.*, vol. 44, no. 45, 2011, doi: 10.1088/0022-3727/44/45/453001.

[89] D. J. Lacks and T. Shinbrot, "Long-standing and unresolved issues in triboelectric charging," *Nat. Rev. Chem.*, vol. 3, no. 8, pp. 465–476, Jul. 2019, doi: 10.1038/s41570-019-0115-1.

[90] J. C. Wilcke, "Dispvtatio Physica Experimentalis, de Electricitatibvs Contrarii,"

Rostochii: Typis Joannis Jacobi Adleri, 1757.

[91] A. Koch and T. Assis, *The Experimental and Historical Foundations of Electricity*. C. Roy Keys Inc., 2010.

[92] W.-G. Kim, D.-W. Kim, I.-W. Tcho, J.-K. Kim, M.-S. Kim, and Y.-K. Choi, "Triboelectric Nanogenerator: Structure, Mechanism, and Applications," *ACS Nano*, vol. 15, no. 1, pp. 258–287, Jan. 2021, doi: 10.1021/acsnano.0c09803.

[93] D. M. Gooding and G. K. Kaufman, "Tribocharging and the Triboelectric Series," in *Encyclopedia of Inorganic and Bioinorganic Chemistry*, Chichester, UK: John Wiley & Sons, Ltd, 2014, pp. 1–9. doi: 10.1002/9781119951438.eibc2239.

[94] P. Taylor and J. Lowell, "Advances in Physics Contact electrification," *Adv. Phys.*, vol. 29, no. October 2012, pp. 947–1023, 1980.

[95] J. Wu, X. Wang, H. Li, F. Wang, W. Yang, and Y. Hu, "Insights into the mechanism of metal-polymer contact electrification for triboelectric nanogenerator via first-principles investigations," *Nano Energy*, vol. 48, no. April, pp. 607–616, Jun. 2018, doi: 10.1016/j.nanoen.2018.04.025.

[96] J. Wu, X. Wang, H. Li, F. Wang, and Y. Hu, "First-principles investigations on the contact electrification mechanism between metal and amorphous polymers for triboelectric nanogenerators," *Nano Energy*, vol. 63, no. June, p. 103864, Sep. 2019, doi: 10.1016/j.nanoen.2019.103864.

[97] L. S. McCarty and G. M. Whitesides, "Electrostatic charging due to separation of ions at interfaces: Contact electrification of ionic electrets," *Angew. Chemie - Int. Ed.*, vol. 47, no. 12, pp. 2188–2207, Mar. 2008, doi: 10.1002/anie.200701812.

[98] Y. Zhang *et al.*, "Electric field and humidity trigger contact electrification," *Phys. Rev. X*, vol. 5, no. 1, p. 011002, Jan. 2015, doi: 10.1103/PhysRevX.5.011002.

[99] S. Pence, V. J. Novotny, and A. F. Diaz, "Effect of Surface Moisture on Contact Charge of Polymers Containing Ions," *Langmuir*, vol. 10, no. 2, pp. 592–596, Feb. 1994, doi: 10.1021/la00014a042.

[100] Y. Awakuni and J. H. Calderwood, "Water vapour adsorption and surface conductivity in solids," *J. Phys. D. Appl. Phys.*, vol. 5, no. 5, pp. 1038–1045, May 1972, doi: 10.1088/0022-3727/5/5/323.

[101] H. T. Baytekin, A. Z. Patashinski, M. Branicki, B. Baytekin, S. Soh, and B. A. Grzybowski, "The mosaic of surface charge in contact electrification," *Science (80-.).*, vol. 333, no. 6040, pp. 308–312, Jul. 2011, doi: 10.1126/science.1201512.

[102] C. Yun *et al.*, "Can Static Electricity on a Conductor Drive a Redox Reaction: Contact Electrification of Au by Polydimethylsiloxane, Charge Inversion in Water, and Redox Reaction," *J. Am. Chem. Soc.*, vol. 140, no. 44, pp. 14687–14695, Nov. 2018, doi: 10.1021/jacs.8b07297.

[103] B. Baytekin, H. T. Baytekin, and B. A. Grzybowski, "What really drives chemical reactions on contact charged surfaces?," *J. Am. Chem. Soc.*, vol. 134, no. 17, pp. 7223–7226, 2012, doi: 10.1021/ja300925h.

[104] M. Sakaguchi, Y. Miwa, S. Hara, Y. Sugino, K. Yamamoto, and S. Shimada, "Triboelectricity in polymers: Effects of the ionic nature of carbon-carbon bonds in the polymer main chain on charge due to yield of mechano-anions produced by heterogeneous scission of the carbon-carbon bond by mechanical fracture," *J. Electrostat.*, vol. 62, no. 1, pp. 35–50, 2004, doi: 10.1016/j.elstat.2004.04.003.

[105] J. Sohma, "Mechanochemistry of polymers," *Prog. Polym. Sci.*, vol. 14, no. 4, pp. 451–596, 1989, doi: 10.1016/0079-6700(89)90004-X.

[106] H. Baytekin, B. Baytekin, T. Hermans, B. Kowalczyk, and B. Grzybowski, "Control of Surface Charges by Radicals," *Science (80-.).*, vol. 341, no. 6152, pp. 1368–1371, 2013.

[107] V. Vivekananthan, A. Chandrasekhar, N. Rao Alluri, Y. Purusothaman, G. Khandelwal, and S.-J. Kim, "Triboelectric Nanogenerators: Design, Fabrication, Energy Harvesting, and Portable-Wearable Applications," in *Nanogenerators*, IntechOpen, 2020, pp. 1–18. doi: 10.5772/intechopen.90951.

[108] C. Wu, A. C. Wang, W. Ding, H. Guo, and Z. L. Wang, "Triboelectric Nanogenerator: A Foundation of the Energy for the New Era," *Adv. Energy Mater.*, vol. 9, no. 1, pp. 1–25, 2019, doi: 10.1002/aenm.201802906.

[109] S. Niu and Z. L. Wang, "Theoretical systems of triboelectric nanogenerators," *Nano Energy*, vol. 14, pp. 161–192, May 2014, doi: 10.1016/j.nanoen.2014.11.034.

[110] H. Zhang, L. Yao, L. Quan, and X. Zheng, "Theories for triboelectric nanogenerators: A comprehensive review," *Nanotechnol. Rev.*, vol. 9, no. 1, pp. 610–625, Jul. 2020, doi: 10.1515/ntrev-2020-0049.

[111] S. Niu *et al.*, "Theoretical Investigation and Structural Optimization of Single-Electrode Triboelectric Nanogenerators," *Adv. Funct. Mater.*, vol. 24, no. 22, pp. 3332–3340, Jun. 2014, doi: 10.1002/adfm.201303799.

[112] S. Niu *et al.*, "Theoretical study of contact-mode triboelectric nanogenerators as an effective power source," *Energy Environ. Sci.*, vol. 6, no. 12, p. 3576, 2013, doi: 10.1039/c3ee42571a.

[113] R. Dharmasena, "Triboelectric Self-Powered Energy Systems," University of Surrey, 2018.

[114] R. D. I. G. Dharmasena, K. D. G. I. Jayawardena, C. A. Mills, R. A. Dorey, and S. R. P. Silva, "A unified theoretical model for Triboelectric Nanogenerators," *Nano Energy*, vol. 48, no. March, pp. 391–400, Jun. 2018, doi: 10.1016/j.nanoen.2018.03.073.

[115] R. D. I. G. Dharmasena *et al.*, "Triboelectric nanogenerators: Providing a fundamental framework," *Energy Environ. Sci.*, vol. 10, no. 8, pp. 1801–1811, 2017, doi: 10.1039/c7ee01139c.

[116] S. A. Lone *et al.*, "Recent advancements for improving the performance of triboelectric nanogenerator devices," *Nano Energy*, vol. 99, no. April, p. 107318, Aug. 2022, doi: 10.1016/j.nanoen.2022.107318.

[117] W. Seung *et al.*, "Nanopatterned textile-based wearable triboelectric

nanogenerator," *ACS Nano*, vol. 9, no. 4, pp. 3501–3509, Apr. 2015, doi: 10.1021/nn507221f.

[118] F. R. Fan, L. Lin, G. Zhu, W. Wu, R. Zhang, and Z. L. Wang, "Transparent triboelectric nanogenerators and self-powered pressure sensors based on micropatterned plastic films," *Nano Lett.*, vol. 12, no. 6, pp. 3109–3114, Jun. 2012, doi: 10.1021/nl300988z.

[119] A. Rovisco *et al.*, "Piezoelectricity Enhancement of Nanogenerators Based on PDMS and ZnSnO3Nanowires through Microstructuration," *ACS Appl. Mater. Interfaces*, vol. 12, no. 16, pp. 18421–18430, Apr. 2020, doi: 10.1021/acsami.9b21636.

[120] K. Y. Lee *et al.*, "Hydrophobic sponge structure-based triboelectric nanogenerator," *Adv. Mater.*, vol. 26, no. 29, pp. 5037–5042, Aug. 2014, doi: 10.1002/adma.201401184.

[121] M. Taghavi, V. Mattoli, A. Sadeghi, B. Mazzolai, and L. Beccai, "A novel soft metal-polymer composite for multidirectional pressure energy harvesting," *Adv. Energy Mater.*, vol. 4, no. 12, p. 1400024, Aug. 2014, doi: 10.1002/aenm.201400024.

[122] S.-H. Shin *et al.*, "Formation of Triboelectric Series via Atomic-Level Surface Functionalization for Triboelectric Energy Harvesting," *ACS Nano*, vol. 11, no. 6, pp. 6131–6138, Jun. 2017, doi: 10.1021/acsnano.7b02156.

[123] Y. Dong *et al.*, "Metallic MXenes: A new family of materials for flexible triboelectric nanogenerators," *Nano Energy*, vol. 44, no. October 2017, pp. 103–110, Feb. 2018, doi: 10.1016/j.nanoen.2017.11.044.

[124] C. Yao, X. Yin, Y. Yu, Z. Cai, and X. Wang, "Chemically Functionalized Natural Cellulose Materials for Effective Triboelectric Nanogenerator Development," *Adv. Funct. Mater.*, vol. 27, no. 30, p. 1700794, Aug. 2017, doi: 10.1002/adfm.201700794.

[125] S. Chen, J. Jiang, F. Xu, and S. Gong, "Crepe cellulose paper and nitrocellulose membrane-based triboelectric nanogenerators for energy harvesting and self-powered human-machine interaction," *Nano Energy*, vol. 61, no. April, pp. 69–77, Jul. 2019, doi: 10.1016/j.nanoen.2019.04.043.

[126] Q. Zheng *et al.*, "Highly Porous Polymer Aerogel Film-Based Triboelectric Nanogenerators," *Adv. Funct. Mater.*, vol. 28, no. 13, p. 1706365, Mar. 2018, doi: 10.1002/adfm.201706365.

[127] H.-Y. Mi *et al.*, "High-performance flexible triboelectric nanogenerator based on porous aerogels and electrospun nanofibers for energy harvesting and sensitive self-powered sensing," *Nano Energy*, vol. 48, pp. 327–336, Jun. 2018, doi: 10.1016/j.nanoen.2018.03.050.

[128] S. Roy, H.-U. Ko, P. K. Maji, L. Van Hai, and J. Kim, "Large amplification of triboelectric property by allicin to develop high performance cellulosic triboelectric nanogenerator," *Chem. Eng. J.*, vol. 385, p. 123723, Apr. 2020, doi: 10.1016/j.cej.2019.123723.

[129] R. Wang *et al.*, "Engineered and Laser-Processed Chitosan Biopolymers for Sustainable and Biodegradable Triboelectric Power Generation," *Adv. Mater.*, vol. 30, no. 11, p. 1706267, Mar. 2018, doi: 10.1002/adma.201706267.

[130] Y. Yu, Z. Li, Y. Wang, S. Gong, and X. Wang, "Sequential Infiltration Synthesis of Doped Polymer Films with Tunable Electrical Properties for Efficient Triboelectric Nanogenerator Development," *Adv. Mater.*, vol. 27, no. 33, pp. 4938–4944, Sep. 2015, doi: 10.1002/adma.201502546.

[131] H. Ryu *et al.*, "High-Performance Triboelectric Nanogenerators Based on Solid Polymer Electrolytes with Asymmetric Pairing of Ions," *Adv. Energy Mater.*, vol. 7, no. 17, p. 1700289, Sep. 2017, doi: 10.1002/aenm.201700289.

[132] L. Shi *et al.*, "Enhanced performance triboelectric nanogenerators based on solid polymer electrolytes with different concentrations of cations," *Nano Energy*, vol.

64, p. 103960, Oct. 2019, doi: 10.1016/j.nanoen.2019.103960.

[133] C. C. Wang and R. Ramprasad, "Dielectric properties of organosilicons from first principles," *J. Mater. Sci.*, vol. 46, no. 1, pp. 90–93, Jan. 2011, doi: 10.1007/s10853-010-4830-8.

[134] G. Pilania *et al.*, "New Group IV Chemical Motifs for Improved Dielectric Permittivity of Polyethylene," *J. Chem. Inf. Model.*, vol. 53, no. 4, pp. 879–886, Apr. 2013, doi: 10.1021/ci400033h.

[135] C. C. Wang, G. Pilania, and R. Ramprasad, "Dielectric properties of carbon-, silicon-, and germanium-based polymers: A first-principles study," *Phys. Rev. B*, vol. 87, no. 3, p. 035103, Jan. 2013, doi: 10.1103/PhysRevB.87.035103.

[136] W. Seung *et al.*, "Boosting Power-Generating Performance of Triboelectric Nanogenerators via Artificial Control of Ferroelectric Polarization and Dielectric Properties," *Adv. Energy Mater.*, vol. 7, no. 2, p. 1600988, Jan. 2017, doi: 10.1002/aenm.201600988.

[137] S. Cheon *et al.*, "High-Performance Triboelectric Nanogenerators Based on Electrospun Polyvinylidene Fluoride-Silver Nanowire Composite Nanofibers," *Adv. Funct. Mater.*, vol. 28, no. 2, p. 1703778, Jan. 2018, doi: 10.1002/adfm.201703778.

[138] E. I. Izgorodina, M. Forsyth, and D. R. MacFarlane, "On the components of the dielectric constants of ionic liquids: ionic polarization?," *Phys. Chem. Chem. Phys.*, vol. 11, no. 14, p. 2452, 2009, doi: 10.1039/b815835e.

[139] Y. Zou *et al.*, "A bionic stretchable nanogenerator for underwater sensing and energy harvesting," *Nat. Commun.*, vol. 10, no. 1, p. 2695, Jun. 2019, doi: 10.1038/s41467-019-10433-4.

[140] K. Parida, V. Kumar, W. Jiangxin, V. Bhavanasi, R. Bendi, and P. S. Lee, "Highly Transparent, Stretchable, and Self-Healing Ionic-Skin Triboelectric Nanogenerators for Energy Harvesting and Touch Applications," *Adv. Mater.*,

vol. 29, no. 37, p. 1702181, Oct. 2017, doi: 10.1002/adma.201702181.

[141] B. Dudem, L. K. Bharat, H. Patnam, A. R. Mule, and J. S. Yu, "Enhancing the output performance of hybrid nanogenerators based on Al-doped BaTiO 3 composite films: a self-powered utility system for portable electronics," *J. Mater. Chem. A*, vol. 6, no. 33, pp. 16101–16110, 2018, doi: 10.1039/C8TA04612C.

[142] J. Chen *et al.*, "Enhancing Performance of Triboelectric Nanogenerator by Filling High Dielectric Nanoparticles into Sponge PDMS Film," *ACS Appl. Mater. Interfaces*, vol. 8, no. 1, pp. 736–744, Jan. 2016, doi: 10.1021/acsami.5b09907.

[143] S. Gao *et al.*, "Wearable high-dielectric-constant polymers with core–shell liquid metal inclusions for biomechanical energy harvesting and a self-powered user interface," *J. Mater. Chem. A*, vol. 7, no. 12, pp. 7109–7117, 2019, doi: 10.1039/C9TA01249D.

[144] M. Lai *et al.*, "Enhancing the performance of NaNbO 3 triboelectric nanogenerators by dielectric modulation and electronegative modification," *J. Phys. D. Appl. Phys.*, vol. 51, no. 1, p. 015303, Jan. 2018, doi: 10.1088/1361-6463/aa9a6c.

[145] D. W. Kim, J. H. Lee, I. You, J. K. Kim, and U. Jeong, "Adding a stretchable deep-trap interlayer for high-performance stretchable triboelectric nanogenerators," *Nano Energy*, vol. 50, no. May, pp. 192–200, Aug. 2018, doi: 10.1016/j.nanoen.2018.05.041.

[146] Y. Feng, Y. Zheng, G. Zhang, D. Wang, F. Zhou, and W. Liu, "A new protocol toward high output TENG with polyimide as charge storage layer," *Nano Energy*, vol. 38, no. March, pp. 467–476, Aug. 2017, doi: 10.1016/j.nanoen.2017.06.017.

[147] L. Zhu, "Exploring Strategies for High Dielectric Constant and Low Loss Polymer Dielectrics," *J. Phys. Chem. Lett.*, vol. 5, no. 21, pp. 3677–3687, Nov. 2014, doi: 10.1021/jz501831q.

[148] S. Fabiano, X. Crispin, and M. Berggren, "Ferroelectric Polarization Induces Electric Double Layer Bistability in Electrolyte-Gated Field-Effect Transistors," *ACS Appl. Mater. Interfaces*, vol. 6, no. 1, pp. 438–442, Jan. 2014, doi: 10.1021/am404494h.

[149] A. González, E. Goikolea, J. A. Barrena, and R. Mysyk, "Review on supercapacitors: Technologies and materials," *Renew. Sustain. Energy Rev.*, vol. 58, pp. 1189–1206, May 2016, doi: 10.1016/j.rser.2015.12.249.

[150] S. Niu, X. Wang, F. Yi, Y. S. Zhou, and Z. L. Wang, "A universal self-charging system driven by random biomechanical energy for sustainable operation of mobile electronics," *Nat. Commun.*, vol. 6, no. 1, p. 8975, Dec. 2015, doi: 10.1038/ncomms9975.

[151] F. Xi *et al.*, "Universal power management strategy for triboelectric nanogenerator," *Nano Energy*, vol. 37, no. May, pp. 168–176, Jul. 2017, doi: 10.1016/j.nanoen.2017.05.027.

[152] W. Liu *et al.*, "Switched-capacitor-convertors based on fractal design for output power management of triboelectric nanogenerator," *Nat. Commun.*, vol. 11, no. 1, p. 1883, Apr. 2020, doi: 10.1038/s41467-020-15373-y.

[153] N. C. Iheaturu, B. C. Aharanwa, K. O. Chike, U. L. Ezeamaku, O. O. Nnorom, and C. C. Chima, "Advancements in Textile Finishing," *IOSR J. Polym. Text. Eng.*, vol. 6, no. 5, pp. 23–31, 2019, doi: 10.9790/019X-06052331.

[154] Y. Chen, Y. Ling, and R. Yin, "Fiber/Yarn-Based Triboelectric Nanogenerators (TENGs): Fabrication Strategy, Structure, and Application," *Sensors*, vol. 22, no. 24, p. 9716, Dec. 2022, doi: 10.3390/s22249716.

[155] A. Yu *et al.*, "Core–Shell-Yarn-Based Triboelectric Nanogenerator Textiles as Power Cloths," *ACS Nano*, vol. 11, no. 12, pp. 12764–12771, Dec. 2017, doi: 10.1021/acsnano.7b07534.

[156] T. Busolo, P. K. Szewczyk, M. Nair, U. Stachewicz, and S. Kar-Narayan,

"Triboelectric Yarns with Electrospun Functional Polymer Coatings for Highly Durable and Washable Smart Textile Applications," *ACS Appl. Mater. Interfaces*, vol. 13, no. 14, pp. 16876–16886, Apr. 2021, doi: 10.1021/acsami.1c00983.

[157] L. Ma *et al.*, "Continuous and Scalable Manufacture of Hybridized Nano-Micro Triboelectric Yarns for Energy Harvesting and Signal Sensing," *ACS Nano*, vol. 14, no. 4, pp. 4716–4726, Apr. 2020, doi: 10.1021/acsnano.0c00524.

[158] Y.-C. Lai, J. Deng, S. L. Zhang, S. Niu, H. Guo, and Z. L. Wang, "Single-Thread-Based Wearable and Highly Stretchable Triboelectric Nanogenerators and Their Applications in Cloth-Based Self-Powered Human-Interactive and Biomedical Sensing," *Adv. Funct. Mater.*, vol. 27, no. 1, p. 1604462, Jan. 2017, doi: 10.1002/adfm.201604462.

[159] K. Dong *et al.*, "Shape adaptable and highly resilient 3D braided triboelectric nanogenerators as e-textiles for power and sensing," *Nat. Commun.*, vol. 11, no. 1, p. 2868, Jun. 2020, doi: 10.1038/s41467-020-16642-6.

[160] L. Guo, T. Bashir, E. Bresky, and N.-K. Persson, "Electroconductive textiles and textile-based electromechanical sensors—integration in as an approach for smart textiles," in *Smart Textiles and their Applications*, Elsevier, 2016, pp. 657–693. doi: 10.1016/B978-0-08-100574-3.00028-X.

[161] A. Chen, C. Zhang, G. Zhu, and Z. L. Wang, "Polymer Materials for High-Performance Triboelectric Nanogenerators," *Adv. Sci.*, vol. 7, no. 14, pp. 1–25, 2020, doi: 10.1002/advs.202000186.

[162] X. Yu *et al.*, "A coaxial triboelectric nanogenerator fiber for energy harvesting and sensing under deformation," *J. Mater. Chem. A*, vol. 5, no. 13, pp. 6032–6037, 2017, doi: 10.1039/C7TA00248C.

[163] W. Gong *et al.*, "A wearable, fibroid, self-powered active kinematic sensor based on stretchable sheath-core structural triboelectric fibers," *Nano Energy*, vol. 39, no. August, pp. 673–683, Sep. 2017, doi: 10.1016/j.nanoen.2017.08.003.

[164] Z. Tian *et al.*, "Performance-boosted triboelectric textile for harvesting human motion energy," *Nano Energy*, vol. 39, no. May, pp. 562–570, Sep. 2017, doi: 10.1016/j.nanoen.2017.06.018.

[165] Y. Yang *et al.*, "Liquid-Metal-Based Super-Stretchable and Structure-Designable Triboelectric Nanogenerator for Wearable Electronics," *ACS Nano*, vol. 12, no. 2, pp. 2027–2034, Feb. 2018, doi: 10.1021/acsnano.8b00147.

[166] K. Dong *et al.*, "Versatile Core–Sheath Yarn for Sustainable Biomechanical Energy Harvesting and Real-Time Human-Interactive Sensing," *Adv. Energy Mater.*, vol. 8, no. 23, pp. 1–12, Aug. 2018, doi: 10.1002/aenm.201801114.

[167] Y. Yang *et al.*, "Coaxial Triboelectric Nanogenerator and Supercapacitor Fiber-Based Self-Charging Power Fabric," *ACS Appl. Mater. Interfaces*, vol. 10, no. 49, pp. 42356–42362, Dec. 2018, doi: 10.1021/acsami.8b15104.

[168] L. Xie *et al.*, "Spiral Steel Wire Based Fiber-Shaped Stretchable and Tailorable Triboelectric Nanogenerator for Wearable Power Source and Active Gesture Sensor," *Nano-Micro Lett.*, vol. 11, no. 1, p. 39, Dec. 2019, doi: 10.1007/s40820-019-0271-3.

[169] W. Gong *et al.*, "Continuous and scalable manufacture of amphibious energy yarns and textiles," *Nat. Commun.*, vol. 10, no. 1, pp. 1–8, 2019, doi: 10.1038/s41467-019-08846-2.

[170] C. Jiang, X. Li, Y. Ying, and J. Ping, "A multifunctional TENG yarn integrated into agrotextile for building intelligent agriculture," *Nano Energy*, vol. 74, no. February, p. 104863, Aug. 2020, doi: 10.1016/j.nanoen.2020.104863.

[171] Y. Tong, Z. Feng, J. Kim, J. L. Robertson, X. Jia, and B. N. Johnson, "3D printed stretchable triboelectric nanogenerator fibers and devices," *Nano Energy*, vol. 75, no. April, p. 104973, Sep. 2020, doi: 10.1016/j.nanoen.2020.104973.

[172] Y. Gao *et al.*, "Scalable core–spun coating yarn-based triboelectric nanogenerators with hierarchical structure for wearable energy harvesting and

sensing via continuous manufacturing," *Nano Energy*, vol. 91, no. October 2021, p. 106672, Jan. 2022, doi: 10.1016/j.nanoen.2021.106672.

[173] T. Jing, B. Xu, J. H. Xin, X. Guan, and Y. Yang, "Series to parallel structure of electrode fiber: an effective method to remarkably reduce inner resistance of triboelectric nanogenerator textiles," *J. Mater. Chem. A*, vol. 9, no. 20, pp. 12331–12339, 2021, doi: 10.1039/D1TA01309B.

[174] M. He *et al.*, "Flexible and stretchable triboelectric nanogenerator fabric for biomechanical energy harvesting and self-powered dual-mode human motion monitoring," *Nano Energy*, vol. 86, no. April, p. 106058, Aug. 2021, doi: 10.1016/j.nanoen.2021.106058.

[175] Y. Yang, B. Xu, Y. Gao, and M. Li, "Conductive Composite Fiber with Customizable Functionalities for Energy Harvesting and Electronic Textiles," *ACS Appl. Mater. Interfaces*, vol. 13, no. 42, pp. 49927–49935, Oct. 2021, doi: 10.1021/acsami.1c14273.

[176] X. Ren, X. Xiang, H. Yin, Y. Tang, and H. Yuan, "All-yarn triboelectric nanogenerator and supercapacitor based self-charging power cloth for wearable applications," *Nanotechnology*, vol. 32, no. 31, p. 315404, Jul. 2021, doi: 10.1088/1361-6528/abfcfe.

[177] B. A. Newcomb, "Processing, structure, and properties of carbon fibers," *Compos. Part A Appl. Sci. Manuf.*, vol. 91, pp. 262–282, Dec. 2016, doi: 10.1016/j.compositesa.2016.10.018.

[178] X. Huang, "Fabrication and Properties of Carbon Fibers," *Materials (Basel).*, vol. 2, no. 4, pp. 2369–2403, Dec. 2009, doi: 10.3390/ma2042369.

[179] P. V. Gulgunje, B. A. Newcomb, K. Gupta, H. G. Chae, T. K. Tsotsis, and S. Kumar, "Low-density and high-modulus carbon fibers from polyacrylonitrile with honeycomb structure," *Carbon N. Y.*, vol. 95, pp. 710–714, Dec. 2015, doi: 10.1016/j.carbon.2015.08.097.

[180] M. JACOBY, "COMPOSITE MATERIALS," *Chem. Eng. News Arch.*, vol. 82, no. 35, pp. 34–41, Aug. 2004, doi: 10.1021/cen-v082n035.p034.

[181] D. He *et al.*, "The effect of sizing and surface oxidation on the surface properties and tensile behaviour of recycled carbon fibre: An end-of-life perspective," *Compos. Part A Appl. Sci. Manuf.*, vol. 138, no. August, p. 106072, Nov. 2020, doi: 10.1016/j.compositesa.2020.106072.

[182] M. S. Folomeshkin *et al.*, "X-ray Diffraction Analysis and Electron Microscopy of the Carbon Fiber Structure," *Crystallogr. Reports*, vol. 64, no. 1, pp. 1–5, 2019, doi: 10.1134/S1063774519010085.

[183] T. K. Das, P. Ghosh, and N. C. Das, "Preparation, development, outcomes, and application versatility of carbon fiber-based polymer composites: a review," *Adv. Compos. Hybrid Mater.*, vol. 2, no. 2, pp. 214–233, Jun. 2019, doi: 10.1007/s42114-018-0072-z.

[184] S. Lee, J. Kim, B.-C. Ku, J. Kim, and H.-I. Joh, "Structural Evolution of Polyacrylonitrile Fibers in Stabilization and Carbonization," *Adv. Chem. Eng. Sci.*, vol. 02, no. 02, pp. 275–282, 2012, doi: 10.4236/aces.2012.22032.

[185] S.-J. Park and L.-Y. Meng, "Surface Treatment and Sizing of Carbon Fibers," 2015, pp. 101–133. doi: 10.1007/978-94-017-9478-7_4.

[186] S. Tiwari and J. Bijwe, "Surface Treatment of Carbon Fibers - A Review," *Procedia Technol.*, vol. 14, pp. 505–512, 2014, doi: 10.1016/j.protcy.2014.08.064.

[187] D. Bücheler, A. Kaiser, and F. Henning, "Using Thermogravimetric Analysis to Determine Carbon Fiber Weight Percentage of Fiber-Reinforced Plastics," *Compos. Part B Eng.*, vol. 106, pp. 218–223, Dec. 2016, doi: 10.1016/j.compositesb.2016.09.028.

[188] A. Khan *et al.*, "Preparation of Styrene-Butadiene Rubber (SBR) Composite Incorporated with Collagen-Functionalized Graphene Oxide for Green Tire Application," *Gels*, vol. 8, no. 3, p. 161, Mar. 2022, doi: 10.3390/gels8030161.

[189] J. C. Passos, "Os experimentos de Joule e a primeira lei da termodinâmica," *Rev. Bras. Ensino Física*, vol. 31, no. 3, pp. 3603.1-3603.8, Sep. 2009, doi: 10.1590/S1806-11172009000300013.

[190] A. Mata, A. J. Fleischman, and S. Roy, "Characterization of Polydimethylsiloxane (PDMS) Properties for Biomedical Micro/Nanosystems," *Biomed. Microdevices*, vol. 7, no. 4, pp. 281–293, Dec. 2005, doi: 10.1007/s10544-005-6070-2.

[191] Y. Xia and G. M. Whitesides, "Soft Lithography," *Angew. Chemie Int. Ed.*, vol. 37, no. 5, pp. 550–575, Mar. 1998, doi: 10.1002/(SICI)1521-3773(19980316)37:5<550::AID-ANIE550>3.0.CO;2-G.

[192] K. Raj M and S. Chakraborty, "PDMS microfluidics: A mini review," *J. Appl. Polym. Sci.*, vol. 137, no. 27, pp. 1–14, Jul. 2020, doi: 10.1002/app.48958.

[193] F. Hua *et al.*, "Polymer Imprint Lithography with Molecular-Scale Resolution," *Nano Lett.*, vol. 4, no. 12, pp. 2467–2471, Dec. 2004, doi: 10.1021/nl048355u.

[194] P. J. Mackenzie, R. M. Schertzer, and C. M. Isbister, "Comparison of silicone and polypropylene Ahmed glaucoma valves: Two-year follow-up," *Can. J. Ophthalmol.*, vol. 42, no. 2, pp. 227–232, Apr. 2007, doi: 10.3129/can.j.ophthalmol.i07-032.

[195] A. Victor, J. Ribeiro, and F. F. Araújo, "Study of PDMS characterization and its applications in biomedicine: A review," *J. Mech. Eng. Biomech.*, vol. 4, no. 1, pp. 1–9, Aug. 2019, doi: 10.24243/JMEB/4.1.163.

[196] M. Younes *et al.*, "Re-evaluation of dimethyl polysiloxane (E 900) as a food additive," *EFSA J.*, vol. 18, no. 5, May 2020, doi: 10.2903/j.efsa.2020.6107.

[197] F. R. Fan, W. Tang, and Z. L. Wang, "Flexible Nanogenerators for Energy Harvesting and Self-Powered Electronics," *Adv. Mater.*, vol. 28, no. 22, pp. 4283–4305, Jun. 2016, doi: 10.1002/adma.201504299.

[198] M. Lee *et al.*, "A hybrid piezoelectric structure for wearable nanogenerators,"

Adv. Mater., vol. 24, no. 13, pp. 1759–1764, Apr. 2012, doi: 10.1002/adma.201200150.

[199] A. S. Dahiya, F. Morini, S. Boubenia, K. Nadaud, D. Alquier, and G. Poulin-Vittrant, "Organic/Inorganic Hybrid Stretchable Piezoelectric Nanogenerators for Self-Powered Wearable Electronics," *Adv. Mater. Technol.*, vol. 3, no. 2, p. 1700249, Feb. 2018, doi: 10.1002/admt.201700249.

[200] R. K. Pandey, H. Kakehashi, H. Nakanishi, and S. Soh, "Correlating Material Transfer and Charge Transfer in Contact Electrification," *J. Phys. Chem. C*, vol. 122, no. 28, pp. 16154–16160, Jul. 2018, doi: 10.1021/acs.jpcc.8b04357.

[201] R. D. I. G. Dharmasena *et al.*, "Triboelectric nanogenerators: Providing a fundamental framework," *Energy Environ. Sci.*, vol. 10, no. 8, pp. 1801–1811, 2017, doi: 10.1039/c7ee01139c.

[202] R. D. I. G. Dharmasena, J. H. B. Deane, and S. R. P. Silva, "Nature of Power Generation and Output Optimization Criteria for Triboelectric Nanogenerators," *Adv. Energy Mater.*, vol. 8, no. 31, p. 1802190, Nov. 2018, doi: 10.1002/aenm.201802190.

[203] L. Shi *et al.*, "Carbon electrodes enable flat surface PDMS and PA6 triboelectric nanogenerators to achieve significantly enhanced triboelectric performance," *Nano Energy*, vol. 55, pp. 548–557, Jan. 2019, doi: 10.1016/j.nanoen.2018.11.012.

[204] H. Zou *et al.*, "Quantifying the triboelectric series," *Nat. Commun.*, vol. 10, no. 1, pp. 1–9, 2019, doi: 10.1038/s41467-019-09461-x.

[205] D. Choi *et al.*, "Recent Advances in Triboelectric Nanogenerators: From Technological Progress to Commercial Applications," *ACS Nano*, vol. 17, no. 12, pp. 11087–11219, Jun. 2023, doi: 10.1021/acsnano.2c12458.

[206] A. Örn, "Degradation studies on polydimethylsiloxane," no. May, p. 63, 2019.

[207] W. N. Nkeuwa, J. Zhang, K. E. Semple, M. Chen, Y. Xia, and C. Dai, "Bamboo-based composites: A review on fundamentals and processes of bamboo

bonding," *Compos. Part B Eng.*, vol. 235, no. February, p. 109776, Apr. 2022, doi: 10.1016/j.compositesb.2022.109776.

[208] M.-Y. Guan, H.-N. Zhong, Z.-W. Wang, W.-W. Yu, and C.-Y. Hu, "Chemical contaminants from food contact materials and articles made from or containing wood and bamboo – a review," *Food Addit. Contam. Part A*, vol. 40, no. 3, pp. 434–453, Mar. 2023, doi: 10.1080/19440049.2023.2167003.

[209] S. S. Kwak *et al.*, "Butylated melamine formaldehyde as a durable and highly positive friction layer for stable, high output triboelectric nanogenerators," *Energy Environ. Sci.*, vol. 12, no. 10, pp. 3156–3163, 2019, doi: 10.1039/c9ee01267b.

[210] T. A. Abdel–Baset and M. Belhaj, "Structural characterization, dielectric properties and electrical conductivity of ZnO nanoparticles synthesized by co-precipitation route," *Phys. B Condens. Matter*, vol. 616, no. February, p. 413130, Sep. 2021, doi: 10.1016/j.physb.2021.413130.

[211] M. S. Al-Ruqeishi, T. Mohiuddin, B. Al-Habsi, F. Al-Ruqeishi, A. Al-Fahdi, and A. Al-Khusaibi, "Piezoelectric nanogenerator based on ZnO nanorods," *Arab. J. Chem.*, vol. 12, no. 8, pp. 5173–5179, Dec. 2019, doi: 10.1016/j.arabjc.2016.12.010.

[212] N. Bhadwal, R. Ben Mrad, and K. Behdinan, "Review of Zinc Oxide Piezoelectric Nanogenerators: Piezoelectric Properties, Composite Structures and Power Output," *Sensors*, vol. 23, no. 8, p. 3859, Apr. 2023, doi: 10.3390/s23083859.

[213] L. Schmidt-Mende and J. L. MacManus-Driscoll, "ZnO – nanostructures, defects, and devices," *Mater. Today*, vol. 10, no. 5, pp. 40–48, May 2007, doi: 10.1016/S1369-7021(07)70078-0.

[214] X. Wu, J. Lee, V. Varshney, J. L. Wohlwend, A. K. Roy, and T. Luo, "Thermal Conductivity of Wurtzite Zinc-Oxide from First-Principles Lattice Dynamics - A Comparative Study with Gallium Nitride," *Sci. Rep.*, vol. 6, no. 1, p. 22504, Apr. 2016, doi: 10.1038/srep22504.

[215] J. E. Mark, "Polymer Data Handbook, 2nd ed.," *J. Am. Chem. Soc.*, vol. 131, no.

44, pp. 16330–16330, Nov. 2009, doi: 10.1021/ja907879q.

[216] C. Moraes, Y. Sun, and C. A. Simmons, "Solving the shrinkage-induced PDMS alignment registration issue in multilayer soft lithography," *J. Micromechanics Microengineering*, vol. 19, no. 6, 2009, doi: 10.1088/0960-1317/19/6/065015.

[217] H. Schmid and B. Michel, "Siloxane polymers for high-resolution, high-accuracy soft lithography," *Macromolecules*, vol. 33, no. 8, pp. 3042–3049, 2000, doi: 10.1021/ma982034l.

[218] H. Wu, T. W. Odom, D. T. Chiu, and G. M. Whitesides, "Fabrication of complex three-dimensional microchannel systems in PDMS," *J. Am. Chem. Soc.*, vol. 125, no. 2, pp. 554–559, 2003, doi: 10.1021/ja021045y.

[219] M. H. Madsen, N. A. Feidenhans'l, P. E. Hansen, J. Garnæs, and K. Dirscherl, "Accounting for PDMS shrinkage when replicating structures," *J. Micromechanics Microengineering*, vol. 24, no. 12, 2014, doi: 10.1088/0960-1317/24/12/127002.

[220] R. Kulkarni and O. Ochoa, "Transverse and longitudinal CTE measurements of carbon fibers and their impact on interfacial residual stresses in composites," *J. Compos. Mater.*, vol. 40, no. 8, pp. 733–754, Apr. 2006, doi: 10.1177/0021998305055545.

[221] C. Pradere and C. Sauder, "Transverse and longitudinal coefficient of thermal expansion of carbon fibers at high temperatures (300-2500 K)," *Carbon N. Y.*, vol. 46, no. 14, pp. 1874–1884, Nov. 2008, doi: 10.1016/j.carbon.2008.07.035.

[222] J. W. Lee *et al.*, "Robust nanogenerators based on graft copolymers via control of dielectrics for remarkable output power enhancement," *Sci. Adv.*, vol. 3, no. 5, pp. 1–10, May 2017, doi: 10.1126/sciadv.1602902.

[223] A. Rovisco *et al.*, "Piezoelectricity Enhancement of Nanogenerators Based on PDMS and ZnSnO3Nanowires through Microstructuration," *ACS Appl. Mater. Interfaces*, vol. 12, no. 16, pp. 18421–18430, 2020, doi: 10.1021/acsami.9b21636.

[224] M. R. Hasan, S. H. Baek, K. S. Seong, J. H. Kim, and I. K. Park, "Hierarchical ZnO Nanorods on Si Micropillar Arrays for Performance Enhancement of Piezoelectric Nanogenerators," *ACS Appl. Mater. Interfaces*, vol. 7, no. 10, pp. 5768–5774, Mar. 2015, doi: 10.1021/am5085379.

[225] Y. H. Ko, G. Nagaraju, S. H. Lee, and J. S. Yu, "PDMS-based triboelectric and transparent nanogenerators with ZnO nanorod arrays," *ACS Appl. Mater. Interfaces*, vol. 6, no. 9, pp. 6631–6637, May 2014, doi: 10.1021/am5018072.

[226] S. H. Shin, Y. H. Kwon, M. H. Lee, J. Y. Jung, J. H. Seol, and J. Nah, "A vanadium-doped ZnO nanosheets-polymer composite for flexible piezoelectric nanogenerators," *Nanoscale*, vol. 8, no. 3, pp. 1314–1321, 2016, doi: 10.1039/c5nr07185b.

[227] S. N. Chen, C. H. Chen, Z. H. Lin, Y. H. Tsao, and C. P. Liu, "On enhancing capability of tribocharge transfer of ZnO nanorod arrays by Sb doping for anomalous output performance improvement of triboelectric nanogenerators," *Nano Energy*, vol. 45, no. January, pp. 311–318, Mar. 2018, doi: 10.1016/j.nanoen.2018.01.013.

[228] S. N. Chen, M. Z. Huang, Z. H. Lin, and C. P. Liu, "Enhancing charge transfer for ZnO nanorods based triboelectric nanogenerators through Ga doping," *Nano Energy*, vol. 65, no. July, p. 104069, Nov. 2019, doi: 10.1016/j.nanoen.2019.104069.

[229] Z. Dang, J. Yuan, J. Zha, T. Zhou, S.-T. Li, and G.-H. Hu, "Fundamentals, processes and applications of high-permittivity polymer–matrix composites," *Prog. Mater. Sci.*, vol. 57, no. 4, pp. 660–723, May 2012, doi: 10.1016/j.pmatsci.2011.08.001.

[230] L. K. Anlin, K. V. Vijoy, K. Pradeesh, S. Thomas, H. John, and K. J. Saji, "Effects of metal nanoparticles on the performance of PDMS based triboelectric nanogenerators," *Phys. B Condens. Matter*, vol. 639, no. January, p. 413952, Aug. 2022, doi: 10.1016/j.physb.2022.413952.

[231] B. Zhao *et al.*, "Improving the performance of nanogenerators via micro-capacitors and enhanced dipoles," *Chem. Eng. J.*, vol. 461, no. December 2022, p. 142086, Apr. 2023, doi: 10.1016/j.cej.2023.142086.

[232] J. Chun *et al.*, "Mesoporous pores impregnated with Au nanoparticles as effective dielectrics for enhancing triboelectric nanogenerator performance in harsh environments," *Energy Environ. Sci.*, vol. 8, no. 10, pp. 3006–3012, 2015, doi: 10.1039/C5EE01705J.

[233] L. de S. Vieira *et al.*, "A review concerning the main factors that interfere in the electrical percolation threshold content of polymeric antistatic packaging with carbon fillers as antistatic agent," *Nano Sel.*, vol. 3, no. 2, pp. 248–260, Feb. 2022, doi: 10.1002/nano.202100073.

[234] G. A. Gelves, B. Lin, U. Sundararaj, and J. A. Haber, "Low Electrical Percolation Threshold of Silver and Copper Nanowires in Polystyrene Composites," *Adv. Funct. Mater.*, vol. 16, no. 18, pp. 2423–2430, Dec. 2006, doi: 10.1002/adfm.200600336.

[235] Q. Lu *et al.*, "Determination of Carbon Nanotube Density by Gradient Sedimentation," *J. Phys. Chem. B*, vol. 110, no. 48, pp. 24371–24376, Dec. 2006, doi: 10.1021/jp063660k.

[236] L. Torrisi, M. Cutroneo, A. Torrisi, and L. Silipigni, "Measurements on Five Characterizing Properties of Graphene Oxide and Reduced Graphene Oxide Foils," *Phys. status solidi*, vol. 219, no. 6, Mar. 2022, doi: 10.1002/pssa.202100628.

[237] S. Lu and D. D. L. Chung, "Viscoelastic behavior of carbon black and its relationship with the aggregate size," *Carbon N. Y.*, vol. 60, no. August, pp. 346–355, Aug. 2013, doi: 10.1016/j.carbon.2013.04.047.

[238] W. Bauhofer and J. Z. Kovacs, "A review and analysis of electrical percolation in carbon nanotube polymer composites," *Compos. Sci. Technol.*, vol. 69, no. 10, pp. 1486–1498, Aug. 2009, doi: 10.1016/j.compscitech.2008.06.018.

[239] M. J. Domínguez-Morales, F. Luna-Perejón, L. Miró-Amarante, M. Hernández-Velázquez, and J. L. Sevillano-Ramos, "Smart Footwear Insole for Recognition of Foot Pronation and Supination Using Neural Networks," *Appl. Sci.*, vol. 9, no. 19, p. 3970, Sep. 2019, doi: 10.3390/app9193970.

[240] N. Cui *et al.*, "Dynamic Behavior of the Triboelectric Charges and Structural Optimization of the Friction Layer for a Triboelectric Nanogenerator," *ACS Nano*, vol. 10, no. 6, pp. 6131–6138, Jun. 2016, doi: 10.1021/acsnano.6b02076.

[241] W.-W. Shen, H.-B. Mu, G.-J. Zhang, J.-B. Deng, and D.-M. Tu, "Identification of electron and hole trap based on isothermal surface potential decay model," *J. Appl. Phys.*, vol. 113, no. 8, pp. 1–7, Feb. 2013, doi: 10.1063/1.4792491.

[242] J. Li, F. Zhou, D. Min, S. Li, and R. Xia, "The energy distribution of trapped charges in polymers based on isothermal surface potential decay model," *IEEE Trans. Dielectr. Electr. Insul.*, vol. 22, no. 3, pp. 1723–1732, Jun. 2015, doi: 10.1109/TDEI.2015.7116370.

[243] D. W. Kim, J. H. Lee, J. K. Kim, and U. Jeong, "Material aspects of triboelectric energy generation and sensors," *NPG Asia Mater.*, vol. 12, no. 1, p. 6, Dec. 2020, doi: 10.1038/s41427-019-0176-0.

[244] N. Wang *et al.*, "Deep Trap Boosted Ultrahigh Triboelectric Charge Density in Nanofibrous Cellulose-Based Triboelectric Nanogenerators," *ACS Appl. Mater. Interfaces*, vol. 15, no. 1, pp. 997–1009, Jan. 2023, doi: 10.1021/acsami.2c16925.

[245] J. Peng *et al.*, "A composite generator film impregnated with cellulose nanocrystals for enhanced triboelectric performance," *Nanoscale*, vol. 9, no. 4, pp. 1428–1433, 2017, doi: 10.1039/C6NR07602E.

[246] C. Miao, L. Reid, and W. Y. Hamad, "Moisture-tunable, ionic strength-controlled piezoelectric effect in cellulose nanocrystal films," *Appl. Mater. Today*, vol. 24, p. 101082, Sep. 2021, doi: 10.1016/j.apmt.2021.101082.

[247] Y. Qi *et al.*, "Nanocellulose: a review on preparation routes and applications in

functional materials," *Cellulose*, vol. 30, no. 7, pp. 4115–4147, May 2023, doi: 10.1007/s10570-023-05169-w.

[248] P. Kaur *et al.*, "Nanocellulose: Resources, Physio-Chemical Properties, Current Uses and Future Applications," *Front. Nanotechnol.*, vol. 3, no. November, pp. 1–17, Nov. 2021, doi: 10.3389/fnano.2021.747329.

[249] N. Wang, E. Ding, and R. Cheng, "Thermal degradation behaviors of spherical cellulose nanocrystals with sulfate groups," *Polymer (Guildf).*, vol. 48, no. 12, pp. 3486–3493, Jun. 2007, doi: 10.1016/j.polymer.2007.03.062.

[250] G. CHAUVE, D. MAURAN, C. FRASCHINI, and J. BOUCHARD, "Critical discussion on the thermal behavior of sulfated cellulose nanocrystals," *TAPPI J.*, vol. 15, no. 6, pp. 383–391, Jul. 2016, doi: 10.32964/TJ15.6.383.

[251] S. Atifi, M. Mirvakili, C. A. Williams, M. M. Bay, S. Vignolini, and W. Y. Hamad, "Fast Self-Assembly of Scalable Photonic Cellulose Nanocrystals and Hybrid Films via Electrophoresis," *Adv. Mater.*, vol. 34, no. 12, pp. 1–9, Mar. 2022, doi: 10.1002/adma.202109170.

[252] T. Kasuga, T. Saito, H. Koga, and M. Nogi, "One-Pot Hierarchical Structuring of Nanocellulose by Electrophoretic Deposition," *ACS Nano*, vol. 16, no. 11, pp. 18390–18397, Nov. 2022, doi: 10.1021/acsnano.2c06392.

[253] W. Li, H. Tian, L. Ma, Y. Wang, X. Liu, and X. Gao, "Low-temperature water electrolysis: fundamentals, progress, and new strategies," *Mater. Adv.*, vol. 3, no. 14, pp. 5598–5644, 2022, doi: 10.1039/D2MA00185C.

[254] C. S. Widodo, H. Sela, and D. R. Santosa, "The effect of NaCl concentration on the ionic NaCl solutions electrical impedance value using electrochemical impedance spectroscopy methods," in *Www.Agilent.Com/Chem*, 2018, p. 050003. doi: 10.1063/1.5062753.

[255] Q. Luo, H. Shen, G. Zhou, and X. Xu, "A mini-review on the dielectric properties of cellulose and nanocellulose-based materials as electronic components,"

Carbohydr. Polym., vol. 303, no. October 2022, p. 120449, Mar. 2023, doi: 10.1016/j.carbpol.2022.120449.

[256] Y. Horikawa, S. Hirano, A. Mihashi, Y. Kobayashi, S. Zhai, and J. Sugiyama, "Prediction of Lignin Contents from Infrared Spectroscopy: Chemical Digestion and Lignin/Biomass Ratios of Cryptomeria japonica," *Appl. Biochem. Biotechnol.*, vol. 188, no. 4, pp. 1066–1076, Aug. 2019, doi: 10.1007/s12010-019-02965-8.

[257] Z. Li *et al.*, "Surface-functionalized cellulose nanocrystals (CNC) and synergisms with surfactant for enhanced oil recovery in low-permeability reservoirs," *Pet. Sci.*, vol. 20, no. 3, pp. 1572–1583, Jun. 2023, doi: 10.1016/j.petsci.2022.11.010.

[258] X. Yue *et al.*, "High acidity cellulose sulfuric acid from sulfur trioxide: A highly efficient catalyst for the one step synthesis of xanthene and dihydroquinazolinone derivatives," *RSC Adv.*, vol. 9, no. 49, pp. 28718–28723, 2019, doi: 10.1039/c9ra05748j.

[259] I. E. Imiete, L. Giannini, L. Tadiello, M. Orlandi, and L. Zoia, "The effect of sulfate half-ester groups on the mechanical performance of cellulose nanocrystal-natural rubber composites," *Cellulose*, vol. 30, no. 14, pp. 8929–8940, Sep. 2023, doi: 10.1007/s10570-023-05432-0.

[260] L. Segal, J. J. Creely, A. E. Martin, and C. M. Conrad, "An Empirical Method for Estimating the Degree of Crystallinity of Native Cellulose Using the X-Ray Diffractometer," *Text. Res. J.*, vol. 29, no. 10, pp. 786–794, Oct. 1959, doi: 10.1177/004051755902901003.

[261] S. Park, J. O. Baker, M. E. Himmel, P. A. Parilla, and D. K. Johnson, "Cellulose crystallinity index: measurement techniques and their impact on interpreting cellulase performance," *Biotechnol. Biofuels*, vol. 3, no. 1, p. 10, Dec. 2010, doi: 10.1186/1754-6834-3-10.

[262] Prateek, V. K. Thakur, and R. K. Gupta, "Recent Progress on Ferroelectric Polymer-Based Nanocomposites for High Energy Density Capacitors: Synthesis,

Dielectric Properties, and Future Aspects," *Chem. Rev.*, vol. 116, no. 7, pp. 4260–4317, Apr. 2016, doi: 10.1021/acs.chemrev.5b00495.

[263] S. Shafiei-Sabet, W. Y. Hamad, and S. G. Hatzikiriakos, "Ionic strength effects on the microstructure and shear rheology of cellulose nanocrystal suspensions," *Cellulose*, vol. 21, no. 5, pp. 3347–3359, Oct. 2014, doi: 10.1007/s10570-014-0407-z.

.

APPENDIX

A.1 Source Arduino code used to program Gravitational Force Actuator Machine (GFAM)

```
/* Driver controller for RS 5350372 */
   /* Raquel Barras, 2019 */

const int stepPin= 11;
const int dirPin = 12;
//const int ENABLE_SM = 6;

void setup() {
 //Serial.begin(9600);

  pinMode(stepPin, OUTPUT);
  pinMode(dirPin, OUTPUT);
}

void loop(){
 //digitalWrite(ENABLE_SM, LOW);                    //Enables the motor
  int cycles = 1000;                                 //   <<< Set here the number of cycles
  float rps = 10;                                    //   <<< Set here the number of rotations per second

  //2.5 = 0.5 Hz
  //5 = 1 Hz
  //10 = 2 Hz

  rotateDeg(cycles, rps);

  //digitalWrite(ENABLE_SM, HIGH);                   //Disbales the motor
  while(1) { }
}

void rotateDeg(long long int cycles, float rps){
  int oneRevolution = 6400;                         //when microsteping in sixteen 200*32)
  long long int steps = (cycles*oneRevolution);
  float usdelay = (156.25*(1/rps));

  for(long long int x = 0;; x++){       /* The machine will run indefinitely. Use this instead to program a
limited number of cycles:  for(long long int x = 0;x<cycles; x++){         */

      digitalWrite(stepPin, HIGH);
      delayMicroseconds(usdelay);

      digitalWrite(stepPin, LOW);
      delayMicroseconds(usdelay);
    }}
```

A.2 Source Arduino code used to program Pneumatic Force Actuator Machine (PFAM)

```
/* Driver controller for Pneumatic Force Actuator Machine - PFAM */
   /* Raquel Barras, 2022 */


int dataPin = 10;  // set data output pin name

void setup() {

  pinMode(dataPin, OUTPUT);
}

void loop() {

  //Choose frequency: 1750 = 0.5Hz || 750 = 1Hz ||  250 = 2Hz  ||  83 = 3 Hz

  int a = 1750;  // 0.5 Hz
  int b = 750;   // 1 Hz
  int c = 250;   // 2 Hz
  int d = 83;    // 3 Hz

  digitalWrite(dataPin, HIGH); // turn on
  delay(250); // in millisec
  digitalWrite(dataPin, LOW); // turn off
  delay(b);

}
```

A.3 Counting the number of CFs in a yarn

The SEM images used to estimate the number of CFs in one CF yarn.

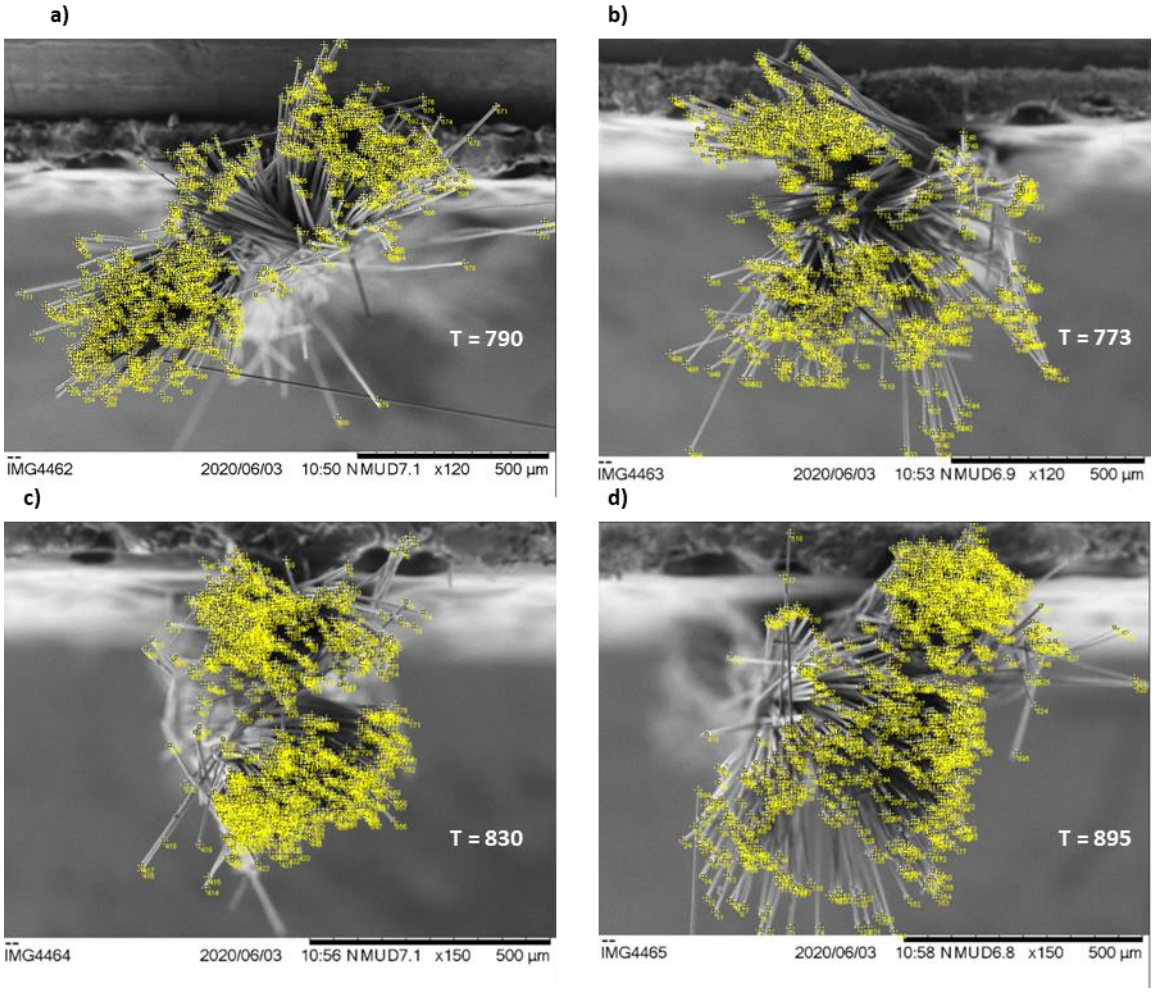

A.4 Energy Efficiency

The energy efficiency (η) of the devices is given by the ratio between the output of converted electrical energy and the input of mechanical energy (Equation 8.23).

$$\eta = \frac{E_{electric}}{E_{mechanic}} \times \ 100\ \% \qquad \text{Equation 8.23}$$

The electrical energy can be obtained using Equation 8.24, where the integral of current squared is the area of the peaks corresponding to the contact and separation processes while using the optimum load resistor R.

$$E_{electric} = \int_{start}^{end} I^2\ R\ dt \qquad \text{Equation 8.24}$$

The area of the peaks was estimated using the software Origin™, and shown in the figure above, with the area considered corresponding to the yellow shadowed regions.

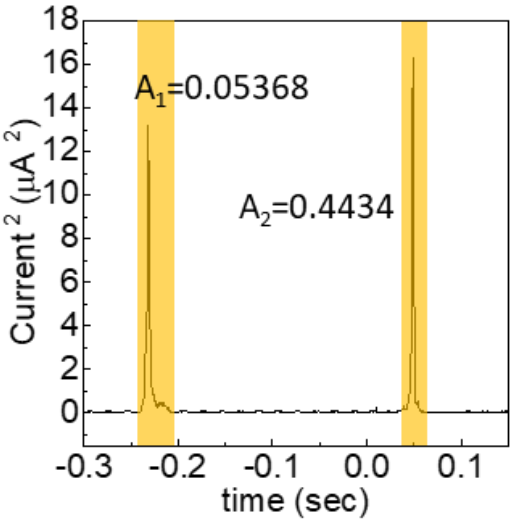

So the value of electric energy can be obtained through the following expression:

$$E_{electric} = \int_{min}^{max} I^2\ R\ dt = (0.05368 + 0.4434) \times 10^{-12} A^2\ sec \times 20 \times 10^6 \Omega$$
$$= \ 1.9604 \times 10^{-6}\ A^2\ \Omega\ sec$$

In the case of mechanical energy, there are several ways to estimate the energy of impact, two of them are shown in Equation 8.25 and Equation 8.26:

$$E_{mechanic\,1} = F \times S \qquad \text{Equation 8.25}$$

Where F is the impact force and S the surface area of contact.

$$E_{mechanic\,2} = mgh \qquad \text{Equation 8.26}$$

Where m is the mass, g is the gravitational constant and h the separation distance between the sample.

It's worth mentioning that both values obtained are underestimations from the real mechanical energy. In the case of $E_{mechanic\,1}$, the area is an estimation, and the force of impact should be higher than the force delivered from the pressure of the piston at rest (utilized for the calculus). In the case of $E_{mechanic\,2}$, the energy is also underestimated, since the impact of PFAM on the sample is not resulting from a free-falling object but from the pressure admitted to the cylinder. The calculus considered the best sample, doped with 2% wt. cCFs (2%wt cCFs Seys-TENG) and the values from the parameter used are presented in the table below:

F	30 N
S	0.0005616 m^2
R	20 MΩ
m	0.0147 kg
g	9.8 m/s^2
h	0.02 m

The values of mechanical energy obtained with the two methods are the following:

$$E_{mechanic\,1} = F \times S = 30\ N \times 0.0005616\ m^2 = \ 0.016848\ N/m^2$$

$$E_{mechanic\,2} = m\ g\ h = \ 0.0147 \times 9.8 \times 0.02 = \ 0.0028812\ kg\ m\ s^{-1}$$

And the values encountered for the energy efficiency of the Seys-TENGs using the two expressions are:

$$\boldsymbol{\eta_1} = \frac{\boldsymbol{E_{electric}}}{\boldsymbol{E_{mechanic}}} \times \ \mathbf{100}\ \% = \ \mathbf{0.011635802}\ \%$$

$$\boldsymbol{\eta_2} = \frac{\boldsymbol{E_{electric}}}{\boldsymbol{E_{mechanic}}} \times \ \mathbf{100}\ \% = \ \mathbf{0.068041094}\ \%$$

2023

RAQUEL ALEXANDRA ANTUNES BARRAS

YARN SHAPED FUNCTIONAL NANOCOMPOSITES FOR TRIBOELECTRIC ENERGY HARVESTING SYSTEMS